Thèse n° 9511

Molybdenum oxide as a case study for the diagnosis of carrier selective contacts in silicon heterojunction solar cells

Présentée le 13 mai 2022

Faculté des sciences et techniques de l'ingénieur
Laboratoire de photovoltaïque et couches minces électroniques
Programme doctoral en photonique

pour l'obtention du grade de Docteur ès Sciences

par

Julie Amandine DREON

Acceptée sur proposition du jury

Prof. C. Moser, président du jury
Prof. C. Ballif, Dr M. G. Boccard, directeurs de thèse
Prof. A. Kaminski-Cachopo, rapporteuse
Prof. J. Bullock, rapporteur
Prof. N. Grandjean, rapporteur

École
polytechnique
fédérale
de Lausanne

2022

Contents

Remerciements

Avant d'entrer au coeur de ce manuscrit de thèse, je tiens à remercier chaleureusement un grand nombre de personnes, qui ont contribué, de près ou de loin, à la réalisation de ce travail.

Je remercie Christophe Ballif pour m'avoir fait confiance et accepté dans ses rangs au PV-lab. Sa motivation perpétuelle a été pour moi une source d'énergie. Merci à Mathieu Boccard, mon co-directeur, qui a donné naissance à ce projet de thèse et a su me guider au travers de nos expériementations diverses et variées en me partageant ses connaissances. Je n'oublierai pas ton assiduité pour le rappel annuel des dégustations de vin à l'hôtel de ville !
Merci aux membres de mon jury de thèse, Pr. Christophe Moser, Pr. Anne Kaminski-Cachopo, Pr. James Bullock et Pr. Nicolas Grandjean, qui ont pris du temps pour évaluer ce travail de thèse et apporter leurs contributions.
Merci également à Aïcha Hessler pour son soutien et pour l'organisation des divers projets au sein du laboratoire.

Je remercie chaleureusement Karine et Marie-Claude pour leur soutien administratif qui m'a été très précieux, et qui n'ont jamais manqué de garder un caractère humain face à toutes les situations. Je tiens à remercier Xavier et Sylvain pour leur services et soutien technique indispensable, tel que l'achat d'un précieux escabeau (et qui, avouons-le, est bien utile à tout le monde !) ou encore le partage de mets délicats ;). Un grand merci à Cédric, Aymeric et Nicolas pour leurs infaillibles pouvoirs de réparation, construction et amélioration de toutes les machines du laboratoire, sans oulier, bien sûr, l'inflexible police Apéro ;)). Sans votre suivi technique, cette thèse n'aurait pas aboutit aux même résultats. Merci à Joël, de l'atelier mécanique, pour nos petites pauses, et qui a toujours su trouver une solution, souvent avec humour ;), à mes demandes. Merci à Hassan pour toutes nos discussions entre les couloirs, et pour son support informatique grâce auquel des données cruciales ont pu être sauvées. Tu n'oublieras sûrement pas pas le nombre d'écrans bleus de mon ordinateur :p.

Merci à tous les membres du Microcity Activity Department (MAD), Jean, Jonathan T., Jonathan C., Chun-Min :), Hassan, Julien G., Luca A., Baptiste. Ensembles, nous avons pu mener de beaux projets et faire vivre cette association.

Je tiens à remercier tous mes amis et collègues au PV-lab et CSEM, Jean, Vincent, Deniz, Julien H., Luca A., Caroline, Jonathan T., Matthias, Peter, Florent, Quentin J., Quentin G., Jérémie,

Joshua, Philippe, Mario, Audrey, Sofia, Ezgi, Joël, Franz, Janina, Samira, Marina, Jordan, Lionel, Nicolas, Olatz, Luca G., Fabiana, Alejandro, Marion, Laurie-Lou, Gabriel, Delphine, Bertrand, Nicolas, Jonathan C., Brahim, et tous les autres. Je n'oublierai pas nos nombreuses collaborations, et tous nos échanges.
Merci Jean pour ton amitié, tes services, ton enthousiasme, nos débats, nos sorties, nos repas, tes "initiations", sans oublier ton coaching sportif ! Vincent, merci à toi pour tes innombrables services Kai ;). Ta culture et tes petites blagues ont bien alimenté nos discussions ;) Merci à Luca A., avec qui j'ai partagé un sujet de thèse, un bureau, des interrogations et de la joie au cours de cette thèse. Ces 4 années de labeur nous auront coûté une vie chère, celle de notre bon vieux (en fait... pas si vieux !) Marley. Merci à Luca G. pour tous nos rires et nos partages dans les moments difficiles comme joyeux. Attention de ne pas abuser sur le café ;). Merci à Matthias pour m'avoir introduit au savoir vivre Suisse, et pour les sorties inoubliables à Lausanne ! Merci à Marion pour sa positivité inébranlable, nos conversations interminables et nos confidences. Tu auras rendu ce séjour au PV-lab encore plus coloré ! Merci enfin à Audrey, avec qui j'ai partagé de longues discussions et qui a su me comprendre et m'entendre sans me juger. Je n'oublierai pas tes conseils. Cette fin de thèse n'aurait pas été la même sans notre amitié.

I would like to warmly thank Caroline Hain for her big help in reviewing the grammar and spelling of this thesis and who worked on a Sunday night for this.

Merci aux étudiants que j'ai pu encadrer au cours de cette thèse, pour leur motivation et leur travail scientifique.

Un chaleureux merci à Baptiste et Julien G. pour m'avoir introduit à leurs collègues et amis, Rita, Margaux, Maxime, Lena, Pieter, Gozden, Hossein, Navid, Claire, et bien d'autres. J'ai beaucoup apprécié toutes ces belles soirées et ces bons moments passés ensmbles.

A particular thanks to Stephanie Essig, who introduced me to the world of PV during my Master thesis and helped me with her guidance, her strong motivation, her respect and her honesty.

Merci à tous mes vieux amis, Houda, Omay, Aloïs, Antoine, Daphnée, Maxime, Pierre, Thomas, Guillaume, Alexandra, Maxence, Gaëlle, Hélène, Eliot, sur qui j'ai toujours pu compter pour passer un moment agréable et déconnecter. Thank you to my friends in Netherlands, Michela and Guido, Abhishta and Letizia, Shyam, Akshada and Yigitcan, that I don't forget :)

Enfin, je voudrais remercier chaleureusement toute ma famille, qui m'a toujours soutenue dans mes choix, et m'a toujours accueillie dans son petit paradis de sérénité ou j'ai pu me ressourcer. Vos questions, discussions, et votre constant intérêt pour les sciences (et autre !) ont toujours été pertinents . Je tiens à remercier particulièrement mes parents sans qui je n'en serai pas là aujourd'hui.
Merci enfin à Julien G. qui m'a supporté pendant une grande partie de cette thèse. Nos

discussions (sérieuses), mais aussi tes blagues et ton imagination débordante m'ont souvent fait m'évader de la vie quotidienne.

Résumé

Les enjeux environnementaux actuels imposent une transition énergétique rapide. La puissance installée issue des énergie renouvelables devrait augmenter de 50 % dans les 5 prochaines années, et les dernière projections prévoient que le photovoltaïque (PV) sera la source d'énergie prédominante. Avec des efficacités record et un processus de fabrication simple, les cellules à hétérojonction à base de silicium (SHJ) ont le potentiel de devenir la technologie principale pour un déploiement mondial du PV. Cependant, plusieurs défis restent encore à relever, en particulier la diminution de l'absorption parasite dans les couches de silicium amorphe hydrogéné a-Si:H utilisés comme contacts dans les SHJ. L'oxyde de molybdène substoechiometrique $MoO_{3\text{-}x}$ s'avère être un des matériaux alternatif les plus prometteurs pour remplacer ce matériaux , de part sa transparance et ses propriétés électroniques excellentes. Cette thèse traite l'analyse et le développement des contacts sélectifs pour les trous à base de $MoO_{3\text{-}x}$, dans les SHJ. La passivation, la sélectivité et les propriétés de transport de ce contact sont évaluées en variant différent paramètres, en comparant avec le contact standard à base de silicium amorphe, ainsi qu'en utilisant des méthodes de caractérisation poussées adaptée pour l'étude des cellules SHJ.
En amincissant la couche de $MoO_{3\text{-}x}$ de 10 nm (épaisseur standard à cette date) à 4 nm, une passivation et une selectivité excellente ont pu être maintenues dans le contact. Un gain en courant de 1.3 $mA\,cm^{-2}$ comparé au contact (*p*)a-Si:H standard a été obtenu, haussant l'efficacité (certifiée) de ce type de cellule sérigraphiée de 2x2 cm^2 à 23.5%, actuellement le record mondial, et surpassant celle des contacts (*p*)a-Si:H du laboratoire. L'utilisation de couches de $MoO_{3\text{-}x}$ plus fines que 4 nm a induit une perte de performance. L'utilisation de diverses méthodes de caractérisation, parmi lesquelles une nouvelle méthode basée sur le modèle développé par Roe *et al.*, les pertes ont été identifiées à une diminution de la passivation combinée à une dégradation de la sélectivité provoquant une réduction du courant de trous (majoritaires) et une augmentation du courant d'électrons parasites (minoritaires) au contact sélectif pour les trous, en raison de la réduction du travail de sortie du $MoO_{3\text{-}x}$.
Le dopage et la puissance de dépôt de la couche d'ITO ont ensuite été modifiés et testé en combinaison avec différentes épaisseurs de couches de $MoO_{3\text{-}x}$ afin d'estimer la longueur d'écrantage de ce dernier vis à vis du travail de sortie de l'ITO. Alors que les couches de $MoO_{3\text{-}x}$ de 4 nm se sont avérées suffisemment épaisses pour écranter efficacement le travail de sortie, celles de 2 nm ont été influencées par ce dernier. L'ITO déposé à la plus basse puissance a permis d'augmenter significativement le *FF* ($\sim 1\,\%_{\text{absolute}}$). Le travail de sortie global du contact sélectif pour les trous ainsi que celui de l'ITO ont pu être estimé à 5.0 eV et 4.6 - 4.8

eV respectivement, en utilisant une méthode d'ajustement des courbes *J-V* expériementales, basée sur le formalism de Roe *et al.*. Une couche de a-SiO_x:H déposée par PECVD, communément utilisée à l'avant des cellules à hétérojonction pour augmenter leur J_{SC}, a provoqué la dégradation des cellules à base de MoO_{3-x}. Cette dernière a été attribuée à la présence d'hydrogène dans le plasma, connu pour réduire chimiquement le MoO_{3-x}.
Les cellules à heterojonction intégrant du MoO_{3-x} se sont montrées étonnemment stable dans le temps. L'étape de recuit parfois effectuée avant le dépôt de MoO_{3-x} a s'avère provoquer un léger abaissement de la passivation fournie par le contact, mais a également prouvé le protéger de la dégradation de la sélectivité généralement observé lors de procédés réalisés entre 130 °C et 170 °C pour ce type de contact. A l'image des SHJ standard, une injection forcée du courant en sens direct et dans le noir ont conduit à une augmentation conséquente du *FF* ($\sim 1.3\,\%_{absolute}$) des dispositifs. Des cellules ont ensuite été encapsulées et dégradées sous rayonnement UV, ayant pour conséquence une dégradation sévère de la sélectivité.
Un examen de la littérature existante traitant des mécanismes de transport pouvant avoir lieu dans les contacts étudiés dans cette thèse a été mené et rassemblé dans le dernier chapitre de ce mansucrit, dans le but de mettre en parallèle avec des mesures de courbes *J-V* effectuées à différentes températures (de -160 à 80 °C) sur des SHJ intégrant du MoO_{3-x}. L'évolution du V_{OC} et du *FF* avec la température s'est avérée similaire à celle observée pour les SHJ standard, confirmant l'analyse du transport préalablement proposée en comparant les diagrammes de bandes des deux structures à 25 °C et basse température. Une extension de la méthode basée sur le modèle de Roe *et al.* est également suggérée pour identifier rapidement une perte par sélectivité via l'analyse des courbes *J-V* présentant une courbe en S.

Mots clés: cellules solaires, silicium, hétérojonctions, oxyde metalliques, métaux de transition, oxyde de molybdène, contact sélectifs, caractérisation, courbe en S, measures en température, basse températures.

Abstract

Environmental challenges impose a rapid energy transition. The renewable power capacity is expected to increase by 50 % in the next 5 years, and recent scenarios plan that photovoltaics (PV) will be leading the new energy sources. Combining high efficiencies and simple fabrication process, silicon heterojunction (SHJ) solar cells have the potential to be the main technology for PV world wide deployment. Challenges yet remain, notably due to the use of amorphous silicon as contact layers. MoO_{3-x} appears to be one of the most promising alternative to tackle some of these challenges, owing its transparency and excellent electronic properties. This thesis focuses on the analysis and development of MoO_{3-x}-based hole contact for SHJ solar cells. Contact passivation, selectivity and transport are assessed by varying the contact parameters, using standard p-type amorphous silicon as a benchmark, and using advanced characterization adapted for contact-limited SHJ.

By thinning down the MoO_{3-x} layer from the standard 10 nm thickness used for such contact to 4 nm, excellent passivation and selectivity were maintained. A current gain of 1.3 $mA\,cm^{-2}$ was obtained as compared with the standard amorphous silicon contact. A 2x2 cm^2 screen-printed certified 23.5% world record device was achieved through this analysis, outperforming the reference device using amorphous silicon. Further thinning the MoO_{3-x} layer provoked several losses. Using many characterization methods combined to fittings using an innovative analytical description of contact-limited solar cells proposed by Roe *et al.*, we could conclude that these losses stem from a passivation decrease combined with a selectivity reduction provoking a drop of the majority hole and an increase of parasitic electron currents in the contact, due to the reduction of the contact's work function.

Doping and deposition power of the ITO top layer was then modified and tested over several MoO_{3-x} layer thicknesses, to estimate MoO_{3-x} screening length towards ITO work function and investigate the influence of ITO on transport. 4-nm-thick MoO_{3-x} showed to efficiently screen the ITO work function on the tested range while the 2-nm-thick-MoO_{3-x}-based contact was affected. The ITO deposited at low power drastically enhanced the *FF* ($\sim 1\,\%_{\text{absolute}}$). In situ work function estimation of the ITOs (4.6 to 4.8 eV) and hole contact ($\sim$ 5.0 eV) was conducted using fittings according to Roe's formalism. PECVD-deposited-a-SiO_x:H, commonly used on top of fully-processed SHJ to boost the J_{SC}, degraded the MoO_{3-x}-based devices *FF*, ascribed to the presence of H in the plasma reducing MoO_{3-x}.

MoO_{3-x}-based devices showed to be remarkably stable over time. An annealing step performed on solar-cell samples prior to MoO_{3-x} deposition was shown to slightly damaged the passivation but protected MoO_{3-x} selectivity degradation for processes temperature up to

170 °C. Similarly to standard SHJ devices, current injection in dark in forward bias significantly improved the *FF* of the devices by ~ 1.3 $\%_{\text{absolute}}$. The cells were encapsulated and degraded by UV radiations, which showed to strongly affect selectivity.
A review of main transport mechanisms was gathered in the last chapter to parallelize with temperature-dependent *J*-*V* measurements (-160 to 80 °C) performed for MoO_{3-x}- and (*p*)a-Si:H-based SHJ. V_{OC}(T) and *FF*(T) evolution showed similar trends in both cases, confirming the expected transport behavior from comparing band-diagrams. An extension of the method based on Roe *et al.* model is proposed to rapidly identify selectivity loss from S-shaped *J*-*V*, and distinguish between contact and carrier selectivities.

Keywords: solar cells, silicon heterojunction, transition metal oxide, molybdenum oxide, selective contacts, characterization, S-shape, temperature-dependent measurements, low temperature.

List of acronyms

ALD	atomic layer deposition.
ARC	anti-reflective coating.
AZO	ZnO:Al.
CBO	conduction band offset.
CEA	commissariat à l'énergie atomique et aux énergies alternatives.
CSEM	Centre suisse d'électronique et de microtechnique.
DARC	double anti-reflective coating.
EDX	Energy-dispersive X-ray spectroscopy.
EELS	Electron energy-loss spectra.
EQE	External quantum efficiency.
F-J	front-junction.
FBC	front-back contacted.
FCA	Free carrier absorption.
FTIR	Fourier-transform infrared spectroscopy.
FTPS	Fourier-transform photocurrent spectroscopy.
FW	forward.
HAADF	high-angle annular dark-field.
HF	hydrofluoric acid.
HSM	high stretching mode.
HTL	hole selective layer.
HWOSD	hot wire oxidation-sublimation deposition.
IBC	interdigitated back contacts.
IEA	International Energy Agency.
IPCC	Intergovernmental Panel for Climate Change.
IQE	Internal Quantum Efficiency.

IR	infrared.
ISFH	Institute for Solar Energy Research in Hamelin.
ITO	tin-doped indium oxide.
LCOE	levelized cost of electricity.
LS-OC	open-circuit light soaking.
LS-SC	short-circuit light soaking.
LSM	low stretching mode.
MPP	maximum power point.
NG	narrow-gap.
NIR	near infra-red.
OC	open-circuit.
OES	optical emission spectroscopy.
PC1D	Solar cell modelling program in 1D.
PDS	photocurrent deflection spectroscopy.
PECVD	plasma-enhanced chemical vapour deposition.
PL	Photo-luminescence.
PV	photovoltaic.
PVD	physical vapour deposition.
R-J	rear-junction.
RCA	Radio Corporation of America.
SC	short-circuit.
SG	standard-gap.
SHJ	Silicon Heterojunction.
SRH	Shockley-Read-Hall.
STC	standard test conditions (25 °C, 1000 $\mathrm{W\,m^{-2}}$).
STEM	Scanning Transmission Electron Microscopy.
TAT	trap (or thermally) assisted tunnelling.
TC	temperature coefficient.
TCO	transparent conductive oxide.
TEM	Transmission Electron Microscopy.
TLM	Transfer Length Measurement.
TMB	trimethylborane gas: $B(CH_3)_3$.
TMO	Transition Metal Oxide.

UV	ultraviolet.
VBO	valence band offset.
XRD	X-ray diffraction.
ZTO	tin-doped zinc oxide.

List of Figures

List of Tables

1 Introduction

1.1 Global challenges

The annual global energy production is exponentially increasing, and currently amounts for 162 200 TWh, among which nearly 155 000 TWh originate from fossil fuels, and 15.7 % are low-carbon sources [BP 2020]. In parallel, the annual CO_2 emission approaches 37 billion tons per year plus other stronger greenhouse gases such as methane, almost entirely emitted by the high-carbon energy sources [GCP 2021]. The latest Intergovernmental Panel for Climate Change (IPCC) report, released in August 2021, shows that greenhouse gases and air pollutants emission related to human activity is mainly responsible for the actual climate change of ~ +1.1 °C compared with pre-industrial times. It is expected to reach or exceed 1.5 °C in the next 20 years. This is likely to amplify the extremes climatic events we began to experience, such as intense rainfalls with flooding, droughts, sea level rise, massive species extinction, permafrost thawing, heatwaves, ocean acidification, and retreat of glaciers [IPCC 2021]. A business as usual model predicts a world temperature increase over +4 °C by the next 80 years, critical for most of the earth life. In another report, IPCC estimated that renewable energies must supply 70% to 85% of global electricity and 49% to 67% of global primary energy for the next 30 years to restrict the global warming to 1.5 °C [IPCC 2018]. The transition already (slowly) started, and the International Energy Agency (IEA) recently predicted, following the new policy roadmaps (to respect the 2015 Paris agreements notably), an annual increase of 2.1 % in global electricity consumption over the next 20 years, provoking an electricity production rise from 28 000 TWh to 40 000 TWh [IEA 2019, Newell 2020, Razzaq 2022]. The renewable power capacity is also expected to increase by 50 % in the next 5 years, and several scenarios predict that photovoltaic (PV) may be the next leader renewable energy source [IEA 2019, LUT 2020]. Photovolataics is a low-carbon energy source (around 40 $gCO_2eq\,kW^{-1}\,h$ in Switzerland, and lower values when clean electricty for the production is used), in addition of being today the cheapest one with a module price around 0.20 $\$/W_p$ [ITRPV 2021] (a temporary bottleneck in the supply of glass, polysilicon and in transport capacity has raised the price of modules to 0.30 $\$/W_p$ in 2021-2022). Yet, the actual global cumulative PV capacity reaches 512.3 GW, which is far from the 2 TW to 10 TW which needs to be installed by 2030, as targeted by the IPCC

[IPCC 2018, Razzaq 2022]. Therefore, further reducing costs and developing this technology is essential to manage the energy transition.
Photovoltaic modules price holds a high learning rate around 23% since 1976, with a total decline of 99.6% over the whole period [Victoria 2021], when energy from coal or nuclear plants has not become cheaper and even increased. Up-scaling is then largely favorable for PV and is a key factor for further cost reduction in this technology. In parallel, to decrease levelized cost of electricity (LCOE), increasing the power conversion efficiency is the most effective way, in addition of minimizing the resources and raw materials consumption [Peters 2019]. For instance, in 2020, a module price reduction by 20% leads to a 3% decrease in the LCOE while a 20% increase of the module efficiency leads to a 20% LCOE reduction [Yu 2018]. Improving solar devices efficiency is thus the mainstay to meet the required PV installed capacity.

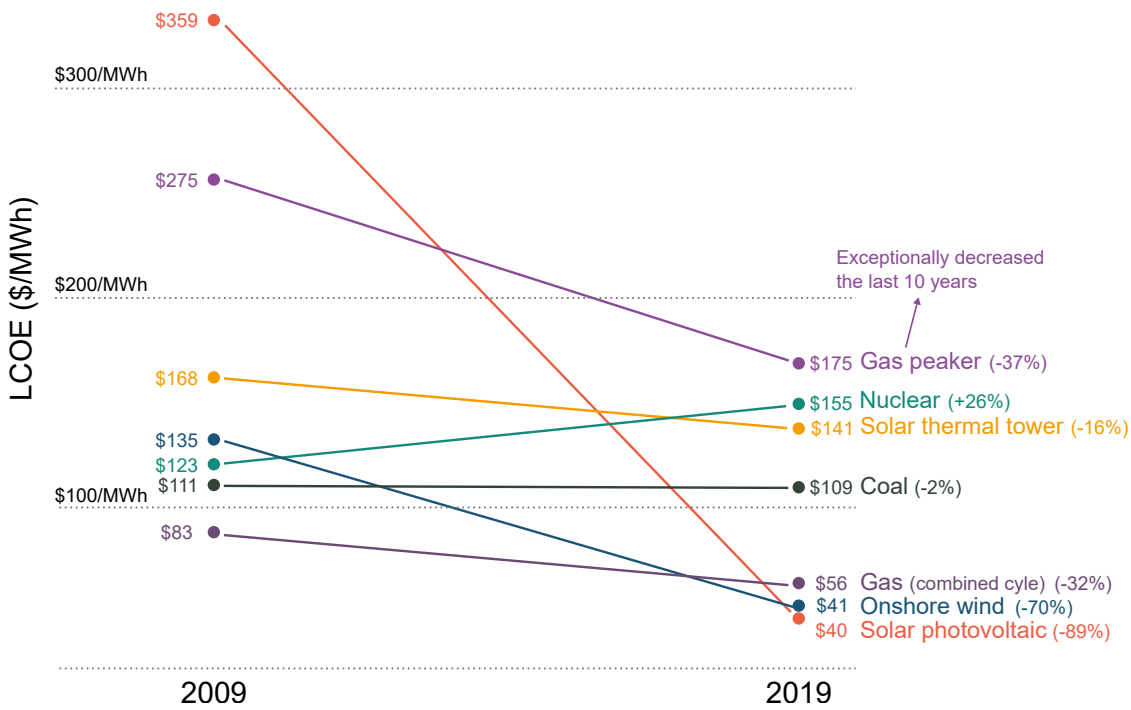

Figure 1.1: LCOE evolution of different energy sources, between 2009 to 2019. Adapted from Our World in Data.[Ray 2021]

1.2 Silicon heterojunction solar cells

1.2.1 Main silicon-based solar cells current industrial technologies

Best technologies for such a world deployment are the silicon-based ones, which already hold a 90% of the global PV market share [ITRPV 2020, Wilson 2020], as Si is a cheap, abundant, stable and non-toxic material, and whose electronic properties knowledge is excellent owing to the early microelectronics developments. The main commercialized technology was the Al-BSF (Aluminum Back surface Field) recently replaced by PERCs (Passivated Emitter and

Rear Contact) solar cells, represented and described hereunder. Recently, technologies like silicon heterojunction or poly-silicon-based solar cells have emerged in the industrial market. Few years ago, solar cells used in tandems (multi-junction devices) arose to push beyond the 29.4 % crystalline silicon-based single junction solar cells theoretical efficiency limit calculated by Shockley and Queisser [Shockley 1960], and already gave promising laboratory results.

1.2.2 Brief historical evolution

Al-BSF were the first worldwide industrialized solar cells, and main production is based in China. It is a homojunction-based technology, in which a $p-n$ junction (contact between hole-rich and electron-rich layers) is created by diffusion of dopants in the absorber Si-substrate (see Fig. 1.2). At the back of the cell, an Al layer is deposited and diffused in the Si absorber, generating a p-type doping, which induces a field effect passivation. With continuous improvement in silicon wafer quality, the Al/Si interface (and more generally at the metal/Si interface) of the Al-BSF cell became a clear factor limiting efficiency increase, prompting a change to the novel structures. As a consequence, the technology has nearly completely disappeared [ITRPV 2021], replaced by PERC, the current mainstream technology. The latter also uses diffused homojunctions, which allowed to easily adapt the production and use the same equipment, however it integrates dielectric layers to passivate the Si surfaces. Local contacts are then opened in the rear dielectrics to enable charge extractions and minimize metal/Si direct contact. However, surface recombination at the local rear contacts cannot be completely removed, and the solar cells till suffer from band-gap narrowing and Auger recombinations due to the highly doped diffused contacts. Additionally, with metal contacts on both sides, industrial processes with limited spatial resolution will likely limit the mainstream PERC solar cell efficiency to 23.5- 24%.
In the race to reach higher efficiencies, silicon heterojunction is a promising technology that circumvents both of these limitations [Descoeudres 2011, DeWolf 2012, Masuko 2014, Adachi 2015, Yoshikawa 2017, Ru 2020]. Most of the SHJs use stacks of intrinsic and doped hydrogenated amorphous silicon (a-Si:H) as passivating and carrier-selective layers [Tanaka 1992], which will be referred to as "standard SHJ" in this thesis. These stacks provide excellent surface passivation and selectivity thanks to the high hydrogen content in these layers and dopability of amorphous silicon, respectively [Le Comber 1970, Taguchi 2000, **?**]. In combination with a TCO layer, required when using resistive a-Si:H layers as selective contacts, for the front lateral carrier collection to the Ag grid, the Si isolation from the metal electrode is physically and fully achieved. Furthermore, what makes them so promising for future global industrialization is their simple 5-step fabrication process, in respect to PERC fabrication, and straightforward adaptation to include bifacial architectures, which have the potential to boost module efficiency by 20 20 $\%_{\text{relative}}$. Since 2015, standard SHJs have held the world record for solar cell efficiency in interdigitated back contacts (IBC) configuration, with the record increasing to 26.7% in 2017 [Adachi 2015, Yoshikawa 2017]. Since then, the number of companies industrializing standard SHJs have been continuously increasing all over the world. European political actors have also seen in SHJ development an opportunity to re-localize energy production and

important European projects and subsidizes emerged to reach this goal. Very recently, leading Chinese companies have started to implement SHJ in their R& D and industrial plans. In the last months, they announced an impressive efficiency of 26.3% in a front-back contacted (FBC) architecture, holding the current FBC solar cell world record [Longi 2021].

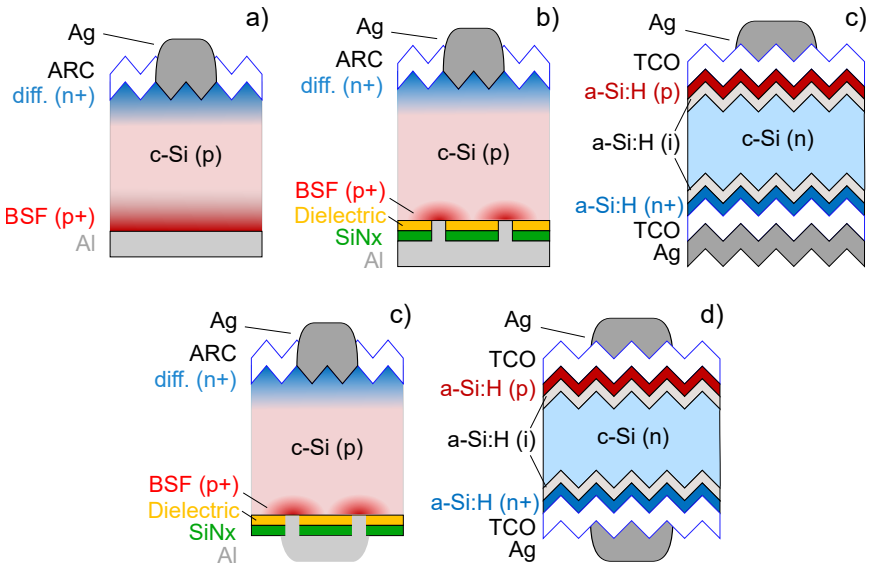

Figure 1.2: Transversal view of: a) an Al-BSF, b) a PERC, c) a standard SHJ solar cells, and d) and e) bifacial PERC and SHJ respectively. They are all represented in a front junction configuration.

1.2.3 Challenges for the global development of SHJ solar cells

Despite the high performances achieved, further increasing and stabilizing the high efficiency of SHJ is required to reduce energy costs.

First, in spite of their higher efficiency potential, their production cost stands above PERCs. In their recent review on the topic, Razzaq *et al.* analyzed that the front and rear Ag metallization is the main process responsible for the cost difference [Razzaq 2022]. Additionally, the process tools would need to be entirely replaced in companies already processing PERC, since both fabrication methods are significantly different, which represents a supplementary obstacle. SHJ's low thermal budget of around 250 °C is an asset for low cost, however their poor tolerance towards heating imposes the use of costly low temperature Ag paste.

Second, from a physical point of view, a couple of challenges remain to be tackled. The excellent passivation performance of this contact architecture often comes at the expense of carrier transport, in comparison with solar cells based on silicon homojunctions, which translate into resistive losses. This effect stems from the lower conductivity of doped a-Si:H compared to crystalline silicon, band offsets between these two crystalline phases [Shah 2010, Van sark 2012], and the formation of an opposing Schottky contact between a-Si:H and the TCO [Centurioni 2003, Zhao 2008, Bivour 2013] (see Fig. 1.4 and section 1.3 for more information). In addition, the use of a-Si:H (band-gap of 1.7 eV) on the light-incoming side of

the device leads to parasitic absorption below 500 nm [DeWolf 2012, Paduthol 2018]. Photons that are parasitically absorbed in the intrinsic a-Si:H ((*i*)a-Si:H) film can partly contribute the cell's short circuit current density (J_{SC}), however photons absorbed in the doped a-Si:H layer are lost [Holman 2012, Paduthol 2018]. This typically causes current density losses of up to 2.8 mA cm^{-2} compared to the one of a cell with an ideal cell front-side.

1.2.4 Replacement of the doped a-Si:H layers by alternative contacts

One highly investigated strategy to overcome this parasitic absorption is to replace the (*i*)a-Si:H and doped a-Si:H front layers by more transparent carrier selective contacts. Silicon-based materials (in their nano-crystalline phase and/or alloyed with carbon and oxygen), and TMO are the most widely followed approaches, alongside a few other organic and inorganic materials. Integration of such alternative materials as contacts in SHJs is also an interesting approach to further understand SHJ contact behavior. TMOs, generally possessing wide band gaps, are likely to be the most promising substitute due to their uncommon electronic properties and high transparency. However, even though theoretically possessing the perfect band alignment, the interface properties of the contact with Si appears to be complex in practice. Many challenges remain to be solved to fully benefit from these materials.
This thesis focuses on the study of one of the most promising materials of this family, sub-stoichiometric molybdenum trioxide (MoO_{3-x}), due to its wide band-gap, high work function and n-type properties. Here, MoO_{3-x} is used use as a front hole selective contact for (*n*)c-Si-based SHJ solar cells, to replace the standard (*p*)a-Si:H layer. The rear side electron contact is not replaced in this study. A schematic transversal representation of the cell is presented in Chapter 2.

1.3 Solar cell working principle

The theoretical maximum power conversion efficiency of a single junction photovoltaic device has been thermodynamically calculated by Shockley and Queisser to be 31.9% for c-Si(bandgap of 1.12 eV) [Shockley 1960]. Including the intrinsic Auger recombinations limits the practical efficiency to 29.4%-29.6% [Richter 2013, Haug 2021]. To reach this value, optical losses have to be minimized and photo-generated carrier collection maximized.

1.3.1 Absorption and photogeneration

When illuminated by the solar spectrum, the Si wafer (the absorber) receives photons that can be reflected, transmitted or absorbed at the surface. Since Si's refractive index is near 4 at 600 nm, losses by reflection exceed 30% over the full spectrum. The application of anti-reflective coatings, generally transparent layers with a refractive index in the range of 1 to 4 (typically around 2), and surface texturization can significantly improve light coupling. The combination of the two methods can reduce reflection losses by a factor 10 over 400-1000 nm, and double

or triple anti-reflective layers can further decrease losses to 1% over this range, increasing the chances for photon absorption in Si.
Photons with a higher energy than the semiconductor band-gap will be absorbed and excite electrons from the valence to the conduction band. The semiconductor is transparent to photons with a lower energy than the band-gap (transmittance losses), and photons with higher energy than the band gap create "hot" carriers, which lose their excess energy by thermalizing (thermalization loss). These two losses are the main phenomena responsible for the aforementioned thermodynamic theoretical limit aforementioned, accounting for 23% and 33%, respectively. The carrier concentration in the illuminated semiconductor can be expressed as:

$$n = n_0 + \Delta n = N_c \exp\left(\frac{E_{Fn} - E_c}{k_B T}\right) \tag{1.1}$$

$$p = p_0 + \Delta p = N_v \exp\left(\frac{E_v - E_{Fp}}{k_B T}\right) \tag{1.2}$$

with n and p being the electron and hole concentrations respectively, n_0 and p_0 the equilibrium (300 K, dark) carrier concentration, Δn and Δp the photo-generated carrier concentration, N_c and N_v the effective density of states in the conduction and valence band, E_{Fn} and E_{Fp} the quasi-Fermi levels, which are the electrochemical potentials describing the excited electrons and holes population systems respectively, k_B the Boltzmann constant and T the temperature. The np product can be described as:

$$np = n_i^2 \exp\left(\frac{E_{Fn} - E_{Fp}}{k_B T}\right) \tag{1.3}$$

with n_i the intrinsic carrier concentration defined by:

$$n_i = \sqrt{np} = \sqrt{N_c N_v} \exp\left(\frac{E_v - E_c}{2 k_B T}\right) \tag{1.4}$$

Eq. 1.3 introduces the difference $E_{Fn} - E_{Fp}$ called the quasi-Fermi level splitting, which increases with the carrier population. This quantity also represents the maximum voltage value than can theoretically be extracted from the semiconductor, called the "implied voltage" iV and represented in Fig. 1.3:

$$iV = \frac{E_{Fn} - E_{Fp}}{q} = \frac{k_B T}{q} \ln\left(\frac{np}{n_i^2}\right) \tag{1.5}$$

with q the elementary charge.

1.3.2 Photo-generated-carrier collection

To extract the highest output power from the device, the output voltage V and current I (or surface current density J) must be maximized. In both cases, the carrier concentration has

to remain high in the whole Si wafer to the metallic electrodes to get V and iV as close as possible, as well as providing a large current density. However, carriers are subject to several loss mechanisms that can be divided into recombination and selectivity losses.

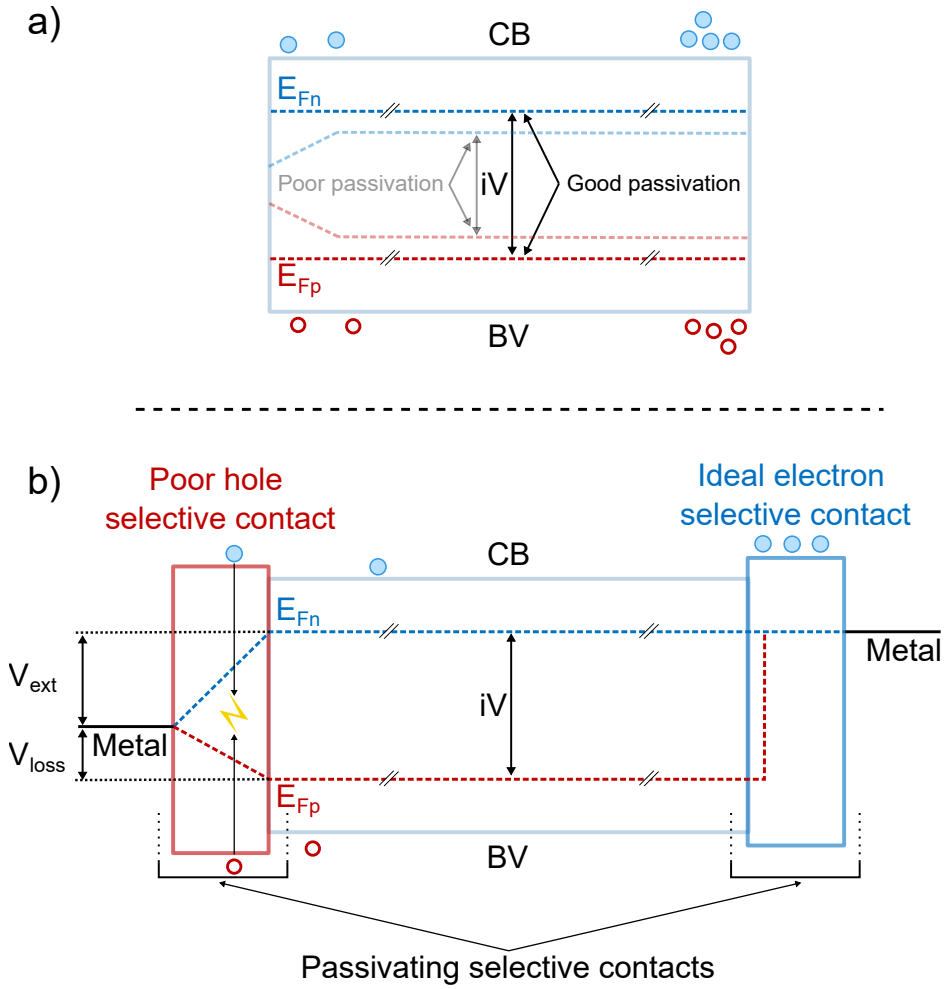

Figure 1.3: Schematic band diagram of a solar cell (a) a single absorber and b) an absorber and two separated passivating selective contacts at the surface of the absorber). a) The quantity iV is represented in the case of a poorly and a well- passivated absorber. b) In the case of good passivation, quasi-Fermi levels E_{Fn} and E_{Fp} are represented for an ideal (electron) and a poor (hole) selective contact. V_{ext} is the measured output voltage. In the poor selective contact, holes and electrons can flow out with similar resistance, provoking a voltage loss V_{loss}.

Recombinations

To reach the solar cell contacts, photo-generated carriers need a high diffusion length L, i.e. high minority carrier lifetime τ. In the bulk of the wafer, they can be lost before extraction through radiative, Auger, and Shockley-Read-Hall (SRH) recombinations mechanisms. Si being an indirect band-gap semiconductor, radiative recombination is negligible compared to

the other ones, and does not limit the performances of Si-based solar cells. Auger recombination is prevalent for carrier concentration above 1×10^{16} cm^{-3} and limits carrier lifetime. SRH recombination is an extrinsic mechanism, which can be controlled by the quality and purity of the absorber [Shockley 1952]. Monocrystalline Si wafers used in this thesis are high quality float zone wafers, which drastically lowers this kind of recombinations.

Unlike the wafer bulk, Si surfaces are very defective, regardless of the wafer quality, due to the presence of highly recombining Si dangling bonds, therefore surface recombination is the main recombination loss for c-Si based solar cells. The amphoteric nature of these defect states requires an adaptation of the SRH theory, and the recombination rate reads [Olibet 2007]:

$$U_s = v_{th} N_S \frac{n_s \sigma_n^0 + p_s \sigma_p^0}{1 + \frac{p_s \sigma_p^0}{n_s \sigma_n^+} + \frac{n_s \sigma_n^0}{p_s \sigma_p^-}} \tag{1.6}$$

With v_{th} the thermal velocity, N_S the three-dimensional bulk dangling bonds density reduced to a surface density, $\sigma_{n,p}^{+,0,-}$ the electrons and holes capture cross-sections corresponding to the three charge states (zero, one or two trapped carriers) and n_s, p_s the electrons and holes density at the surface.
The dangling bond surface density of a non-passivated Si (100) surface is typically around $D_{it} \sim 7 \times 10^{14}$ cm^{-2}. Two strategies are relevant to mitigate surface recombination. Passivation can be obtained through the reduction of Si dangling bond concentration by chemically bonding them with atoms of the layer, generally Si, H or O, and dedicated passivation layers are deposited on the Si surface to achieve this goal. (i)a-Si:H provides excellent surface passivation through the creation of Si-H bond (specifically used in SHJ), however, dielectrics like SiO_x or SiN_x usually hydrogenated (more used for PERCs or poly-Si technologies), are also often used [Cuevas 2018]. For instance, the deposition of an SiO_x or (i)a-Si:H layer reduces D_{it} to 1×10^{10} cm^{-2} and 1×10^{9} cm^{-2}, respectively [Eades 1984a, Eades 1984b, Cuevas 2015]. The minority carrier lifetime can also be maximized by controlling the carrier population at the surface [Cuevas 2018]. When one of the carrier surface concentrations becomes small compared to the other at the surface/interface, the probability to recombine in a defect state is lowered. A simple simulation with an SRH recombination model using the same capture cross-section for both carriers shows that concentrations at equilibrium (dark) have to be different by a factor of 10^8 to keep sufficient asymmetry under illumination [Cuevas 2015]. Passivation by carrier population control can be achieved by implementing fixed charges or inducing band bending (upward or downward), through doping or work function differences at the interface. Fixed charge and doping are for instance used in Al-BSF and PERC architectures, provided by SiN_x and Al_2O_3 layers. Minority carriers' lifetime can be increased to tens or hundreds μs [Cuevas 2018], which is lower compared to chemical passivation, typically ranging from hundreds μs to ms, and is generally used complementarily.
The passivation quality of a device can be evaluated through iV_{OC} (the implied voltage in open circuit conditions), which is directly linked to the carrier concentrations, as described by Eq.

1.5. Fig. 1.3 shows a poor versus good passivation scenario, highlighting that the former case produces a small iV, which will result in a poor voltage.

Selectivity

Carriers must subsequently be extracted to the metallic electrodes. The forces driving their movement is governed by the gradient of the quasi-Fermi level (electrochemical potentials), and can be expressed as [Wurfel 2015, Würfel 2016]:

$$J_n = \frac{\sigma_n}{q} \nabla E_{Fn} \tag{1.7}$$

$$J_p = -\frac{\sigma_p}{q} \nabla E_{Fp} \tag{1.8}$$

with J_n and J_p the electron and hole surface current densities, σ_n and σ_p the electron and hole conductivities respectively. The conductivity σ of a semiconductor is defined as:

$$\sigma_n = qn\mu_n \tag{1.9}$$

$$\sigma_p = qp\mu_p \tag{1.10}$$

with μ the carriers drift mobility. The extraction can be hindered by work function mismatch, unfavourable energetic barriers, high bulk resistivity or presence of recombination centers in the contact, etc., which increase recombination events.
To efficiently extract the carriers, a solar cell may have two separated contacts, each tolerating the flow of one type of carrier to avoid any recombination prior to the extraction. Eq. 1.7 indicates that carrier currents can be controlled via the quasi-Fermi level gradients and carrier conductivity. A "selective" carrier flow can therefore be obtained by inducing an asymmetry in conductivities. In practice, carrier concentration is the main contributor to achieve this function. As shown in the previous section, it can be controlled by upward/downward band bending with doping, the presence of fixed charges or a work function difference. The asymmetry at the contact should be sufficiently high so that it is maintained under illumination. Fig. 1.3 schematizes poor and ideal selective contacts. As for passivation, poor selectivity will result in a voltage loss. Even though the concept of an ideal selective contact, at which the partial current of one carrier type is zero, is commonly accepted, there is no consensus on the definition of selectivity and several metrics have been introduced to qualify it. Among them, Wurfel *et al.* describe contact selectivity as the difference between electron and hole conductivities [Wurfel 2015], Brendel and Peibst define it as the ratio of majority to minority carrier resitivities [Brendel 2016], Mora-Sero and Bisquert use partial currents [Mora-Seró 2005], while Tress *et al.* employ surface recombination velocities [Tress 2012]. More recently, a novel definition of "carrier" selectivity was proposed by Roe *et al.* and is presented in chapter 2 section 2.3.5 [Roe 2019].

Case of standard SHJ solar cells

In the case of standard SHJ solar cells, hydrogenated amorphous Si is used to form the passivating selective contacts. The intrinsic material is used on both sides to provide the surface chemical passivation through Si-H bonding. Doped (*p*)a-Si:H and (*n*)a-Si:H induce the band bending in (*i*)a-Si:H and the (*n*)c-Si absorber to selectively collect holes and electrons respectively, as shown in the band diagram in Fig. 1.4. The a-Si:H band-gap difference with c-Si (1.7 eV and 1.12 eV respectively) provokes band offsets at the interfaces, ΔE_c for the conduction band offset and ΔE_v for the valence band offset. ΔE_c was measured to be around 0.15 eV while ΔE_v is approximately 0.45 eV [Schmidt 2007, Kleider 2008]. The higher value for ΔE_v is though to hinder hole extraction at the hole contact, and to help stop the holes at the electron contact. Additionally, the presence of the TCO at the hole contact (recombination junction) is also supposed to create a counter Schottky diode, and (*p*)a-Si:H cannot be as doped as (*n*)a-Si:H, both disadvantaging the hole extraction.

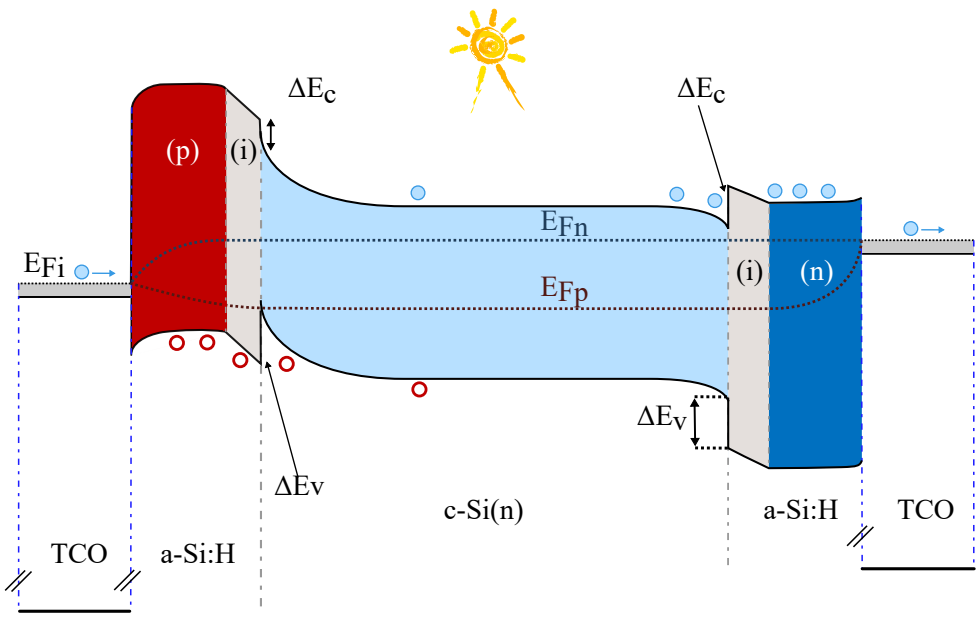

Figure 1.4: Band diagram at open circuit under illumination, representing the standard SHJ for which intrinsic and doped a-Si:H are used as carrier selective passivating contacts.

1.4 Thesis work

For the definition of J_{SC}, *FF*, and V_{OC}, the reader is referred to chapter 2.

1.4.1 Objectives

This thesis aims at exploring the potential of MoO_{3-x}-based alternative contacts for SHJ and improving the understanding of hole-selective contacts for Si solar cells in general. The

work focuses at refining the understanding of contacts and bringing new insights on SHJ contact-limited solar cells through the comparison of the two architectures. Despite flourishing literature about bare MoO_{3-x} films, not many studies have focused on the material as a layer in the selective contact stack, due to restrictive material characterization methods. This thesis aspires to implement alternative methods of probing the whole contact stack characteristics using both standard and less conventional solar device characterization methods. Optical, passivation, selectivity and transport properties of the ITO/MoO_{3-x}/(*i*)a-Si:H/(*n*)c-Si full contact will be assessed. Finally, stabilizing the solar cell efficiency closer or beyond their a-Si:H-based counterparts, with developing processes suitable for industry is the last goal of this work.

1.4.2 Structure of the thesis

The thesis is structured as follow:

Chapter 2: wafer design and standard deposition processes used in this thesis are described, as well as the standard characterization tools and methods.

Chapter 3: current research on TMO used as contacts in silicon solar cells research is contextualized. It presents a comprehensive and detailed literature review of TMOs, properties, historical background for solar cells devices, integration as contacts in Si-based solar cells and their limitations, among which MoO_{3-x}.

Chapter 4: both (*i*)a-Si:H and MoO_{3-x} thicknesses are varied to explore passivation and selectivity evolution, as well as maximizing the J_{SC} gain provided by the replacement of the (*p*)a-Si:H layer by the TMO. Pushing the MoO_{3-x} thickness down to 4 nm, and with the development of efficient low temperature Ag paste, we achieved a 23.5% efficient MoO_{3-x}-based cell, currently holding the SHJ with not-Si-based contact world record. An novel characterization method, based on *J-V* curves fitting with a physical model developed by Roe *et al.*[Roe 2019], is used to further analyse the selectivity of the contact. Results suggest that parasitic electrons are prone to pass through the contact in case of reduced MoO_{3-x} work function.

Chapter 5: the influence of ITO on two different MoO_{3-x} layer thicknesses and a sample with no dedicated selective layer is evaluated by varying its carrier concentration and sputtering deposition power. The development of a new ITO enhances MoO_{3-x}-based SHJ *FF* by more than 1 $\%_{absolute}$, stabilizing the efficiency of these type of solar cells around 23%. The application of the previous characterization method based on the Roe *et al.* model allows to estimate the in situ hole contact work function. We further investigate the effect of DARC treatment with PECVD-deposited SiO_x:H, commonly used for standard SHJ, which is known to alter the ITO characteristics and also the underlying selective contact. It proved to degrade the MoO_{3-x}-based solar cell, most probably due to the presence of H in the plasma. Yet, the results should be repeated with highly performing solar cell prior to the DARC treatment, which was not the case for this study.

Chapter 6: stability tests for MoO_{3-x}-based SHJ solar cells and modules are performed to probe their resilience to field conditions. Effect of the combination of pre- and post-annealings, stability in the air through time, application of a dark forward bias, and encapsulation followed by UV-radiation exposure, are discussed. Apart from the forward bias, all treatments degraded the cells. The post-annealings and UV treatment are thought to degrade the cells through selectivity loss, while encapsulation and forward bias induce mainly passivation-related phenomena.

Chapter 7: this chapter, more exploratory, presents an overview of the possible transport mechanisms prone to exist in a-Si:H and MoO_{3-x}-based SHJ. It also provides preliminary results of a non-conventional characterization method based on low temperature *J-V* characteristics measurements applied to not-Si-based SHJ for the first time. The measurements showed unexpected similarities with a-Si:H-based SHJ, tentatively explained by transport and recombination mechanisms. A new characterization method, based on the *J-V* characteristics derivative, proposes an extension of the use of the Roe *et al.* model. First results, using previous experiment measurements, are paralleled with former conclusions and show that the method could provide complementary information on contact selectivity.

1.4.3 Context of the thesis

At the beginning of this thesis in 2018, SHJ solar cells best world record efficiency reached 25.1% in the front-back contacted structures [Adachi 2015], while the common SHJ device's efficiency is stabilized around 22-23%. Interest for PV production industries was scarce and few of them started developing plans for potential future production. The SHJ contact understanding lacked insight, with characterization methods being not fully adapted. TMO based contacts for crystalline silicon SHJ appeared four years ago [Battaglia 2014b, Battaglia 2014a]. The world record SHJ cell in this category was achieved in 2015, using MoO_{3-x} as a hole selective contact and reaching 22.5% [Geissbühler 2015]. The success of the 22.5% MoO_{3-x}-based cells was based in the use of copper plating for the front grid metallization, instead of the common Ag screen printing. The latter technique is indeed used at ambient temperature, while the paste used in Ag screen printing requires a curing of up to 210 °C to attain acceptable conductivity, a fatal temperature for MoO_{3-x}-based cell. The development of low temperature Ag pastes (e.g. 130 °C) is on-going, however it does not provide good contact properties. In addition, thinner Cu fingers are deposited through Cu plating compared to screen-printed Ag fingers, reducing shadowing from the front grid and enabling reaching higher J_{SC}. However, Cu plating is not widely adopted at the moment in industry, and the 22.5% one-off efficiency was way ahead of the typical 17%-20% efficiencies for 6-step-processed MoO_{3-x}-based SHJ, still prevalent in 2018.

1.4.4 Contribution to the research field

This thesis work brings key elements for future research in the transparent TMO-based and a-Si:H-based silicon heterojunction solar cells. We proved that MoO_{3-x}-based hole contact SHJs can reach efficiencies of 23.5% with no deep optimization, in a simple 6-step process and the use of low temperature Ag screen-printed front electrode grid. The result was obtained following deep evaluation of the contact transparency, passivation and selectivity, and by thinning the MoO_{3-x} layer as low as 4 nm for the first time in the TMOs-based SHJ contacts' history. The latter upgrade drastically enhanced the J_{SC} of the device by minimizing the parasitic sub-gap absorption in the MoO_{3-x} layer, while maintaining excellent electrical performances. We evidenced the role of ITO in the performance of MoO_{3-x}-based devices, and developed a new one, for which the devices *FF* increased by more than 1 $\%_{absolute}$. MoO_{3-x}-based cells efficiency could be stabilized at around 23% with this progress and surpass our (*p*)a-Si:H-based SHJ baseline efficiency, which is an essential achievement. The first stability tests for not-Si-based contacts SHJ were also performed, and a dark forward bias treatment appeared to be more beneficial for the *FF* of MoO_{3-x}-based than (*p*)a-Si:H-based SHJ, with a rise of more than 1 $\%_{absolute}$. The study also questions the role of H in the induced process. Solar cell implementing a 2-nm-thick MoO_{3-x} layer, as well as MgF_2 DARC, reached an efficiency of 23.5% after a dark forward bias treatment, another milestone for TMO development as contacts in SHJ. Finally, a more fundamental study of the transport involving measurements at low temperatures down to −160 °C of devices using MoO_{3-x}-based (performed for the first time for such contacts) and (*p*)a-Si:H-based were made and results showed similar V_{OC} saturation and *FF* decrease. This study has opened new questions and has brought more insights to this unconventional characterization. Overall, all the presented experiments and characterizations brings new outlooks to the SHJs selective contacts and can be used for the development of future alternative contacts or serve as comparison to the standard a-Si:H-based behavior.

This work resulted in three peer-reviewed papers as first author and shared first author [Dréon 2020, Dréon 2021, Ibarra-Michel 2022], several as co-author and three conference orals among which one plenary oral presentation. A detailed publication and oral list can be found at the end of this manuscript.

2 Experimental and characterization details

In this chapter, we briefly present the standard deposition techniques and the process flows for solar cell fabrication used for SHJ solar cells fabrication,as well as the main characterisation instruments and methods used during this thesis.

2.1 Deposition processes

2.1.1 Plasma enhanced chemical vapor deposition

Plasma enhanced chemical vapor deposition is a deposition technique in which thin film precursors are vapours which chemically react at the substrate surface. The chemical reaction is assisted by a plasma which allows for low temperature deposition processes (200 °C to 300 °C). Fig. 2.1 presents a typial PECVD chamber. The chamber is generally kept at low pressure ($\sim 1 \times 10^{-6}$ mbar) to avoid contaminations. The two electrodes, RF generator and matchbox enable plasma creation and stabilization. The substrate is placed on one of the electrode whose temperature is controlled. In the case of SHJ solar cell fabrication, PECVD is

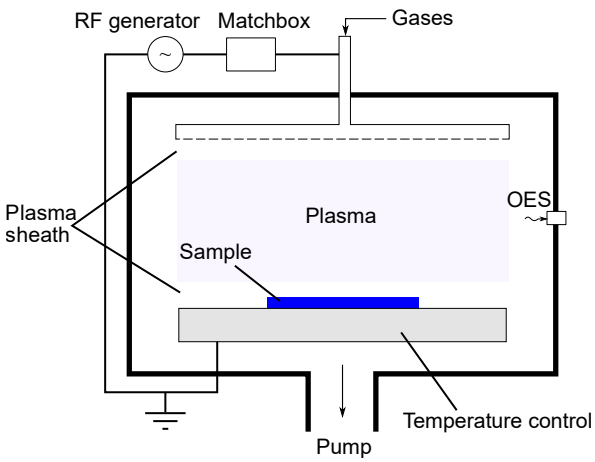

Figure 2.1: Scheme of a parallel plate PECVD reactor.

mainly used to deposit the a-Si:H layers. Gas precursors are silane (SiH_4) and H_2 for the a-Si:H layers, and phosphine (PH_3) and trimethylboron ($B(CH_3)_3$, TMB) are additionally used during the deposition to dope the n-type and p-type layers respectively.

2.1.2 Thermal evaporation

Thermal evaporation is a physical vapour deposition (PVD) which consists in evaporating through heat solid materials generally under the form of powder or wires, in a high vacuum chamber (typically 1×10^{-3} mbar to 1×10^{-6} mbar. In this thesis, resistive evaporation is mainly used, for which heat is produced via Joule effect. The material is placed in a boat (tungsten or molybdenum for instance) through which an elevated current is applied, dissipating by joule effect. The substrate is placed on a rotating plate above the heat source, perpendicularly to the deposition direction. Here, MoO_{3-x} and MgF_2 are deposited with this method. SiO_x is also deposited with thermal evaporation, using an electron beam to heat the source. In both case, a piezoelectric device is used to measure the deposition rate and estimate the film thickness.

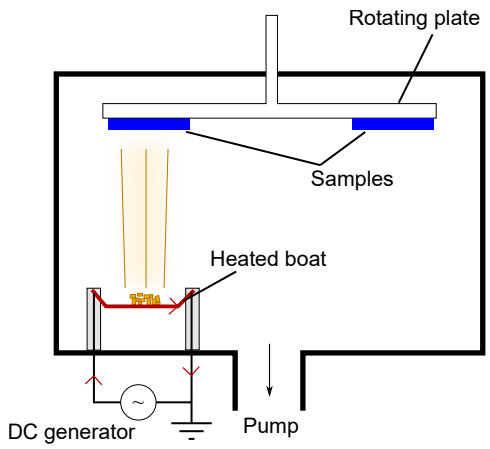

Figure 2.2: Scheme of a thermal evaporator.

2.1.3 Magnetron sputtering

Sputtering is a PVD technique used to deposit or etch thin films. For the deposition, the deposition chamber is maintained at high vacuum before the deposition. After setting a base pressure, a plasma is generated by applying a high potential difference in the chamber (between a cathode and an anode), in which neutral atoms (Ar generally) are expelled with a high kinetic energy on a target made of the material precursor (cathode), desired to be deposited. Following the collision, atoms of the material are expelled on the desired surface (anode) on which they grow as a layer. In this work, the substrates are fixed on a vertical plate translating in front of the material target at a constant speed. In magnetron sputtering, strong magnets are used behind the targets to confine the plasma near the surface of the target. They enable higher deposition rate and prevent damages caused by accelerated electron or Ar

collisions on the substrates. In this work, this technique is used to deposit front and rear ITO and IZrO, and Ag back electrode.

2.1.4 Screen printing

Screen printing is a widely used method to deposit the front or/and rear Al and Ag metallic grid for solar devices. The technique consists in depositing a metallic paste made of the metal and solvents on a dedicated screen placed on the substrate, possessing openings where the metal should be deposited. A blade moves across the screen to fill the openings. A post curing is necessary to dry the paste and make it conductive. For SHJ, curings of ~ 200 °C during 30 min are used, and recent development of low-temperature curing pastes brings down the screen-printed grids resistivity with values down to 3.8 μ■cm [Faes 2018] (an Ag paste cured at 130 °C is typically used for MoO_{3-x}-based cells).

2.2 SHJ solar cell fabrication

Fig. 2.3 a.) and .b) shows the two architectures presented in this thesis work, a standard a-Si:H-based and a MoO_{3-x}-based SHJ solar cell respectively. The standard process flow followed for their fabrication is described hereunder. In this thesis, all thicknesses are given on textured surfaces, calculated from measurements on flat c-Si or glass divided by a ratio of 1.6 accounting for the pyramids geometry [Mrazkova 2018].

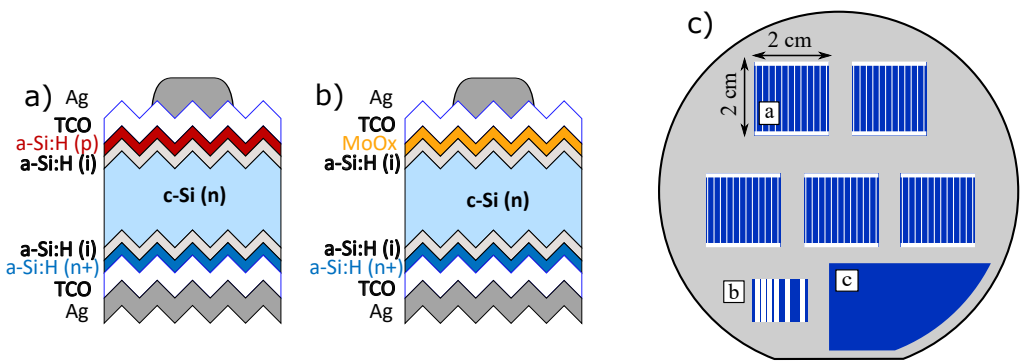

Figure 2.3: Cross section scheme of **a)** a standard Si-based contacts silicon heterojunction, **b)** a MoO_{3-x}-based hole contact silicon heterojunction processed in our laboratory;**c)** Top view of our standard 4 inch silicon wafers, with 5 identical solar cells of 2x2 cm^2 (1), TLM pad (2), and spectrometry measurement pad (3).

2.2.1 Wafer cleaning

190±5 μm-thick float-zone monocrystalline (100) Si wafers are used as the solar cells absorbers, with a resistivity of $2.0 \pm 0.3\,\Omega$ cm. Sawing damages are removed by surfaces cleaning following the Radio Corporation of America (RCA) process [Kern 1990]. Both surfaces of the wafer

are then texturized in a potassium hydroxide (KOH) anisotropic etching along the (111) c-Si crystallographic plane.
Prior to layers deposition, the wafers are dipped during 60 s into an hydrofluoridric (HF) acid aqueous solution diluted at 5%, to remove the native a-SiO_x formed at the surface of the wafers by oxidation with ambient air.

2.2.2 a-Si:H layers deposition

The rear electron contact stack, composed of amorphous and micro-crystalline hydrogenated silicon, (*i*)a-Si:H/(*n*)a-Si:H/(*n*)μc-Si:H, is deposited at the back side of the wafer by PECVD at 200 °C with a RF generator frequency set at 13.56 MHz. The phosphine gas for doping the n-doped layers is diluted at 2% in H_2. The (*i*)a-Si:H is ~ 6 nm thick while the n-doped total stack thickness is around 20 nm.
On the front side, 6-nm-thick (*i*)a-Si:H is deposited by PECVD at 200 °C.
In case of standard SHJ processing, the (*p*)a-Si:H layer is deposited subsequently to the front (*i*)a-Si:H deposition, at the same temperature and RF generator frequency. The (*p*)a-Si:H layer thickness is ~ 8 nm.

2.2.3 Pre-annealing step

Some of the $MoO_{3\text{-}x}$-based samples were "pre-annealed", a step developed in the study of Essig *et al.*, beneficial to reduce the hydrogen content in the front-side (*i*)a-Si:H layer to prevent unwanted H effusion in the $MoO_{3\text{-}x}$ layer [Essig 2018]. The method consists in annealing the sample prior to $MoO_{3\text{-}x}$ deposition in an oven (ambient air) at 250 °C during 20 min. The pre-annealing step was shown to induce no detectable thickness variation by ellipsometry. When not precised in the chapters, the pre-annealing step is not used.

2.2.4 $MoO_{3\text{-}x}$ layer deposition

The wafer is dipped again in the HF bath during 30 s to remove potential Si oxidation after the PECVD or pre-annealing steps. Subsequently, $MoO_{3\text{-}x}$ is thermally evaporated in a vacuum chamber (base pressure before deposition: $\sim 4 \times 10^{-6}$ mbar; during deposition: $\sim 7 \times 10^{-6}$ mbar) from a stoichiometric MoO_3 powder at a deposition rate of about 0.03 nm s^{-1}.

2.2.5 Transparent conductive oxides deposition

Standard ITOs and Ag rear electrode

The standard (used as a baseline) front ITO is deposited by DC magnetron sputtering on the front (70 nm) through a mask to form five 2x2 cm^2 devices per wafer (see Fig. 2.3.c)). The ITO target is composed of 90% SnO and 10% In_2O_3 with a purity of 99.99%. The working

pressure is set at 1×10^{-2} mbar, with a base pressure of 4×10^{-6} mbar prior to deposition, and a pre-sputtering time os 120 s. During deposition, an atmosphere containing 2% of oxygen diluted at 20% in Ar was used. The DC generator power is set to 1000 W.
The back side ITO is deposited in the same conditions, but with an atmosphere containing 3% of oxygen, and for a final thickness of 150 nm.
The Ag rear electrode is also sputtered with using the same settings, but a pre-sputtering time of 60 s and an atmosphere containing pure Ar. The final thickness is 100 nm.

TCOs of Chapter 5

In this chapter, two other ITOs were deposited at the same power than the standard one (1000 W) but oxygen rate of 1% and 3% in the atmosphere chamber.
An ITO with a lower power was deposited with a power of 600 W, and an oxygen rate of 1.2% - calibrated by a dedicated experiments on glass samples and Hall effect measurements - to match doping of the standard ITO (so that power is the only variation). The other settings remain the same than the standard one.

For the other TCOs of Chapter 5, the ITO processed at Centre suisse d'électronique et de microtechnique (CSEM) was deposited in an Octopus II from Indeotec. The last ITO was sputtered in our Leybold evaporator tool, which possesses a 3 inch target sputtering element, with a 90% SnO and 10% In_2O_3 target composition, a 30 sccm O_2 (diluted at 750 ppm in Ar) flow, a DC power of 600 W and a working pressure of around 5×10^{-3} mbar (base pressure: 1×10^{-5} mbar).
IZrO:H was deposited in the same tool used for our ITOs using a 98% In_2O_3 and 2% ZrO target (purity: 99.99%), an O_2 flow of 0.2% for a working pressure of 8×10^{-3} mbar (base pressure: 4×10^{-6} mbar), and an RF power of 600 W.
Finally, ZnO:Al (AZO) was deposited at CSEM in a Clusterline 200 from Evatec. Deposition times were adjusted so that all TCOs have the same thickness, which is around 70-75 nm on textured surfaces.

2.2.6 Ag front grid screen printing

In the end, a silver grid is screen-printed on the front side using a low-temperature paste, cured at 130 °C for MoO_{3-x}-based SHJ, and cured at 210 °C for standard SHJ, during 30 min.

2.2.7 Double anti-reflective coatings

Front DARCs were deposited once the solar cell was entirely fabricated.
The SiO_x:H layer was deposited by PECVD in an Octopus I from Indeotec. We used a deposition temperature of 180 °C, a working pressure of 5×10^{-1} mbar, an AC generator power of 40 W with a radio frequency of 40.68 MHz. The gases precursors species for the chemical reaction were

SiH_4, CO_2, and H_2, at flow rates of 1 sccm, 25 sccm and 10 sccm respectively. The deposition duration was 300 s so that the final SiO_x:H thickness was around 100 nm on textured wafers. An SiO_x was also deposited via electron-beam, in the Leybold evaporator chamber at the base pressure around 2×10^{-5} mbar. The deposition rate was 15 Å s^{-1}.
MgF_2 was thermally evaporated in the Leybold evaporator, in a vacuum of $\sim 1 \times 10^{-5}$ mbar, with a deposition rate of 0.5 nm s^{-1} for a final thickness of 80 nm.

2.3 Characterization methods

2.3.1 Minority carrier lifetime and Suns-V_{OC} measurements

Minority carrier lifetime variation with illumination can be measured through the photo-conductivity evolution of a flashed sample. The measured photo-conductivity provides the excess carrier density Δn or Δp (the photo-generated carriers) and so the injection level in the wafer. Lifetime measurements are performed with a Sinton Instrument WCT-120 by photoconductance decay in transient mode [Sinton 1996a]. In Chapter 4, for each wafer, measurement is performed at the five different solar cell location then lifetime τ is averaged. The implied voltage iV can be estimated for the different carrier injections. The injection corresponding to a 1 sun illumination gives the implied open-circuit voltage iV_{OC}. The recombination current J_0 can also be evaluated with this measurement. Suns-V_{OC} characterization are realized with a Sinton Instrument WCT-120 with an Illumination-Voltage tester stage.
For both characterizations, not finished devices can be measured.

2.3.2 *J-V* measurements

The *J-V* characterization is performed with a class AAA Wacom WXS-90S-L2 solar simulator, under standard test condition (AM 1.5G, 100 mW cm^{-2} at 25 °C). The solar spectrum is reproduced by an halogen and a xenon lamp. The cells are measured one by one, on the wafer through a black mask which shades the external edges of the cell and the entire inactive area of the wafer. Busbars, which define the perimeter of the cells, are excluded from the measurement area. The light spectrum intensity is calibrated every week through reference solar cell, over 315-800 nm, 650-1180 nm, and 315-1180 nm. Before each measurement, a reference solar cell is also used to adjust the calibration and normalize the current accordingly. The wafers are placed on a metallic chuck for which the temperature is controlled, and measured in a 4 point probes configuration with Kelvin probes.

2.3.3 Characteristic quantities

The *J-V* characteristic of a solar cell is illustrated in Fig. 2.4.a), in which the characteristic quantities are:

- J_{SC} is the current density in short-circuit (SC) conditions, i.e. when the external voltage is null.

- V_{OC} is the voltage in open-circuit (OC) conditions, i.e. when the current delivered by the cell is null. In this condition, there is no charge extraction out of the cell, and the recombination rate equals the generation rate.

- V_{mpp} and J_{mpp} are respectively the voltage and current density at maximum power point (mpp), i.e. the voltage and current whose product $J_{mpp}V_{mpp}$ gives the maximum power density p_{mpp} (or equivalently the product $I_{mpp}V_{mpp}$ give the maximum power P_{mpp}, with I_{mpp} the current at mpp) that can be delivered by the cell.

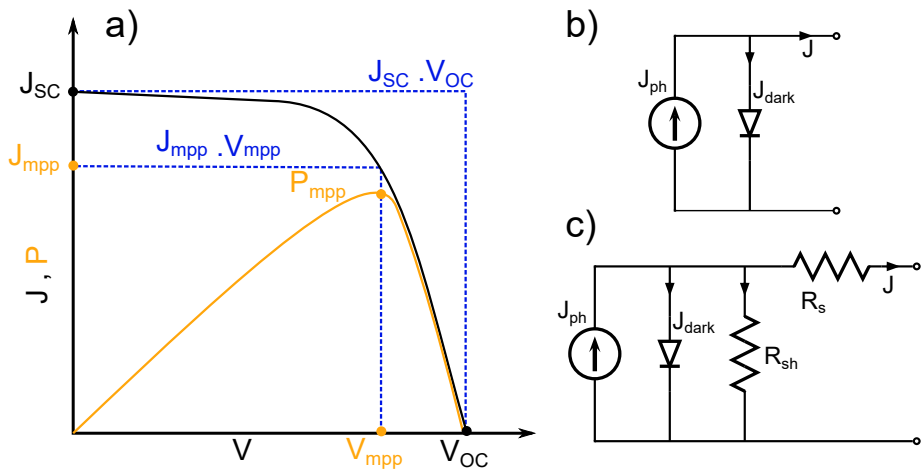

Figure 2.4: a): Sketch of a standard J-V characteristic for a solal cell. b) Associated ideal (no resistance losses) one diode equivalent electrical circuit and c) standard one diode equivalent electrical circuit including the series and shunt resistance effects (R_s and R_{sh} respectively).

The power conversion efficiency (PCE or η) is given by the ratio of the maximum output power to the incident power density provided by the light source p_{in}:

$$\eta = \frac{P_{mpp}}{p_{in}} = \frac{J_{mpp}V_{mpp}}{p_{in}} \tag{2.1}$$

The last solar cell figure of merit is called the fill factor FF and includes the transport and recombination losses. It is defined by the ratio of the two squared areas in Fig. 2.4.a), and can be expressed as:

$$FF = \frac{J_{mpp}V_{mpp}}{J_{SC}V_{OC}} \tag{2.2}$$

2.3.4 Basic equivalent electrical circuits

An ideal solar cell with no resistance losses can be electrically represented by the "one-diode" model (a diode in dark conditions, and a diode in parallel with a current generator under illumination), as sketched in Fig. 2.4.b). The equation of the system is:

$$J = J_{ph} - J_0(\exp\frac{qV}{nk_BT} - 1) \tag{2.3}$$

with J the surface current density, J_{ph} the photo-generated current density, q the elementary charge, J_0 the recombination current, n the ideality factor of the diode, k_B the Boltzmann constant and T the temperature. The case $n = 1$ corresponds to the ideal diode case with radiative recombination only and no traps involved in the processes, while the case $n = 2/3$ stands for a diode where Auger recombination is predominant [Sze 1995, Kirchartz 2013]. For recombination dominated by SRH mechanism, $1 < n < 2$.
It is often assumed that $J_{ph} = J_{SC}$, generally validated for most solar cells with decent efficiencies.
From Eq. 2.3, V_{OC} can be linked to J_0 via the expression:

$$V_{OC} = \frac{k_BT}{q}\ln\frac{J_{ph}}{J_0} = \frac{k_BT}{q}\ln\frac{J_{SC}}{J_0} \tag{2.4}$$

Which underlines that increasing J_0 will provoke a voltage loss.

For a more realistic description, the one-diode model includes parasitic resistances as represented in Fig. 2.4.c) , with R_{sh} the shunt resistance modelling the current loss from shunts, and R_s the series resistance which incorporates bulk and contact resistances. For best device efficiencies, the first one should be maximized while the second one minimized. The characteristic equation becomes :

$$J = J_{ph} - J_0(\exp\frac{qV + JR_s}{nk_BT} - 1) - \frac{V}{R_{sh}} \tag{2.5}$$

2.3.5 Passivation, selectivity and transport losses estimation

Several techniques have been developed to measure the passivation or selectivity losses, and some, used in this thesis work, are succinctly summarized here.

R_s* and *FF_0 Determination of R_s under illumination can be performed by measuring the same J-V curve at different illuminations [Swanson 1960, Wolf 1963]. By measuring a J-V characteristics at 1 sun (standard condition) and a "shaded" one corresponding to an injection near the maximum power point (for instance, it corresponds to all illumination of around 0.07 sun for our solar cells), one can estimate the R_s at maximum power point [Bowden 2001, Pysch 2007]. As long as V_{OC} and J_{SC} are not affected by R_s, which is always verified for V_{OC}

by definition and verified for J_{SC} if R_s is below $10\,\Omega\,cm^2$ [Altermatt 1996], the shaded curve can be translated by a certain J and V quantity to coincide with the 1 sun J-V curve. These J translation corresponds to $\Delta J_{SC} = J_{SC1sun} - J_{SCshaded}$, and the V translation represents the voltage loss due to R_s: $\Delta V = V_{OCshaded} - V_a = R_s \Delta J_{SC}$ with $V_a = V_{OCshaded}(J_{SC1sun} - J_{SCshaded})$. Fig. 2.5 illustrates the method. R_s is then given by:

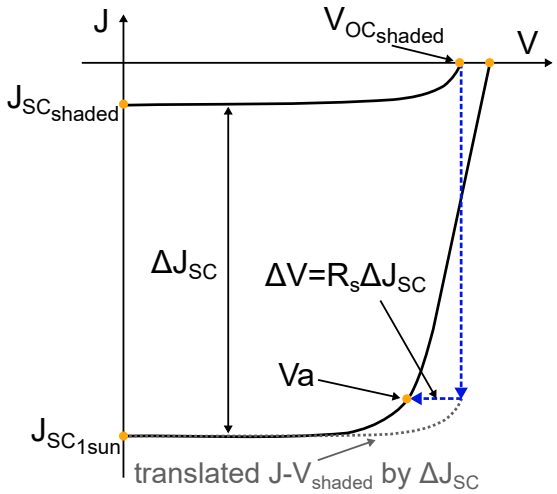

Figure 2.5: Scheme presenting the method developed by Bowden*et al.*. The "shaded" J-V curve is the J-V curve of the cell at lower than 1 sun illumination.

$$R_s = \frac{\Delta V}{\Delta J_{SC}} \tag{2.6}$$

The FF of the cell without the effects of R_s, called FF_0, is given by [Green 1982]:

$$FF_0 = \frac{v_{oc} - \ln v_{oc} + 0.72}{v_{oc} + 1} \tag{2.7}$$

with:

$$v_{oc} = \frac{qV_{OC1sun}}{nk_BT} \text{ and } n = \frac{V_{OC1sun} - V_{OCshaded}}{\ln\left(I_{sc_{1sun}}\right) - \ln\left(I_{sc_{shaded}}\right)} \frac{q}{k_BT} \tag{2.8}$$

This FF_0 should be identical —though less accurate— with the pseudo FF extracted from Suns-V_{OC} curves, and differs from the standard ideal FF_0 defined by Green. The divergence lies in the definition of the ideality factor n: the FF_0 calculated by Bowden *et al.*, used in this thesis, defines an ideality factor linked to the solar cell state change from the maximum power point to the open circuit condition operation (see Eq. 2.8), while the n used in the standard ideal FF_0 calculation is the one of the recombination diode in the one diode model presented above.

***V*$_{OC}$- *iV*$_{OC}$** Bivour *et al.* introduced a practical measurement of the voltage loss provoked by non-ideal selectivity as the difference $iV_{OC} - V_{OC}$ [Bivour 2014]. According to scheme 1.3 in Chapter 1, iV represents the quasi-Fermi level splitting and the highest extractable voltage with passivation losses only, while V_{ext} includes the selectivity losses as well. Hence, the difference between these two quantities provides by nature the voltage loss due to selectivity. Devices with $V_{OC} \approx iV_{OC}$ are passivation limited, while devices with $V_{OC} < iV_{OC}$ are selectivity limited.

Roe *et al.* S-shape simulation A novel characterization method to get information on "S-shaped" curves is proposed by Roe *et al.* [Roe 2019]. In this thesis, the method will be adapted and extended to extract the MoO_{3-x}-based hole contact stack work function and information about the carrier flow. One strength of the model is that the inputs do not rely on specific materials properties (work functions, barriers height, nature of carrier transport).
In the model, the absorber is sandwiched between the two contacts — electron- and hole-selective contacts — which are simultaneously taken into account, each of them involving both a minority and majority current, giving rise to four exchange current densities characterizing the rate of charge carrier transfer between two materials in a dynamic equilibrium. They are: the electron exchange current J_{0n}^{e-} (majority) and hole exchange current j_{0p}^{e-} (minority) at the electron contact, and the hole exchange current J_{0p}^{h+} (majority) and electron exchange current j_{0n}^{h+} (minority) at the hole contact. The currents densities are schemed in Fig. 2.6.a), and the equation used to model the S-shaped J-V curves, involving the exchange current densities, can be expressed as:

$$J(V) = -\left(J_L + j_{0_n} + j_{0_p}\right) + \frac{J_L + j_{0_n + J_{0_n}}}{1 + \frac{J_{0_n}}{j_{0_n}} \exp\left(\frac{-V}{V_T}\right)} + \frac{J_L + j_{0_p} + J_{0_h}}{1 + \frac{J_{0_p}}{j_{0_p}} \exp\left(\frac{-V}{V_T}\right)} \tag{2.9}$$

where J_L is the photo-generated density current, V_T the thermal voltage ($k_B T/q$, k_B the Boltzmann constant, T the temperature and q the elementary charge). The J-V curve produced by the equation is plotted in Fig. 2.6.b), and presents a solar cell limited by its hole contact (the step appearing at the lowest voltage involves the carrier exchange currents at the hole contact).

In Chapter 4, J-V curves fitting gives an estimation of the J_0 and j_0 evolution at the MoO_{3-x} contact for different MoO_{3-x} thicknesses and Chapter 5 introduces a contact work function estimation based on this method.
The S-shape characteristic quantities highlighted in Fig. 2.6.b) (V_n, V_p and the heights of the plateaus) are useful metrics for selectivity. Chapter 7 details the information they provide and proposes an extension the model for easy graphical selectivity trend analysis.

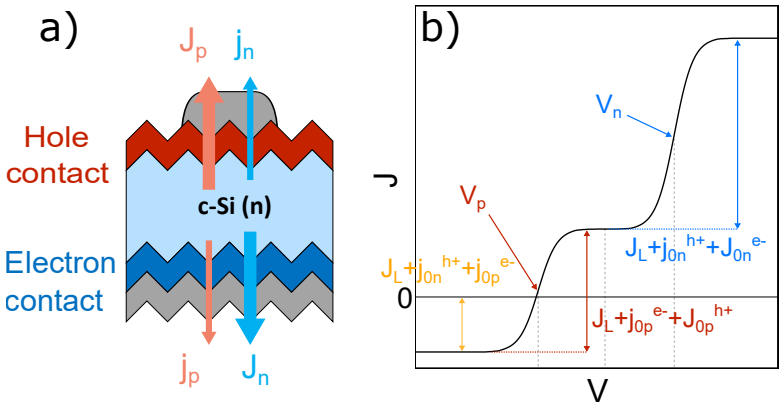

Figure 2.6: a) illustration of the four currents used in the Roe *et al.* model. b)Simulated *J*-*V* curves using Eq. 2.9.

2.3.6 EQE

The external and internal quantum efficiency (EQE and IQE respectively) measurements, which evaluate the ratio of incident photon flux to the electrons flux existing the device, are made utilizing in-house built setup, with a rectangular illumination beam which is 2 mm x 1 mm large and whose photon flux for a given wavelength is calibrated with a reference device. The beam spans wavelength from 320 nm to 1180 nm. The measurement does not include finger shading, leading to a higher integrated current value compared to the one measured in *J*-*V* characterization.

2.3.7 Photoluminescence imaging

Photoluminescence imaging consists in illuminating a semiconducting sample to photo-generate free carriers, and measure through a camera the radiative recombination. The latter is proportional to the excess carrier density Δn and Δp and can thus give an information about the wafer passivation quality. The images provide a mapping of the wafer, for which the "counts" (arbitrary unit) measured by the camera are proportional to Δn. Carrier which are not radiatively emitted recombine through non-radiative processes (like SRH recombinations), meaning that areas with low number of counts are highly recombinative. The measurement is contactless and can be used at any step of the solar cell fabrication.
In this thesis, the samples are placed on a chuck whose temperature is regulated at 25 °C, and are illuminated with a laser emitting at 808 nm.

2.3.8 Temperature-dependent *J*-*V* measurements

Temperature-dependent measurements are performed in an in-house instrument in which illumination and temperature can be adjusted. Like for standard *J*-*V* measurements, the solar cell is placed on a metallic chuck whose temperature is adjusted and controlled by

Peltier modules and PT100 probe respectively. The temperature is stabilized during the *J-V* measurement. Temperature can be varied from −160 °C to 80 °C.
For the low temperature measurements (−160) to −20), the chuck is placed in a thermally insulated tank constituted of insulating foam covered with waterproof EVA sheet, in which liquid nitrogen is introduced. The tank is closed by an optical glass window on which air is circulated to prevent condensation. Gaseous nitrogen flow is maintained inside the tank to prevent humidity entering the sample environment. The liquid nitrogen is used as a cold reservoir while the Peltier modules heat up the system and stabilize the temperature with an accuracy of 0.1 °C (0.5 °C for the lowest temperatures).

2.3.9 Hall effect

A Hall effect measurement instrument is used to measure carrier concentration, Hall mobility and sheet resistance of thin film materials. Carrier concentration and Hall mobility are measured using the Hall effect method by applying a magnetic field perpendicular to the carrier flow. The sheet resistance is measured in 4 points Vand der Pauw configuration. In the present work, Hall effect measurements are performed with a HMS-5000 from Ecopia using a magnetic field of 0.56 T. Squared 1x1 cm^2 samples are placed on dedicated printed circuit board holder. The contact is made in the four corners of the samples, coated with Ag paste to ensure a ohmic contact.

2.3.10 UV-visible-near infrared spectrophotometry

Spectrophotometry is used to determine the total absorptance A of layers deposited on glass samples, and total reflectance R of textured wafer surfaces. A is assessed by calculating $A = 1 - R - T$ with T the total transmittance.
Measurements are performed on a Perkin Elmer Lambda950 UV-Vis-IR spectrophotometer including a 150-mm integration sphere coated with Spectralon®. T and R are measured through two different dedicated holders, over a wavelength range of 250 nm to 2500 nm using a R928 photomultiplier tube detector for the range 250 nm to 860 nm and an InGaAS detector for the range 860 nm to 2500 nm. Illumination is provided by deuterium and tungsten-halogen lamps over 250-350 nm and 350-2500 nm respectively.

2.3.11 X-ray diffraction (XRD)

XRD is a method based on the analysis of the scattered X-ray at a sample surface, revealing the preferential scattered direction of the rays, to determine the material crystallographic structure.
In this work, the XRD measurements are performed in a PanAnalytical X'Pert Pro Diffractometer with an angle step size of 0.0262°, a step time of 2.86 s and an angle range of 15° to 70°. Measurements recorded in this thesis were performed by Julien Hurni.

2.3.12 TEM and STEM characterization

The structure and chemistry of the MoO_{3-x}-based hole contact was assessed by TEM and STEM analysis, performed by Quentin Jeangros. For that purpose, a layer stack of (*i*)a-Si:H/MoO_{3-x}/ITO was deposited on a <111>-oriented mechanically polished (*n*)c-Si wafer. After annealing at 130 °C for 30 minutes, mimicking curing of the low temperature paste, a thicker MoO_{3-x} layer of 20 nm was deposited on top of ITO to serve as a freshly evaporated MoO_{3-x} reference. The contact stack was finalized by sputtering a Ag layer. A thin lamella was prepared using the conventional focused ion beam lift-out technique with a final thinning voltage of 2 kV in a Zeiss Nvision 40. Scanning TEM (STEM) high-angle annular dark-field (high-angle annular dark-field (HAADF)) images and energy-dispersive X-ray spectroscopy maps were recorded in a FEI Titan Themis microscope operated at 200 kV with a beam current of 200 pA. Electron energy-loss spectra (Electron energy-loss spectra (EELS)) were acquired at 80 kV and at cryogenic temperature (−165 °C) to assess the oxidation states of the thin (4 nm) and thick (20 nm) MoO_{3-x} layers without introducing electron beam artefacts [Lajaunie 2015]. A convergence semi-angle of 30.5 mrad was employed, while the collection semi-angle was 47 mrad. A dispersion of 0.1 eV/channel was employed for the dual EELS scans. For comparison purposes, M3 edges were aligned and rescaled to a value of 1 after removing the conventional power law background (using data within the ranges 380-390 eV and 445-450 eV to fit the background). Experimental data was compared to the reference MoO_2 and MoO_3 EELS spectra of [Lajaunie 2015] to assess qualitatively the oxidation state of MoO_{3-x} as a function of its thickness and processing history.

2.3.13 Ellipsometry

Ellipsometry is a characterization method used to estimate the thickness of thin films, based on the change of polarization of an incident beam reflected on the film (or film stack) surface. The measured data is interpreted through a model fitting to estimate the refractive index n and extinction coefficient k dispersion. In this work, a Horiba Jobin Yvon Uvisel ellipsometer was used to estimate the thin film thicknesses on flat samples. A single Tauc-Lorentz dispersion law model was used to fit the data in most cases, and a Drude dispersion law was added to the model for highly doped materials.

2.3.14 UV degradation chamber

For the UV radiation exposure, the mini-modules were aged following the IEC 62788-7-2 standard for a total duration of 1000 h. A Q-sun Xenon chamber from Q-Lab was used for the degradation, with a air temperature set at 65 °C (with a maximum temperature of 90 °C measured on a black panel) and a relative humidity of 20%. The UV exposure is provided by a Xe-arc lamp artificial source with daylight filter and an irradiance of 0.8 $W m^{-2}$ at 340 nm, and has a UV dose of 63 $W m^{-2}$ over 295 nm to 395 nm (representing a total UV dose of 63 $kWh m^{-2}$ after 1000 h of exposure).

3 Transition metal oxides as novel contacts for silicon heterojunction solar cells

The present review work covers latest researches of the TMO-based silicon solar cells, including global researches led after the thesis beginning, as well as some results achieved in this thesis.

3.1 Transition metal oxides

3.1.1 Fundamental properties

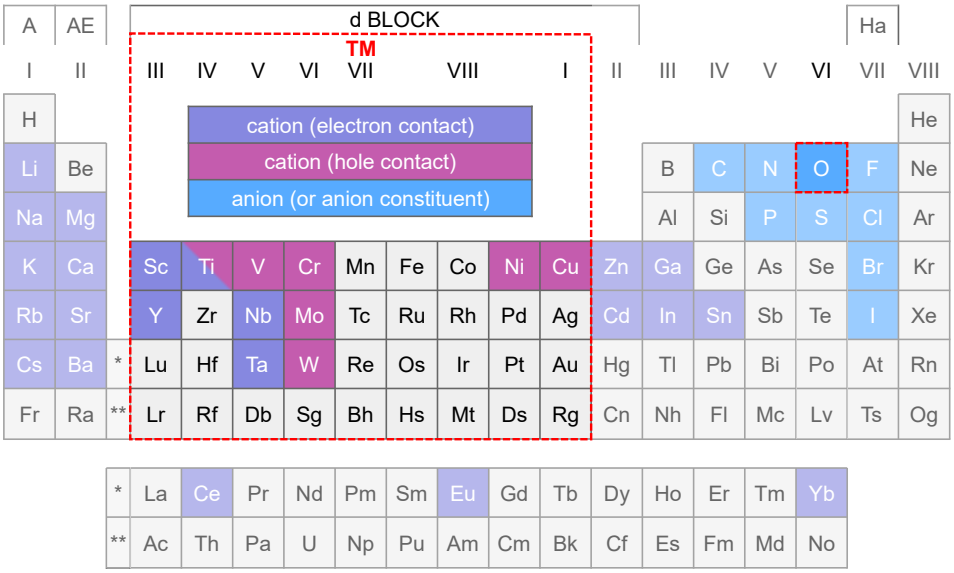

Figure 3.1: Periodic table highlighting elements utilised in metal compound based selective contacts for c-Si solar cells. The blocks corresponding to alkali (A), alkaline-earth (AE), transition metals (TM) and halides (Ha) are shown on top of the group numbers. The present review focuses on TM oxides used as hole selective contacts. Adapted from [Ibarra-Michel 2022], with the permission of Mathieu Boccard.

Transition metal oxides are widely studied in most microelectronics fields due to their unique physical and chemical features [Rao 1997, Goodenough 1971]. By definition, transition metals

are elements which can give rise to cations whose sub-shell *d* is partially filled [McNaught 1997], forming most of the *d*-block in the periodic table, as represented in Fig. 3.1. Their numerous available outer *d* electrons enable a very wide range of stable oxidation states, from -III to +VIII over the whole *d*-block. The small overlap between metal *d* and oxygen *p* orbitals and strong polarisation of the metal-oxygen bond give rise to narrow electronic *d* bands whose bandwidth is 1 eV to 2 eV instead of the usual 5 f to 15 for most metals [Rao 1989]. Because of narrow bands and numerous outer *d* electrons, TMOs can also act as correlated materials, i.e. materials in which electrons behave neither as localized electrons nor as collective delocalized electrons (electron-sea-like in a solid) but have an intermediate behavior due to non-negligible Coulombic interaction with neighboring electrons. Correlated electrons can further reduce the bands width or open gaps in the band. The present quantic behaviors are at the origin of TMOs singular properties and makes them behave like metals (e.g. TiO, WO_2, VO_2, MoO_2), semi-metals (e.g. VO), n- or p-type semiconductors (MoO_{3-x}, $Ni_{1-x}O$), or insulators (e.g. FeO, TiO_2, MoO_3). Most of them can also switch between two states e.g. from metal to insulator under composition, temperature or pressure variation [Rao 1989]. Other mechanisms such as the presence of potentially mobile and correlated O^- holes (*p* sub-shell partially filled) —in addition to divalent O^{2-} (filled *p* sub-shell)— in the solid state [Rao 1989], ordered point defect structures leading to sub-stoichiometry accompanied by crystallographic shears like in WO_3 MoO_3 and TiO_2 structures, or mixed valence compounds —-thanks to their various stable oxidation states— like in FeO [Greenwood 1997], give rise to continuous series of compositions (e.g.: $TiO_{1.900}$ to $TiO_{1.934}$) [Rao 1989], [Anderson 1974, Rao 1978, Tilley 1980, Rao 1989] hence rich diversity in properties and transitions. For these reasons, TMOs are used and studied in several areas like organic electronics [Tokito 1996, Chang 2005, Kanno 2006, Janssen 2007, Kröger 2009, Meyer 2012b], smart windows and gas sensors [Hotovy 1999, Kim 2010, Soleimanpour 2013], battery-cathode materials [Tsumura 1997, Li 2006, Oukassi 2009], electronic and optical switches [Hirashima 1986, Talledo 1995] like resistance random access memory (ReRam) or memristors [Chua 1971, Yang 2008a, Strukov 2008, Tour 2008].

3.1.2 Historical background

Interest for the introduction of TMOs in c-Si PV arose from the organic light emitting diodes (OLED) domain, whose first electronic device was realized in 1965 [Helfrich 1965]. Researchers, pushed by the high potential applications such as flat panels, raced to reduce the operating voltage while increasing emission efficiency and durability [Tang 1987, Adachi 1988a, Adachi 1988b, Adachi 1990]. After several groups noticed that the band alignment and carrier confinement in the heterostructure was closely linked to the device performance [Ohmori 1993, Burrows 1994, Shirota 1994], Adachi *et al.* demonstrated that decreasing the barrier height at the interface between the hole selective layer (HTL) and the anode improved operating voltage and durability [Adachi 1995]. Tokito *et al.* [Tokito 1996] extended their study in 1996 using different metal oxides (V_2O_{5-x}, MoO_{3-x} and RuO_{2-x}), linking metal-oxide work function to device performance. Since then, metal oxides were extensively studied and used in this field and that of organic photovoltaics, and recently came to inorganic silicon-based PV to be

used as electron or hole contacts.

Here, we will discuss the performance and limitations of different metal oxides used as hole contacts in silicon solar cells. A review of TMOs used as electron contacts, and more generally metal-compounds-based contacts in silicon solar cells, is available in [Ibarra-Michel 2022].

3.1.3 TMO classification through the *d* band occupancy

The diverse and complex interactions between transition metals and oxygen, as well as the variety of crystallographic structures, result in a wide range of optoelectronics properties for the TMOs. Sub-grouping them under similar electronic behavior is thus challenging. However, a common criterion for classification, adopted by several chemists and physicists, lies in the oxide d bands occupancy since it is closely linked to their electronic behavior [Henrich 1996]. In a simple approach, the d-band of the TMO is generally build by the transition metal d orbitals while the p-band by the oxygen p orbitals. In principle, the latter is filled first due to oxygen superior electro-negativity. The d-band occupancy depends on the transition metal valence electrons amount and coordinated oxygen. To illustrate this, Fig. 3.2 schematizes two hypothetical examples arbitrarily chosen of TMO formation for two different transition metals.

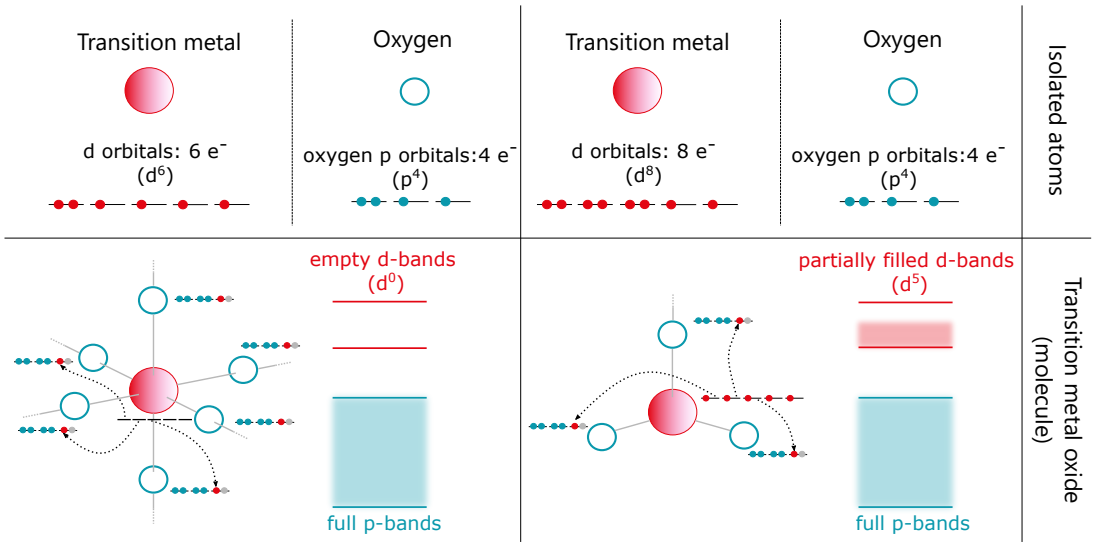

Figure 3.2: Formation of two TMOs with different transition metal atoms. The resulting d-band occupancy depends on the number of the initial transition metal valence electrons and its coordination with oxygen (=oxidation state). Valence electrons of the transition metal are depleted to first fill the oxygen ones, more favourable energetically.

In their review on TMOs for organic electronics, Greiner and Lu used it to divide them under 4 classes [Greiner 2013b], which we illustrate in Fig. 3.3. Class 1 groups oxides with empty d bands (d^0), which simply follows the collective delocalized electrons models and have a

natural tendency to form oxygen vacancies which result in defect donor states in the band-gap (oxygen-deficient TMOs), mostly due to unstable oxygen interstitials. These states are occupied and reside below the band conduction minimum, making the TMOs from class 1 generally behaving as n-type semiconductors (sub-class *1a*), such as MoO_{3-x}, TiO_{2-x}, WO_{3-x}, ZrO_{2-x}, V_2O_{5-x}, CrO_{3-x}. Reduction of these oxides tends to form TMOs with metallic behavior (d bands partially filled) stemming from the filling of few electrons in the d bands (e.g.: d^1, d^2, d^3). They can be regrouped in class 2 as for instance WO_2, TiO, MoO_2, $Cr_{2-x}O_3$. In class 3, d bands are also partially filled but the large number of electrons in the bands makes TMOs of this class behave as strongly correlated materials, with differing electronic band structure compared to the one predicted by the delocalized electrons theory. They can be Mott-Hubbard and charge-transfer insulators, with transitions from metallic to insulator behavior according to pressure, doping, etc. Materials of this class have complex behavior, not really well modelled yet, and $Ni_{1-x}O$, $Cu_{1-x}O$ and $Co_{1-x}O$, which are p-type semiconductors, may belong to this class. Oxides with completely filled bands (d^{10}), the class 4, tend to be p-type semiconductors, generally due to metal-cation vacancies, like $Ag_{2-x}O$ or $Cu_{2-x}O$.
Metals from the last column of the d-block are usually not considered as transition metals and referred to as poor metals. Their oxides have a different electronic behavior due to their full d band. Some of these oxides are used as passivating layers (e.g. Al_2O_3, Ga_2O_3) or TCOs (ZnO, SnO_2, In_2O_3) sometimes used as electron selective contacts.

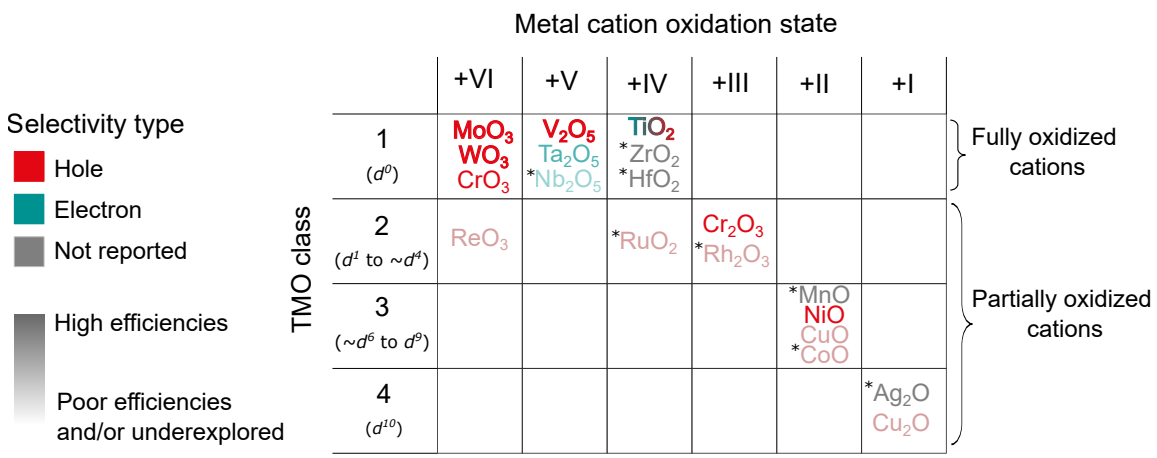

Figure 3.3: Classification of the most common TMOs used for LED and PV applications according to the d band occupancy and the metal cation oxidation state. Oxides of poor metals like SnO_2 or ZnO, and unsuited oxides with metallic behavior like MoO_2, WO_2 or CrO_2 are not represented. Metal cations in their highest oxidation state (fully oxidized, class 1) have empty s and d valence orbitals (so empty d bands, d^0, in the solid case): all electrons are captured in surrounding oxygens (more electronegative) p orbitals. Darkest shades represent most investigated and efficient TMOs as selective contacts, while lightest the less investigated and/or efficient. For more information about their properties and (potential) use, the reader is referred to the text. * Stars indicate the TMO has never been reported as a carrier selective contact in c-Si PV.

3.1.4 Mechanisms for carrier selectivity

When used as hole or electron transport layers, selectivity is typically provided by the TMO work function which produces upward or downward band bending. Their wide band gap ensures optical transparency, and can also be used as an additional barrier for the undesired carrier, when an electron (resp. hole) selective contact is formed by a n-type (resp. p-type) TMO [Greiner 2013b]. However, this is usually not the case, and in particular for high work function n-type TMOs acting as hole contact, such as MoO_{3-x} or WO_{3-x}, for which the TMO/Si interface acts as a recombination junction. A lowering of the work function for these TMOs of a few hundreds of meV would enhance parasitic thermionic emission of electrons and hamper V_{OC}.
Precise knowledge of the work function of the TMOs used in solar cells is hard to achieve, and even more so when incorporated in a contact stack. Indeed, work function measurement is in general highly sensitive to small changes at the material surface such as defects (dangling bonds, vacancies, adsorbates, surface reconstruction, etc.), dipole creation, or Fermi level pinning. For TMOs, the work function is notoriously more sensitive since these materials can additionally be easily oxidized or reduced [Henrich 1996] with ambient air or in proximity to the material/metal-oxide interface [Greiner 2013b, Greiner 2012a, Greiner 2013a] through an exchange of oxygen (redox reaction) and/or electrons (Fermi level differences at the interface). This sensitivity of TMOs is at the origin of oxygen or metal cation deficiency, generally introducing band-gap defects or changes in the cation oxidation state. The band-gap defects tune the TMO carrier concentration (electrons or holes) and shift the Fermi level towards one band whereas changing the oxidation state modifies electronegativity, which is directly linked to the material work function [Greiner 2012a]. We generally observe that the higher the metal cation oxidation state, the higher the electronegativity, the higher the work function. From Fig. 3.3, it is also worth to note that the TMO for which highest device efficiencies are achieved by the oxides which are fully oxidized.

3.2 TMOs as hole selective contacts in silicon solar cells

3.2.1 MoO_{3-x}, V_2O_{5-x}, and WO_{3-x}

Among the various TMOs having hole-selective properties, MoO_{3-x}, V_2O_{5-x} and WO_{3-x} are the ones with the highest work function and are the most investigated. The first silicon solar cell to integrate a TMO as a selective contact, namely molybdenum oxide (MoO_{3-x}), was made in 2011 with the thin-film a-Si:H-based technology [Il Park 2011], and in 2014 in a c-Si heterojunction solar cell with the same material [Battaglia 2014b, Bullock 2014]. MoO_{3-x} remains by far the most tested [Battaglia 2014a, Gerling 2015a, Gerling 2015c, Bullock 2015, Geissbühler 2015] [Bivour 2015, Um 2016, Wu 2016, Bullock 2016, Bivour 2017] and [Sacchetto 2017, Essig 2018, Wu 2018, Li 2020b, Dréon 2020, Zhong 2020, Mazzarella 2021]. It is today the TMO providing the best performance amongst devices using at least one metal-compound contact. Fewer studies were conducted with V_2O_{5-x} [Gerling 2015a, Gerling 2015c, Bivour 2016, Gerling 2016,

Wu 2017b, Almora 2017, Masmitjà 2017, Masmitjà 2018, Kim 2020, Yang 2020, Du 2021b], [Ros Costals 2021] and WO_{3-x} [Bivour 2015, Gerling 2015a, Gerling 2015c, Wu 2016, Mews 2016, Bivour 2017, Mews 2017] with highest efficiencies achieved of 21.6% [Yang 2020] and 17.9% [Bivour 2015], respectively. Less interest in the latter material could come from the too high contact and bulk resistivity it provides when implemented in SHJ cells [Gerling 2015a, Gerling 2015c, Wu 2016].

Passivation quality

One limitation of hole-selective TMOs lies in the fact that they do not provide excellent passivation to c-Si surfaces. In their work, Gerling *et al.* [Gerling 2015c] showed that MoO_{3-x}, V_2O_{5-x} and WO_{3-x} have an inherent (but limited) passivation that stems from the reduced density of surface electrons induced by the high work function, as well as the presence of a sub-stoichiometric SiO_x layer originating from the redox reaction between the TMO and c-Si. The authors emphasize that the induced band bending is probably lowered by dipole effects, and the SiO_x layer formed may be too defective, which limits passivation of the interface. Among the three, V_2O_{5-x} is the one providing the highest passivation on n-type c-Si with an implied V_{OC} of 653 mV and saturation current of 150 fA cm^{-2}, followed by MoO_{3-x} (637 mV and 230 fA cm^{-2}) and WO_{3-x}(543 mV and 420 fA cm^{-2}). Those results and range of values have been confirmed by several groups [Bullock 2015, Um 2016, Wu 2016, Bivour 2016, Sacchetto 2017, García-Hernansanz 2018], yet with an iV_{OC} record above 670 mV provided by V_2O_{5-x} [Yang 2020] (see below). Structures involving a TMO as hole selective contact without passivation layer did not exceed 16.7% for MoO_{3-x} [Gao 2018], 17.7% for WO_{3-x} (after annealing at 180 °C) [Bivour 2015] and recently 19.0% for V_2O_{5-x} [Ros Costals 2021]. For the case of V_2O_{5-x}, Masmitjà *et al.* could push the efficiency to 19.7% by the introduction of a thin Ni interlayer between V_2O_{5-x} and the metal electrode in an IBC structure [Masmitjà 2017]. Later, Kim *et al.* manage to reach 17.25% in a standard front-back contacted cell, with the same additional Ni layer, fully dopant free contacts and a double anti reflective coating [Kim 2020]. Still both solar cells are limited by a low V_{OC} (656 mV and 621 mV respectively). To date, achieving higher efficiencies requires the presence of an additional passivation layer at c-Si interface as for standard SHJ, like (*i*)a-Si:H, SiO_x:H or Al_2O_3, partially offsetting the current gain provided by their transparency.

Deposition methods

For all the deposition methods presented hereunder, the TMOs all grow in an amorphous arrangement. In the case of MoO_{3-x}, thermal evaporation is the most used deposition method and provides the highest solar cell performance. However, it is far from the ideal deposition process since it is difficult to control the oxygen concentration, a critical factor for TMOs as mentioned in the previous sections. A few studies have explored more tunable deposition processes such as reactive sputtering [Bivour 2017, Boccard 2015] and atomic layer deposition (ALD) [Macco 2015, Ziegler 2015, Li 2020b]. Final devices in these studies showed systemati-

cally limited performance —low V_{OC} and *FF* — ascribed to poorer selectivity compared with thermally evaporated MoO_{3-x} which appears as the most straightforward method to prepare contact-grade MoO_{3-x} films. The reason is yet unclear, and possibly stems from excessively oxygen-deficient material or too resistive oxides, and/or degradation due to the deposition atmosphere (plasma, hydrogen (typically 3-11% [Vos 2016]), water, etc.). In view of the limited amount of publications explaining this underperformance, and vast parameter space, it is nevertheless premature to conclude authoritatively on the (un)suitability of sputtered or atomic layer deposited MoO_{3-x} to act as carrier-selective contacts to silicon heterojunction solar cells. In a recent study, Li *et al.* [Li 2020a] used hot wire oxidation-sublimation deposition (HWOSD), claiming this novel technique could be easily upscaled and in which MoO_{3-x} oxygen rate can be well controlled —without showing the effect of oxygen rate on cell performance though. The present deposition method could be a promising alternative to the standard Joule effect evaporation, combining evaporation and controlled oxygen rate. In a configuration with a full area 14-nm-MoO_{3-x} layer placed at the back side of the absorber, an (*i*)a-Si:H passivation interlayer annealed prior to MoO_{3-x} deposition ("pre-annealing"), they reached an efficiency of 21.10% and remarkable V_{OC} of 714 mV.
The same tendency is observed for WO_{3-x} and V_2O_{5-x} with a predominance of thermal evaporation and few results with alternative deposition techniques. Sputtered WO_{3-x} also provides lower V_{OC} and *FF* compared with the thermally evaporated one [Bivour 2017, Mews 2017, Tran 2020]. In the latter work, Mews *et al.* reached 16.6% efficiency and a V_{OC} around 700 mV with front-contact sputtered WO_{3-x} and (*i*)a-Si:H passivation layer. The best thermally-evaporated V_2O_{5-x} involved as front hole contact, with an efficiency of 21.0% and an impressive *FF* of 83.25% ascribed to UV/O_3-treated SiO_x passivation layer, was recently achieved by Du *et al.* [Du 2021b]. In 2020, Yang *et al.* [Yang 2020] demonstrated superior performance for V_2O_{5-x} deposited by ALD at 230 °C compared with evaporated —J_0 of 44 fA cm^{-2} and iV_{OC} above 670 mV on both p- and n-type c-Si. As above-mentioned, a record efficiency for V_2O_{5-x}-based hole contact SHJ of 21.6% was achieved, with pre-annealed (*i*)a-Si:H passivation layer and V_2O_{5-x} deposited by ALD at 230 °C as full-area back contact. The improvement is partly attributed to the high deposition temperature which results in a high work function, a result also reported in [Parashar 2019]. Again, strong conclusions are hard to make due to the limited amount of published studies on the different ways of depositions, yet forming good contacts with WO_{3-x} and V_2O_{5-x} seems less particular to thermal evaporation compared to the use of MoO_{3-x}.

Architectures and their record efficiencies

A rich variety of structures, principally involving n-type c-Si for the absorber, have been used for the different hole-selective TMOs. The structures presented in this paragraph involve a dedicated passivation layer in addition with the TMO selective contact. Results achieved without passivation layers are mentioned above.
For front-back-contacted structures, the highest-efficiency device using a TMO-based hole contact reached 23.5% and was achieved by Dréon *et al.* using MoO_{3-x} [Dréon 2020]. It utilized a thermally evaporated 4-mn thick MoO_{3-x} layer in between an (*i*)a-Si:H passivating layer

and an ITO film. The MoO_{3-x} contact is placed on the front-side of the device, which uses an Ag-screen printed metallization cured at a temperature of 130 °C, and a traditional SHJ architecture on the rear side. The high efficiency is mostly attributed to excellent passivation provided by the (*i*)a-Si:H layer, and the high transparency (higher than (*p*)a-Si:H) and good selectivity of the thin MoO_{3-x} layer. The best V_2O_{5-x} double-side contacted solar cell (21.6% efficient) was already mentioned in the deposition methods paragraph, made by Yang *et al.* [27]. For the WO_{3-x}-based double-side contacted cells, no devices with record efficiency were made recently and the best cell remains the above-mentioned one processed by Bivour *et al.* [Bivour 2016] in 2015 reaching 17.9%. Solar cells employing both front and back (electron and hole contacts) Si-free contacts were also processed [Bullock 2015, Kim 2020] with record efficiency for this category of 21.4% using Ag/ITO/ MoO_{3-x}/(*i*)a-Si:H as a front hole contact and Al/ZnO/LiF_x/(*i*)a-Si:H, achieved by Zhong *et al.* [Zhong 2020]. The same structure was used in a bifacial architecture by Lin *et al.* in 2021 and could reach 21 mW cm^{-2} in bifacial operation considering a 0.15 sun rear irradiance [Lin 2021].

More complex structures were also explored. Among them, IBC architectures are the most investigated, typically using MoO_{3-x} in the hole-contact stack [Um 2016, Wu 2016]. The highest efficiency of 22.1% was obtained by Wu *et al.* [Wu 2020] using (*i*)a-Si:H as a passivation layer and thermally evaporated MoO_{3-x}/Ag and MgF_x/Mg/Al as hole- and electron-selective contacts. In addition, WO_{3-x} with no passivation layer achieved an efficiency of 16.6% [Wu 2016], and finally V_2O_{5-x} attained 19.7% [Masmitjà 2018], again with no passivation layer, and a V_2O_{5-x}/Ni contact stack are also worth notice. Structures with partial rear contacts, like with MoO_{3-x} on a p-type wafer by Bullock *et al.* [Bullock 2015] (20.4%), or with chromium oxide (see section 3.2.2) have demonstrated the versatility of such contacts.
The group of Shen further tested hole contact TMOs in a multilayer stack for selective transparent conductive electrodes, following the organic electronic alternative TCO exploration [Han 2008, Jeong 2010, Hong 2011, Shen 2011, Kim 2015, Le 2016]. For Si-based solar cells, stacks of WO_{3-x}/Ag/WO_{3-x}[Bao 2016], V_2O_{5-x}/Ag, Ca or Au/V_2O_{5-x}[Wu 2017b], MoO_{3-x}/Ag/ MoO_{3-x} [Wu 2017a] and CrO_x/Ag/CrO_x [Lin 2018b] (see section 3.2.2 for more details about CrO_{3-x}) were all evaluated via thermal evaporation, with notable efficiencies of 19.0% in the V_2O_{5-x}/Au/ V_2O_{5-x} IBC configuration with no dedicated passivation layer (V_{OC} of 651 mV). Yet, such electrodes generally require more than 5-10 nm of metal to reach good conductivities which still limits transmittance and reflectance of the stack.

Stability towards air exposure, reducing species and thermal treatments

The electronic properties of TMOs are known to be sensitive to air exposure, contact with reducing species and heating, which are all involved when fabricating a solar cell, and might affect the solar cell final performance. Air exposure can reduce the metal oxide through reaction with hydrogen, water, or adsorption of other elements like carbon [Gerling 2015c] and other metals. This applies typically to MoO_{3-x} [Battaglia 2014b, Irfan 2012, Meyer 2010],

V_2O_{5-x} [Meyer 2011a] and WO_{3-x} [Meyer 2007, Song 2012]. Some studies reported that reduction of the TMO occurs at the interface TMO/element (Si, perovskites, metals, TCOs), by oxygen (redox reaction) or electron (charge transfer) exchanges [Greiner 2013a, Schulz 2016]. Upon thermal treatments above 150 °C —as often required for Si-based solar cells— V_2O_{5-x} [Zilberberg 2011, Wu 2004] and MoO_{3-x} [Battaglia 2014a, Geissbühler 2015, Sacchetto 2017, Essig 2018, Zhang 2018, Cho 2019] undergo severe degradation. This degradation was ascribed to H effusion from the underlayers (reducing the TMO), thickening of the SiO_x interlayer, or oxygen exchange with the top TCO. All these degradation mechanisms tend to raise a barrier to hole extraction, be it by work function reduction or introduction of an insulating layer, resulting in an "S-shape" in the solar cell *J-V* characteristics that can strongly impede V_{OC} and *FF*. Yet, WO_{3-x} seems more resilient than its counterparts to air exposure (tends to have a fully or over-oxidized surface [Gerling 2015a]), plasma treatment [Werner 2016] and thermal post-annealing at 180 °C at least [Bivour 2015] (showed to turn non-ohmic after annealing at 180 °C on test structures [Ali 2018]). More investigation is required to conclude on WO_{3-x} layer stability. A couple of pre-treatment strategies have been developed to prevent TMOs from some of the aforementioned degradations, more particularly for MoO_{3-x}-based contacts. Essig *et al.* [Essig 2018] recommended to anneal the (*i*)a-Si:H passivation layer prior to MoO_{3-x} deposition at 250 °C to restrict the amount of effused H from the intrinsic layer to the MoO_{3-x} layer during subsequent annealing (e.g. Ag-paste curing in case of screen-printing). This resulted in significantly improved performance for final cells cured at 190 °C when the Ag-paste was the limiting factor. Recently, Mazzarella *et al.* suggested a plasma treatment before MoO_{3-x} deposition, with the aim of mitigating the dipole moment formed at the MoO_{3-x}/SiO_x/a-Si:H interface [Mazzarella 2021]. Applying it prior to the deposition of MoO_{3-x} layers of 3.5-8 nm thickness mitigated the S-shape in the *J-V* characteristics. Nevertheless, a pretreatment is not mandatory for high performance, as the 23.5%-efficient MoO_{3-x}-based device using a 4-nm-thick layer was achieved without any pre-treatment, albeit restricting the post-MoO_{3-x}-growth thermal treatments to 130 °C [Dréon 2020]. During evaporation of the TMO, increasing the oxygen rate to increase work function was attempted by some groups, yet with limited success probably explained by MoO_{3-x} thermodynamic nature of being oxygen deficient [Greiner 2013b].

3.2.2 Other hole-selective TMOs

Other TMOs, less common in the c-Si PV field, have been tried as hole contacts as well, including chromium oxide, nickel oxide and copper oxide.

Chromium oxides

Chromium oxide is known to have numerous oxide phases like Cr_2O, CrO, Cr_3O_4, Cr_2O_3, CrO_2, Cr_8O_{11}, and CrO_3 [Ingle 2001, Qin 2011b]. Cr_2O_3 (+III oxidation state, belonging to class 2) is the most stable phase, with a tendency to be Cr deficient ($Cr_{2-x}O_3$) making it p-type with a work function around 5.0 eV [Greiner 2012b, Greiner 2013b]. The second most stable phase is

CrO_3 (+VI oxidation state, class 1), which tends to be oxygen deficient (CrO_{3-x}) and behaves as an n-type semiconductor with a high work function around 6.75 eV in absence of air exposure [Greiner 2012b, Greiner 2013b]. However, pure CrO_{3-x} or $Cr_{2-x}O_3$ phases are hard to reach, and oxidation states of +III, +IV and +VI generally coexist [Ingle 2001], with a predominance of +III or +VI depending on the ambient environment. A couple of studies from perovskite and organic photovoltaics reported the use of $Cr_{2-x}O_3$-predominant chromium oxide [Wang 2010, Qin 2011a, Qin 2011b, Kaltenbrunner 2015, Qin 2016, Qin 2018], obtained by evaporation or RF sputtering of pure Cr, and initially used as a barrier to chemical reactions and metal diffusion then as a hole transporting layer. In 2018, Lin *et al.* used CrO_{3-x}-predominant oxide, obtained by evaporation of stoichiometric CrO_3 particles, as a hole contact in SHJ [Lin 2018b, Lin 2018a]. They studied the phases' predominance under different annealing temperatures in N_2- or O_2-rich atmospheres. The best solar cell efficiency obtained was 20.3%, using a p-type c-Si absorber and aforementioned multilayer stack CrO_{3-x}/Ag/CrO_{3-x} (with CrO_{3-x}: 67.9%, $Cr(OH)_3$: 16.1% and $Cr_{2-x}O_3$: 16% for the chromium oxide layer) as partial rear hole-contact and an Al_2O_3/SiN_x rear passivation layer. A work function of 4.8 eV was obtained, probably limited by reduction with H and presence of the $Cr_{2-x}O_3$ phase. Recently, Xu *et al.* processed aqueous solution of a copper doped chromium oxide (mixed phase of $Cr_{2-x}O_3$, $Cr(OH)_3$, CrO_{3-x}, and CrO_2), spin-coated at the rear side of p-type Si absorber, post annealed at 150 °C [Xu 2021]. They obtained a work function of 5.04 eV for the films, and solar cell efficiency of 16.6% (15.9% without Cu doping). Other work has not been reported yet, maybe due to CrO_{3-x} high toxicity.

Titanium oxide

TiO_{2-x} is a well known TMO electron-selective contact, a selectivity widely attributed to the specific band alignment with c-Si. However, Matsui *et al.* have demonstrated that under the right conditions, a stack of TiO_{2-x}/ITO can also be used as a hole-selective contact, resulting in an efficiency of 21.1% [Matsui 2017, Matsui 2020]. The contact has proper characteristics, as witnessed by the external voltage and *FF* of 677 mV and 76.8%, respectively. Owing to the high transparency of the stack, a noteworthy J_{SC} of 40.5 mA cm^{-2} was obtained. The authors examined both plasma and thermal ALD TiO_{2-x} and showed that for the case of thermal ALD, a proper hole-selective contact can be formed by the application of a hydrogen plasma to the TiO_{2-x}, followed by ITO sputtering and annealing in an oxygen-containing ambient. This leads to the formation of a TiO_x/SiO interface, which is thought to aid in passivation and selectivity. The hole-selectivity is attributed to a strong upward band bending in the c-Si which originates from a combination of the negative fixed charge in the TiO_{2-x}, the high work function of the ITO and the de-pinning of the Fermi level by the passivating TiO_{2-x}. Furthermore, the authors demonstrated that the *FF* does not strongly depend on the TiO_{2-x} thickness for at least 5-10 nm, suggesting that the valence band offset does not affect transport, indicating transport is dominated by hopping through defects in the TiO_{2-x} layer.

Nickel oxide

NiO is the most studied class-3 TMO, both fundamentally and experimentally. Even though understanding its electronic behavior is still highly challenging and debated [Gao 2020, Li 2019, Shin 2017], NiO is a long-time-known p-type semiconductor – due to its natural tendency to be metal-deficient ($Ni_{1-x}O$) –, which must belong to the Mott (or "charge transfer") insulators family [Adler 1970, Hüfner 1994, Greiner 2013b]. With a band-gap reported to vary from 3.2 eV to 4.3 eV [Powell 1970, Misho 1988, Pramanik 1990, Varkey 1993, Sato 1993, Hüfner 1994, Patil 2002, Irwin 2008] – depending on computation and theoretical models, measurements methods, or how the band edge is defined – and a work function ranging from 6.3 eV with no air exposure, to 5 eV [Irwin 2008, Chan 2002, Greiner 2013b], it seems to be a perfect hole contact for solar cells applications. It has been widely used in organic, dye-sensitized and perovskite photovoltaics and is well established to help for hole transport [Jeng 2014, Zhang 2016a, Zhu 2014, Chen 2015, Park 2015, Wang 2014, Irwin 2008, Gibson 2009, Powar 2013], [Nattestad 2010, Ratcliff 2013, Odobel 2013, Garcia 2012, Manders 2013, Irwin 2011], limited however by non ideal interfacial conditions [Berry 2010, Islam 2017, Si 2018]. For crystalline silicon solar cells, modelling was largely used to investigate the suitability of NiO as hole contact [Islam 2014, Imran 2016, Menchini 2016, Woods-Robinson 2020, Woods-Robinson 2021]. Experimentally, a few SHJ devices were processed since 2016 [Menchini 2016, Grilli 2016, Xue 2017, Yang 2018, Nayak 2019] with no passivation layers for most of them, and performances limited by non-ideal interface (low V_{OC}) in all cases. The best efficiency of 15.2% was obtained by Nayak *et al.* with a thermally-evaporated 10-nm-thick $Ni_{1-x}O$ on a chemically grown silicon oxide as passivation layer, n-type c-Si as the absorber and $SiO_x/LiF_{1-x}/Al$ as electron contact [Nayak 2019]. The V_{OC} was limited to 580 mV indicating poor passivation or selectivity. Yet, the study does not precise if the limitation comes from the liF_x-based electron contact or the $Ni_{1-x}O$-based hole contact. Woods-Robinson *et al.* tried sputtered $Ni_{1-x}O$ with (*i*)a-Si:H passivation layer as hole contact on an n-type c-Si absorber, giving very poor results [Woods-Robinson 2020]. Surprisingly, thermally evaporated $Ni_{1-x}O$ in combination with a high quality passivation layer (e.g. SiO_x:H or (*i*)a-Si:H) has not been reported to date.

Copper oxides

Cuprite oxide ($Cu_{1-x}O$, class 3 oxide) and cuprous oxide ($Cu_{2-x}O$, class 1 oxide) are the two most stable phases of copper oxide, and well known to be naturally p-type semiconductors through Cu cation deficiency [Meyer 2012a, Chen 2013, Bao 2009]. They are abundant and non-toxic materials, with high work functions (5.9 eV and 4.8-5 eV respectively) [Tsur 1999, Yang 2008b, Greiner 2013b, Meyer 2012a]. However, they both have small to moderate band-gaps of 1.2-1.8 eV for $Cu_{1-x}O$ and 2.1-2.2 eV for $Cu_{2-x}O$ [Kidowaki 2012, Gao 2012, Greiner 2013b], making them quite absorbent if used as front contacts. In fact, they were used as absorbers in the diode industry before c-Si became standard. In the field of perovskite solar cells, these materials were shown to improve the hole extraction [Bao 2009, Shao 2010, Zuo 2015]. In contrary, for crystalline Si solar cells, mostly using $Cu_{2-x}O$, the few available studies showed very lim-

ited efficiencies up to 3.5% [Elfadill 2015, Ravindra 2017, Zhang 2016b, Masudy-Panah 2014], probably due to the particularly defective interface with Si.

3.3 Middle d-block transition metal oxides

Referring to the periodic table in Fig. 3.1, one can note that most transition metals from the center of the *d*-block (like group VII and VIII), with some others on the edges, are not highlighted as hole or electron selective contacts. Their oxides have indeed not or sparsely been investigated in c-Si solar cells technology, for clear or unclear reasons. To our knowledge, HfO_{2-x} and ZrO_{2-x} have not been reported as carrier selective contact for c-Si probably due to their insulating properties. ALD-deposited HfO_2 has however been recorded as an excellent passivation layer for c-Si surfaces [Lin 2012, Cui 2017]. Group VII of the periodic table rallies transition metals whose oxides are mostly not usable in standard conditions (liquid, volatile, highly reactive and/or highly toxic) like Mn_2O_7, MnO_3, Tc_2O_7, TcO_3, to which one can add RuO_4, OsO_4 and Ir compounds from group VIII, not tried as contacts for the aforementioned reasons. Re_2O_7 and ReO_3 have moderate stability. The former is reported to be more stable —yet highly reactive with water— than the latter but has a low melting point around 220 °C. ReO_3 is known to have a low resistivity (1×10^{-5} Ω cm 300 K) behaving like a metal [Greenwood 1997], and was used in organic electronics as hole transport layer —yet with no clear information on the final stoichiometry of the film— [Leem 2007, Kim 2012, Tan 2013]. Some groups attempted to use it as hole contact for (*n*)c-Si which showed similar properties than MoO_{3-x}, but actually appeared to be very unstable [Gerling 2015b]. $Mn_{1-x}O$ is the most stable oxide of Mn, but has not been reported as selective contact for c-Si solar cells. From group VIII, OsO_2 and RhO_2 exhibit metallic behavior, as well as the more famous MoO_2, WO_2 and Ti_4O_7 —generally met in c-Si PV as undesired product of the reduction of MoO_{3-x}, WO_{3-x} and TiO_{2-x}—, less suited for PV applications. Rh_2O_3 holds interesting TCO properties suited for hole contacts, as recorded in OLED literature [Kim 2005], with no results demonstrated in c-Si PV yet. Cobalt oxide has been used as an efficient hole contact in organic and perovskite photovoltaics [Shalan 2016, Chiang 2018, Ndione 2013], and RuO_{2-x} in the past as a hole transport layer for OLED [Tokito 1996], both never reported in c-Si field so far. Iron oxides are not reported neither, presumably because diffusion of Fe ions into Si would induce active recombination centers. In addition, Re, Ru, Rh, Pd and Pt are noble, expensive and scarce materials, which lowers the probability for investigation of their oxides. $Ag_{2-x}O$ and AgO are used as absorbers in dye sensitized solar cells [Wei 2014], with a band-gap around 1.4 eV which is too small for transparent contact applications.

3.4 Perspectives and limitations

To conclude, it can be seen that great strides have been made in pushing selective TMO contacts, and efficiencies well above 20% have been demonstrated. In principle, TMOs hold the promise to be a versatile contact material, as they are generally highly-transparent, have

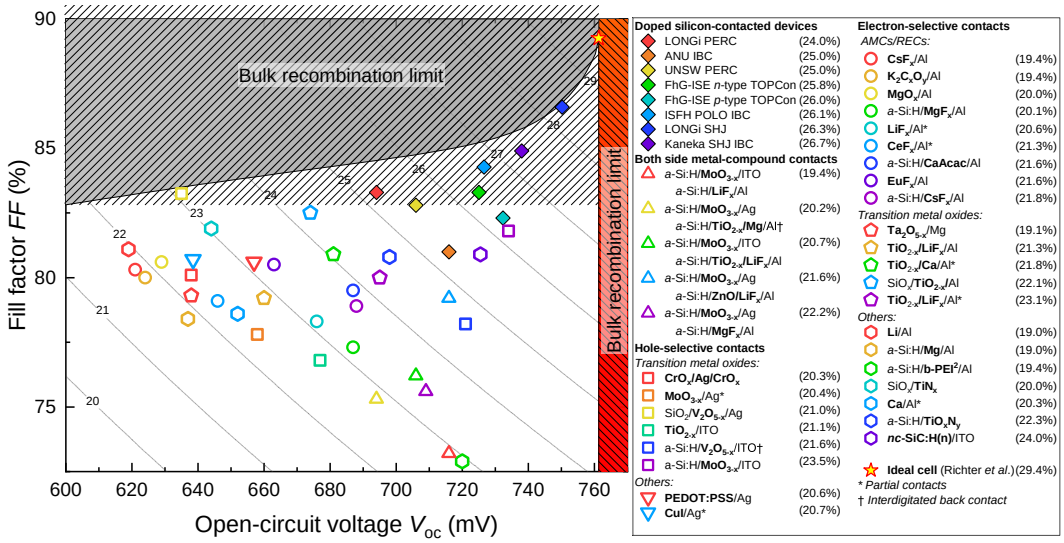

Figure 3.4: Literature overview of cell V_{OC}, *FF* and efficiency values. The comparison includes reference contacts based on doped silicon, hole-selective metal compound contacts, electron-selective metal compound contacts and fully dopant-free solar cells. The contour plot shows the ideal cell efficiency assuming a J_{SC} of 43.31 mA cm^{-2}, which corresponds to the idealised J_{SC} of the 110 μm-thick c-Si solar cell as modelled by Richter *et al.* [Richter 2013]. Reproduced with the permission of Bart Macco and from [Ibarra-Michel 2022].

tunable properties and can reach high selectivity. However, these concepts so far don't seem to contest the status quo of doped silicon, be it diffused junctions, doped a-Si:H or doped poly-Si contacts, as shown in Fig. 3.4 which groups the best silicon solar cells achieved using the standard Si-based contacts and metal-compounds-based ones. Despite their impressive electronic properties, TMOs are sensitive toward air exposure, reducing elements or thermal treatments which generally tend to reduce their work function, and special care needs to be taken when manipulating them as nm-thin contacts. In addition, they do not yet yield obvious process simplifications as several layers are still required to form an excellent selective contact. Hole-selective TMOs reach efficiencies over 23%, but since they do not provide excellent passivation to c-Si surfaces so far, the use of additional passivation layers, generally Si-based, is indispensable to obtain such results. This aspect hinders their transparency and the potential of the investigated hole-contact TMO to be the ideal "all-in-one" material for metal compound-based contacts to c-Si. Hole selective TMOs are often deposited by thermal evaporation, a process not really suited for industrial applications. Fortunately, among all the available compounds, only a few binary oxides have been reported in c-Si PV literature, some intensively like MoO_{3-x}, WO_{3-x}, V_2O_{5-x} or TiO_{2-x}, some are under-explored compared to their potential like $Ni_{1-x}O$, while others not reported, partly due to physical instability in standard conditions. In addition, various deposition methods start to be further explored and give promising results, as an alternative to the standard thermal evaporation, like ALD for V_2O_{5-x} or HWOSD for MoO_{3-x}. Overall, significant progress was made in just a few years both in terms of performance and understanding of Si-TMO contacts. This progress is still

ongoing, and the diversity of the material library is largely under-explored considering the option of using ternary, quaternary or even more complex metal oxides. This gives hope that an allround ideal contact might be unveiled in the near future and motivates the current and future research on that topic.

4 Study of $MoO_{3\text{-}x}$ thickness variation as a hole selective contact in SHJ solar cells

This chapter is based on the following publications:
Julie Dréon, Quentin Jeangros, Jean Cattin, Jan Haschke, Luca Antognini, Christophe Ballif and Mathieu Boccard, “23.5%-efficient silicon heterojunction silicon solar cell using molybdenum oxide as hole-selective contact,” Nano Energy, vol. 70, 2020, doi: 10.1016/j.nanoen.2020.104495. [Dréon 2020]
Julie Dréon, Jean Cattin, Gabriel Christmann, Davi Fébba, Vincent Paratte, Luca Antognini, Wenjie Lin, Sylvain Nicolay, Christophe Ballif and Mathieu Boccard, "Perfroamnce limitations and analysis of silicon heterojunction solar cells using $MoO_{3\text{-}x}$ hole selective contact", IEEE Journal of Photovoltaics, 2021, doi: 10.1109/JPHOTOV.2021.3082400. [Dréon 2021]

4.1 Abstract

Interest in silicon heterojunction solar cells is growing due to their manufacturing simplicity and record efficiencies, as detailed in the introduction of this thesis. However, a significant limitation of these devices still stems from parasitic light absorption in the amorphous silicon layers. This can be mitigated by replacing the traditional (p) and (n) doped amorphous silicon selective layers by other materials. While promising results have been achieved using $MoO_{3\text{-}x}$ as a front-side hole-selective layer, charge transport mechanisms in that contact stack have remained elusive and device efficiencies below predictions. In this chapter, we carefully analyze the influence of the $MoO_{3\text{-}x}$ and intrinsic (*i*)a-Si:H thicknesses on current-voltage properties and discuss transport and performance-loss mechanisms. In particular, we find that thinning down the $MoO_{3\text{-}x}$ and (*i*)a-Si:H layers down to 4 nm and 6 nm respectively, mitigates parasitic sub-bandgap $MoO_{3\text{-}x}$ optical absorption and drastically enhances charge transport, while still providing excellent passivation and selectivity. Even though such thin $MoO_{3\text{-}x}$ layer enables a considerable current-density gain of over 1 $mA\,cm^{-2}$ compared to the use of p-type amorphous silicon, and outperforms thicker $MoO_{3\text{-}x}$ layers, devices still suffer from substantial parasitic absorption from this layer. We then investigate the impact of the $MoO_{3\text{-}x}$ hole-selective layer for thickness between 4 to 0 nm. Based on opto-electrical characterization of the device at various processing stage and novel *J*-*V* curve fitting with

a model recently developed by Roe *et al.* , we discuss the optical and electrical effects of such variation on the solar-cell performances. We notably identify a loss of passivation and selectivity for MoO_{3-x} films thinner than 4 nm, that we link to a reduced work-function for such thin MoO_{3-x} films. We confirm experimentally that the optimal MoO_{3-x} thickness is around 4 nm, yet evidence that close to 0.5 mA cm^{-2} is still parasitically absorbed in such a thin layer. High-resolution transmission microscopy reveals that such thin MoO_{3-x} layer remains continuous and, while slightly sub-stoichiometric, exhibits a chemistry close to MoO_3. A screen-printed device reaching a certified world record efficiency of 23.5% and a fill factor of 81.8% is processed, demonstrating that dopant-free selective contacts can rival traditional approaches.

4.2 Introduction and motivations

SHJ solar cells using hydrogenated-amorphous-silicon a-Si:H passivating contacts, (namely "standard" SHJ) are known for simple processing combined with high efficiencies [Adachi 2015, Yoshikawa 2017, Longi 2021]. Yet, their performances are hindered by parasitic absorption in the a-Si:H layers, with current losses up to 2.8 mA cm^{-2} from p-type (*p*)a-Si:H and 1.9 mA cm^{-2} from intrinsic (*i*)a-Si:H [Tanaka 1992, Fujiwara 2007, Holman 2012]. In the pursuit of current-loss mitigation, many wide-bandgap silicon-based materials such as (*n*)μc-Si:H [Watahiki 2015], (*n*)nc-SiO_x:H (nano-crystalline SiO_x) or (*p*)μc-SiO_x:H [Mazzarella 2015, Mazzarella 2018], SiO_x/(*p*)μc-Si:H [Fioretti 2019], SiO_x/(*n*)μc-Si:C [Kohler 2020] or (*n*)nc-Si:H/ (*p*)nc-SiO_x:H [Boccard 2021] stacks have been developed to replace a-Si:H. New Si-free materials are promising alternatives to Si-based contacts, due to the wide amount of available compounds and unlimited tunable properties to investigate. Integrated in solar cells, they have already proved high performances, like with PEDOT:PSS [Sheng 2014, Zielke 2015, Yang 2017], TiN_x [Yang 2016], b-PEI/Al [Ji 2020], TiO_x/LiF_x/Al [Bullock 2019], ZnO/LiF_x/Al [Zhong 2020], MgF_x/Mg/Al [Wu 2018] or (n)GaP/(p)c-Si [Gudovskikh 2017], mostly used as rear electron contact, and WO_{3-x}, V_2O_{5-x} [Gerling 2016] or $Ni_{1-x}O$ [Imran 2016, Nayak 2019] to replace front hole contact. Si-free contacts replacing both holes and electron contacts with different architectures, such as bifacial [Lin 2021] or interdigitated back contacted (IBC) [Wu 2018] solar cells, have also been developed. A more detailed state of the art about alternative hole contact TMOs is given in Chapter 3.

Sub-stoichiometric molybdenum trioxide (MoO_{3-x}) stands so far as the most successful non-silicon-based approach to replace the p-doped hydrogenated amorphous silicon (*p*)a-Si:H front hole selective layer [Battaglia 2014a, Bivour 2015, Geissbühler 2015, Bullock 2018, Wu 2018]. However, MoO_{3-x} is still subject to parasitic absorption due to sub-bandgap defect states (see Chapter 3). Reducing the MoO_{3-x} thickness is therefore a promising strategy, especially since TMOs have been reported to protect (*i*)a-Si:H layers more efficiently from damage induced by TCO sputtering compared to (*p*)a-Si:H [Chan 2004, You 2007, Kim 2011, Werner 2015, Sacchetto 2017]. However, since electrical transport in the MoO_{3-x} layer is carried by electrons through defect states, the MoO_{3-x}/(*i*)a-Si:H interface is expected to be more

recombining than the (*p*)a-Si:H/(*i*)a-Si:H one. This could affect passivation, and call for a thicker (*i*)a-Si:H layer than when using a (*p*)a-Si:H contact. In this chapter, we explore the influence of (*i*)a-Si:H thickness increase from 6 nm (baseline) to 10 nm, and MoO_{3-x} thickness reduction on solar cell performances, from 9 nm (our baseline MoO_{3-x} thickness) to 4 nm, then from 4 nm to 0 nm (as a no-selective-layer reference), in order to reduce parasitic absorption in the MoO_{3-x} layer, while controling if a good passivation and selectivity can be maintained, through standard and novel characterization methods.

4.3 Study of devices with 9-to-4-nm-thick MoO_{3-x} layers and (*i*)a-Si:H layer thickness variation

4.3.1 Experimental details

Fig. 4.1 details the processing sequence followed here. For details about the depositions and process parameters, see Chapter 2, section 2.2. We processed nine wafers with same electron contact stack on each. Three different thicknesses of (*i*)a-Si:H (6 nm, 8 nm, and 10 nm) were used on the front side of the wafers (three co-processed wafers per thickness), and three different MoO_{3-x} layer thickness (4 nm, 6 nm and 9 nm) were also deposited.

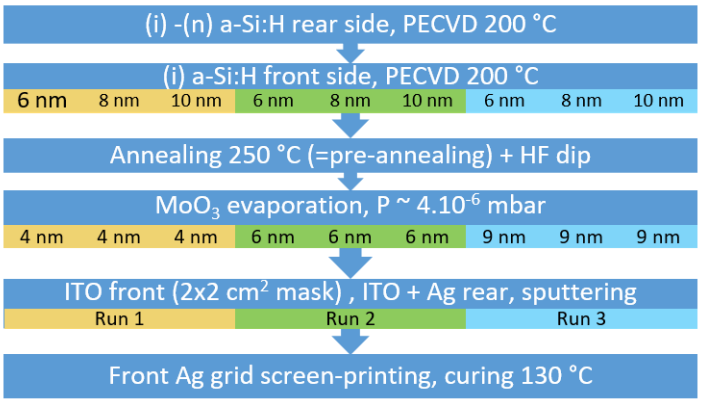

Figure 4.1: Process steps for the MoO_{3-x}-based silicon heterojunction solar cells realisation in the current study.

Standard SHJ solar cells are processed as references, using the procedure described in Chapter 2, section 2.2.

4.3.2 Thickness influence on optical and electric performances

Fig. 4.2 shows the parameters extracted from *J*-*V* measurements of the devices with different (*i*)a-Si:H and MoO_{3-x} thicknesses. To evaluate accurately the influence of MoO_{3-x} and (*i*)a-Si:H thicknesses on the different solar-cell electrical parameters, we performed a statistical analysis through p-value estimation. The latter is a statistical criteria which estimates the analysis

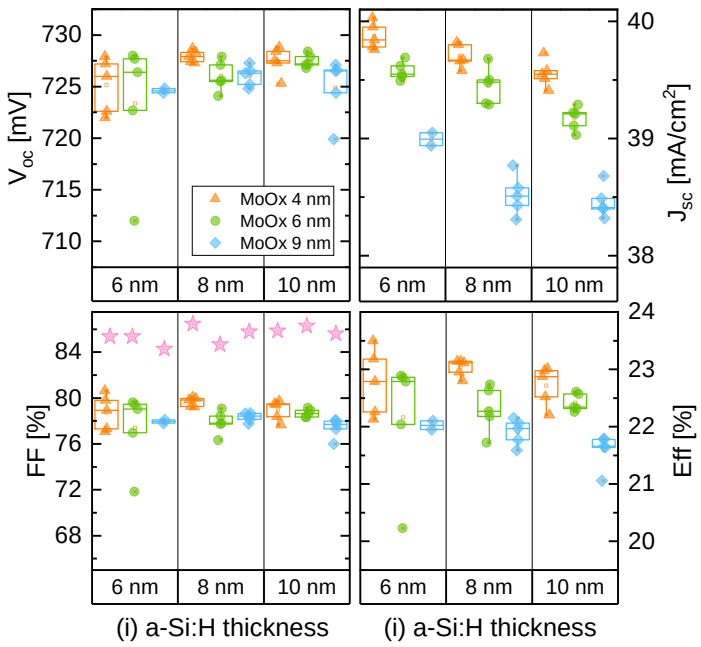

Figure 4.2: **a)** V_{OC}, **b)** J_{SC}, **c)** *FF*, and **d)** Efficiency of MoO_{3-x}-based solar cells with different thicknesses for the front (*i*)a-Si:H and MoO_{3-x} layers. Each dot represents one of five cells on a wafer. One wafer was prepared per condition. The pink stars represent the pseudo *FF*, *pFF*, extracted from the Suns-V_{OC}measurements.

significance [Fisher 1946, Goodman 2008]. We set the significance at 0.05, meaning that all statistical data with a p-value below 0.05 is considered significant and is not a result obtained by chance only. We performed here our statistical study through linear regression, analyzing the influence of (*i*)a-Si:H and MoO_{3-x} thickness on V_{OC}, J_{SC} and *FF*. The results are summarized in Table 4.1, taking (*i*)a-Si:H and MoO_{3-x} thicknesses as two independent parameters. When doing the analysis setting them correlated, results shows there is no correlation between the two thicknesses concerning their influence on the three electrical parameters.

Influence on V_{OC}

The open circuit voltage (V_{OC}) values in Fig. 4.2.a) are similar for all MoO_{3-x} and (*i*)a-Si:H thicknesses. Yet, the statistical analysis indicates a relevant V_{OC} gain upon thickening the (*i*)a-Si:H layer of $0.61 \pm 0.27\,\mathrm{mV\,nm^{-1}}$ (see Table 4.1) and a V_{OC} loss of $-0.41 \pm 0.25\,\mathrm{mV\,nm^{-1}}$ when changing the MoO_{3-x} thickness. But with a p value around 0.1, indicative of a limited statistical validity, no evident correlation between thickness and V_{OC} can be established. The thinnest MoO_{3-x} globally yields a V_{OC} around 2 mV higher than for the thickest layers. Part of this gain (0.6 mV) can be attributed to the photogeneration difference, as estimated using a

Table 4.1: Summary of the statistical analysis on the influence of MoO_{3-x} and (*i*)a-Si:H thickness on V_{OC}, J_{SC}, and *FF* respectively .

Layer	Slope (mV/nm)	Std error (mV/nm)	p-value
(*i*)a-Si:H	0.61	0.27	0.03
MoO_{3-x}	-0.41	0.25	0.11

Layer	Slope ($mA/cm^2/nm$)	Std error ($mA/cm^2/nm$)	p-value
(*i*)a-Si:H	-0.10	0.01	1.90E-8
MoO_{3-x}	-0.25	0.01	2.0E-16

Layer	Slope ($\%_{absolute}/nm$)	Std error ($\%_{absolute}/nm$)	p-value
(*i*)a-Si:H	-0.11	0.14	0.44
MoO_{3-x}	-0.28	0.12	0.03

one-diode model employing the J_{SC} of Fig. 4.2.b) as the photogenerated current. PL imaging on Fig. 4.3 suggests that the thinnest MoO_{3-x} also provides better passivation and/or selectivity than thicker films. Indeed, the signal intensity seems to increase when thinning down the MoO_{3-x} layer. Yet, this slight difference in PL also correlates with the stronger absorption of thicker MoO_{3-x} layers. While no significant difference can be observed between the PL images, it can be concluded that the thinnest layers of both (*i*)a-Si:H and MoO_{3-x} are sufficiently thick to provide efficient passivation and hole selectivity.

Influence on J_{SC}

Fig. 4.2.b) shows that J_{SC} decreases when thickening either the MoO_{3-x} or (*i*)a-Si:H layer. The optical loss induced by MoO_{3-x} , estimated at $0.25 \pm 0.01\,mA\,cm^{-2}$ per nm of MoO_{3-x} thickness irrespective of the (*i*)a-Si:H thickness in the range tested, is higher than that induced by (*i*)a-Si:H of $0.10 \pm 0.01\,mA\,cm^{-2}$ per nm of a-Si:H irrespective of the MoO_{3-x} thickness, and as reported in [Holman 2012].

To identify accurately the origin of these losses, external quantum efficiency (EQE) and reflectance measurements are shown in Fig. 4.4.a) and b) and Table 4.2, highlighting gains in J_{SC} compared to the reference (*p*)a-Si:H SHJ cell. For all the MoO_{3-x}-based devices, there is only a slight variation in the 400 nm to 600 nm range, which may originate from batch-to-batch ITO variations rather than a real optical effect since the minimum of reflectance is shifted to shorter wavelength for thicker MoO_{3-x} or (*i*)a-Si:H, which is not consistent with a thickness influence. From Fig. 4.4.a), the (*i*)a-Si:H thickness influences absorption mostly for wavelengths below 600 nm and has no effect on reflection. On the other hand, Fig. 4.4.b) shows that the use of MoO_{3-x} influences absorption over the whole wavelength range. Noticeably,

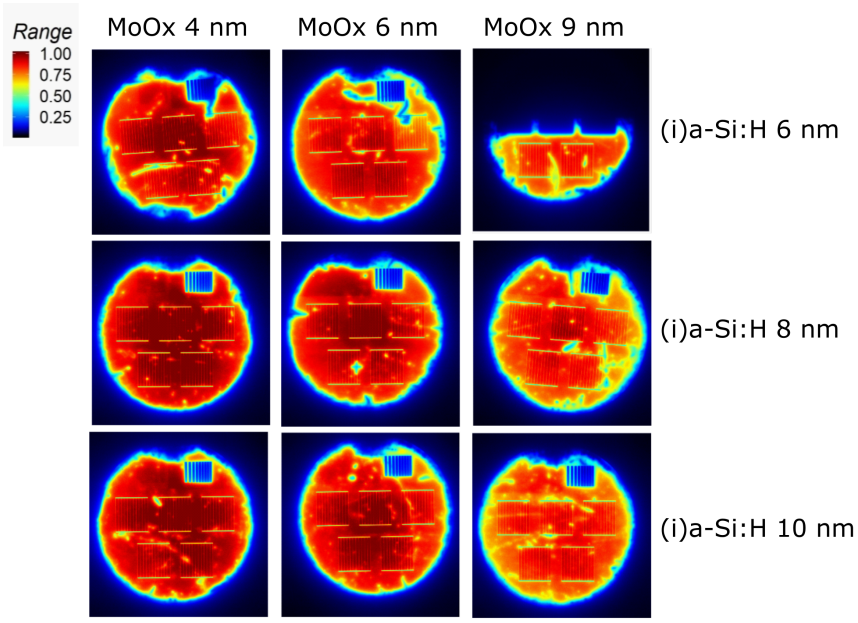

Figure 4.3: PL imaging of the nine wafers processed, at an injection corresponding to open circuit condition (one sun). All images are normalized to the same scale.

the EQE signal is reduced from 600 nm to 1200 nm when increasing the MoO_{3-x} thickness. This is due to sub-band-gap parasitic absorption in this range, as previously observed in Refs. [Geissbühler 2015, Sacchetto 2017, Werner 2016]. The fact that this effect occurs in the visible range may also explain why MoO_{3-x} sub-band-gap absorption impacts the J_{SC} more strongly than the UV-blue absorption of (*i*)a-Si:H —as the photon flux is lower in the UV. In our study, a J_{SC} loss of 0.4 mA cm^{-2} on 600 nm to 900 nm, compared with the standard (*p*)a-Si:H-based SHJ, is recorded for the thickest MoO_{3-x} but interestingly no loss is observed for the thinnest MoO_{3-x} . An IQE comparison in Fig. 4.4.c) and d) suggests that even though parasitic sub-bandgap absorption is strongly reduced when using the thinnest MoO_{3-x} layer, there is still a slight parasitic absorption between 700 and 900 nm. Calculation shows that the IQE signal loss on this range is proportional to MoO_{3-x} thickness, with a coefficient of 4.9×10^{-3} nm^{-1}. On the 320 nm to 600 nm range, gains in J_{SC} vary from 0.5 to 0.8 mA cm^{-2} depending on the MoO_{3-x} thickness (see Table 4.2). Although larger J_{SC} gains compared to standard SHJ cells were reported in literature in this range —1.9 mA cm^{-2} in [Battaglia 2014a], 1.3 mA cm^{-2} in [Bivour 2015], and 0.9 mA cm^{-2} in [Geissbühler 2015])—, these gains were mitigated by a strong loss at longer wavelengths, reducing the total J_{SC} gain. In [Battaglia 2014a], the replacement of ITO by more transparent hydrogen-doped indium oxide IO:H presumably compensated losses associated with sub-band-gap absorption in the MoO_{3-x} layer. In this study, final cells featuring the thinnest MoO_{3-x} film exhibited a total J_{SC} gain of 1.3 mA cm^{-2}. These results demonstrate that an adequate device architecture enables to fully benefit from the improved transparency of MoO_{3-x} compared to (*p*)a-Si:H .

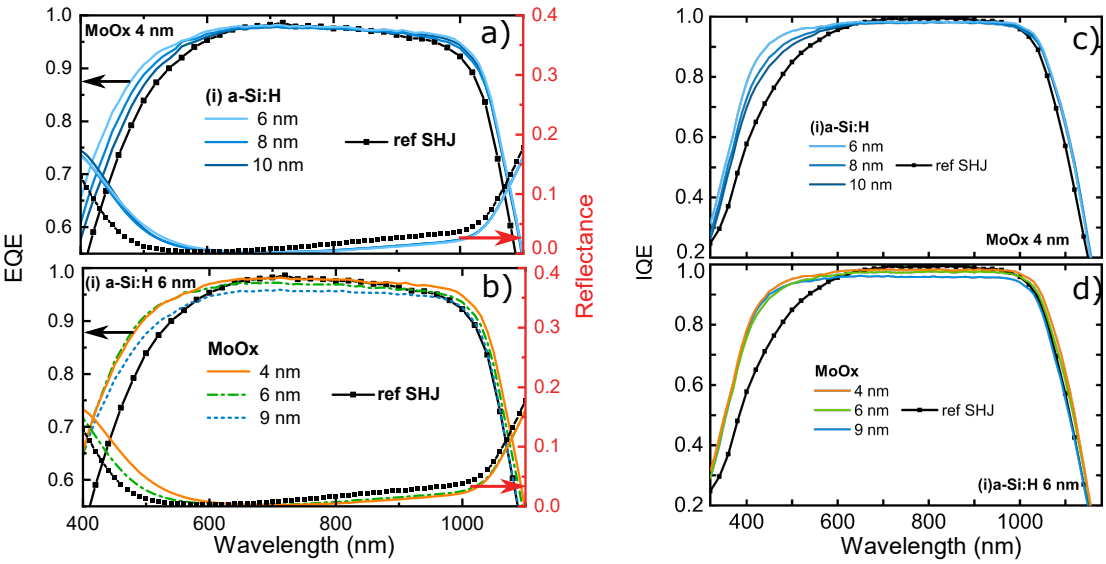

Figure 4.4: EQE and reflectance of **a)** devices with 4 nm MoO_{3-x} and variable (*i*)a-Si:H thickness; **b)** devices with 6 nm (*i*)a-Si:H and a variable MoO_{3-x} thickness. **c)** and **d)**: IQE of the same devices.

Table 4.2: J_{SC} gain or loss for MoO_{3-x}-based solar cells using 6 nm of (*i*)a-Si:H, compared to the reference SHJ cell, calculated from EQE curves over various wavelength ranges.

MoO_{3-x} thickness	J_{SC} gain (mA/cm^2)			
	320-600 nm	600-900 nm	900-1180 nm	Total
MoO_{3-x} 4nm	0.84	0.03	0.46	1.33
MoO_{3-x} 6 nm	0.83	-0.16	0.27	0.94
MoO_{3-x} 9 nm	53	-0.43	0.05	0.15

Influence on *FF*

Fig. 4.2.c) shows *FF* and *pFF* trends with MoO_{3-x} and (*i*)a-Si:H thickness. The thinnest layers —both MoO_{3-x} and (*i*)a-Si:H — combination investigated exhibit a *FF* up to 81%, proving that these thicknesses are sufficient to ensure efficient charge extraction and passivation. Statistical analysis indicates a stronger influence of the MoO_{3-x} thickness, with a *FF* loss of $-0.3 \pm 0.1\,\%_{\text{absolute}}\,\text{nm}^{-1}$ and no significant impact from the (*i*)a-Si:H thickness. Interestingly, [Holman 2012] reported that for standard SHJ with (*p*)a-Si:H the (*i*)a-Si:H thickness affects the *FF* significantly, suggesting that the MoO_{3-x} layer imposes stronger selectivity than the (*p*)a-Si:H one. Indeed, if MoO_{3-x} is more selective (e.g. thanks to the higher work function compared to (*p*)a-Si:H [Bivour 2015]), the hole population in (*i*)a-Si:H would be larger, which should lower the *FF* dependency on the (*i*)a-Si:H thickness. For standard SHJ solar cells, it is known that an increase in (*p*)a-Si:H thickness leads —to a certain extent— to a higher *FF* [Fujiwara 2007, Holman 2012, Bivour 2013], which might be due to the screening effect

provided by the (*p*)a-Si:H layer thickness ("screening length") towards the reverse Schottky diode induced at the interface ITO/(*p*)a-Si:H originating from work function mismatch [Bivour 2013]. The same trend for *FF* was observed by increasing the p-type layer doping [Martin de Nicolás 2011]. Increasing the MoO_{3-x} thickness, however, leads to a drop in *FF* , which suggest that MoO_{3-x} contact behaves differently. This could be due to its n-type character and higher work function, preventing the formation of a Schottky contact with ITO (contrary to (*p*)a-Si:H). The *FF* drop could come from an increase of the cell series resistance R_s as exhibited in Fig. 4.5 which shows the R_s at maximum power point (MPP) extracted from *J*-*V* characteristics with the method developed in [Bowden 2001]. From 4 to 6 nm of MoO_{3-x} ,R_s at MPP increases to $0.15\,\Omega\,cm^{-2}$ and R_s dependency on MoO_{3-x} thikness seems less important when increasing (*i*)a-Si:H thickness, yet spreading of the data impede an accurate conclusion. To probe the contribution of MoO_{3-x} layer thickness vertical resistance to the total solar cell series resistance R_s we measured the layer resistivity on glass. With 8 nm of MoO_{3-x} we measured a resistivity of $4.5 \times 10^4\,\Omega\,cm$ after evaporation, and $300\,\Omega\,cm$ after annealing at 180 °C. This corresponds to literature values spanning from $200\,\Omega\,cm$ [Battaglia 2014a] to $5 \times 10^4\,\Omega\,cm$ [Bullock 2014], a wide range which is linked to TMO nature of MoO_{3-x} as explained in Chapter 3. Choosing an upper limit MoO_{3-x} resistivity of $4.5 \times 10^4\,\Omega\,cm$ would give a series resistance increase of $0.005\,\Omega\,cm^{-2}$ per nm of MoO_{3-x} (see Table 4.3) which is way under the observed increase of solar cell total series resistance.

It was empirically showed that a $0.2\,\Omega\,cm^{-2}$ increase gives a 1 $\%_{absolute}$ *FF* loss [Pysch 2007]. $0.005\,\Omega\,cm^{-2}$ of R_s increase per nm of MoO_{3-x} would approximately give a 0.03 $\%_{absolute}$ *FF* loss, which is too low to explain the *FF* decrease. It suggests that transport is not only limited by materials bulk resistance losses in this kind of contact.

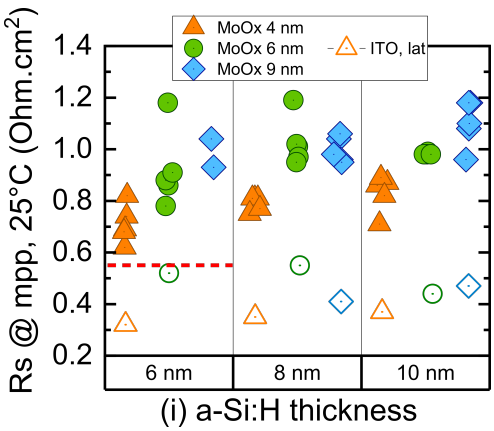

Figure 4.5: Calculated R_s of all MoO_{3-x}-based cells, extracted from *J*-*V* curves using the method reported in [Bowden 2001]. The dashed red line indicates the average R_s of the reference SHJs. Empty symbols represent the ITO lateral series resistance contribution to R_s, calculated from sheet resistance measurements following [Schroder 1984] and [Haschke 2019a].

Fig. 4.6 brings more insights on the nature of this *FF* loss by showing the *J*-*V* plots of cells with different MoO_{3-x} thicknesses. We observe a non-linear characteristic, usually referred to as an

Table 4.3: MoO_{3-x} vertical R_s, calculated with a MoO_{3-x} resistivity of $4.5 \times 10^4\ \Omega\,cm$.

MoO_{3-x} thickness	R_s vertical (Ohm.cm^2)
4 nm	0.02
6 nm	0.03
9 nm	0.04

"S-shape," which is typical for contact-limited solar cells. This effect arises when the extraction rate of majority carriers of the contact becomes limited at this contact, or when the leakage rate of these carriers at the opposite contact is not negligible [Roe 2019]. Although thinning down the MoO_{3-x} layer mitigates this effect, it is still present in the thinnest layer as evidenced by the lower current at high forward voltages compared to the reference SHJ. Thus *FF* might still be impacted by this phenomenon even with 4-nm-thick MoO_{3-x} layers. The impact on cell performance is however small, as the reference SHJ and the thinnest MoO_{3-x} cells (orange) have a similar characteristic in the fourth quadrant. In the end, the higher J_{SC} of the cells with a thin MoO_{3-x} leads to a higher efficiency compared to the reference SHJ cell. Overall, for a 4-nm-thick MoO_{3-x}-based SHJ with 6 nm of (*i*)a-Si:H, both MoO_{3-x} vertical bulk resistance and ITO lateral resistance account for $0.02\ \Omega\,cm^2$ (and even lower for (*i*)a-Si:H layer) and $0.3\ \Omega\,cm^2$ respectively of the global series resistance, leaving the remaining $0.3\ \Omega\,cm^2$ to $0.5\ \Omega\,cm^2$ for the different contact resistances.

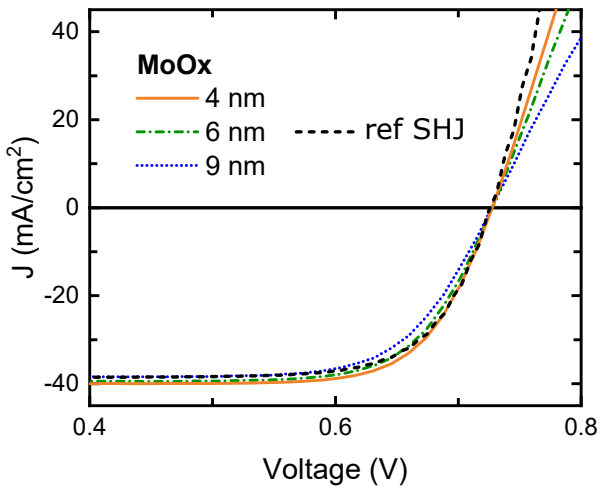

Figure 4.6: *J-V* of the three different cells featuring different MoO_{3-x} thicknesses, with 6 nm of (*i*)a-Si:H for all devices. The dashed black line represents the reference SHJ cell ((*p*)a-Si:H of 8 nm and (*i*)a-Si:H of 6 nm for the front hole contact.

4.4 MoO_{3-x} layer thickness reduction from 4 to 0 nm and integration of an innovative characterization method

In the previous section, we demonstrated that thinning down the MoO_{3-x} front hole selective layer from 9 nm to 4 nm significantly improved photocurrent while maintaining excellent hole-selectivity and front surface passivation, enabling high operating voltages. As a result, we demonstrated a 23.5% efficient 4-nm-MoO_{3-x}-based heterojunction solar cell, notably thanks to a 1.3 mA cm^{-2} photocurrent gain compared with the reference device using (*p*)a-Si:H as hole selective layer. However, the best efficiency of the series was obtained for the thinnest tested layer, intimating that the optimum may not be reached yet. Extrapolating the current-density trends observed between 9-nm- and 4-nm-thick MoO_{3-x} films to a 1-nm-thick MoO_{3-x} layer suggested a possible current density gain of another 0.75 mA cm^{-2}. We thus investigate here if thinning down the MoO_{3-x} layer below 4 nm indeed enables this current-density gain. More fundamentally, we also explore in detail how MoO_{3-x} thickness lower than 4 nm influences selectivity and passivation of devices using MoO_{3-x} as a hole-selective layer, as well as probing for a MoO_{3-x} critical thickness towards ITO.

4.4.1 Experimental details

Five silicon wafers each consisting of five silicon heterojunction solar cells were fabricated following the same process sequence as described in Chapter 2, varying MoO_{3-x} thickness between 0 nm (no MoO_{3-x} layer) to 4 nm and using a 6-nm-thick (*i*)a-Si:H as front passivation layer. No pre-annealing step was used. Fig. 4.7 summarizes the process flow of the present work.

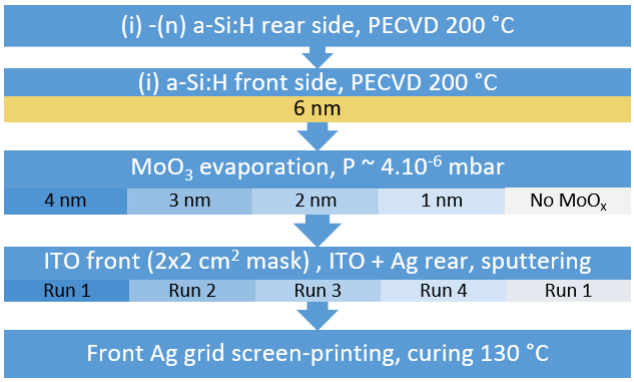

Figure 4.7: Process flow of the MoO_{3-x} -based solar cells fabrication of this study.

4.4.2 Thickness influence on optical performances

Fig. 4.8.a) shows the IQE of all MoO_{3-x}-based cells in addition to a standard SHJ cell reference processed the same week, and Table 4.4 summarizes the MoO_{3-x}-based cells J_{SC} gain compared

to this reference. The 4 nm-thick MoO_{3-x} sample has a gain identical to the one obtained in the previous experiment, confirming the robustness of this metric. J_{SC} is increasing for samples with a thinner MoO_{3-x} layer, from 4-nm to 1-nm-thick MoO_{3-x}. This increase partially originates from the reduced MoO_{3-x} sub-band-gap parasitic absorption – due to a thinner layer— which occurs on the range 600 nm – 900 nm [Geissbühler 2015, Sacchetto 2017, Werner 2016], as shown by the zoomed in plot on Fig. 4.8.a). It is completely evicted for devices with a MoO_{3-x} layer thickness strictly below 3 nm since their IQE values on this range are above the ones of the reference IQE cell. This demonstrates that there is still parasitic absorption even in an optimal MoO_{3-x} layer as thin as 4 nm, amounting to $0.5\,mA\,cm^{-2}$.

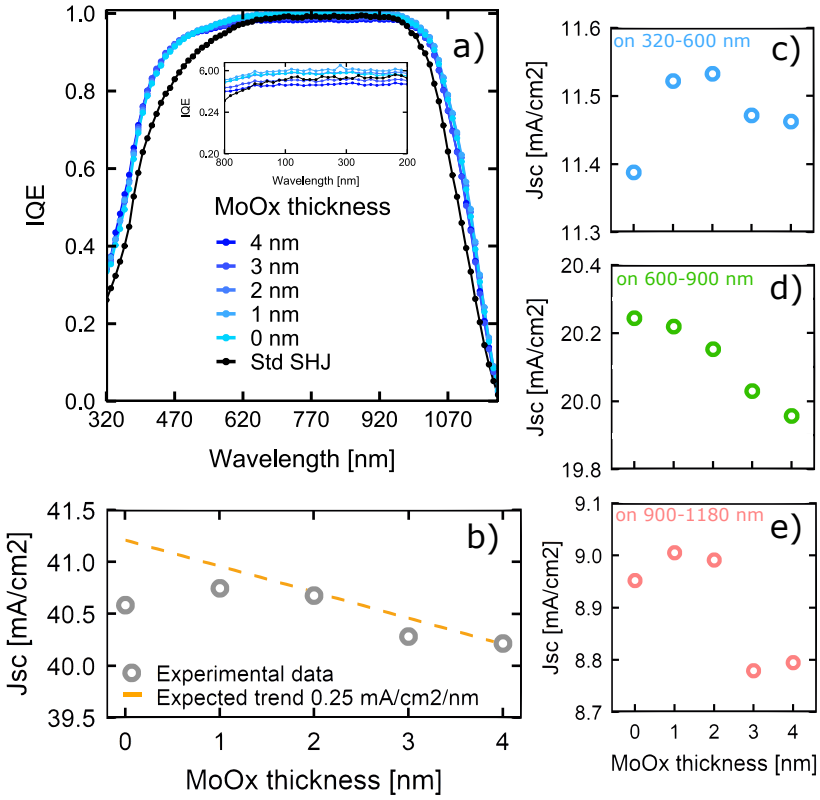

Figure 4.8: **a)** IQE plots of the six different samples; **b)** current density evolution with MoO_{3-x} thickness; **c) d) e)**: the different spectral contribution to short circuit current density against MoO_{3-x} thickness.

The trend reverses from 1 nm to 0 nm thick MoO_{3-x}. This is also highlighted in Fig 4.8.b, where experimental J_{SC} extracted from EQE for all samples are plotted together with the expected trend of $0.25\,mA\,cm^{-2}$ (discussed in previous section). To identify the origin of this deviation, the J_{SC} contribution from three spectrum regions (320-600 nm, 600-900 nm, and 900-1180 nm) are displayed in Fig. 4.8.c)-e). The J_{SC} departure from the expected trend mostly originates from the wavelength range 320-600 nm (see Fig. 4.8.c)) and affects both the 0-nm and 1-nm-thick MoO_{3-x} samples. On one hand, thinning down the ITO/MoO_{3-x}-stack thickness is expected to shift the minimum of reflection to shorter wavelengths, thus to increase the

EQE response in this range. On the other hand, a drop in front passivation would reduce at a point the J_{SC}, particularly on this short-wavelength range, since high front recombination will interfere with charge extraction. These two effects were qualitatively simulated using Solar cell modelling program in 1D (PC1D), a commonly used simulation software for solar cells, to evaluate their expected magnitude. Thinning down the anti-reflective coating (anti-reflective coating (ARC)) by 4 nm increases J_{SC} on the 320-600 nm range by $0.4\,\mathrm{mA\,cm^{-2}}$, which is opposite to the observed deviation. Conversely, increasing the front-surface recombination velocity from $10\,\mathrm{cm\,s^{-1}}$ (simulating a well-passivated surface for SHJ) to $10 \times 10^7\,\mathrm{cm\,s^{-1}}$ (corresponding to a very poor surface passivation) resulted in a J_{SC} loss of $0.4\,\mathrm{mA\,cm^{-2}}$ on this same wavelength range, which is consistent with the observed deviation. Although simplistic, these qualitative simulations correspond to the same order of magnitude of J_{SC} variation as the one we observed in our experiment, and suggest that the observed J_{SC} loss when using a too thin MoO_{3-x} film can be attributed to passivation damage, which will be discussed in the following. The small J_{SC} loss for the 0-nm-thick MoO_{3-x} sample on the range 900-1180 nm (Fig. 4.8.e)) can be attributed to the aforementioned effect of minimum of reflection shift towards shorter wavelengths.

Table 4.4: Summary of all the short circuit current densities gain of MoO_{3-x}-based cells with different MoO_{3-x} thickness, compared with a standard (*p*)a-Si:H-based one

MoO_{3-x} thickness	Total J_{SC} gain (mA/cm^2)
0 nm	1.72
1 nm	1.88
2 nm	1.81
3 nm	1.42
4 nm	1.35

4.4.3 Thickness influence on passivation and selectivity: investigation with standard and novel methods

The extracted *J-V* electrical parameters of the five devices (V_{OC}, J_{SC}, *FF*, efficiency (Eff.)) are plotted in Fig. 4.9. In addition, data from the previous experiment (same process flow but MoO_{3-x} thickness from 9 to 4 nm) are displayed with pink shades on the same graph, for the sake of comparison. Globally, the 4-nm-thick MoO_{3-x}-based device of this new study has poorer performances (lower J_{SC} and *FF*) compared to the previous processed one, which can be explained by two aspects. First, the lower *FF* and slightly lower V_{OC} originate from a poorer passivation from the very beginning in the process steps, due to mechanical damage during the cleaning process, as well as possible wafer-quality or (*i*)a-Si:H batch-to-batch variability. Secondly, *FF* was also slightly impacted by higher series resistance due to screen-printing issue during the front grid metallization. Nevertheless, the device employing a 4-nm-thick MoO_{3-x} layer exhibits globally good performances compared to the thinner-MoO_{3-x} devices.

From devices employing 9-nm-thick to 4-nm-thick MoO_{3-x} films, V_{OC} upholds above 700 mV whereas it drops from the 3-nm-thick to 0-nm-thick MoO_{3-x}-based samples, with an increasingly steep slope. The same behavior is observed for *FF*, with an even more drastic drop. We investigated the influence of passivation and selectivity on these losses, based on novel methods combining lifetime measurements, photo-luminescence (PL) imaging, suns-V_{OC} at high illumination, and *J*-*V* curve fittings.

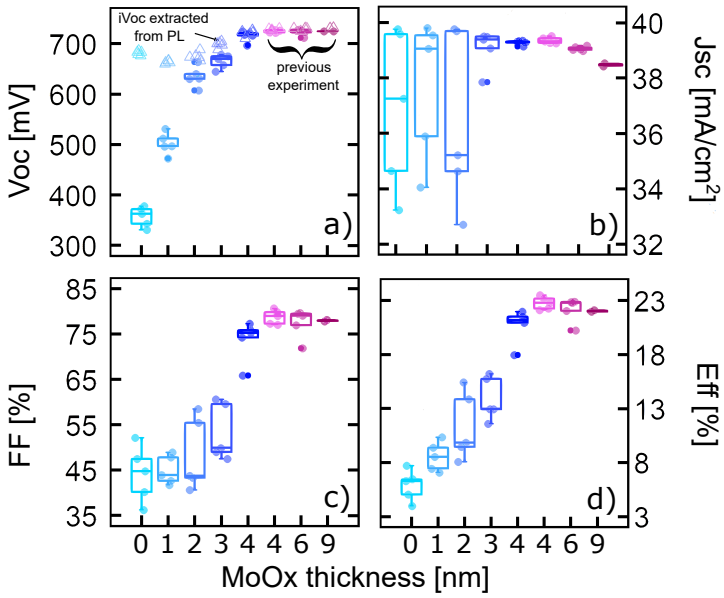

Figure 4.9: Electrical parameters (**a**): V_{OC}, **b**): J_{SC}, **c**): *FF*, **d**): efficiency) extracted from the *J*-*V* characteristics of the solar cells processed in this work and the previous one. The iV_{OC} values on graph **a)** are extracted from photo-luminescence imaging on final solar cells structures (see next sections).

4.4.4 iV_{OC} and V_{OC} comparison

Fig. 4.10 shows the lifetime of the different samples after each process step, measured at a carrier injection of 5×10^{15} cm^{-3} which is around the range of solar cells standard operating carrier densities. The measurement after ITO front deposition is done prior to the screen printing and 130 °C curing of the contacts. Here again, data from the previous experiment is added (pink shades). Highest-lifetime samples after PECVD remain the best after MoO_{3-x} deposition, however an overall lifetime decrease is seen for all the samples after MoO_{3-x} deposition. Such drop is common after deposition of hole-selective contacts (including (*p*)a-Si:H layers), and is attributed to the shift of the Fermi level in the (*i*)a-Si:H layer towards the valence band edge [De Wolf 2009, Beyer 1989]. After the ITO front sputtering, all samples experience a lifetime decrease, attributed to sputtering damage (the measurement was done prior to any curing), but devices from 9-nm-thick to 4-nm-thick MoO_{3-x} in both experiments hold a lifetime around 1 ms whereas the lifetime of the devices with thinner MoO_{3-x} layer

plunge down to 0.01 ms to 0.2 ms. Interestingly, the device with bare (*i*)a-Si:H maintains a lifetime superior to the devices having an additional 1-nm- or 2-nm-thick MoO_{3-x} layer. This could be due to the higher initial lifetime, or to a stronger impact of the sputter-damage when even a very thin MoO_{3-x} film is present, presumably due to the aforementioned shifting of the Fermi-level closer to the valence band.

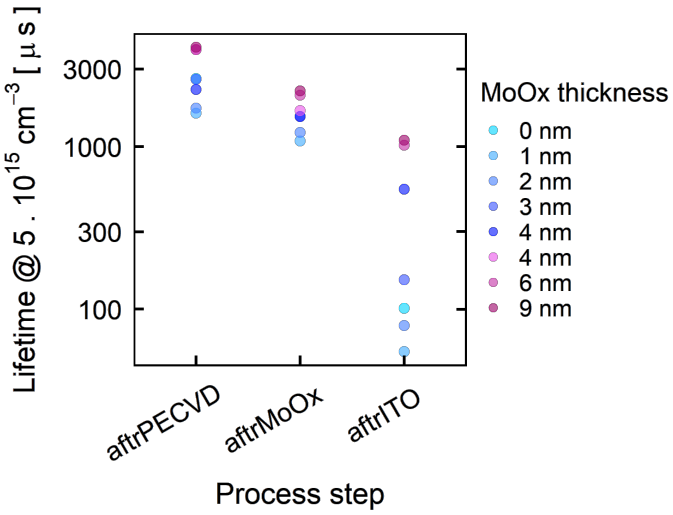

Figure 4.10: Evolution of cells lifetime, taken at a carrier injection of 5×10^{15} cm^{-3}, through the different process steps.

PL imaging of Fig. 4.11 gives a qualitative information about lifetime in the final device structure (the full area silver sputtering at the backside makes lifetime measurement by photoconductance decay impossible) after curing at 130 °C. It pictures the wafer with an injection equivalent to open circuit condition at one sun. The PL intensity (arbitrary unit) is directly proportional to the radiative recombination rate, itself proportional to the $n * p$ product (n being the electrons concentration, p the holes one). Here, PL images were normalized to a common scale. The five solar cells per wafer appear as squares, corresponding to the ITO-pad areas. Around these squares, ITO is not present, but those surfaces still received the MoO_{3-x}/(*i*)a-Si:H deposition. Scratches are visible on several images due to previously discussed mechanical damage during processing. The signal intensity for the 4-nm-thick MoO_{3-x}-based solar cells (with ITO) remains almost as high or half high as the signal intensity around these cells (no ITO sputtering), whereas the contrast between the solar cells (low response) and their surrounding (high response) for devices which received less than 4-nm-thick MoO_{3-x} is much stronger. The MoO_{3-x} being too thin, it may not protect the (*i*)a-Si:H layer enough from sputtering damage during ITO deposition, irreversibly damaging the cell surface passivation even after curing. It is worth mentioning that although the drop in PL imaging looks drastic on the active squared area of devices with MoO_{3-x} layers thinner than 4 nm, iV_{OC}

is actually logarithmically dependent on $p * n$ so that the iV_{OC} loss is not as large as one might think from the dark blue color of the squares. For a more quantitative analysis, we extracted the implied open circuit voltage iV_{OC} from our PL images, which can be deduced from the $n * p$ product [Glatthaar 2010, Shen 2013]. We calibrated the proportionality coefficient between the PL counts and $n * p$ by assuming that the lifetime in the areas not covered by ITO is similar to the lifetime prior to ITO deposition. We thus used the iV_{OC} measured by photo-conductance decay prior to ITO and Ag deposition as corresponding to the PL counts around the squared ITO-covered cells. The small differences in the front contact stack between samples are not expected to impact significantly the PL counts with respect to the passivation losses we observe. Fig. 4.9.a) shows the iV_{OC} of the final devices. It drops by around 70 mV between the 4-nm-MoO_{3-x} sample and the 1-nm-MoO_{3-x} sample, vouching for the expected passivation loss. Nevertheless, the actual V_{OC} drops much more than iV_{OC}, and the difference between the measured external V_{OC} of the devices and their iV_{OC} (noted ΔV_{OC}=iV_{OC}-V_{OC}, see Chapter 2 for more details about the method) increases when thinning down the MoO_{3-x} layer, witnessing at a selectivity loss as well, in line with work from Bivour *et al.* [Bivour 2014].

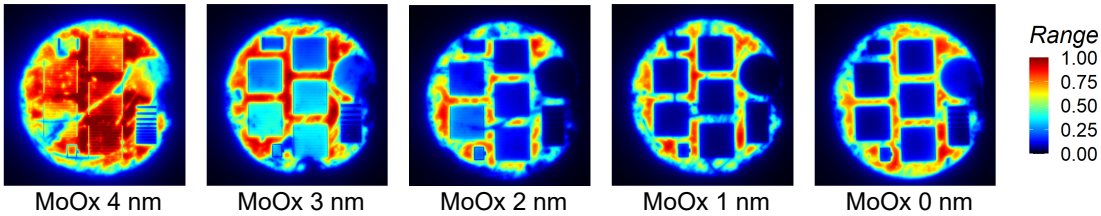

Figure 4.11: PL imaging of the different cells, in open circuit conditions (1 sun).

4.4.5 High illumination Suns-V_{OC} results

In light of the previous result which hints to a selectivity loss, we probed the latter of our front hole contact for all the different MoO_{3-x} layers thicknesses, through high illumination Suns-V_{OC} measurements and fitting.
For this, we plotted illumination versus V_{OC} [Sinton 1996b, Sinton 2000, Glunz 2007], of the best cell for each condition, from low (0.01 sun) to high (135 sun) illumination. In previous works, this kind of measurement at high illumination was demonstrated to highlight transport issues that can impact the cell selectivity, passivation and transport at one sun, [Glunz 2007, Bivour 2014]. Notably, a deviation from the logarithmic V_{OC} increase with illumination was shown to be a signature of poorly selective hole contacts originating from the formation of a counter Schottky barrier due to work function misalignment.

As depicted in Fig. 4.12, instead of stronger reversal in the curve appearing at lower illumination as the MoO_{3-x} layer is thinned down from 4 to 0 nm, like it was observed in [Glunz 2007] and [Bivour 2014] for cells with weaker contact quality, we noticed no difference in our cells response at high illumination. It hints that there is no reverse Schottky diode impeding carrier extraction, even for the thinnest MoO_{3-x} layers. The green dashed and red dotted linear slopes are added to the plot as guide for the eyes, and correspond to the response of an ideal p-n

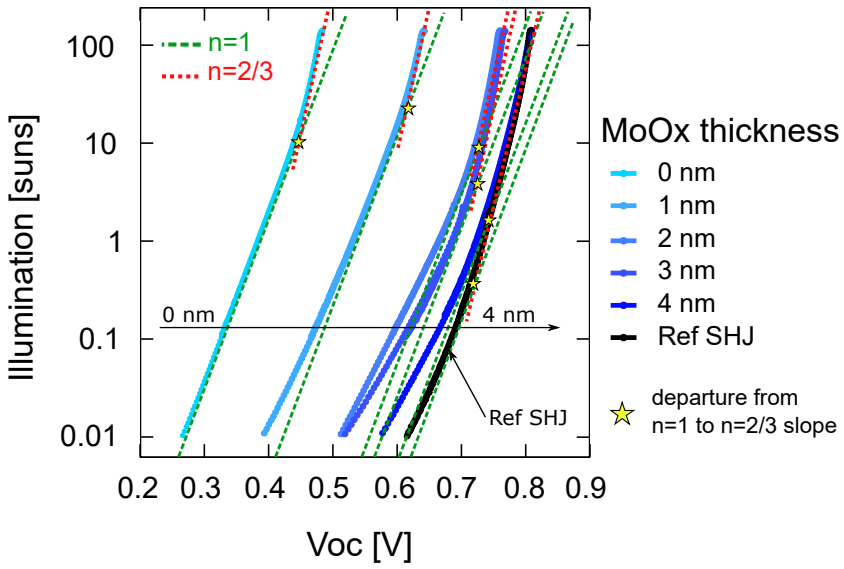

Figure 4.12: Suns-V_{OC} measurements of the different cells, on a wide illumination range (0.01 sun to 135 sun

junction case with an ideality factor of $n = 1$ and $n = 2/3$ respectively, following the Shockley diode equation:

$$J(V) = J_0(\exp \frac{qV}{nk_BT} - 1) \tag{4.1}$$

Globally, from 0.5 to 100 sun, all the cells follow these two regimes, switching from $n = 1$ to $n = 2/3$ at different illuminations according to the different MoO_{3-x} thicknesses. The cell with 4 nm of MoO_{3-x} works in high injection at an illumination a bit higher than 1 sun already (it changes regime from $n = 1$ to $n = 2/3$ at that illumination), which is typical of silicon heterojunction solar cells with good working contacts, whereas the cell with only 1 nm of MoO_{3-x} only reaches Auger regime around a 20-sun illumination. This correlates well with the lifetime variations reported in Fig. 4.10 and 4.11, with higher-lifetime samples reaching Auger regime at lower illumination.

At lower illuminations (below 0.1 sun), so lower carrier injection, MoO_{3-x}-based cells show an ideality factor between 1 and 2, in general attributed to Shockley Read Hall recombination involving traps in the transport and recombination process [Sze 1995, Kirchartz 2013, McIntosh 2000]. Interestingly and contrary to the other samples, the cell without MoO_{3-x} (0 nm MoO_{3-x}) keeps an ideality factor of n=1 with a straight slope sticking to the ideal diode behavior. The same behavior is measured on a reference standard SHJ in a lower extent (see Fig. 4.12). This effect is unlikely linked to shunt resistance —which was not considered in the calculation—, since the calculation from dark J-V curves showed they were all above $1 \times 10^5\,\Omega\,cm^2$. The higher ideality factor for samples involving MoO_{3-x} could either come from inhomogeneity of the MoO_{3-x} layer or even local pin-holes in this layer [Cattin 2019] (which

would obviously not be present when no MoO_{3-x} layer is present), or from a drop of passivation in low injection due to defects in a-Si:H following the shift of Fermi level closer to the valence band previously evoked [De Wolf 2009, Beyer 1989]. These Suns-V_{OC} measurements show that sub-optimal MoO_{3-x} thickness has a fundamentally different influence on selectivity compared to too-lightly doped —or too thin— (*p*)a-Si:H [Bivour 2014].

4.4.6 Modelling through Roe *et al.* method, and application for MoO_{3-x}-based SHJ in situ hole contact work function determination

Saturation currents fitting through Roe *et al.* modeling

To further understand the origin of the selectivity loss —and somehow the V_{OC} and *FF* drop— of our thin-MoO_{3-x} contacts, we fitted the *J-V* curves with the model of Roe *et al.* [Roe 2019], presented in Chapter 2 section 2.3.5, which is adapted for contact-limited devices. For an easier understanding, the four exchange currents are noted accordingly with the MoO_{3-x} and (*n*)a-Si:H hole and electron contact respectively, as described in Fig. 4.13.a). The details about the model and the equation used are given in Chapter 2 section 2.3.5.

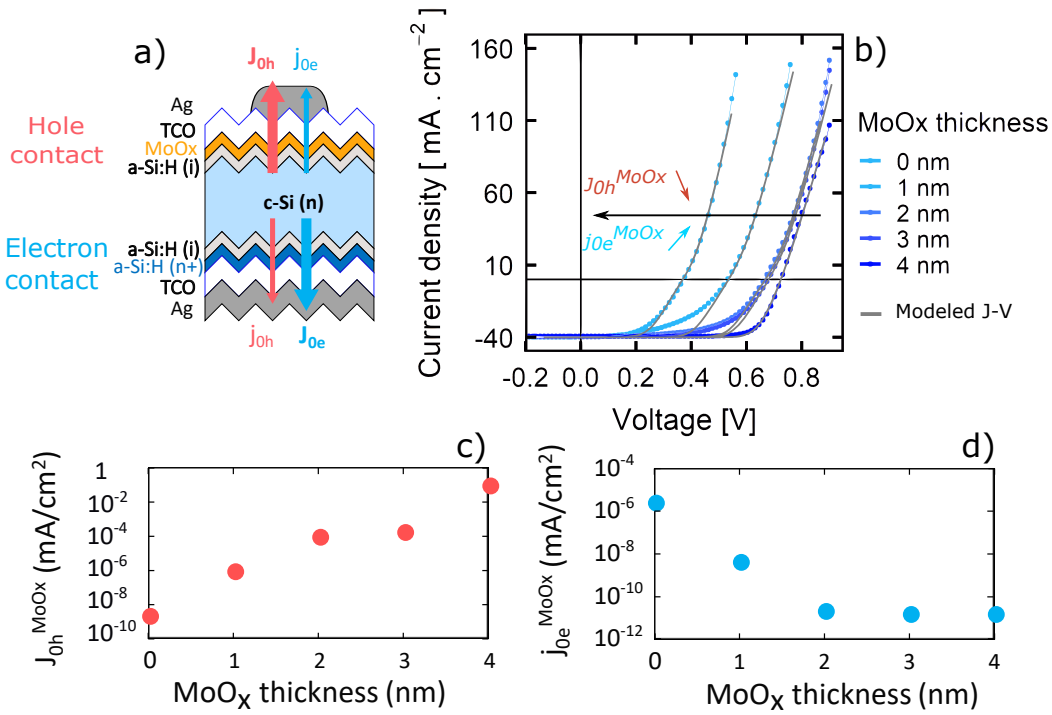

Figure 4.13: **a)** schematic representation of the four different current density involved in Roe *et al.* model; **b)** *J-V* experimental (shades of blue) curves and their fitted data (grey); **c)** and **d)** evolution of j_{0e}^{MoOx} and J_{0h}^{MoOx} with MoO_{3-x} layer thickness.

Here, the current-voltage curve can be derived following equation 4.2, which is the original equation developed by Roe *et al.* (see Eq. 2.9 in Chapter 2) to which we added the R_s contri-

bution, an ohmic series resistance, to account for non-contact related resistive losses (in the $MoO_{3\text{-}x}$, ITO, and Ag electrodes). In light of the previous results on shunt resistance, the latter was not considered in the equation. J_{0h}^{MoOx} and j_{0e}^{MoOx} stand for the hole and electron equilibrium exchange current densities at the hole $MoO_{3\text{-}x}$-based contact, and $j_{0h}^{(n)aSiH}$ and $J_{0e}^{(n)aSiH}$ stand for the hole and electron equilibrium exchange current densities at the (n)a-Si:H-based contact.

$$J(V) = -\left(J_L + j_{0_e}^{MoOx} + j_{0_h}^{(n)aSiH}\right) + \frac{J_L + j_{0_e}^{MoOx} + J_{0_e}^{(n)aSiH}}{1 + \frac{J_{0_e}^{(n)aSiH}}{j_{0_e}^{MoOx}} \exp\left(\frac{-V - R_s J}{V_T}\right)} + \frac{J_L + j_{0_h}^{(n)aSiH} + J_{0_h}^{MoOx}}{1 + \frac{J_{0_h}^{MoOx}}{j_{0_h}^{(n)aSiH}} \exp\left(\frac{-V - R_s J}{V_T}\right)} \tag{4.2}$$

To reproduce the J-V curves of samples with various $MoO_{3\text{-}x}$-layer thicknesses, we varied J_{0h}^{MoOx}, j_{0e}^{MoOx}, $J_{0e}^{(n)aSiH}$, $j_{0h}^{(n)aSiH}$, and R_s. The experimental J-V curves and the fitted ones are plotted on Fig. 4.13.b). The disagreement between experimental and simulated data around the rectifying region of the J-V curves for cells from 3-nm to 1-nm-thick $MoO_{3\text{-}x}$ can tentatively be attributed to strong passivation damages that occurred during the cleaning step or/and to the aforementioned screen-printing issue, or eventually micro-shunts which could impact the FF [**?**, Cattin 2020] and could originate from island nucleation growth regime from 1 to 3 nm [Gerling 2015c]. A more accurate fitting —even for $MoO_{3\text{-}x}$ layer thickness below 4 nm—, performed with the same method on another batch of solar cells is presented in Chapter 5 and discard the second hypothesis concerning micro-shunts.
The shunt resistance was kept constant at $10\,\mathrm{k\Omega\,cm^2}$, and the series resistance decreased from 1.3 to $0.85\,\Omega\,\mathrm{cm^2}$. For all $MoO_{3\text{-}x}$ thicknesses, $J_{0e}^{(n)aSiH}$ and $j_{0h}^{(n)aSiH}$barely varied around $103\,\mathrm{mA\,cm^{-2}}$ and $1.3\times10^{-14}\,\mathrm{mA\,cm^{-2}}$ respectively, while J_{0h}^{MoOx} decreased in a quasi-exponential way (see Fig. 4.13.c)), from $1\,\mathrm{mA\,cm^{-2}}$ to $4\times10^{-9}\,\mathrm{mA\,cm^{-2}}$, with $MoO_{3\text{-}x}$ thickness decrease. On the contrary, j_{0e}^{MoOx} interestingly started increasing for $MoO_{3\text{-}x}$ of 2 nm and less, from $1.8\times10^{-11}\,\mathrm{mA\,cm^{-2}}$ to $3\times10^{-6}\,\mathrm{mA\,cm^{-2}}$. We can deduce from this evolution that the selectivity loss is caused by a worsening of both the electron-blocking (j_{0e}^{MoOx} increase) and hole-collecting (J_{0h}^{MoOx} decrease) ability of the contact.

In situ hole contact work function estimation

One explanation to the selectivity loss with $MoO_{3\text{-}x}$ layer thickness could be a decrease of its work function. Such phenomenon was often reported in literature [Essig 2018, Messmer 2018], and Greiner *et al.* notably reported that $MoO_{3\text{-}x}$ work function is diminished near interfaces due to chemical (redox) and physical (charge exchange) reactions with the substrate material it grows on [Greiner 2013a], which provokes $MoO_{3\text{-}x}$ work function dependency with thickness. Accordingly, under a critical thickness, $MoO_{3\text{-}x}$ work function is affected over the whole layer.

As a TMO, MoO_{3-x} is also known to have a fluctuating work function sensitive to external factors (see Chapter 3). In our case, an oxygen/hydrogen exchange could occur at the (*i*)a-Si:H/MoO_{3-x} interface [Essig 2018, Sacchetto 2017] as well as charge exchange due to work function mismatch, and provoke MoO_{3-x} reduction decreasing its work function. Same can occur at the ITO/MoO_{3-x} interface, (oxygen exchange (thermodynamically possible) or charge transfer) [Greiner 2013a].
To support this point, we propose a qualitative scheme of band diagrams, drawn in Fig. 4.14. It shows the band bending at the hole contact induced by the MoO_{3-x} layer, in case of high (Fig. 4.14.a)) or lower (Fig. 4.14.b)) work function for the latter. We added a simplified carrier transport, schematized by the blue and red arrows. Electrons coming from the circuit and ITO (red arrow) transfer from the MoO_{3-x} conduction band to (*i*)a-Si:H valence band to recombine with holes —generated from the wafer— at the MoO_{3-x}/(*i*)a-Si:H interface. Electrons can be transported through band to band tunnelling or/and trap (or thermally) assisted tunnelling (TAT) [Scirè 2020, Procel 2020] (see Chapter 7), whereas parasitic electrons (blue arrow) face a high energetic barrier due to band bending. In case of a lower work function, the misalignment between the MoO_{3-x} conduction band and the (*i*)a-Si:H valence band would force transport through TAT on a longer distance (to reach (*i*)a-Si:H valence band) which would reduce the extraction efficiency. Simultaneously, the energetic barriers preventing electrons to pass is also lowered, enhancing parasitic electron thermionic emission and unintended recombination. To verify the hypothesis of a TAT dominant —in case of lower MoO_{3-x} work function— versus band to band dominant transport —for high MoO_{3-x} work function—, temperature-dependent mobility should be performed (see Chapter 7). A mobility characteristic of TAT transport would be highly dependent on temperature while a band to band transport would involve a mobility barely depending on temperature. Yet, measuring the vertical mobility of a full contact stack remains highly challenging, and a new characterization tool should be designed to achieve it. Measuring contact resistivity with temperature could also be worth it —and simpler— for such kind of analysis.

In a simple approach, assuming parasitic electrons at hole contact travel through thermionic emission, we can calculate the barrier height ϕ_b, the energy difference between the Fermi level at the interface with (*n*)c-Si and the (*i*)a-Si:H conduction band maximum represented in Fig. 4.14, thanks to the electron current density j_{0e}^{MoOx} we found with the Roe *et al.* model and using the thermionic emission equation 4.3 [Sze 1995]:

$$j_{0_e} = A^* T^2 \exp \frac{-\phi_b}{qV_T} \tag{4.3}$$

with A^* the effective Richardson constant and T the temperature. With an analysis in temperature from 0 °C to 70 °C summarized in Fig. 4.15 , we confirmed that the electron current passing through the hole contact indeed follows this law. Following thermionic emission mechanism, decreasing the barrier height provokes thermionic current increase. Here, according to Fig. 4.13.d), parasitic thermionic electron current is increasing with decreasing MoO_{3-x} thickness, so the barrier height blocking electrons might indeed reduce —and so is the MoO_{3-x} work

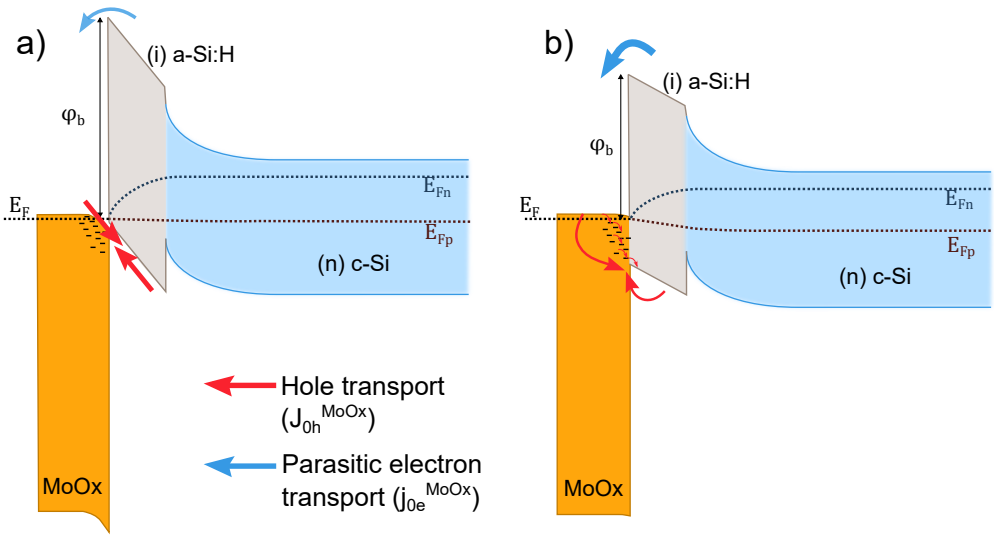

Figure 4.14: Qualitative band diagram scheme of the hole contact for a MoO_{3-x}-based SHJ under illumination and at open circuit, with **a)** a high work function and **b)** a low work function. E_{Fn} and E_{Fp} are the quasi Fermi levels for electrons and holes respectively.

function— as MoO_{3-x} thickness reduces. We did not model J_{0h}^{MoOx} due to complexity involved in trap or multi-trap assisted tunneling mechanisms, and to the lack of information linking J and the energy barrier ϕ_b in such transport. Yet, fitting of the parasitic electron current can be used to estimate the hole contact work function through calculation of ϕ_b. Fig. 4.13.d) indicates that above 2 nm of MoO_{3-x} j_{0e}^{MoOx} is plateauing even though J_{0h}^{MoOx} is still variating. This mean that our work function estimation with j_{0e}^{MoOx} will also saturate for MoO_{3-x} layers above 2 nm, which might be physically incorrect as J_{0h}^{MoOx} still increases from 2 nm to 4 nm. Due to the significant mismatch between the data and the model, ascribed to damaged wafers, the quantitative MoO_{3-x} work function was not estimated here, but is done in Chapter 5 for 0-, 2- and 4-nm-thick MoO_{3-x}-based devices for which data is well fitted.

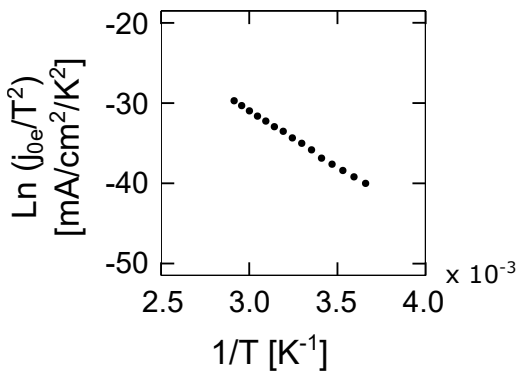

Figure 4.15: Plot of $\ln(j_{0e}^{MoOx}/T^2)$ as a function of $1/T$, over 0 °C to 70 °C. Linearity of the plot proves the thermionic emission nature of electron transport. The different j_{0e}^{MoOx} were extracted from a MoO_{3-x}-based cell experimental J-V fitted with Roe *et al.* $J(V)$ equation.

4.5 $MoO_{3\text{-}x}$ micro structure investigation

The microstructural properties of the $MoO_{3\text{-}x}$ contact stack were investigated by STEM HAADF imaging and Energy-dispersive X-ray spectroscopy (EDX), as shown in Fig. 4.16.a)-c). The EDX line profile shown in Fig. 4.16.c) highlights the presence of a thin amorphous a-SiO_x layer at the (*i*)a-Si:H/$MoO_{3\text{-}x}$ interface, as reported in many works (see Chapter 3). This layer appears too thick (>2 nm) to be solely resulting from the growth of a native a-SiO_x layer in between the HF dip and the deposition of the $MoO_{3\text{-}x}$ layer (total air exposure of 20 min). To assess the oxidation state of Mo, the Mo M3-M2 EEL spectrum of the thin $MoO_{3\text{-}x}$ contact layer was compared to that of an as-deposited $MoO_{3\text{-}x}$ layer (20 nm-thick), which was not subject to any annealing or plasma exposure, and to MoO_2 and MoO_3 reference spectra taken from [Lajaunie 2015] (Fig. 4.16.d)-f)). While the signal-to-noise ratio of the data prevents a detailed analysis of the oxidation state of the layer, these Mo EELS spectra indicate that the thin contact layer and the as-deposited one have a composition closer to MoO_3 than MoO_2. Indeed, their M3/M2 ratio approaches that of the MoO_3 reference (see arrows in Fig. 4.16.f)). While this observation does not entail that the thin oxide is stoichiometric (it is sub-stoichiometric based on optical data, see above and Chapter 3), its overall oxidation state remains close to +6 after being sandwiched between (*i*)a-Si:H and ITO and subjected to an annealing at 130 °C, even though both conditions could have significantly altered its oxidation state. Either the Mo oxidation sate remained mostly unchanged during processing or the higher oxygen affinity of Si compared to Mo led to a slight reduction of the Mo cations after deposition (leading in part to the observed interfacial a-SiO_x layer), but this initial reduction was cancelled to some extent by a subsequent oxidation by the plasma involved in the ITO deposition.

4.6 Optimized $MoO_{3\text{-}x}$ contact design for record performance

The highest efficiency of these series was obtained for a 4 nm-thick $MoO_{3\text{-}x}$ layer and a 6-nm-thick (*i*)a-Si:H film. Given that results with the thinnest (*i*)a-Si:H are quite spread, we processed another 4 nm $MoO_{3\text{-}x}$ -based cells —with no pre-annealing treatment— with thicker (*i*)a-Si:H layer of 8 nm, and a obtained a certified efficiency of 23.5% (Fig. 4.17), with a remarkable *FF* close to 82%. This record efficiency was obtained with low optimization, no masking step or photo-lithography, and used a low-temperature Ag screen-printed metallization, inducing 3% of shadowing [Kamino 2019, Haschke 2019a]. The 39.15 $mA\,cm^{-2}$ current density reached for this record device is significantly below the 44.1 $mA\,cm^{-2}$ Lambertian limit for a 180 μm-thick silicon wafer [Sai 2018]. Using the analytical model presented in [Boccard 2012], we estimate that the measured J_{SC} could be improved by 0.8 $mA\,cm^{-2}$ by suppressing all absorption in the $MoO_{3\text{-}x}$ layer and by another 0.8 $mA\,cm^{-2}$ by suppressing all absorption in the front (*i*)a-Si:H. Another 0.8 $mA\,cm^{-2}$ and 1.2 $mA\,cm^{-2}$ could be gained by suppressing primary reflection and grid shading, respectively. In addition, about 1.2 $mA\,cm^{-2}$ could be recovered from parasitic absorption in the other layers (front ITO and rear ITO and Ag), and 0.2 $mA\,cm^{-2}$ by improving light trapping. Finally, the cells presented here were found to be stable after 11 months of storage in air (un-encapsulated) (see Chapter 6).

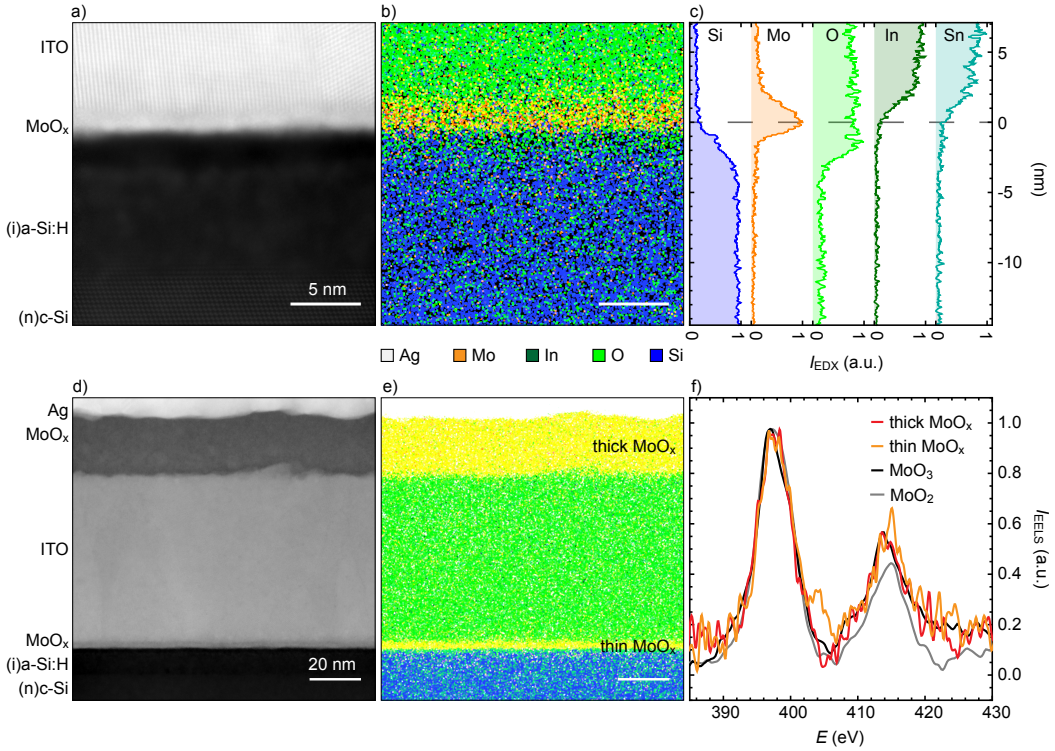

Figure 4.16: **a)** STEM HAADF image of the (*i*)a-Si:H/MoO_{3-x}/ITO contact deposited on a <111>-oriented (*n*)c-Si wafer, **b)** corresponding EDX map and **c)** background-subtracted EDX line profiles of the Si K, O K, In L, Sn L edges. Arrowheads in **c)** highlight the presence of a-SiO_x at the MoO_{3-x}/(*i*)a-Si:H interface. **d)** STEM HAADF image of the contact coated with an as-deposited MoO_{3-x} layer/Ag stack, **e)** corresponding EDX map and **f)** EELS Mo M3-M2 edges of the thin and thick MoO_{3-x} layers compared to reference spectra for MoO_2 and MoO_3. Arrows highlight the difference in M3/M2 ratio between MoO_2 and MoO_3. The images and full analysis were performed by Quentin Jeangros.

4.7 Conclusion

In this chapter, we studied the influence of the thicknesses of the MoO_{3-x} and (*i*)a-Si:H films used as hole contacts in SHJs. The thinnest layers studied here (4 nm and 6 nm for MoO_{3-x} and (*i*)a-Si:H respectively) resulted in best device performances, highlighting that such thin contact stacks enable simultaneously high selectivity, passivation, and good charge carrier transport. Thicker layers were found to lead to higher series resistance or charge carrier selectivity losses, without any strong correlation between the two. The device employing the thinnest MoO_{3-x} showed a higher optical response (higher EQE) than the reference (*p*)a-Si:H -based SHJ over the whole wavelength range (320 nm to 1180 nm). The recorded gain in photocurrent of 1.3 mA cm^{-2} resulted from the mitigation of parasitic absorption losses. We then showed that an appreciable short circuit current gain is still possible when decreasing MoO_{3-x} thickness from 4 nm to 1 nm, but at the cost of a severe degradation of *FF* and V_{OC}. The latter is due to both surface passivation and mainly selectivity loss, possibly caused by

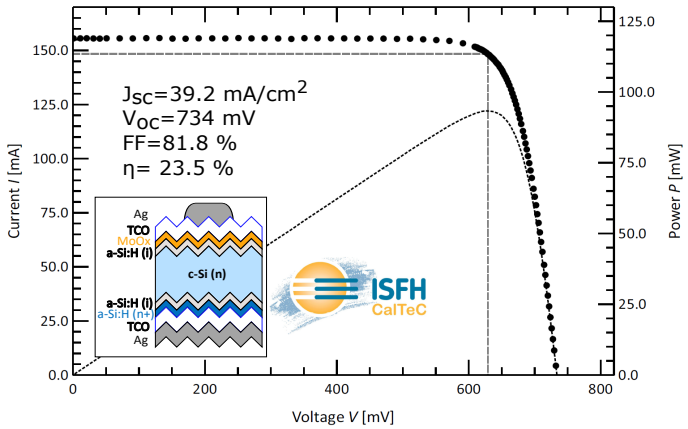

Figure 4.17: Certified *J*-*V* and power plots of the best MoO_{3-x}-based cell processed in the lab (certified by ISFH)

a too thin protection against ITO sputtering and a probable reduction of the MoO_{3-x} work function respectively. Below 1 nm of MoO_{3-x}, we also discovered that the J_{SC} value was limited by the strong surface passivation damage. Yet, those results are obtained for initially damaged substrate and should be repeated to corroborate the conclusions. We experimentally demonstrated that MoO_{3-x} optimal thickness appears to be 4 nm, a figure in agreement with Mazzarella *et al.* work [Mazzarella 2020]. These conclusions were possible to draw thanks to adapted implementation of different methods for SHJ solar cells. For the first time, an innovative characterization for in situ whole contact work function determination, in contrast to classical single layer work function measurement, is used experimentally. It enabled to understand how currents are affected by MoO_{3-x} work function reduction by estimating the majority hole and minority electron exchange current densities at the hole contact. We found that the parasitic electron current is increased due to lower thermionic barrier at this contact. However, the mismatch between the model and the experimental data is not well explained. New fitted data of next chapter unveils that the present mismatch is most probably due to wafer damage during the cleaning step.

High-resolution transmission electron microscopy imaging and electron energy-loss spectroscopy revealed that the 4 nm-thick evaporated MoO_{3-x} layer is continuous and that Mo, while slightly sub-stoichiometric, has an overall oxidation state approaching its initial +6 state, even after its evaporation on (*i*)a-Si:H, the sputtering of the overlaying ITO layer and the annealing of the contact stack.

Overall, the high J_{SC} allowed by this contact stack enabled the demonstration of a 23.5%-efficient device, highlighting that MoO_{3-x} is an excellent hole contact for c-Si heterojunctions. By reaching a similar efficiency to that of best SHJs cells produced in our laboratory (at that time) [Haschke 2019c], this study demonstrates carrier-selective contacts relying on non-Si materials are relevant for high-efficiency silicon photovoltaics. As a possible, the power used in ITO deposition on top of thin MoO_{3-x} layers could be lowered to explore its influence on passivation and MoO_{3-x} ability to both protect the (*i*)a-Si:H underlayer from sputtering dam-

age and ITO work function by varying carrier doping in the latter layer. Such study could help improving devices performances with thinner-than-4-nm MoO_{3-x} layer —in the goal of further reducing parasitic absorption— an is presented in Chapter 5.

5 Transparent conductive oxide and double anti-reflective coating influence on MoOx-based SHJ

Abstract

In this chapter, we examine the influence of the front ITO carrier concentration on the selectivity and transport properties of the MoO_{3-x}-based contact. The MoO_{3-x} layer is also varied (0, 2 and 4 nm) to verify the previous conclusions (on undamaged wafers). An additional ITO deposited at lower power is tested to inspect the possible link with the contact passivation for the different MoO_{3-x} thicknesses. Contrary to the previous chapter, we find that 2 nm of MoO_{3-x} are suitable to provide respectable performances. The use of a low-power-deposited ITO does not influence passivation properties, however the TCO exhibits a quasi-amorphous crystallographic structure which results in an *FF* increase by more than 1 $\%_{absolute}$ for MoO_{3-x}-based devices and allows to stabilize the efficiencies of those devices at 23%. Remarkable efficiencies of 23.7% for devices employing MoO_{3-x} layers of 4 nm and the above-mentioned novel ITO could be reached after applying a current in forward bias (a procedure described in the next chapter). The influence of ITO carrier concentration on the contact with no selective layer (0 nm of MoO_{3-x}) is carefully studied. Finally, an SiO_x:H DARC is post-deposited on the front side of the MoO_{3-x}-based SHJ. The treatment improved the J_{SC} but significantly degraded the cells *FF* and V_{OC}, probably linked to the presence of H in the plasma, which tends to degrade MoO_{3-x} work function. The use of MgF_2 as DARC showed preliminary good results. With the same forward bias treatment on a MgF_2-DARC-coated device involving a 2-nm-thick-MoO_{3-x}-based contact, we achieved the impressive efficiency of 23.5 %, bridging the gap with the world-record 4-nm-MoO_{3-x}-based SHJ.

5.1 Introduction and motivation

In crystalline SHJ technology, TCO plays a key role. At the front contact, it is used as a transparent electrode, an anti-reflective coating and to transport extracted carriers laterally to the Ag fingers. At the rear side, a thicker and less doped TCO is used as a buffer layer to minimize both plasmonic absorption [Zhong 2020] and recombination at the interface with

the metallic electrode, to which direct contact between silicon and metal is highly sensitive (see Chapter 1). There, a thicker layer is generally used to further reduce the metal plasmonic absorption, and less doped to limit the infrared (IR) parasitic absorption in the layer (see below) when used in conjunction with a full metallic rear side.

In the framework of MoO_{3-x}-based solar cells and from our precedent work (see Chapter 4), some points remained unresolved. First, the observed decrease in iV_{OC} for cells with MoO_{3-x} below 4 nm was mostly ascribed to sputtering damage during the front ITO deposition —the rear ITO deposition is not of a concern since the electron contact is at least four times thicker than its MoO_{3-x}-based hole counterpart. The role of deposition power in this phenomenon could be evaluated by depositing ITO at different powers. Additionally, following the conclusions of Chapter 4, a better combination of low power deposited ITO with an MoO_{3-x} layer thinner than 4 nm could enhance transparency of the front stack, reducing MoO_{3-x} sub-gap parasitic absorption still existing in 4-nm-thick-MoO_{3-x}-based devices, without being limited by iV_{OC} degradation. Secondly, we showed that no counter Schottky diode exist for any MoO_{3-x} thickness over 0-8 nm and using our standard ITO, at the ITO/MoO_{3-x} interface as it is usually the case for ITO/(*p*)a-Si:H. However, a critical MoO_{3-x} thickness toward ITO work function influence, meaning a minimal thickness under which MoO_{3-x} is not able to efficiently screen ITO work function, provoking reduction in final device V_{OC}, have not been estimated. ITOs with different doping (to vary their work function), deposited on different MoO_{3-x} layer thicknesses would permit to estimate this critical thickness. It would also provide the opportunity to investigate resistive effects of the different ITOs deposited on MoO_{3-x} as we observed that the TCO had a lower sheet resistance when deposited on MoO_{3-x} (see Chapter 4). Finally, reprocessed devices integrating MoO_{3-x} layers from 0 to 4 nm not damaged during cleaning would enable to explain the origin of the *J*-*V* curve fitting mismatch of the previous study. It may then be possible to disentangle between layer discontinuity (intrinsic issue) and damaging during processes or printing process problems (extrinsic issues). To address the aforementioned questions, we processed one front ITO with a lower power deposition than our standard one, and three front ITOs at same power, however, with different carrier concentration.

Even though they are advantageous for the solar cell performances, TCOs still cause losses in the solar cells. To overcome their drawbacks, DARC —deposited on top of the TCO— are now commonly employed in SHJ photovoltaic devices since they help circumvent TCOs weaknesses, as described in section 5.4. To our knowledge, no DARC treatment have been used for MoO_{3-x}-based SHJ yet. The standard DARC for SHJ is a-SiO_x:H, known to boost the ITO resistivity through the presence of H in the material, in addition of the optical benefits, is generally deposited by PECVD at temperatures above 150 °C. Both H and temperatures higher than 150 °C are known to deteriorate the MoO_{3-x} layer. The influence of such treatment is evaluated in the second part of this chapter, in which we present preliminary results of a-SiO_x:H deposited at the front of MoO_{3-x}-based hole contact solar cells.

5.2 Experimental details

In the first section, three different series (one per MoO_{3-x} layer thickness) of 4 wafers (one per ITO), each integrating five identical solar cells, were prepared. Devices implementing MoO_{3-x} layer thickness of 0 (no MoO_{3-x}, first batch), 2 (second batch) and 4 (third batch) nm were processed. The fabrication process of the solar cells is described in Chapter 2. In each series, four different ITOs were used whose deposition parameters are described in Chapter 2 section 2.2.5. Quarter wafer dedicated samples for lifetime measurements were co-processed with the solar cell devices.

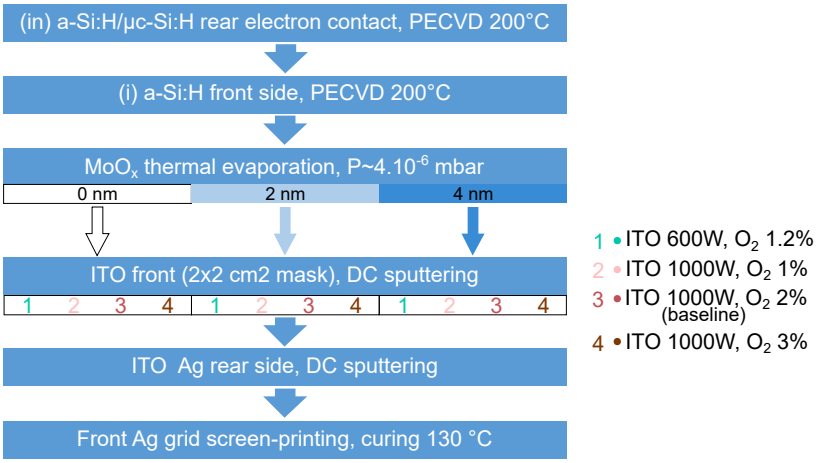

Figure 5.1: Process flow for the MoO_{3-x}-based cells fabrication in the current study.

To go further in the investigation of TCOs influence on the MoO_{3-x}-based contact behavior, we deposited ITOs sputter-deposited in different tools —so different properties—, ZnO:Al(AZO) and IZrO on MoO_{3-x}-based and (*p*)a-Si:H-based solar cells in the last paragraph of the section. Their fabrication process can be found in Chapter 2 section 2.2.5.

The second section of this chapter discuss the integration of a DARC to MoO_{3-x}-based solar cells. SiO_x:H, SiO_x and MgF_2 deposition process is described in Chapter 2 section 2.2.7.

5.3 Use of different TCOs for MoO_{3-x}-based SHJ

5.3.1 TCOs general properties

For TCOs, achieving sufficient transparency and conductivity to satisfy c-Si SHJ standards requires compromises. For a proper application to this field, the TCO resistivity should not exceed $1 \times 10^{-3}\,\Omega\,\mathrm{cm}$ —as a comparison, bulk pure silver resistivity is $1.6 \times 10^{-6}\,\Omega\,\mathrm{cm}$. To reach a high conductivity σ, one can increase the carrier concentration N and/or mobility μ, following the equation: $\sigma = Ne\mu$, with e the carrier charge (here the elementary charge). In a TCO, N can be tuned by varying oxygen vacancies [Bellingham 1991a], substitutional or interstitial impurities concentration. A high carrier concentration would shift the Fermi

level into the conduction band (degenerated semiconductor), increasing the optical band-gap $E_{VBM} - E_F$ with E_{VBM} the energy of the valence band maximum and E_F the Fermi level, according to the Burstein-Moss (BM) effect (see Fig. 5.2) [Burstein 1954, Moss 1954]. Equation 5.1 describes the mechanism, with ΔE_g the band-gap shift in eV, h the Planck constant (J.s), m^* the excited carrier effective mass (kg) which is around 0.3 times the electron mass m_0 for ITO [Bellingham 1991b, Rucavado 2019] and N the carrier concentration (cm^{-3}) [Fay 2003].

$$\Delta E_g = \frac{h^2}{8em^*}\left(\frac{3N.10^6}{\pi}\right)^{2/3} \tag{5.1}$$

The band-gap shift is proportional to $N^{2/3}$ and amounts to 0.16 eV and 0.77 eV for carrier concentration of 5×10^{19} cm^{-3} and 5×10^{20} cm^{-3} respectively. Yet, the semiconductor/metal transition, occurring for degenerated semiconductors, provokes a band-gap narrowing. For carrier concentration around 1×10^{20} cm^{-3}, a typical value for PV applications, TCOs are generally degenerated and the benefits from the BM effect are concealed by the band-gap narrowing (experimentally, the gap shift is limited to ~ 0.1 eV) [Roth 1981, Roth 1982, Fay 2003]. The BM effect thus has a negligible influence on solar cell absorption performances. A high carrier concentration will also provoke Free carrier absorption (FCA) from near infra-red to near UV depending on the concentration, provoking an increased parasitic absorption (see Fig. 5.2) (Drude theory, [Drude 1900]). Under reasonable assumptions for TCOs, the absorption coefficient related to FCA can be given by [Rucavado 2019]:

$$\alpha_{FCA} = \frac{\lambda^2 e^3 N d}{4\pi\epsilon_0 c^3 n m^{*2} \mu} \tag{5.2}$$

with λ the wavelength, N the carrier concentration, d the TCO thickness, ϵ_0 the vacuum dielectric constant, c the light speed in the vacuum, n the refractive index, m^* the excited carrier effective mass and μ the mobility. The parasitic absorption then depends on N/μ, and is negligible in the Si-based PV scope (over the c-Si absorption spectrum) for films with N in the range of 1×10^{19} cm^{-3} and below. Experimentally, a typical carrier concentration for TCOs for avoiding a strong impact of FCA while being conducting enough, is around 1×10^{20} cm^{-3} [Calnan 2010]. Above this limit, carrier transport would also be strongly impacted by ionized impurities scattering, reducing the mobility.

It is then complicated to increase conductivity by increasing carrier concentration only, particularly due to the critical impact of FCA on parasitic absorption. On the contrary, increasing mobility will reduce FCA, as shown in equation 5.2, which appears to be the ideal solution to decrease the resistivity. In a simple approach, with 1×10^{20} cm^{-3} and resistivity below 1×10^{-3} Ω cm, mobility should be above 60 cm^2 V^{-1} s^{-1}. However, below 1×10^{20} cm^{-3}, mobility would need a drastic increase to keep the same conductivity. For instance, a carrier concentration of 1×10^{19} cm^{-3} would require a mobility above 600 cm^2 V^{-1} s^{-1} to keep resistivity below 1×10^{-3} Ω cm. However, for TCOs commonly used in c-Si SHJ field, mobilities generally do not exceed 70 cm^2 V^{-1} s^{-1} because the limited thermal budget allowed during SHJ processing leaves the TCO poly-crystalline with lots of grains, which limits the mobility by

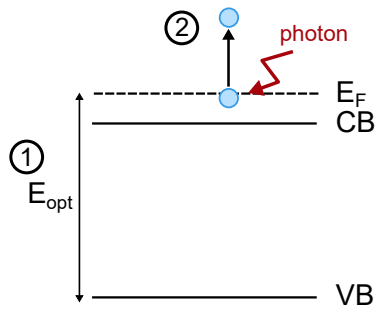

Figure 5.2: Schematic representation of (1) Burstein-Moss effect and (2) free carrier absorption.

grain boundary scattering. These considerations are summarized in Fig. 5.3.

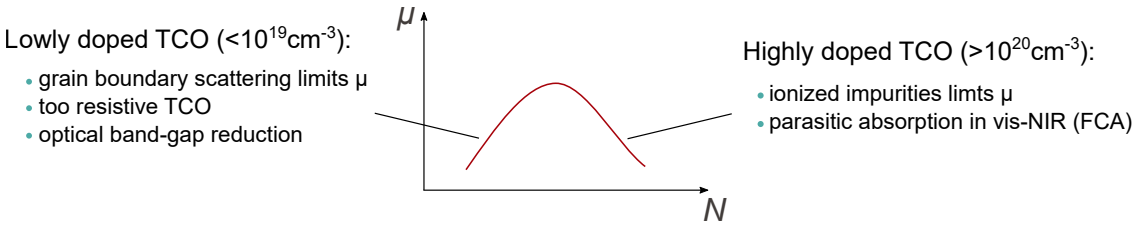

Figure 5.3: Schematic representation of mobility μ evolution with the carrier concentration N, in the case of a polycrystalline film

5.3.2 Material properties of the investigated ITOs

Crystallographic structure

To examine the ITOs crystallographic structure, we performed XRD measurement with an incident angle scan from 0° to 70°. Diffractograms of the reference and the low power ITOs are presented in Fig. 5.4. From the as deposited state, the reference ITO shows a high intensity narrow peak indicating a polycrystalline growth. After annealings at 130 °C and 210 °C (not showed here) during 20 min in ambient atmosphere, the ITO structural properties did not change. The peak position hints at a preferential growth along the plane (222), which is a common growth direction for polycrystalline ITOs [Pashmakov 1993, Cruz 2004]. Further analysis from the measurement revealed an averaged grain size of around 20 nm, rather small compared to the typical size (~ 100 nm). On the contrary, the low power ITO shows to grow in a quasi-amorphous structure. This result is in agreement with literature which stipulates that for high power, TCOs tend to grow more crystalline since more energy is available to generate more crystalline arrangement [Cruz 2004]. Upon annealing at 130 °C, the material did not change phase. The difference in the two structures will induce different transport properties. In an amorphous layer, carriers would not be hindered by grain boundaries that are present in polycrystalline materials. Additionally, the conductivity in amorphous ITO films proved to be high and was shown to be limited by ionized impurity scattering despite the disordered amorphous structure. Extended state conduction through the defect states orbitals overlap

(detailed in Chapter 7), happening in amorphous materials, seems to be the responsible. In conclusion, we expect the amorphous TCO to have a high mobility. To verify the hypothesis, the next paragraph presents the Hall effect measurements.

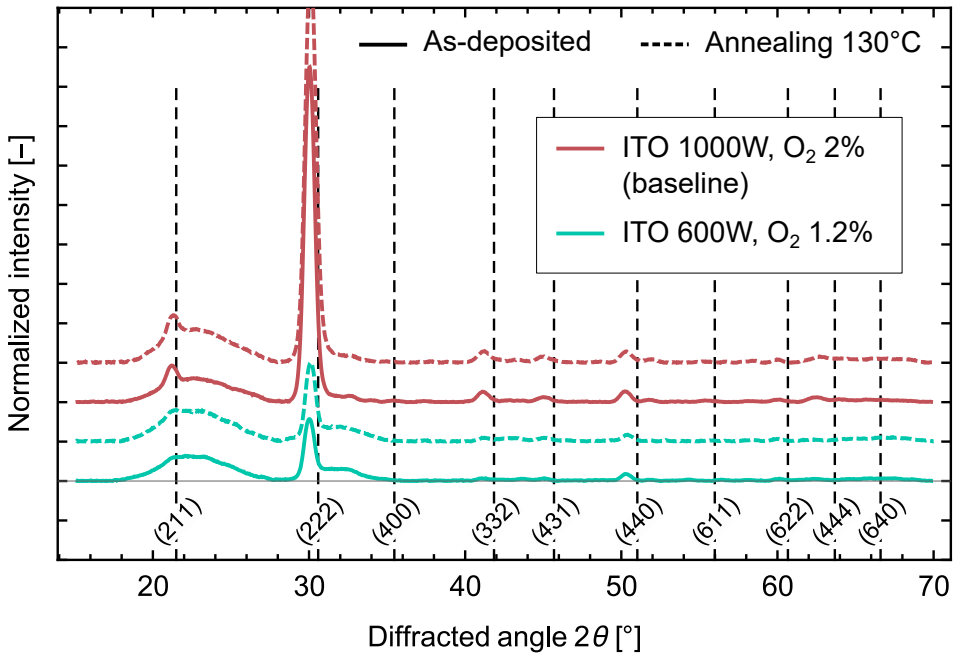

Figure 5.4: Diffractogram of the low power ITO and the reference one deposited on glass samples, following XRD measurements, as deposited and after annealing at 130 °C during 20 min in ambient air atmosphere. Performed by Julien Hurni.

Carrier concentration, mobility and resistivity

Fig. 5.5 shows the different electrical properties of the four different ITOs from the three different batches measured by Hall effect on glass samples (100 nm films). As deposited and annealed films at 130 °C gave similar results. Value ranges (colored values) indicates batch to batch deposition variation, which is higher than the measurement standard deviation (grey values). For the three ITO deposited at a power of 1000 W but different oxygen rates, carrier bulk concentration increases exponentially when increasing O_2 (see Fig. 5.5.a)). The low power ITO exhibits a carrier concentration more than three times higher than the baseline ITO (2% O_2), yet similar mobility. The latter is maintained instead of dropping, most probably compensated by the above-mentioned increased mobility due to the amorphous structure. Conversely, the ITO with the highest carrier concentration has poor mobility. The highest oxygen rate (3%) ITO mobility is comparable to the reference one, margin error included. Resistivity, in Fig. 5.5.c), of the low power ITO and the ITOs deposited with 1% oxygen atmosphere lay below the one of the baseline ITO by around 1 mΩ cm. Considering purely resistive effects only, a resistivity decrease of 1 mΩ cm translates into an approx. 0.29 Ω cm^2 ITO lateral series resistance decrease (calculated using the method developed in [Schroder 1984, Haschke 2019a] with our

front metal grid design (pitch = 1.85 mm, ITO thickness of ~ 100 nm). According to Pysch *et al.* empirical law [Pysch 2007], the present lateral R_s reduction could lead to a ~ 1 $\%_{absolute}$ enhancement. Finally, the resistivity of the ITO with the highest oxygen rate during deposition is 5 to 6 times above the baseline one, which could severely hinder a solar cell *FF*. Among the differently doped ITOs deposited at the same power, resistivity increases with increasing O_2 rate, in accordance with the carrier density evolution.

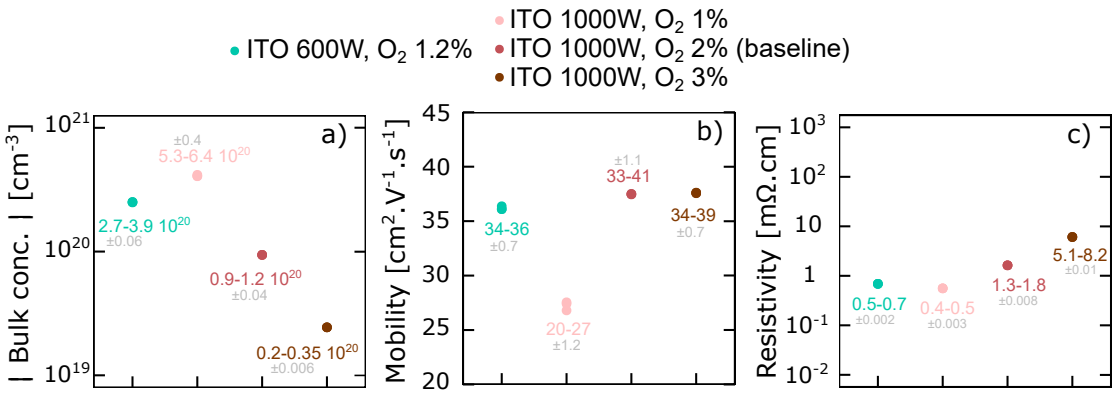

Figure 5.5: ITOs electrical properties (a) bulk concentration, b) mobility, c) resistivity) measured by Hall effect on glass samples. Colored numbers on the plots indicate the value range measured for the three different batches and give a hint of deposition tool variability. Numbers in grey are the measured standard deviation of the Hall effect measurement tool.

Optical features

The optical properties investigation, presented in Fig. 5.6, was lead through spectrophotometry and EQE characterizations. Fig. 5.6.a) shows the absorptance spectra of the four ITOs deposited on glass sample. From the plot, the hump existing in the near IR region is increasing with ITO doping, the signature of the FCA. Over the full wavelength range, the ITO with the lowest N (2×10^{19} cm^{-3} to 3.5×10^{19} cm^{-3}, see previous section) is almost unaffected by the phenomenon, while the highest one (5.3×10^{20} cm^{-3} to 6.4×10^{20} cm^{-3}) is severely impacted from the blue visible region. The actual observation highlights the doping strong influence on absorption in this narrow critical carrier concentration range. On the restricted c-Si absorption region, representative of the utile range for solar cells, both reference and lowest doped ITO are unaffected by FCA. EQE measurements on the front of the different solar cells brings quantitative insight and FCA impact on final J_{SC} devices. The J_{SC} were calculated by integrating the solar cells EQE signal over the photon flux solar spectrum, from 320 nm to 1180 nm, separated in three wavelength regions. On the short wavelength range (Fig. 5.6.b)), no correlation is observed between doping and J_{SC}. The ITO deposited at low power exhibit a superior current compared with its high power counterparts, probably owing its different crystallographic structure. Over 600-900 nm (Fig. 5.6.c)), all ITOs have equivalent J_{SC}s except the highest doped one, again presumably because the strong FCA impinges this region. Finally, in the near infra-red (NIR) region (5.6.d)), where FCA should be the most impactful, the ITO

with the highest N exhibits a strongly reduced J_{SC} compared to all its counterparts. Overall, FCA seems responsible for a 0.5 mA cm^{-2} J_{SC} loss for the ITO with the highest N, compared to the lowest one (for which FCA does not occur). Despite a doping level closer to the highest doped ITO than the reference one, the low power ITO shows similar J_{SC} than the latter. With a lower resistivity (see previous section) and J_{SC} as high as the baseline ITO, it promises excellent electrical and optical properties for c-Si SHJ.

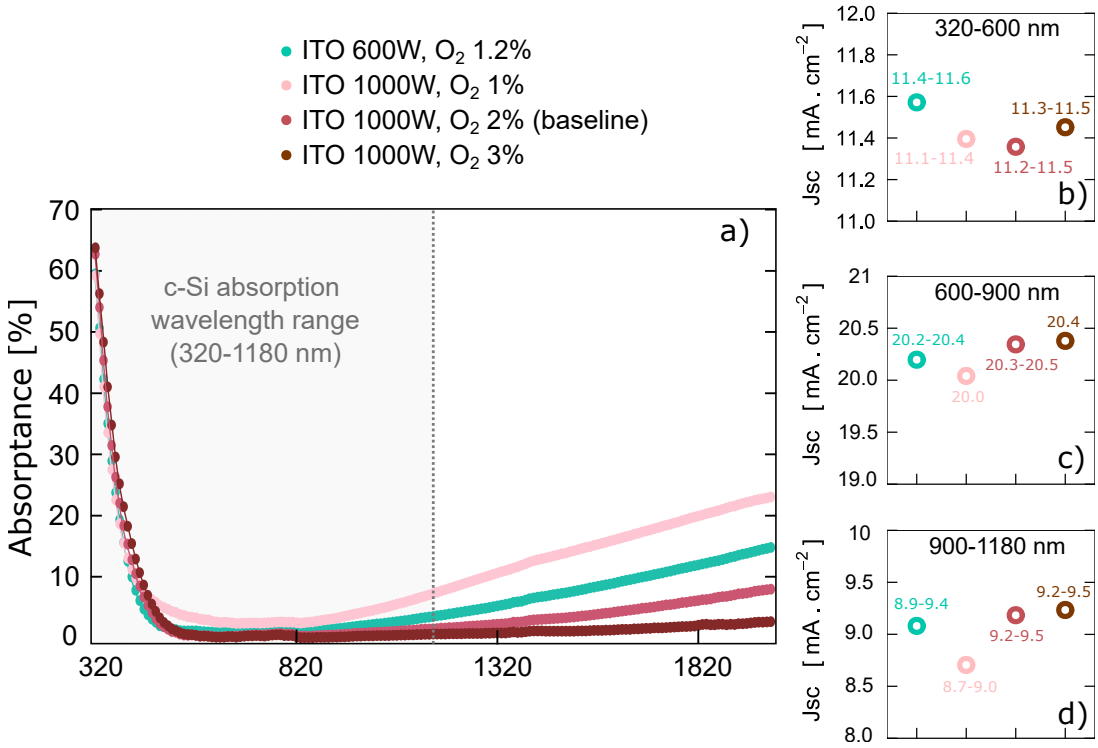

Figure 5.6: Optical characterizations. a): Plot of the four ITOs absorptance over 320-2000 nm, deposited on glass samples. The greyed area identifies the c-Si absorption domain to highlight the solar cells absorption range. b), c), d): Short circuit density current J_{SC} calculation extracted from EQE front measurements of the solar cells integrating the different ITOs, over 320-1180 nm. Values range on the plots indicate limits of the values measured from the three different batchs.

5.3.3 ITOs influence on passivation and transport

To address the aforementioned discussion about the role of front ITO sputtering power in the solar cell front passivation, we studied the evolution of the iV_{OC} and iV_{mpp}(more representative of solar cell carrier population state under real operation) for the samples with ITOs deposited at 600 W compared to the three others with ITOs deposited at 1000 W. The measurement were made on the dedicated quarter wafers (see the section on experimental details). The four different samples iV_{OC} and iV_{mpp} evolution throughout the process steps, for the three different MoO_{3-x} thicknesses, are shown in Fig. 5.7. As expected and previously

highlighted in Chapter 4, the ITO front step deposition drastically affects the device *iV*, with a stronger impact with decreasing MoO_{3-x} thickness. Contrary to the others, devices with no MoO_{3-x} (Fig. 5.7.a)) do not recover their initial iV_{OC} after curing (at 130 °C during 20 min) and undergo a drop of more than 100 mV, indicating a highly recombinative ITO/a-Si:H interface. For the iV_{mpp} data, values after the ITO front deposition are not accurate due to trapping effect, generally active at low injection when the carrier concentration is equal or lower to trap density, which results in a drastically increased photo-conductance of the sample [Macdonald 1999a, Macdonald 1999b, Macdonald 2000].
Devices implementing a layer of 2 nm and 4 nm of MoO_{3-x} present same trends —and comparable values, contrary to previous chapter study— between iV_{OC} and iV_{mpp} (Fig. 5.7.b), c), e), f)).
They both regain their initial iV_{OC} after all the process steps, even though the drop after the ITO front deposition step is stronger for the 2-nm-MoO_{3-x}-based device than its 4-nm counterpart. Yet, iV_{mpp} is only partially restored.
It is interesting to note that devices with MoO_{3-x} significantly recover iV_{OC} and iV_{mpp} after the back ITO deposition —so before the dedicated post-annealing. This would arise from a curing effect originating from wafer heating during the deposition process, and parallel experiments were led to support this hypothesis (see appendix B). They showed that wafers temperatures of around 130 °C to 140 °C were reached on the front side during deposition of backside ITO, enough to properly anneal the cell.
For both MoO_{3-x} thicknesses, samples with highest doping, which include ITO deposited at low power, exhibit the lowest iV_{OC} and iV_{mpp} after the front ITO sputtering. The reasons are unclear, but could stem from less efficient Fermi level splitting according to a lower ITO work functions —due to higher doping— compared with the two others, or hazardous reasons like batch-to-batch wafer quality variability, defective passivation layer, or not homogeneous MoO_{3-x} layer thickness. The 2-nm-MoO_{3-x}-based samples with lowest iV_{OC} after front ITO sputtering do not recover iV_{OC} nor iV_{mpp} after annealing as well as the the 4-nm-MoO_{3-x} ones do. One could advance that it is a result of weaker ITO work function screening by thinner MoO_{3-x}. Yet, a higher amount of data for accurate statistics is required to formulate rigorous conclusions on these points.

In the end, the devices with ITO deposited at the lowest power did not exhibit higher iV_{OC} nor iV_{mpp} in the end of the process, compared with the other three ITOs and independently from MoO_{3-x} layer thickness. No obvious correlation could be drawn between ITO deposition power over the range 600-1000 W,neither with carrier concentration, and the devices *iV*.

Fig. 5.8 shows the *FF*, FF_0, and R_s of the final solar cells processed in this experiment. As a general trend and for every MoO_{3-x} thicknesses, *FF* increases with increasing ITO doping (decreased oxygen percentage during ITO deposition) for the ITOs deposited at 1000 W while the lower-power deposited ITO exhibits the best *FF* among all samples as expected by the preliminary analysis of previous sections —even though it is not the highest doped ITO. The poor performances of most cells using the lowest-doped ITO (brown) and 4 nm of MoO_{3-x}

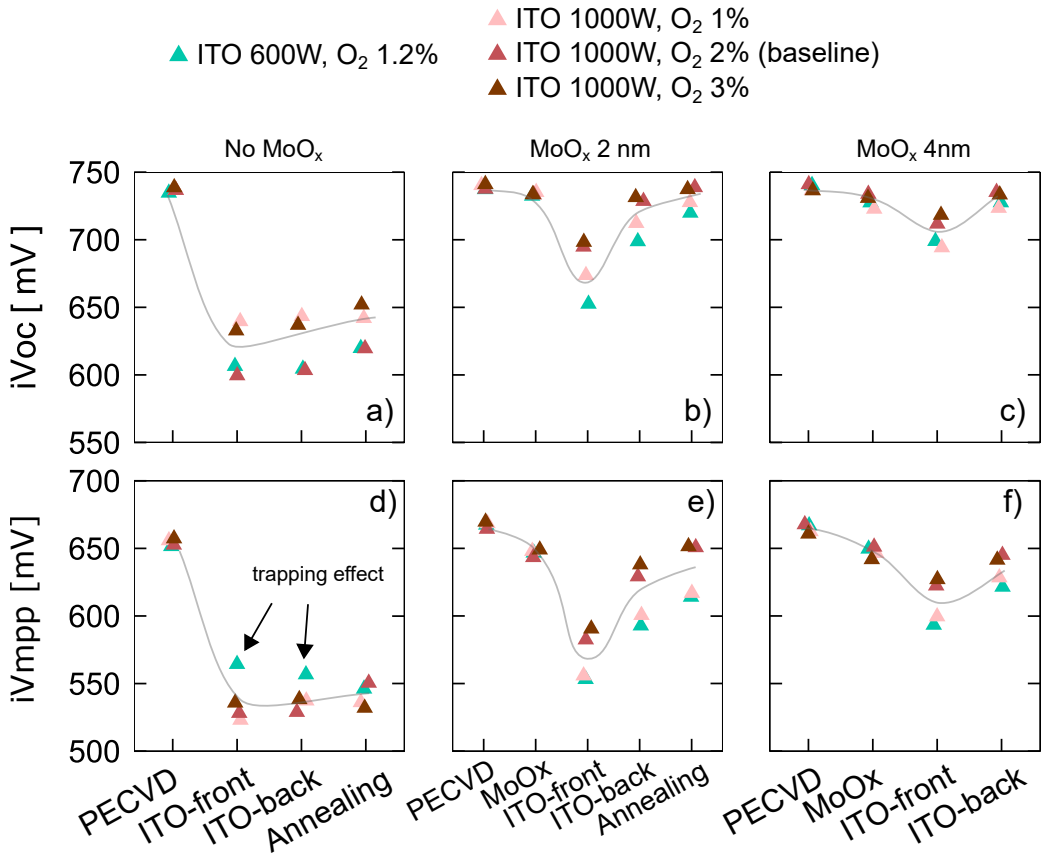

Figure 5.7: Evolution of iV_{OC} (a), b), c)) and iV_{mpp} (d), e), f)) throughout the process steps, of devices with different MoO_{3-x} thicknesses (a) and d): no MoO_{3-x}; b) and e): 2 nm of MoO_{3-x}; c) and f): 4 nm of MoO_{3-x}), and different ITOs sputtered at the front side.

originate from bulk wafer inhomogeneities (see Fig. C.1 in appendeix) and the highest value data point only will be considered in the analysis. A look at Fig. 5.8.d), e), f) shows that R_s follows the conductivity trend from the Hall measurements in Fig. 5.5, and also indicates a strong correlation with the previous observation on *FF*, the sample with the highest series resistance resulting in the lowest *FF*.

Yet, the significant *FF* difference between the ITO deposited at 600 W and the highest-*N* one (O_2 1%), that is 3.1 $\%_{absolute}$ difference for the samples with no MoO_{3-x} and 0.9 $\%_{absolute}$ for the 2-nm-MoO_{3-x}-based ones, despite the similar R_s, evidences the influence of another mechanism on *FF*. For *FF* variations that originate from purely resistive effect, the FF_0 (presented in Chapter 2) should, by definition, be identical between the different samples at a given MoO_{3-x} thickness. This is rather the case for the 4-nm-MoO_{3-x}-based samples, but an FF_0 variation of 2 $\%_{absolute}$ and 5 $\%_{absolute}$ maximum is observed for the 2-nm-MoO_{3-x}-based samples and devices with no MoO_{3-x} respectively. In both case, the trend for FF_0 follows ITOs doping —for all ITOs—, with increasing values for decreasing doping. The latter result suggests an influence from the ITO work function —higher work function for lower *N* — in the extraction of holes, which vanishes when increasing MoO_{3-x} thickness. Another possible explanation resides in the

better interconnection —related to higher ITO conductivities— between local surface defects for not well passivated devices [Cattin 2019]. This would enhance surface recombinations and reduce *FF*.

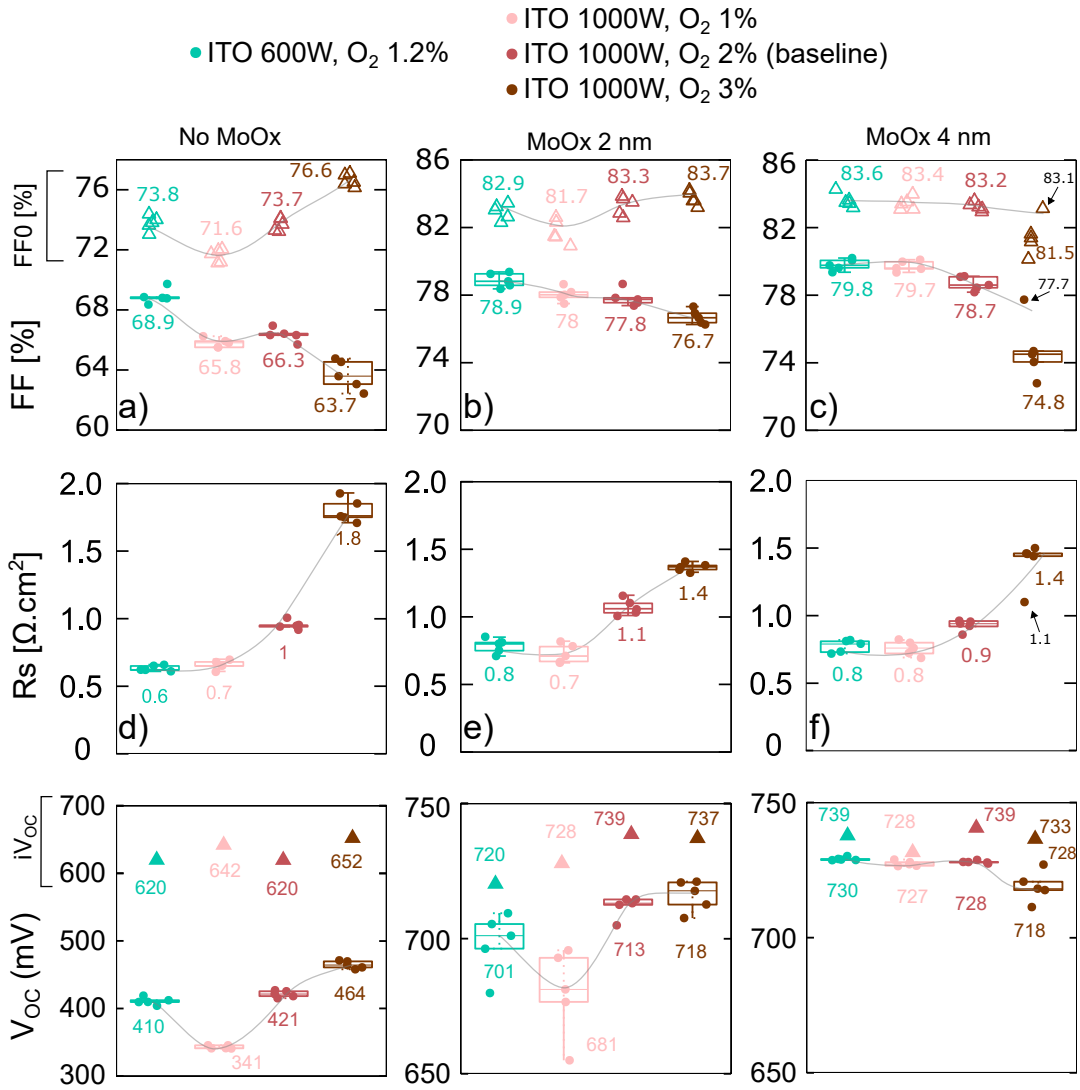

Figure 5.8: Plots of *FF*, FF_0, R_s, V_{OC} and iV_{OC} of final devices for the four different ITOs tested in this chapter ad three MoO_{3-x} layer thickness.

In the end, the ITO deposited at low power gave best *FF* due to improved series resistance compared with the standard ITO used as a baseline (gain of >~ 1 $\%_{absolute}$, for all conditions) with no negative influence from work function. Despite a higher *N* than the baseline ITO, they display equivalent optical response as a result of different crystallographic structure. Combination of these two features induces enhanced performances for MoO_{3-x} devices using the low power ITO by more than 1 $\%_{absolute}$ on the efficiency compared to baseline, bringing MoO_{3-x}-based cells standards to perform as 23 % efficient devices. When forced under forward

current in the dark during one week, a treatment as known as "forward bias" and described in the next chapter, the present solar cell integrating 4 nm of $MoO_{3\text{-}x}$ and the new ITO deposited at low power reached the impressive efficiency of 23.7% surpassing the 23.5% world record in this category.

5.3.4 ITOs and $MoO_{3\text{-}x}$-based contact work function estimation

To verify the previous hypothesis on work function change with ITO doping, we fitted the measured *J-V* curves of the three ITOs deposited at 1000 W using the method of Roe *et al.* presented in Chapter 2 to estimate the hole contact work function. Fig. 5.9 illustrates the obtained result, with both experimental (symbols) and fitted (lines) data, and was split in two for the sake of clarity. As for the previous series of Chapter 4, we observe the same trend for V_{OC}, which is decreasing with thinner $MoO_{3\text{-}x}$ layer thickness, even though the performances of the 2-nm-thick $MoO_{3\text{-}x}$-based samples of this work are close to their 4-nm-thick counterparts. Comparing now the influence of ITO carrier concentration, a strong influence is observed when ITO is directly in contact with (*i*)a-Si:H (0 nm of $MoO_{3\text{-}x}$) as it constitutes the only —poorly, considering the low V_{OC}s— selective layer in this case. As expected, the ITO with the lowest N —-so the highest work function one— is the one providing the highest V_{OC}. Applying 2 nm of $MoO_{3\text{-}x}$ already efficiently screens the ITO influence since the V_{OC} spread between the different samples is much narrower (125 mV difference between the samples with the highest and lowest doped ITO and no $MoO_{3\text{-}x}$, compared with 25 mV for the 2-nm-$MoO_{3\text{-}x}$-based ones). The presence of the 2 nm $MoO_{3\text{-}x}$ layer also enhances selectivity and passivation with a V_{OC} gain of around 300 mV compared to the cells with no $MoO_{3\text{-}x}$. With 4 nm of $MoO_{3\text{-}x}$, ITO influence seems completely screened —at least on this range of TCO carrier concentration— with V_{OC} of the different samples spanning over 3 mV only, and it is still slightly improved compared to 2-nm-$MoO_{3\text{-}x}$-based cells. These results, in line with the previous *FF* and FF_0 analysis, highlight that even though j_{0e}^{MoOx} is similar for 4 nm or 2 nm thick $MoO_{3\text{-}x}$ (see the Roe *et al.* analysis of Chapter 4), the work function of a 2-nm-$MoO_{3\text{-}x}$ thick layer in this contact stack is not high enough to completely screen the ITO work function mismatch influence on carrier extraction, contrary to a 4 nm $MoO_{3\text{-}x}$ layer. Consequently, using a lightly doped ITO could be preferable with $MoO_{3\text{-}x}$ layers thinner than 4 nm.

With the approach developed in Chapter 4, we can use thermionic emission law to extract the barrier height ϕ_b, and quantitatively estimate the hole contact work function of this set of data —which match better the simulations than those in the previous chapter. For all solar cells, we set $A^* = 70\,\mathrm{A\,cm^{-2}\,K^2}$ assuming A^* for a-Si:H is close to those of c-Si [Deneuville 1979], and approximates this value for p-type c-Si [Sze 1995]. Assuming that the cells operate in low to moderate injection under one sun, what is suggested by Suns-V_{OC} measurements of Chapter 4, and that there is no Fermi level pinning at the interface $MoO_{3\text{-}x}$/(*i*)a-Si:H, we can suppose that the energy difference between the Fermi level at the interface with (*n*)c-Si and the (*i*)a-Si:H conduction band maximum ϕ_b (see Chapter 4 section 4.4.6) also represents the barrier height between $MoO_{3\text{-}x}$ (or ITO) Fermi level and (*i*)a-Si:H conduction band. Using 3.9 eV for

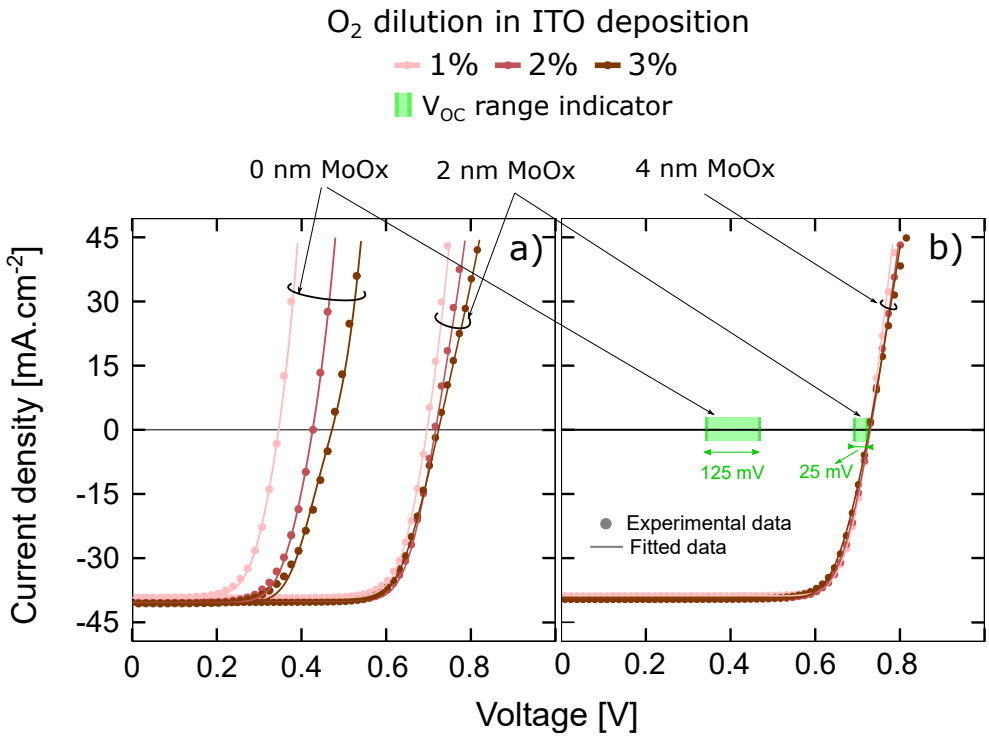

Figure 5.9: *J-V* experimental and fitted curves of solar cells with 0 nm, 2 nm and 4 nm of $MoO_{3-x}$with three different ITO oxygen doping each. For more clarity, solar cells with 0 and 2 nm of MoO_{3-x} are plotted on graph a), and 4-nm-MoO_{3-x}-thick cells are plotted on graph b) in which 0-nm and 2-nm-MoO_{3-x}-based samples V_{OC} range are added for comparison.

a-Si:H electron affinity (EA) [Schmidt 2007, Kleider 2008], we can extract MoO_{3-x} and ITOs work function, so that: $WF^{MoO_{3-x} or ITO} = \phi_b + EA^{a-Si:H}$. The calculated work function are around 5 eV for devices integrating MoO_{3-x} layers of 2 nm and 4 nm. The similar work function found for both 2 nm and 4 nm MoO_{3-x} originates from the previously mentioned limitation of extracting work function through j_{0e}^{MoOx}, but must be different according to results of Fig. 4.13 (see Chapter 4) and noting that V_{OC} difference between the samples with less doped ITO and most doped one represents 25 mV for 2-nm-MoO_{3-x}-based layers while 3 mV for the 4 nm ones. Yet, beyond the fitting limitations, it is possible that the 4-nm-thick MoO_{3-x} work function inside the contact is lower compared to literature (typically around 6 eV to 6.5 eV [Battaglia 2014b, Greiner 2013a]) since it is exposed to air between process steps (work function easily reduced by 1 eV [Battaglia 2014b, Meyer 2011b, Gerling 2015c]), and is sandwiched between two lower-work-function layers prone to oxidation (thermodynamically and electronically [Greiner 2013a, Gerling 2015c]). Additionally, significant sub-gap absorption is observed optically for a-Si:H/MoO_{3-x}/ITO stacks [Sacchetto 2017]. A low value could also be understood as our calculated work function is an effective work function of the entire hole contact stack ITO/MoO_{3-x}/(*i*)a-Si:H/(*n*)c-Si(still with MoO_{3-x} (or ITO) work function playing a central role in the thermionic emission). For samples with no MoO_{3-x}, corresponding to direct contact of (*i*)a-Si:H with ITO, work functions amounted for 4.6 eV, 4.7 eV and 4.8 eV for front

ITO with a deposition oxygen rate of 1%, 2% and 3% —so decreasing N— respectively. Fig. 5.10 illustrates the band diagram of the contact in case of two different ITO work function. The obtained values are in agreement with the range of 4.5 eV to 5.1 eV found in literature [Centurioni 2003, Kim 2000, Sugiyama 2000]. This mid-gap position correlates well with our obtained V_{OC} value that are around 350 mV in absence of MoO_{3-x}, and the one found in literature for such TCO work function on (n)c-Si [Bivour 2012, Ritzau 2014], corresponding to the absence of any selectivity at the hole contact. It suggests that this methodology coupling J_0s with energy barriers and band diagram theory could be a valuable approach to characterize the work function of electrodes in use within the solar cells contact stack. A weakness of the method in case of devices with no MoO_{3-x} lies in the fact that low V_{OC} values also originates from the high Si surface defects concentration due to the direct contact with sputtered ITO, which is not taken into account in the calculation method. The work functions obtained in that case should then not be as precise as samples with protective layers like MoO_{3-x}. However, the work function difference of 0.2 eV calculated between the less to most doped ITO remains an accurate evaluation.

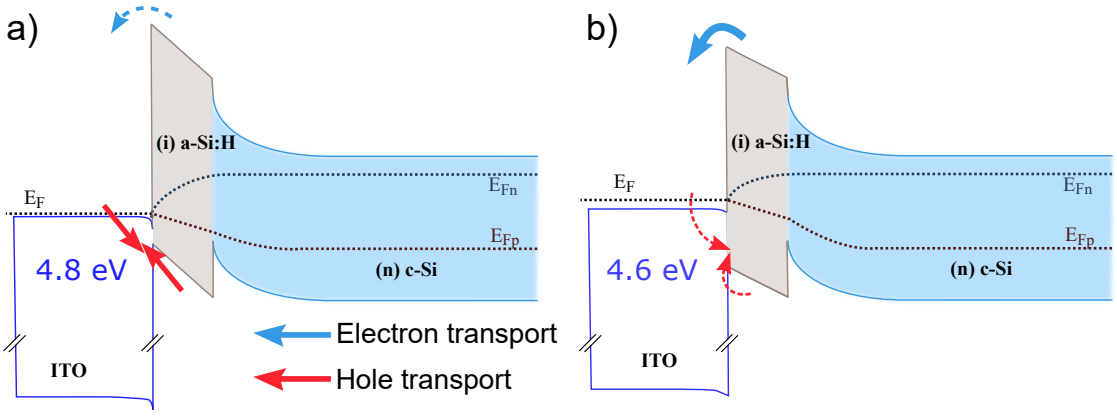

Figure 5.10: Schematic representation of band diagram for devices with direct contact between ITO and (i)a-Si:H. The glsitos have two different work functions (a) 4.8 eV and b) 4.6 eV). In the first case, the hole current is favorized, while in the second the thermionic barrier to electrons is decreased, favorizing their flow. The sketch exaggerates the changes in band alignment, and one should keep in mind that this contact remains poorly selective (similar current flows between holes and electrons).

5.3.5 Implementation of various TCOs

To further explore TCO influence on the MoO_{3-x} contact —using TCOs with more diversified properties between each others than the previously tested ITOs— and to probe the strength of the previous conclusions, we deposited four different ITOs, hydrogenated IZrO (IZrO:H) and aluminum doped zinc oxide (AZO), on (p)a-Si:H-based and 4-nm-thick MoO_{3-x}-based contacts to compare the different behaviors. The two first ITOs were processed as references using the previous recipes of the baseline and the low power (600 W) ITOs. ITO deposited by sputtering with CSEM tool, ITO deposited by sputtering in the Leybold evaporator, IZrO and

AZO were deposited as described in the experimental details section. The four ITOs, optimized for front hole contacts SHJ, are expected to have similar work functions even though their electrical and optical properties might differ due to the different deposition tools used. IZrO is expected to have a similar work function than ITO, with an improved IR optical response than the latter. AZO is known to be an electrode suited for electron contacts due to a smaller work function compared to ITO or IZrO, and is often used at the backside of a fully metallized solar cell because of its high resistivity originating from poor mobility. Therefore, it is expected to have the strongest impact on V_{OC} and FF.

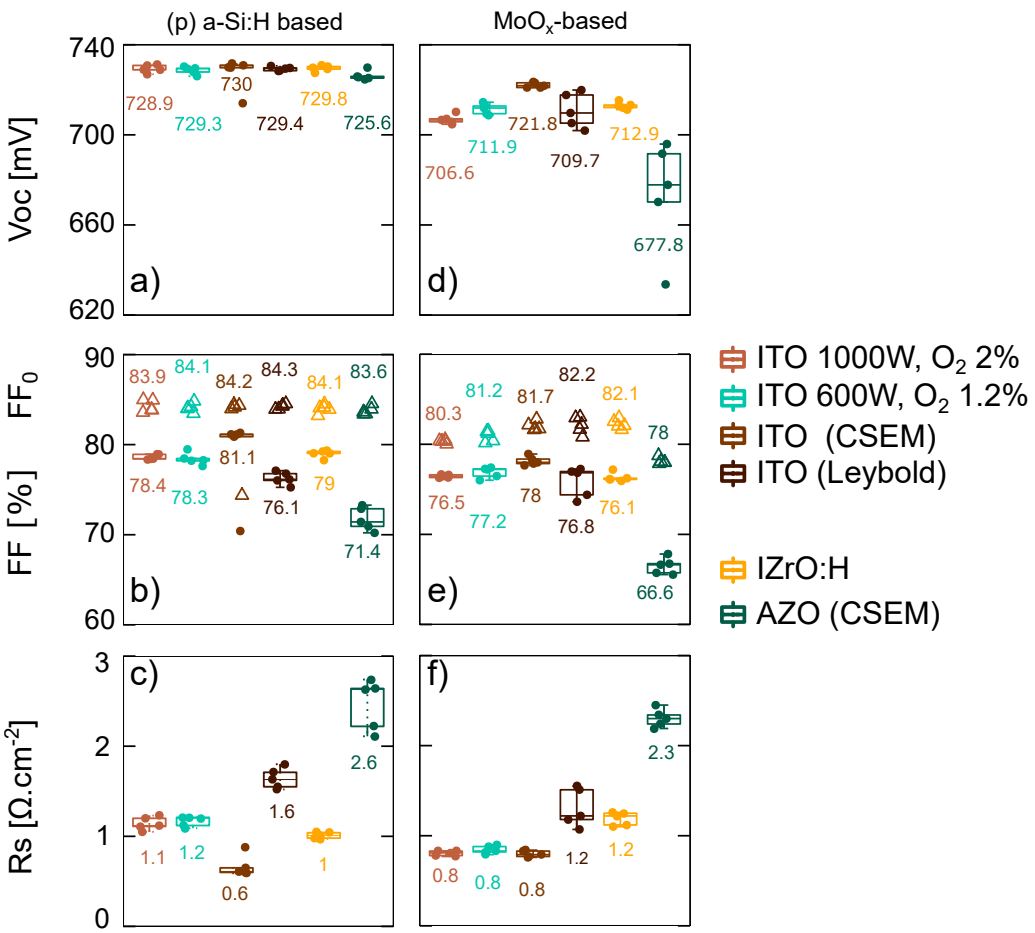

Figure 5.11: Electrical performances extracted from the J-V characteristics of the different processed samples. FF_0 and R_s are calculated using the method presented in Chapter 2. Results on J_{SC} are showed in appendix C.

Final solar cells electrical properties are shown in Fig. 5.11 for hole contacts integrating (p)a-Si:H or MoO_{3-x}. For (p)a-Si:H-based solar cell, both V_{OC} and FF_0 are very similar for the different TCOs (730 mV and 84 % respectively) —even though the samples with AZO presents slightly lower parameters. FF variations are then entirely explained by R_s variations. In the case of MoO_{3-x}-based devices, V_{OC} and FF_0 values are not as steady as for the previous case. V_{OC} and FF —as well as FF_0— of the two reference ITOs samples are significantly lower than

the usual values (supposed to be around 728 mV and near 80 % according to previous results, see previous paragraphs). In the present experiment, the MoO_{3-x}-based contact is then not performing as well as it should —be it due to atmosphere composition variation during ITO sputtering or thinner MoO_{3-x} than expected—, which might also influence the effect of the different TCOs. Neither the MoO_{3-x}-based V_{OC} nor FF_0 trend are following the implied voltage one —comparing *iV* of the different samples after PECVD and after TCO deposition, and for which samples with AZO hold the highest *iV* values, see Fig. C.2 in appendix— thus cannot be explained by passivation issues. The most impacted FF_0 is obtained for the samples with AZO which also has the lowest work function among the different TCO, as expected. To get an idea of the different TCO work functions, we fitted the *J*-*V* curves of dedicated samples with no selective layers —no (*p*)a-Si:H neither MoO_{3-x}— in the same way as the one used to determine previous ITO work functions. We found that all TCOs work function was around 4.7 eV, except the one of AZO being around 4.5 eV.
In the end, samples using (*p*)a-Si:H as front hole contact were found to be much less sensitive to the work function influence while the 4-nm-thick-MoO_{3-x}-based contact was highly impacted. As expected, AZO is not a suitable TCO fort he hole contact, both in term of band alignment (especially for MoO_{3-x}-based contacts) and series resistance losses. Yet, the sheet resistance of the ITO deposited in our tool was unusually low and is suspected to originate from a higher humidity rate due to climatic conditions. Such situation would be dramatic for the MoO_{3-x} layer and could also explain the unusual under-performance of this latter contact compared to the typical values. For accurate conclusions, the experiment should be repeated.

5.4 Influence of PECVD-deposited SiOx as a double ARC

This section is based on the work achieved during the Master thesis of Corentin Sthioul.

5.4.1 Expectation from standard SHJ DARC coatings and motivations

TCOs strongly reduce reflectance as their refractive index are lower than the one of c-Si or a-Si:H. Yet, the mismatch with air refractive index remains high and still causes reflectance losses (for instance, refractive index of ITO at 600 nm ranges from 1.7 to 2.1 [Yang 2006, Haschke 2019b, Du 2021a]. The addition of a lower-refractive-index double anti-reflective layer (DARC) on top of the TCO, would further reduce such losses and was effectively implemented in standard SHJ solar cells [Zhang 2013, Herasimenka 2016, Du 2021a, Boccard 2021]. The DARCs provide several other benefits like improve sustainability by reducing the amount of TCO —which generally contains indium— as the required thickness when combined with a DARC is decreased(see next paragraph), reduce NIR parasitic absorption for the same reason, or enhance solar cell reliability when integrated in module [Du 2021a, Liu 2020]. There is no need for DARC to be conductive, and common materials are dielectrics, such as SiO_x or SiO_x:H, SiN_x, Al_2O_3, LiF or MgF_2 [Du 2021a].
To date, DARCs have never been tested on MoO_{3-x}-based cells and this section aims to provide

preliminary results about such treatment on these devices. For the study, we chose PECVD-deposited SiO_x:H as the DARC as it provides optical and electrical improvements when on top of ITO/(*p*)a-Si:H-based standard hole contact solar cells, is cheap, and stable. The optical enhancement stem from the use of a thinner ITO and better anti-reflective property, while the electric one is ascribed to influence of annealing and/or hydrogenation of the ITO during the SiO_x:H deposition, which tend to reduce its resistivity [Morikawa 1999, Morikawa 2000, Cruz 2004, Barraud 2013, Kobayashi 2016b, Ritzau 2016]. In the present work, we investigate how the SiO_x:H coating impacts the MoO_{3-x}-based devices electric and optical properties. The SiO_x:H deposition parameters are described in the experimental details section.

5.4.2 Optical simulations and measured performances

The optical benefits using an DARC such as SiO_x combined with ITO has been considerably reported in literature for standard a-Si:H-based SHJ contacts, and the optimal thicknesses were found to be around 90 nm to 110 nm for SiO_x with 40 nm to 60 nm of ITO [Zhang 2013, Herasimenka 2016, Cruz 2019, Du 2021a]. To estimate optimal thicknesses in the case of MoO_{3-x}-based solar cells, we performed simulations on OPAL 2 (PV-Lighthouse) [McIntosh 2021] using random upright pyramids for the surface morphology, the AM1.5g spectrum as the incident illumination, and a material stack of SiO_2/ITO/MoO_{3-x}/a-Si:H/c-Si —to reproduce our MoO_{3-x}-based front contact devices— with variable thickness for two anti-reflective coatings, and 4 nm, 6 nm and 180 µm for the other materials, respectively. Optical properties (refractive index n, absorption coefficient k) of the different materials were chosen from the website library. The ITO thickness was varied by step of 10 nm, and the SiO_2 one was calculated accordingly by an optimization algorithm so that the photon current absorbed in the substrate was maximal. Results of the total current density reflectance loss —output of the simulation and calculated over 250-1400 nm— versus ITO thickness, with or without the SiO_x layer, are showed in Fig. 5.12.a). Reflectance losses are minimized for an ITO thickness of 70 nm with no SiO_x DARC —ITO thickness commonly used on our wafers—, and 40 nm with an SiO_x thickness near 100 nm (see Fig. 5.12.b)). These figures are similar to that obtained for the standard SHJ. Following the calculation, using 100 nm SiO_x as DARC with a 40-nm-thick ITO —best combination according to simulation— should reduce the photo-current losses by 0.8 mA cm^{-2} for a 70-nm-thick ITO, and 1.4 mA cm^{-2} for a 40-nm-thick one, both used without SiO_x.

To compare with the previous results, we processed devices with the 4-nm-MoO_{3-x}-based front contact stack deposited on textured wafers, using baseline ITO of 70 nm and 40 nm, with and without SiO_x DARC. Reflectance was measured by spectrophotometry and results are plotted in Fig. 5.13. Even though the reflectance is slightly increased around 600 nm —ITOs are optimized to have a minimum of reflectance in this range— with the SiO_x layer, the response in the NIR range is significantly reduced. We calculated the current density loss over 320-1050 nm for a realistic evaluation of the current density loss by reflectance from the front stack —c-Si absorption is over 320-1180 nm -, while removing c-Si substrate reflectance losses above

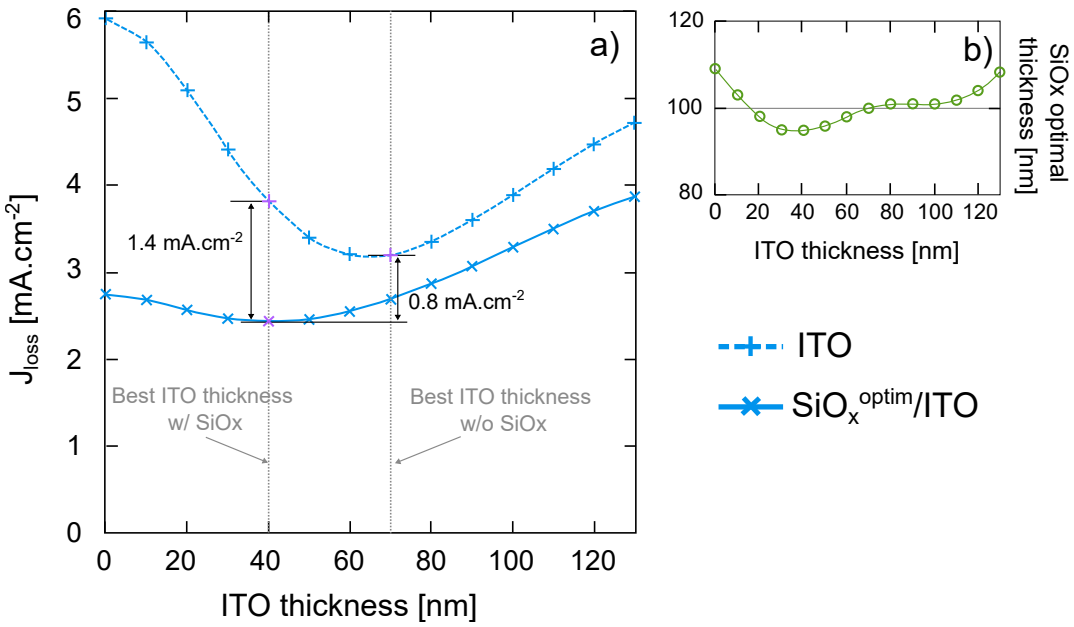

Figure 5.12: Results of the simulation performed on OPAL 2 (PV Lighthouse) for a MoO_{3-x}-based hole contact SHJ. a) Calculated photo-current reflectance losses according to ITO thickness, without and with (optimal thickness) SiO_x DARC. b) Optimal SiO_x thickness obtained for the different ITO thicknesses.

1050 nm since absorption is not as efficient above this value and so measured reflectance is not only composed of primary reflections. The obtained current losses summarized in the table of Fig. 5.13 follow the same trend than that suggested by simulation, yet with lower current gain between the stack with and without SiO_x (0.3 mA cm^{-2} and 1 mA cm^{-2} for 70-nm-thick and 40-nm-thick respectively, instead of the expected 0.8 mA cm^{-2} and 1.4 mA cm^{-2}). The reason could be batch-to-batch or films thickness variability, or different refractive index n and absorption coefficient k of SiO_x:H and ITO compared to the simulated data, or also a change in the ITO carrier concentration N following the SiO_x:H treatment.

5.4.3 Material properties

As a first attempt of MoO_{3-x}-based cells DARC treatment, we used our standard SiO_x:H deposition recipe developed at 180 °C, combined with the baseline ITO. The ITO resistivity was indeed lowered —yet not as much as expected according to literature— but the solar cells *FF* was drastically affected. To elucidate mechanisms in place, we prepared dedicated glass samples, on which we deposited the ITO alone (that will be called here "bare ITO"), and a stack of ITO/MoO_{3-x}/(*i*)a-Si:H imitating the front hole contact of the solar devices. We tested three different ITO doping using the same O_2 rate variation during the sputtering deposition as in the previous section. Carrier concentration and mobility measurements of the ITOs are displayed in Fig. 5.14. Measurement were done upon three successive annealing of the

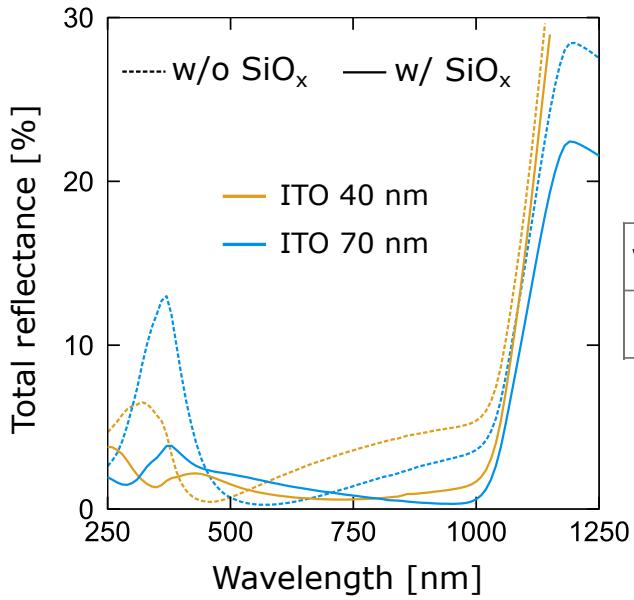

		J_{SCloss} [mA.cm^{-2}]
w/o SiOx	ITO 40 nm	2.3
	ITO 70 nm	1.6
w/ SiOx	ITO 40 nm	1.3
	ITO 70 nm	1.1

Figure 5.13: Total reflectance of the device front surface, with and without SiO_x and for two different ITO thickness.

samples (130 °C, 150 °C and 180 °C) followed by a 180 °C-SiO_x:H deposition, to decorrelate the effects of temperature and PECVD process. From literature, annealing on ITO is known to have two main effects [Morikawa 1999, Morikawa 2000, Cruz 2004]. In a first phase at low temperatures (from 25 °C to around 180 °C), recovering damages from sputtering deposition via atoms rearrangement occurs, while keeping the crystallographic structure unchanged (amorphous or multi-crystalline). Mobility tends to be improved and carrier concentration is left unchanged. Above 180 °C, the crystallized area of ITO starts to increase, which generally provokes a significant increase in carrier concentration —ascribed to Sn dopant activation— and decreases mobility due to ionized impurity scattering. These threshold temperatures may be shifted depending on the ITO doping, initial crystallographic structure, thickness, or substrate. It has also been reported that if H is involved in processes like during SiO_x:H deposition, or present in nearby layers, it can diffuse or effuse in ITO and act as a dopant or assist crystallization, increasing carrier concentration of the latter [Ritzau 2016, Barraud 2013, Kobayashi 2016b], or passivates the existing grain boundaries and surface, which improves ITO mobility [Du 2021a].

In the present work, these two phases as well as the influence of H could be identified. Results are showed in Fig. 5.14. From the as deposited state to 150 °C annealing —which would correspond to the first phase—, carrier concentration remains constant or slightly increases for the full stack glass samples, but slightly decreases for the less doped samples with bare ITO layer. In the case of the lowest doped ITO (highest O_2 rate), the strong discrepancy between the two kind of test architectures testifies of a possible H effusion from the (*i*)a-Si:H under-layer. It could also stem from an oxygen exchange between MoO_{3-x} and ITO, or differen ITO properties due to the different template for growth. This effect is not noticeable for the two other ITOs

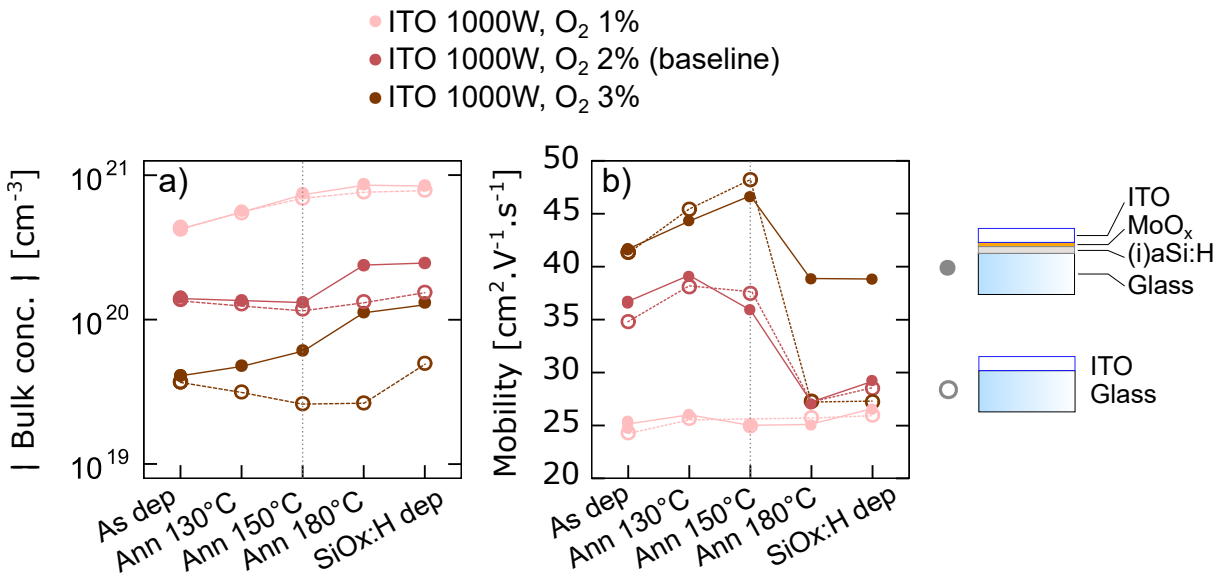

Figure 5.14: Hall measurement of the different ITOs bulk carrier concentration and mobility, under consecutive annealings and SiO_x:H deposition. Lines are guides for the eye only, and do not represent experimental data.

probably because the change in carrier concentration is small compared to their initial doping. On this temperature range, mobility globally increases as expected for the less-doped-ITO-based samples. It remains low for the highest doped one, evidencing that the latter mobility is limited by ionized impurities scattering. The elevated carrier density of this ITO could also induce micro-structural changes that impede the mobility too. Above 150 °C, the carrier concentration increases in a steeper way while mobility is drastically reduced, marking the second phase. Again, the changes are not noticeable for the highest doped ITO for the same aforementioned reasons. The SiO_x:H deposition does not seem to strongly influence the 180 °C-annealed-ITO carrier concentration neither mobility. The significant concentration increase —compared this particular sample carrier concentration— of the lowest doped bare ITO could be both attributed to annealing or H influence, and no clear conclusion can be drawn without additional data. The investigation of the same stack without the MoO_{3-x} layer or without the (*i*)a-Si:H layer would help isolating the causes.

In conclusion, investigation of the electrical properties suggested that H effusion through the full contact stack or O exchange is likely to occur from temperatures as low as 130 °C. From the as deposited state to around 150 °C, annealing is favourable for reducing ITO resistivity —both carrier concentration and mobility increase— while above 150 °C mobility drops. SiO_x:H deposition did not show to degrade the properties more than an annealing at 180 °C. The *FF* drop we observed on MoO_{3-x}-based solar cells could then be explained by the H effusion, which is known to strongly affect MoO_{3-x} performances as a hole selective contact.

5.4.4 Results on solar devices and discussion

According to the previous results and because MoO_{3-x}-based solar cells hardly withstand annealing temperatures above 130 °C, SiO_x:H as DARC applied to such cells should be deposited at temperatures under 130 °C, and eventually H should be removed from the recipe to help improving such devices performances. Yet, it is not possible to conclude on a possible harmful H flow influence from the SiO_x:H deposition on the solar cells under 180 °C at that stage. To verify conclusions of the previous paragraph and probe the H influence, we processed identical 4-nm-MoO_{3-x}-based solar cells integrating a baseline 40-nm-thick ITO, on top of which we deposited SiO_x:H as DARC with the standard recipe (see experimental details section) using temperatures of 70 °C, 100 °C, 130 °C, and one recipe at 100 °C removing the H_2 flow —the process is however not completely H-free due to the presence of SiH_4 precursor. An electron-beam-deposited SiO_x was added as a reference of H-free and plasma-free SiO_x deposition process. Fig. 5.15 presents the electrical performances of the processed solar cells, before and after SiO_x:H deposition. The performances of solar cells prior to SiO_x:H deposition were again well below their usual values, probably due to higher humidity rate in the ITO deposition chamber. Comparing before and after SiO_x deposition, the e-beam-evaporated reference device exhibits a slight V_{OC} and *FF* decrease (2 mV and 0.4 $\%_{absolute}$ respectively), and a J_{SC} increase of 0.4 mA cm^{-2} resulting in equal efficiency between the two steps. The *FF* diminution could stem from wafer overheating during deposition —and thus H effusion through MoO_{3-x}— or the impact of X-rays. All the other samples, including the SiO_x recipe without the H_2 flow, performed worse after the DARC deposition. The global J_{SC} increase by around 0.7 mA cm^{-2} is in line with the experimental current density gain calculated for 40-nm-thick ITO in previous section. For the process without H_2, the solar cells undergo the lowest *FF* —yet still significant— and V_{OC} reduction (1 $\%_{absolute}$ and 8 mV respectively), and displays considerably better performances than its 100 °C-hydrogenated counterpart. This result underlines that H_2 flow plays an important role in the solar cell degradation, and that an H diffusion in the hole contact from the upper SiO_x:H layer might occur in addition to possible H effusion from the (*i*)a-Si:H. Increasing SiO_x:H temperature deposition worsens the performance of the devices with the DARC treatment (not showed here).

Recent preliminary results of 80-nm-thick evaporated MgF_2 used as DARC provided a J_{SC} gain of 0.6 mA cm^{-2} without damaging the V_{OC} and *FF* of the devices, inducing a gain above 0.4 $\%_{absolute}$ minimum in all the treated devices efficiencies. With such treatment, the present best 2-nm-thick-MoO_{3-x}-based solar cell could reach an efficiency of 23.1%. Following a current forward bias treatment, the same cell efficiency was pushed to the remarkable value of 23.5%.

5.5 Conclusion

As a conclusion, we could show that a lower sputtering power during ITO deposition (600 W) did not help preserving iV_{OC} of the devices after this step. Yet, this low power ITO presented

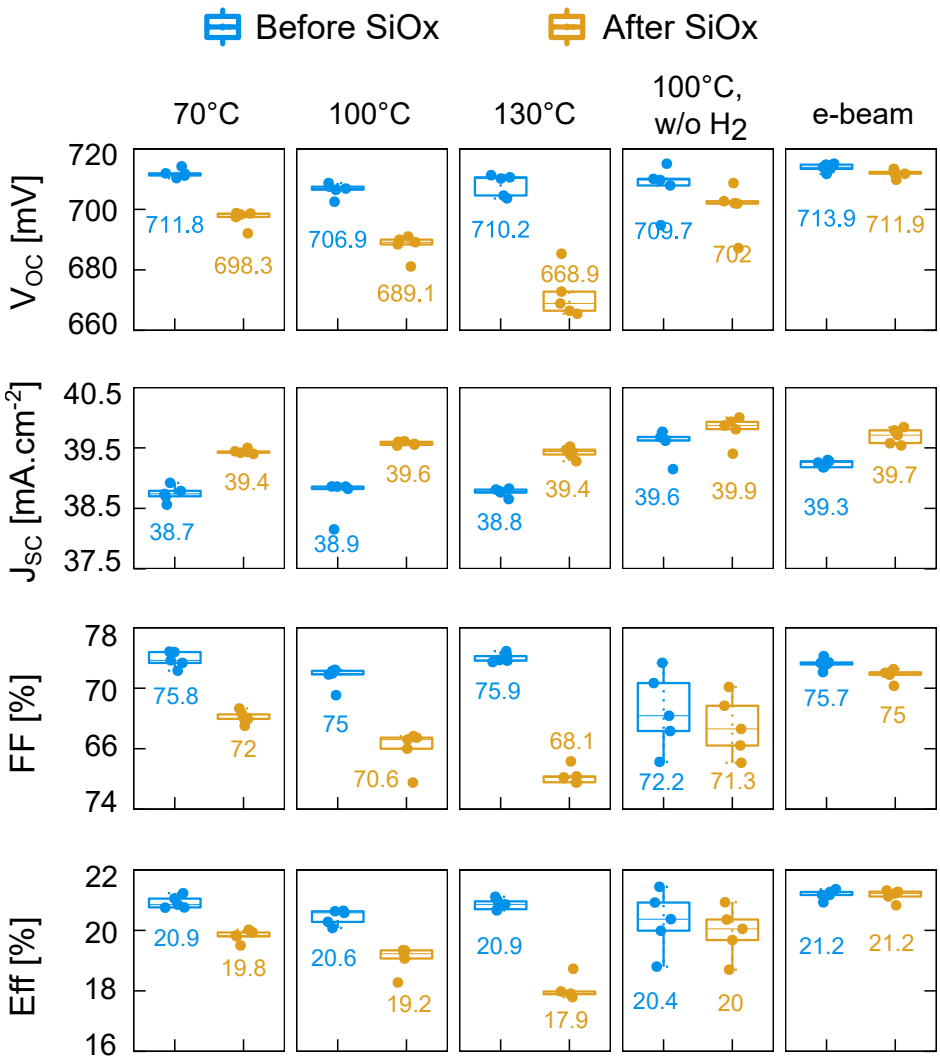

Figure 5.15: Electrical parameters of MoO_{3-x}-based SHJ before and after the PECVD deposition of SiO_x as a DARC.

lower resistivity compared to our baseline ITO deposited at 1000 W while remarkably conserving similar optical properties than the latter, apparently due to a different crystallographic structure. Combination of these two properties could lead to a 1 $\%_{absolute}$ improvement in *FF* of MoO_{3-x}-based solar cells.

Influence of ITO work function on the contacts electrical performances with different MoO_{3-x} thicknesses was also highlighted and quantified through *J-V* fit with an equation developed by Roe *et al.*. We could additionally estimate the work function of the hole contact to be above 5 eV when integrating more than 2 nm of MoO_{3-x}, and the one of ITOs with different dopings, thanks to dedicated samples, ranging from 4.6 eV to 4.8 eV. At the present time, the method has limitations and more studies are necessary to validate it for more general applications. An appropriate measurement of the contact resistance for each sample could also bring new information about the R_s evolution. It is also worth noticing that the conclusions about the

MoO_{3-x}-based devices efficiencies drop for MoO_{3-x} layers below 4 nm (through V_{OC} and *FF* drop), drawn in Chapter 4, is only valid for damaged wafer precursors. We could indeed obtain excellent V_{OC} of around 713 mV and *FF* around 78 % with the 2-nm-MoO_{3-x}-based devices of the present series, providing efficiencies above 22 % (see Fig. 5.16). For the first time, thanks to the development of an optimized ITO, it was also possible to get around 23 % efficient MoO_{3-x}-based (see Fig. 5.16) devices for numerous solar cells deposited on wafers with ordinary passivation properties (reproducible), while it was limited to 22.5 % on average for such conditions and using a baseline ITO, or above 23 % for wafers with remarkable passivation properties only. Procel *et al.* also highlighted a higher contact resistance dependency on TCO carrier concentration in case of a transport dominated by TAT (see Chapter 7 for more details about this transport mechanism) [Procel 2020]. This approach could be a an interesting path to evaluate the dominant transport mechanism in MoO_{3-x}-based cells and compared to other material-based contacts.

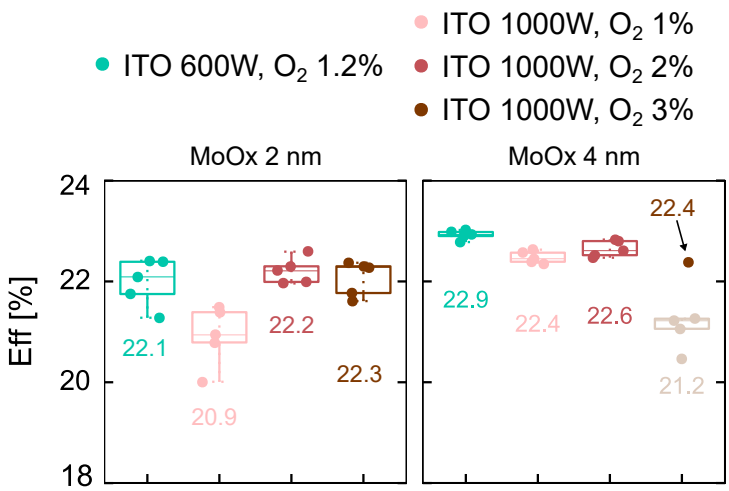

Figure 5.16: Efficiencies of 2-nm- and 4-nm-thick MoO_{3-x}-based SHJ using the different ITOs presented in the first section.

We also tested the application of a DARC, SiO_x:H, commonly used forstandard SHJ, which proved to be harmful for MoO_{3-x}-based SHJ. We measured the electrical properties evolution of ITO under annealings and SiO_x:H deposition to investigate the origin of MoO_{3-x}-based solar cells degradation under such treatment. From the Hall measurement of dedicated samples and solar devices electrical performances, we concluded that presence of H in the plasma during SiO_x:H deposition is detrimental. Our standard SiO_x:H DARC treatment could not be adapted to the MoO_{3-x}-based cells, even with lower temperatures, as it induces a V_{OC} and *FF* reduction which wipes out the J_{SC} gain from optical improvement. Yet, the devices under-performances prior to SiO_x deposition could also bias the present results (e.g. presence of H at the ITO/MoO_{3-x} interface due to humidity), and for instance an experiment combining a low temperature deposition and no H in the recipe should be repeated in proper climatic conditions. A thicker MoO_{3-x} layer, or pre-annealed samples, could also be tested with this

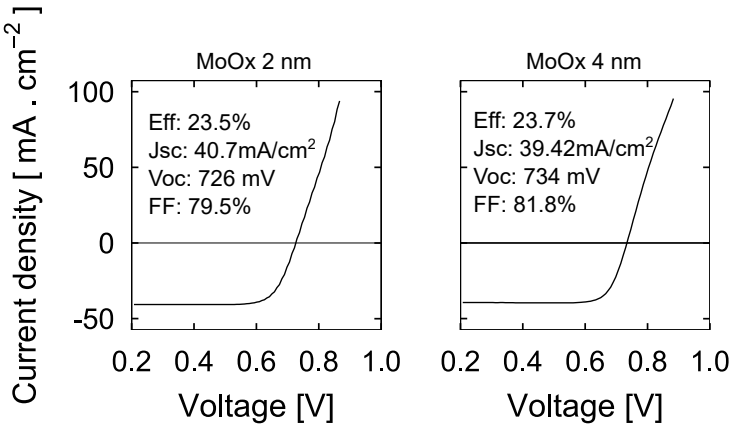

Figure 5.17: *J-V* and electrical parameters of best solar cells obtained in this study.

SiO_x:H recipe. To fully benefit from the DARC coating, the use of SiO_x with no H in the plasma, like an optimized e-beam recipe or PECVD using another precursor than SiH_4, may be preferable for MoO_{3-x}-based solar cells. Even though the use of PECVD-deposited SiO_x:H is more suitable for industry purposes, an evaporated MgF_2 should be preferable for MoO_{3-x}-based SHJ as hilighted by preliminary results.
DARC treatment or ITO optimization are first steps for MoO_{3-x}-based SHJ eventual integration to the field. Yet, before this, solar cells also have to be tested under harsh conditions that could exist outdoors. The next chapter introduces couple of reliability tests as well as first MoO_{3-x}-based SHJ encapsulation into mini-modules.

6 Stability tests of MoO_{3-x}-based SHJ solar cells for field operating conditions

6.1 Abstract

This chapter contains different stability tests for MoO_{3-x}-based SHJ solar cells. Stability towards annealing, air exposure, or more common tests like forward bias and UV-induced degradation are discussed. Annealing temperatures over ~ 150 °C are shown to increase series resistance, likely linked to a selectivity loss. This degradation can be mitigated by a pre-MoO_{3-x}-deposition annealing at temperatures around 250 °C, which seems beneficial to preserve V_{OC} and *FF* during annealing processes from 140 °C to 170 °C. However, too high temperatures for this pre-treatment slightly damages passivation. The solar cells appeared to be quite stable with air exposure over time, presumably thanks to the front ITO protection to reduction from air. Inducing recombinations in the finished device through forward current injection proved to significantly enhance the cells *FF*, for different MoO_{3-x} thicknesses or ITO kind, mainly due to passivation increase. Finally, UV-induced degradation severely damages V_{OC} and *FF*, linked with both passivation and selectivity issues, most probably H-related.

6.2 Motivations

Previous chapters have introduced and presented several variations and analysis of the MoO_{3-x}-based hole contact for SHJ solar cells, focusing on internal physics of the contact stack in standard test conditions. However, such studies do not completely reflect the outdoor conditions they will be subjected to once integrated in the field, and under which they must withstand different effects impacting their performances. Moreover, no study concerning not-Si-based SHJ contacts have been conducted so far in terms of stability to air exposure or response to specific forced conditions, mimicking operations in the field. Testing our MoO_{3-x}-based SHJ solar cells will introduce new experimental data to the reliability research field. It will additionally bring precious information to further understand the behavior of more classical SHJ contacts. In this chapter, we provide a short overview of MoO_{3-x}-based SHJ stability upon annealing and some field-condition-induced degradations.

6.3 Impact of pre- and post-annealings

Experimental data of this section has been produced by Maxim Simmonds during his semester project.

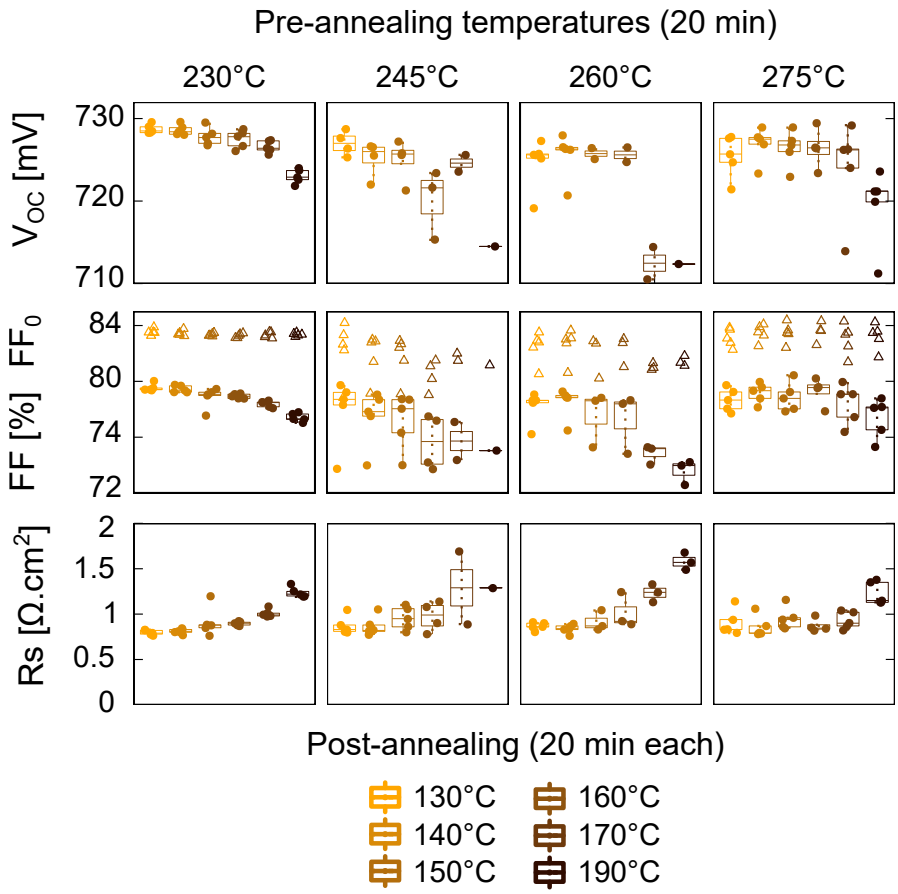

Figure 6.1: V_{OC}, FF, FF_0 and R_s of the four wafers pre-annealed at different temperatures, extracted from J-V characteristics, as a function of post-annealing temperature. Samples pre-annealed at 245 °C and 260 °C were broken during the measurements and data should not be considered as accurate.

The pre-annealing step, that is an annealing of the wafer prior to MoO_{3-x} deposition, was introduced by Essig *et al.* in MoO_{3-x}-based SHJ fabrication couple of years ago [Essig 2018]. The optimal pre-annealing temperature was found to be around 250 °C. The purpose was to partly remove H from the passivating (*i*)a-Si:H layer to avoid a subsequent H effusion into the above MoO_{3-x} layer during the 190 °C post-annealing process. The latter step was indeed required to cure the front low-temperature screen-printed silver paste. A post annealing at this temperature is indeed prone to provoke a MoO_{3-x} chemical reduction that lowers its work function, resulting in a poor hole selectivity. However, even though beneficial, the pre-annealing step slightly damaged the passivation provided by (*i*)a-Si:H and added an extra step in the fabrication process. Improvements in the low temperature silver paste enabled

curing at 130 °C, sufficient to reach high *FF*. We proved that this temperature was low enough to avoid MoO_{3-x} strong reduction, and then get rid of the pre-annealing step (see Chapter 4 and [Dréon 2020]). Yet, the pre-annealing step could still be useful in terms of MoO_{3-x}-based stability with temperatures above-130 °C processes and post-treatments, like encapsulation or new electron selective contact deposition for instance. Indeed, the higher the pre-annealing temperature, the higher the H eviction from the (*i*)a-Si:H layer and the less H effusion in MoO_{3-x} layer.
To examine this dimension and estimate the pre-annealing possible MoO_{3-x}-based SHJ protection towards post-annealings, we prepared four identical wafers with 4 nm of MoO_{3-x}, and as detailed in Chapter 2, each were pre-annealed at a different temperature from 230 °C to 275 °C. Subsequently, they all endured post-annealing series from 130 °C to 190 °C. Electrical parameters extracted from the *J*-*V* curves are plotted in Fig. 6.1. The wafers post-annealed at 245 °C and 260 °C were severely damaged in the middle of the experiment. For this reason, the second part of the measurement (from post-annealing temperatures of 150 °C and 160 °C respectively) cannot be considered accurate.

As a global remark, data of the 230 °C pre-annealed sample is significantly less spread compared to the samples pre-annealed at higher temperatures, an effect which seems to be amplified by increasing the post-annealing temperature as well. This could mean that the (*i*)a-Si:H layer passivation is impacted, inhomogeneously, by pre-annealings from 245 °C and defects impact on V_{OC} and *FF* is exacerbated by post-annealings. Precisely, surface quality becomes critical and should be as good as possible prior to the thermal treatments to avoid drops in V_{OC} and *FF*.
For the lowest-pre-annealing-temperature sample, both V_{OC} and *FF* start to decrease from post-annealing temperature of 140 °C, while its 275 °C-pre-annealed counterpart preserve them until post-annealing temperatures of 160-170 °C. As expected, the latter seems less affected by H effusion thus more resilient to higher temperature processes. FF_0s, extracted with the method described in Chapter 2, show very little degradation (from 83.5 percent to 83.4 percent) throughout the post-annealing treatments, but exhibit a slight improvement of $\sim 0.5\,\%_{absolute}$ (from 83.1 % to 83.6 %) over 130 °C to 160 °C post-annealing, for the samples pre-annealed at the lowest and highest temperatures respectively. On the contrary, R_s is highly impacted by post-annealing temperatures and follows *FF* variation for the two samples. The result suggests that transport might be impeded by contact resistance, possibly due to lower MoO_{3-x} work function, i.e. bigger band mismatch with (*i*)a-Si:H, in which case band to band transport would be disadvantage against TAT (see Chapter 7 for more information about transport processes at and interface) and so a lower hole current. The V_{OC} loss, amounting for around 5 mV for both 230- and 275-pre-annealed samples, also indicates a possibly increased parasitic electron current at the hole contact. At this stage, it is not possible to quantify which loss is the most impacting the contact performances.

6.4 Stability in air over time

Stability in air of finished MoO_{3-x}-based SHJ was evaluated over one year. Fig. 6.2 shows the electrical parameters evolution for not-encapsulated solar cells stored in the dark, gathering contacts with various MoO_{3-x} and (*i*)a-Si:H thicknesses, with and without pre-annealing and with equivalent performances. No difference in stability was observed between the three MoO_{3-x} thicknesses, or the thin and thick (*i*)a-Si:H layer. Among solar cells pre-annealed (columns (a) and (b)), both V_{OC} and *FF* exhibit an impressive stability (identical after one year). The V_{OC} of the devices with the thickest (*i*)a-Si:H (column (b)) is slightly higher than the 6-nm-thick-(*i*)a-Si:H-based ones, while their *FF* is lower, both presumably originating from the thicker (*i*)a-Si:H layer. The not-pre-annealed 4-nm-thick-MoO_{3-x}-based solar cells with a thin (*i*)a-Si:H layer (column (c)) globally have a 2 mV higher V_{OC} compared to their pre-annealed counterpart (column (a)) probably due to the aforementioned effects of pre-annealing on the passivation. They manifest a tiny V_{OC} degradation (0.6 mV) and *FF* increase (0.1 $\%_{absolute}$), which both fall in the instrument error range. For all devices, the difference in J_{SC} stem from a recalibration of our *J-V* measurement instrument, between the first and the second measurement, which accounted for a ~ 0.8 $mA\,cm^{-2}$ loss and correspond to the present J_{SC} loss. Finally, the lowered efficiency is only due to the instrument recalibration between the two measurements, amounting for 2 $\%_{relative}$ for the pre-annealed samples. Yet, the not pre-annealed samples exhibit an efficiency loss of 3 $\%_{relative}$, while the J_{SC} loss corresponds to 1.3 $\%_{relative}$ only, a result which is not explained at present.

6.5 Effects of forward bias

Once mounted in the field, solar modules will endure long term sunlight. Light soaking imitates this condition by illuminating the sample under AM1.5g (1 sun) at 50 °C, however, in general, at open circuit. Solar devices performances involving a-Si:H can be improved or degraded following complex H diffusion mechanisms [Stabler 1977, Plagwitz 2008, De Wolf 2011, Mahtani 2013, El Mhamdi 2014, Lee 2016, Kobayashi 2016a, Kobayashi 2017]. Cattin *et al.* highlighted that mechanisms provoked by light soaking could be separated into independent positive (injection related) and negative (light related) effects on the cell performance [Cattin 2021]. The beneficial effect would be mainly ascribed to high minority carrier injection from the bulk to the contacts that promotes H diffusion from the bulk to the the interfaces [Kobayashi 2016a, Cattin 2021]. The creation of an electric field induced by the selective layer band bending was also mentioned. A carrier injection can also be produced by the application of a forward bias in the dark, and Kobayashi *et al.* proved that such treatment at least equals the light soaking benefits [Kobayashi 2016a]. A *FF* and V_{OC} increase of 0.6 $\%_{absolute}$ and 5 mV were respectively obtained on standard (*p*)a-Si:H-based SHJ [Cattin 2019].
Since the forward bias treatment seems to provide light soaking advantages without the negative impact, we test the forward bias treatment on not-pre-annealed 4-nm-thick MoO_{3-x}-based SHJ solar cells prepared as in Chapter 2, and using the ITO deposited at low power (developed in Chapter 5), to examine their response and compare with the standard SHJs. Contrary

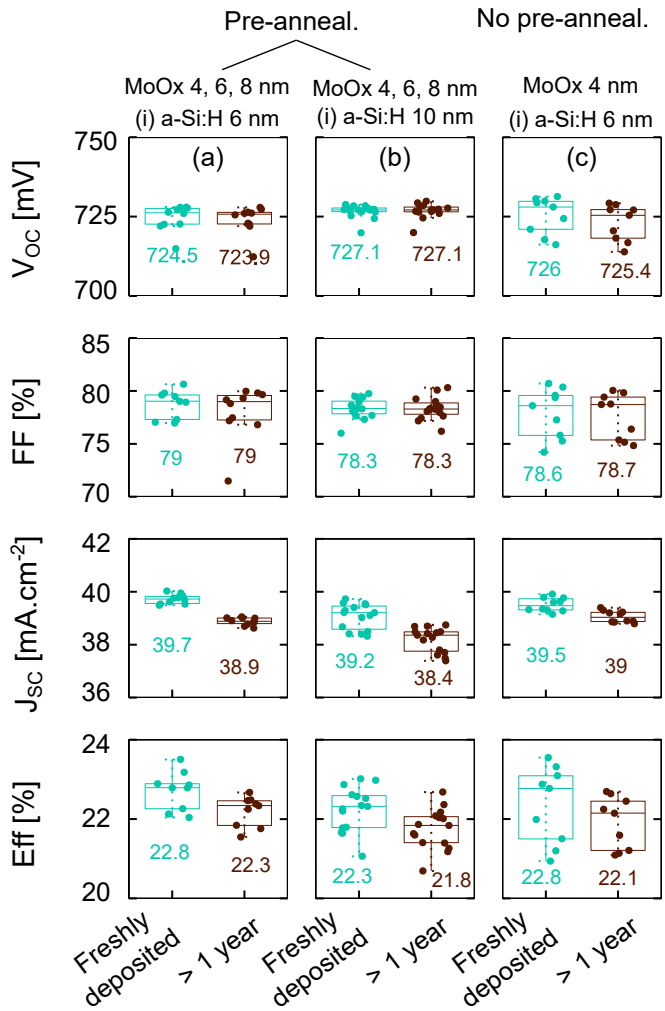

Figure 6.2: Stability of various MoO_{3-x} solar cells over time. The J_{SC} difference stems from a measurement instrument recalibration amounting for a 0.8 mA cm^{-2} loss.

to (*p*)a-Si:H- based selective contacts, the hydrogen movement could invade the MoO_{3-x} layer and harm its work function (see previous section), impacting *FF* and V_{OC} instead of improving them. To force the devices in forward bias, we sandwiched the MoO_{3-x}-based solar cells between two aluminum foil contacts, to which we applied a forward current density of 40 mA cm^{-2} —corresponding to the carrier injection level obtained under open circuit condition and AM1.5g illumination— using *TPAE IC-triple* power supplies, during one week. The sample temperature was not controlled, but measurements indicated a heating around 30 °C.

Fig. 6.3 shows the electrical parameters extracted from the devices *J*-*V* characteristics. An increase of 3.5 mV and a significant improvement of 1.3 $\%_{absolute}$ for V_{OC} and *FF* respectively is observed following the forward bias exposition for all solar cells, resulting in a 0.6 $\%_{absolute}$ gain in efficiency. The present *FF* increase is more than twice higher than that recorded for the aforementioned (*p*)a-Si:H-based devices, and equivalent to the enhancement observed

for a 30-nm-thick (*p*)μc-Si:H-based device with thin (*i*)a-Si:H (7.2 nm) layers [Cattin 2021]. Most of the *FF* improvement (1.1 $\%_{absolute}$) comes from the FF_0 increase, that we ascribe to a passivation amelioration according to literature. The remaining 0.2 $\%_{absolute}$ could be due to a slightly better selectivity, for which further analysis is required to properly conclude. Since both MoO_{3-x}-based and (*p*)a-Si:H-based devices performances are enhanced, the origin of the improvement is probably common in the two devices. Yet, the first ones improve more than the second ones, hence the (*p*)a-Si:H layer or (*p*)a-Si:H/(*i*)a-Si:H interfaces are not involved in the enhancement process. It also means that the key effect of such forward bias treatment is correlated to the (*i*)a-Si:H/c-Si interface. The fact that MoO_{3-x}-based SHJs are (superiorly) enhanced by a forward bias treatment and did not degrade proves that H does not diffuse in the MoO_{3-x} layer. It could mean that the H diffusion is stopped at the MoO_{3-x} surface, restrained by the defective SiO_x layer formed between (*i*)a-Si:H and MoO_{3-x} for instance (see Chapter 3), or does not involve H at all. According to the first section of this chapter, and in the case of H would be involved in the forward-bias-induced process, it would imply that H diffusion is less massive in the case of forward bias than for thermal treatments, since H is likely to diffuse into MoO_{3-x} and degrades it in the latter process. A complementary analysis of *J*-*V* characteristics S-shapes is proposed in Chapter 7. Forward bias was also applied on 2-nm-thick MoO_{3-x}-based cells from the previous chapter series. Contrary to the (*p*)a-Si:H-based samples case when thinner layers are used, the same *FF* improvements and a higher V_{OC} gain of around 10 mV than their 4-nm-thick counterpart were obtained. MoO_{3-x}-based solar cells integrating the baseline high power ITO also showed the same improvements than the present samples.

After eight months stored in the air (and dark), V_{OC} and *FF* partially lost their augmentation obtained with forward bias. The loss comes by half from FF_0 decrease, supposedly originating from passivation. The second part does not come from an R_s increase (not shown here) neither. Results from another experiment showed that the loss was not recovered by a second forward bias treatment, so far not explained.

6.6 Stability towards encapsulation and UV-induced degradation

For long term operation in the field, solar devices have to be encapsulated into modules to withstand the various meteorological events. For modules fabrication, SHJ solar cells are embedded into polymer foils (the encapsulant) sandwiched in a front-side glass sheet and rear-side glass or plastic sheet by lamination. Another outdoor parameter prone to degrade solar cells is the UV light part of the solar spectrum, expending from 250 nm to 380 nm. Until the recent use of fully-UV-transparent encapsulants, UV degradation was related to the poly(ethylene-co-vinyl acetate) (EVA) —UV-absorbent widely used polymer encapsulants— transmittance decrease [Pern 1991]. Yet, performances of PERC, n-PERT and standard SHJ solar cells and modules incorporating UV-transparent encapsulants were not transmittance-limited but were impacted by UV light. While the Al-BSF technology is insensitive, UV degradation is likely to

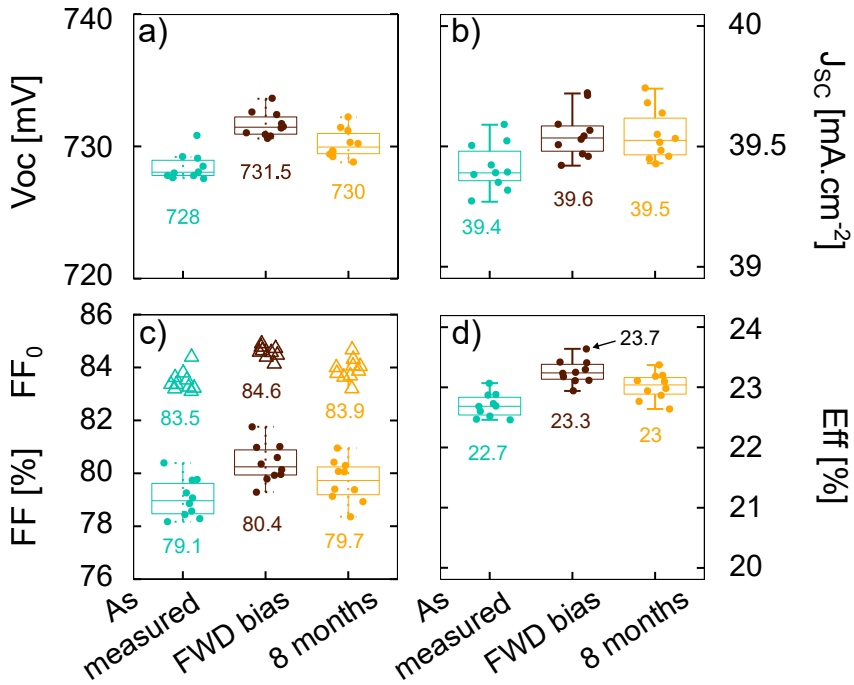

Figure 6.3: Electrical parameters of 4-nm-thick MoO_{3-x}-based SHJ before, after and height months after a forward bias treatment imposing a forward current density of 40 mA cm^{-2}.

cause 2.5 $\%_{relative}$ to 6 $\%_{relative}$, 1 $\%_{relative}$ to 15 $\%_{relative}$ and 8 $\%_{relative}$ to 13 $\%_{relative}$ efficiency losses for PERC, n-PERT and SHJ, respectively [Witteck 2017b, Witteck 2017a, Sinha 2021]. Losses in PERC and n-PERT cells were mainly due to J_{SC} decrease, while it was mostly coming from V_{OC} and *FF* degradation in standard SHJ cells and PERT cells involving an hydrogenated SiN_x passivation layer, which showed the strongest degradations for both. For the latter architectures, the degradation is attributed to UV photons ranging from 280 nm to 400 nm, and whose energy is high enough to deteriorate the Si-H bond (energy around 3.5 eV, corresponding to a wavelength of 360 nm). It would facilitate the increase in dangling bond density at the interface and, in turn, recombinations [Witteck 2017a]. Part of the *FF* loss was also ascribed to ITO sheet resistance increase.

In the present study, we tracked the evolution of MoO_{3-x}-based SHJ electrical parameters through encapsulation process steps and UV-induced degradation. Two wafers of five 4x4 cm^2 solar cells each were co-processed to fabricate the front hole contacts with (*i*)a-Si:H and MoO_{3-x} layers of 6 nm and 4 nm respectively, as described in Chapter 2, and with no pre-annealing. To compare the UV light influence on TCO, an ITO was deposited with our standard recipe (deposition power of 1000 W, carrier concentration of $\sim 1 \times 10^{20}$ cm^{-3}, polycrystalline) on one wafer, while the low power ITO (deposition power of 600 W, carrier concentration of $\sim 3 \times 10^{20}$ cm^{-3}, amorphous) was deposited on the second wafer (see Chapter 5 for more information about the ITO properties and deposition). Both TCOs were 50 nm-thick.

For the encapsulation, the final wafers were cut by hand with a diamond scraper to isolate

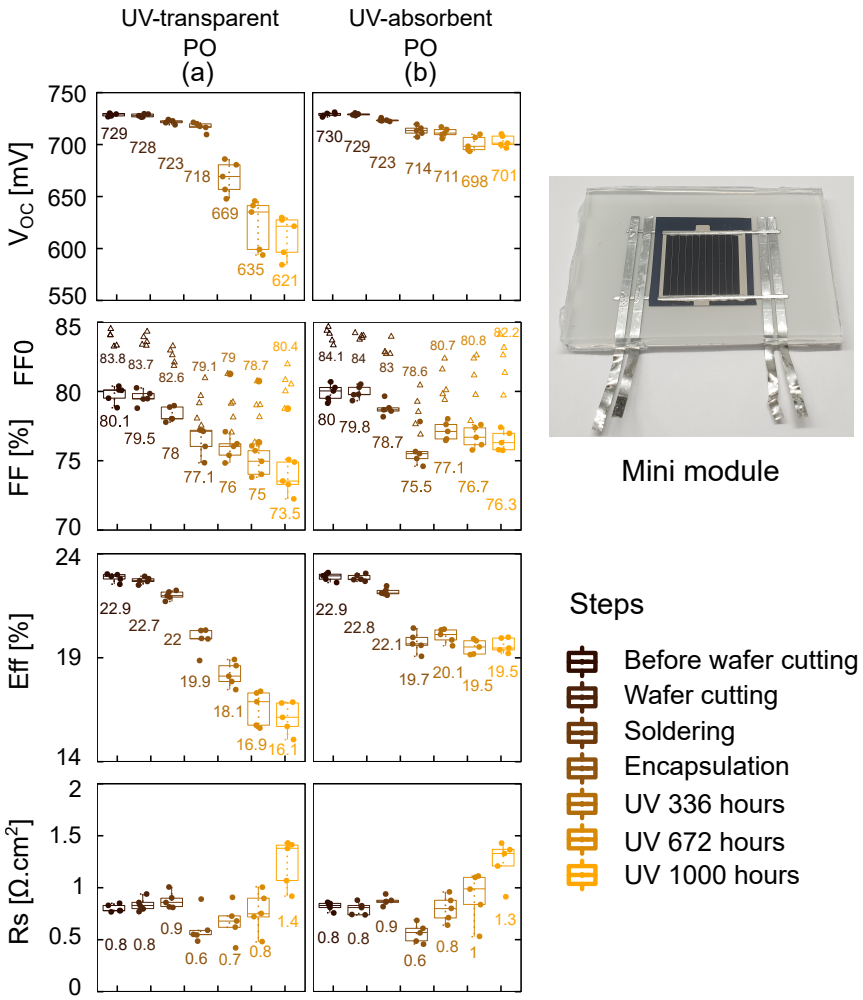

Figure 6.4: Electrical parameters box-plots evolution the different modules before and after encapsulation, and UV degradation through time. Modules encapsulated with the UV-transparent(UV-absorbent) polymer is shown on the left(right) column.

each solar cells. Ribbons with a Cu core and and external PbSnAg alloy (62%, 36% and 2% respectively) were soldered on the solar cells busbars with a low temperature Ag paste and cured at 80 °C for 45 min. They were then encapsulated in UV-transparent poly-olefin (PO)(unknown properties, from commissariat à l'énergie atomique et aux énergies alternatives (CEA)) and standard UV-absorbent PO (PO8510, thickness of 0.69 mm, water vapor transmission rate of 5.5 $g\,m^{-2}\,d^{-1}$ and electrical bulk resistivity of $1 \times 10^{14}\,\Omega\,cm$) with UV-cutoff wavelength of 333 nm and 383 nm, respectively (see Fig. D.1 in appendix) in a glass/backsheet configuration through a lamination process at 155 °C to 160 °C during 15 min. The glass is a solar grade soda-lime 3.2-mm-thick layer, with an optical transmission of 93.6 ± 0.5 % over 300-1200 nm (ISO 9050), and the backsheet polymer is a three-layer composite made of Tedlar (PVF, polyvinyl-fluoride)-PET (polyethylene terephthalate)-Tedlar. In that way, modules with the standard encapsulant will be partially protected from UV light and used for a comparison with

the ones integrating its UV-transparent counterpart. Solar cells were separated so that the two different encapsulants were used on both of the ITOs. A picture of the resulting mini-modules is shown in Fig. 6.4.

Electrical parameters evolution through the process steps, shown in Fig. 6.4, globally highlight that the encapsulation process of MoO_{3-x}-based cells is responsible for a strong degradation. The wafer cutting —for solar cell separation— barely affects V_{OC} and *FF*. During the soldering step, both are significantly reduced by 5 mV and around 1.3 $\%_{absolute}$, respectively. Around 1 $\%_{absolute}$ (corresponding to the FF_0 decrease) of the *FF* loss mostly comes from a passivation degradation, possibly induced by defects created during the wafer hand-cutting and exacerbated by the soldering thermal curing. The remaining 0.3 $\%_{absolute}$ can be attributed to the 0.1 $\Omega\,cm^2$ increase, since a 0.2 $\Omega\,cm^2$ increase approximately corresponds to a 1 $\%_{absolute}$ *FF* reduction [Pysch 2007]. After encapsulation, the FF_0 suffers another 3.5 $\%_{absolute}$ and 4.4 $\%_{absolute}$ drastic loss for the two encapsulants respectively, that we link to the temperature and physical pressure endured by the modules during lamination. Even though significant, the *FF* reduction (~ 1.5 $\%_{absolute}$ to 3.2 $\%_{absolute}$ respectively) is lower than the FF_0 one, which is explained by a R_s improvement (0.3 $\Omega\,cm^2$ decrease). The latter may be due to further curing of the solar cells screen printing Ag paste, as well as ribbons solders. At that step, the J_{SC} is also dramatically decreased by 3 $mA\,cm^{-2}$ for both encapsulants, as shown in Fig. 6.5, and around 5-10 mV decrease in V_{OC}. The former is mostly due to reflections in the front glass, which impacts the whole spectrum as shown in Fig. 6.5. The FF_0 loss follows the V_{OC} decrease.

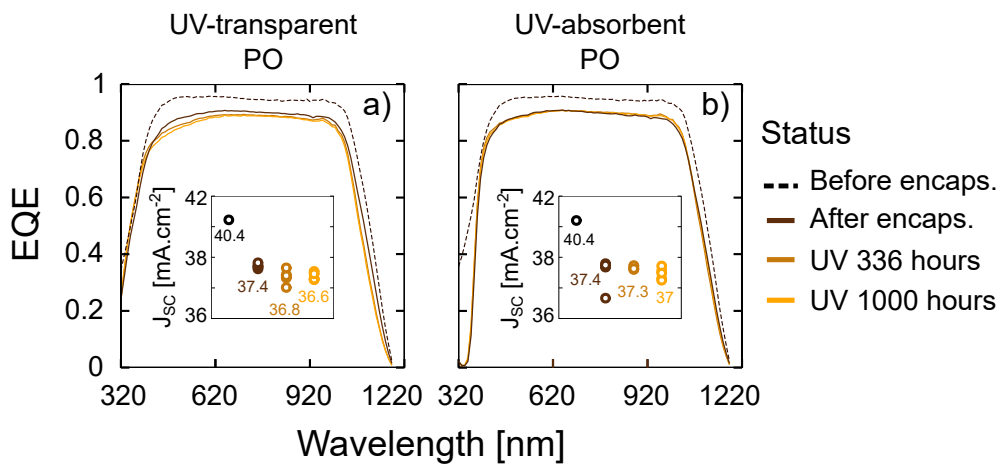

Figure 6.5: EQE and extracted J_{SC} of the different modules before and after encapsulation, and UV degradation through time. The extracted J_{SC} calculation does not include the front silver grid shadowing. J_{SC} after wafer cutting and soldering was identical to the initial one.

Specifications about the UV-induced degradation and chamber parameters are detailed in Chapter 2, section 2.3.14. Results are shown in Fig. 6.4. During the UV degradation, modules with the two different encapsulants showed distinct *FF* evolution and soften V_{OC} decrease for the standard UV-absorbent encapsulant. In both cases, the FF_0 is improved, particularly for modules with the UV-absorbent encapsulant, indicating a passivation improvement. This

possibly originates from a passivation recovery induced by a UV-free light soaking, proved to provide equivalent improvement than a forward bias treatment [Cattin 2021].
In the case of the UV-transparent PO, a UV exposition of 672 h severely damages *FF* and V_{OC} by 2.1 $\%_{absolute}$ and 77 mV respectively while FF_0 remained quite constant. 1 $\%_{absolute}$ of the *FF* loss can be ascribed to the R_s increase of 0.2 $\Omega\,cm^2$. R_s could rise following an increased TCO sheet resistance, according to literature. We exposed the two ITOs, deposited on a glass sample and placed under the same glass sheet as the modules, to the same UV treatment during 328 h and observed a minor sheet resistance decrease, which does not explain the R_s rise. The R_s shift could then be related to selectivity issues, involving a contact resistance increase for instance, or eventually an increase in the MoO_{3-x} layer resistivity, even though the R_s boost might be too strong to be explained by the latter. Considering that the UV-absorbent (right box-plot) FF_0 significantly increases while the UV-transparent remains constant —during the first 672 h—, we propose that two phenomena are competing here. One improves performance (FF_0 increase) (present in both cases) and one degrades FF_0 through a drastic V_{OC} decline, linked to UV light passing through the encapsulant and reaching the solar cell. This is thought to stem from the aforementioned passivation related to the Si-H bond breakage, according to literature. In the case of MoO_{3-x}-based cells, the freed H could also diffuse to the MoO_{3-x} layer and additionally impact selectivity. The latter loss would then be related to higher parasitic electron current at the hole contact (see Chapter 4), strongly impacting V_{OC} without affecting R_s. It is also possible that MoO_{3-x}-based cells are more sensitive to UV degradation than their (*p*)a-Si:H-based counterpart since the latter absorbs more UV, preventing the (*i*)a-Si:H passivation layer UV radiation degradation. MoO_{3-x} is also known to change composition under UV light (photochromism), for which the two mostly accepted mechanisms are intervalence-charge transition (involving H protons) and small polarons absorption [He 2003, Faughnan 1975, Granqvist 1995]. All these hypothesis need supplementary data about UV-induced degradation of our standard mini-modules (*p*)a-Si:H-based SHJ for comparison. In the UV-absorbent encapsulant case, the V_{OC} is slightly decreased —over the whole UV treatment— by around 10 mV, and FF_0 and *FF* increase by 2.1 $\%_{absolute}$ 1.6 $\%_{absolute}$ respectively, between the encapsulation final step and a 336-h UV exposure. The V_{OC} decrease suggests that some UV light may still reach the solar cell surface, despite the UV screen provided by the front polymer. Yet, these modules suffer from the same severe R_s increase as their UV-transparent-based counterparts, limiting the *FF* full improvement potential. This observation, affecting both module types, evidences that the R_s-related selectivity decrease is not caused by UV light. After 1000 h of UV exposure, R_s strongly increases, while passivation increase (probable recovery from encapsulation damages) and selectivity decrease are still competing for both module types.

The EQEs plotted in Fig. 6.5 show that the UV-transparent-based samples are affected by the UV treatment in the blue part of the spectrum, while the UV-absorbent-based ones are not. The weaker EQE response in this region of the spectrum indicates a collection issue on the front side, and could be related to the previously discussed FF_0 decrease in the UV-

transparent case. In the former case, the EQE response in the visible and near IR response is also slightly affected, probably related to the MoO_{3-x} photochromism. The J_{SC} extracted from these measurements is decreased by 2.1 % and 1.1 % in the UV-transparent and UV- absorbent cases respectively, which is higher than the one reported for standard a-Si:H-based SHJ large modules (0.2 %) [Sinha 2021].
To summarize, three main mechanisms may occur in the MoO_{3-x}-based SHJ devices during the UV-induced degradation.

1. **UV-induced passivation degradation**
   A passivation decrease mechanism, induced by UV radiations, provokes a significant V_{OC} decline —and so FF_0— without increasing R_s, most probably because of Si-H breaking and dangling bond density increase, according to literature. Eventually, in MoO_{3-x}-specific case, a selectivity loss originating from (*i*)a-Si:H-UV-freed H migration in the MoO_{3-x} layer, or photochromic properties of the later, could also explain the V_{OC} decrease. It could provoke an increase in the parasitic electron current at the hole contact through the MoO_{3-x} work function reduction.

2. **UV independent selectivity decrease**
   A second mechanism, linked to a selectivity decrease but independent from UV radiation, drastically increases R_s and affects FF without influencing V_{OC}. In that case, the R_s increase could vouch for a majority hole current —at the hole contact— decrease. Yet, the reasons are still not clear but they could be linked to the MoO_{3-x} work function reduction as well, which also impedes the hole extraction (see Chapter 4).

3. **Passivation improvement**
   Finally, a passivation increase, linked to beneficial effects of UV-free radiation light soaking, compensates or overcompensates the passivation and selectivity decrease. The increase could also be due to the soft annealing recovery effect (chamber air temperature set at 65 °C). The present samples, strongly damaged during the encapsulation process, do not allow to conclude properly on this last aspect.

In conclusion, the encapsulation process more likely affects passivation while UV-induced degradation affects both selectivity and passivation. The handling processes might provoke lots of defects inside the solar cells layers, whose impact may be exacerbate during thermal treatments and UV-treatment. Less harsh cutting and soldering processes, so far not optimized for mini-module fabrication, should be used to investigate the encapsulation and UV-induced degradation impact more accurately. During this work, no clear correlation was found between the two ITOs, yet the poor statistics does not allow to conclude accurately on their potential influence under UV exposure.

6.7 Conclusion

This chapter groups different stability studies of MoO_{3-x}-based SHJ, led for the first time on such devices. The first one, examining pre- and post-annealing influence, suggests that a pre-annealing at 230 °C is preferred for processes or post processes involving a temperature below 140 °C. Otherwise, a 275 °C-pre-annealing step should be used for processes above ~ 160-170 °C, without which a selectivity loss is expected. The other tests, gathering stability in air, forward bias and UV-induced degradation, are more commonly used in reliability testing. MoO_{3-x}-based cells showed to be stable with time, in the dark and ambient air, probably protected be the above ITO layer. The forward bias treatment unexpectedly showed a significant *FF* improvement, which was superior to the (*p*)a-Si:H-based SHJ case. The improvement was independent of the MoO_{3-x} layer thickness (same improvement for the 2-nm-thick MoO_{3-x}-based samples). Finally, the UV-induced degradation exhibited interesting preliminary results involving both passivation and selectivity issues under UV irradiation. A comparative study with similar mini-modules (*p*)a-Si:H-based SHJ, or ITO sheet resistance evolution under longer UV treatment would be meaningful to address some of the remaining interrogations. The encapsulation process degradation is mostly due to damaged passivation ascribed to the not-optimized mini-module fabrication process.
These analysis all highlighted that various physical mechanisms may occur, mainly involving hydrogen, such as MoO_{3-x} chemical reduction or H migration to the interfaces, influencing passivation, selectivity, and transport. Their influence on electrical parameters is still not well understood, since it is hard to decorrelate between (chemical) passivation and selectivity influence. More detailed transport analysis could bring a valuable information to shed light on the phenomena at stake. The next chapter will make a start on this by looking at transport fundamental mechanisms and S-shapes in *J*-*V* characteristics, oftentimes occurring outside of the active quadrant.

7 Temperature-dependent measurements and S-shape exploration for transport analysis

7.1 Abstract

This chapter proposes novel analysis and characterization methods which provide new insight, or/and confirms previous results, on transport in MoO_{3-x}-based SHJ solar cells. We first remind the main transport mechanisms that exist in semiconductors or at the interface of silicon heterojunctions and narrow band or polar compounds semiconductors, as rudiments for present and future work. A low temperature *J-V* characterization, rarely used in the field of photovoltaics, based on V_{OC} saturation and *FF* decrease under cooling is then presented. We use the method for the first time on a not-Si-based (MoO_{3-x}) SHJ selective contact to compare the V_{OC} and *FF* evolution with temperature to previous —but sparse— results obtained on standard SHJ (a-Si:H-based selective contacts). With MoO_{3-x}-based hole selective contact, the solar cells exhibit a similar behavior than the standard SHJ. We also spot a singular J_{SC} behavior that may be related to predominant recombination mechanism over a specific temperature range. Finally, we introduce a method to characterize solar cells S-shaped *J-V* curves features, based on Roe *et al.* model that we extend to develop a fast transport examination. The method strives for selectivity investigation and is used to further analyse previous conclusions drawn about MoO_{3-x} and a-Si:H layer thickness variations, effects of pre- and post-annealing or forward bias treatment. The results suggest a possible decorrelation between contact selectivity and carrier selectivity. Yet, the method remains exploratory and this work is limited to preliminary qualitative conclusions. However, it sets the basis for promising future generalization and could be reinforced by further calculation to extract the S-shapes features quantitatively.

7.2 Motivations

In previous chapters, the solar cells integrating MoO_{3-x}-based contact performances were analysed by comparing common parameters in standard test conditions (STC, 25 °C) and studying their evolution with different layer stacks properties, or under stability tests. Yet, a

full understanding of the contact was not obtained. In particular, the precise mechanisms of transport through the full contact stack are not elucidated. Temperature-dependent measurements are commonly used in semiconductor physics for dominant transport determination since most of the mechanisms follow specific laws in temperature. In the field of solar cell, temperature-dependent *J-V* measurement are mostly performed above 25 °C to determine temperature coefficients. Even though rare publications report on *J-V* measurement at very low temperatures, the existing literature (particularly on SHJ) reveals interesting comportment of solar cells parameters that could be used to interpret the physics operating in the contacts. Silicon heterojunction solar cells using materials other than Si as contacts have never been probed at such temperatures. Performing measurements of this kind could bring broader insight and comparative data to this type of characterization, as well as possibly clarify transport mechanisms at stake in alternative contacts. Moreover, most of the SHJ PV literature has focused on carrier transport in c-Si and a-Si:H, and finding information on transport existing in alternative-material-based SHJ is not obvious.
Therefore, as a basis for the present study and for future work, we shortly summarize here the main transport mechanisms occurring in crystalline and amorphous semiconductors, but also mechanisms that can additionally exist in less classical materials. For this second aspect, we center the literature review on polar and/or narrow band semiconductors such as transition metal oxides, which are of particular interest in this thesis work. To further investigate the MoO_{3-x}-based contact features, and to contribute to the development of the low-temperature characterization, we performed MoO_{3-x}-based SHJ solar cells measurements at temperatures from −160 °C to 80 °C (115 K to 355 K). Another (widely) investigated method to figure out contact transport issues lies in the analysis of S-shapes, visible in some *J-V* curves like in our MoO_{3-x}-based devices characteristics. Even though still subject to interrogations, the abundance of modelizations provides useful information about carrier transport in the contacts. Yet, it can be time consuming as it generally involves many parameters which can lead to overfitting and/or non-physical fits. In this work, we propose a fast graphical method, complementary to the other existing ones, by using the *J-V* derivative as an extension of the model elaborated by Roe *et al.*. The method is tested with data analyzed in previous chapters to extract additional transport components or consolidate the conclusions drawn.

7.3 Main theory about interface and bulk transport in crystalline, amorphous and narrow band polar compounds semiconductors

Carrier conduction mechanisms, be it through bulk or at interfaces, have a critical influence on solar-device performances and ability to extract charges. Even though we generally use nm-thick layers in this work, when the thickness of the passivating and carrier selective layers is more than 2 nm, carriers will need to cross through the bulk of the material to reach the metal electrodes. Moreover, in view of the defective nature and wide band gap of some of the materials considered here —such as MoO_{3-x}—, the classical band conduction is not expected to be the only mechanism [Goodenough 1971, Roberts 1980, Cox 1992]. For these reasons, this

paragraph aims at reviewing the main bulk mechanisms and their temperature dependency that describe the carrier transport in such layers, as well as the interfacial mechanisms that generally occur at a contact. The different mechanisms listed hereunder are represented in Fig. 7.1.

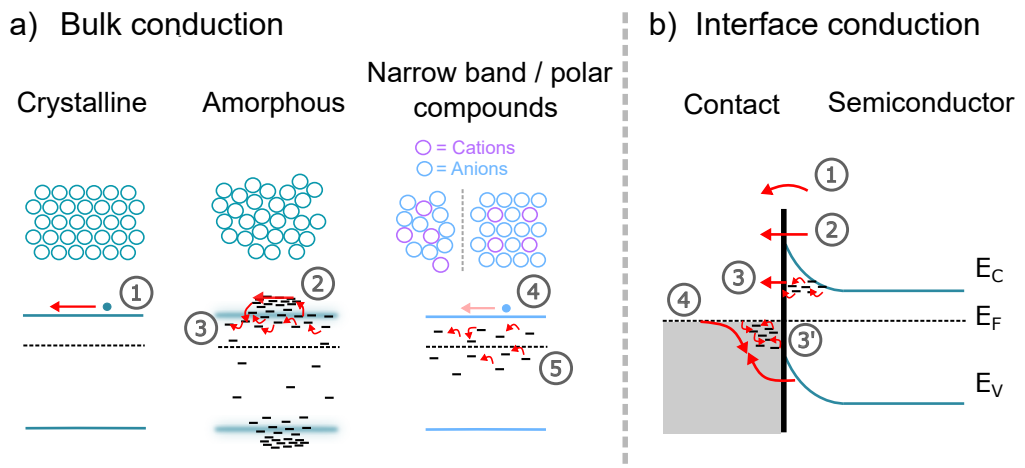

Figure 7.1: The main transport mechanisms that can exist in the materials presented in this review. a): transport through a bulk crystalline or an amorphous semiconductor, and a narrow-band and/or polar semiconductor compound: 1. metallic-like band conduction, 2. conduction through extended defect states, 3. thermally/trap assisted tunneling (TAT) in localized sub-gap defect states, 4. large polaron conduction, 5. hopping of localized polarons. b): possible charge transport at the interface between two materials: 1. thermionic emission, 2. direct tunneling of thermally activated carriers, 3. trap assisted tunnelling (hopping). In case of recombination junctions, additional recombination via 3'. trap assisted tunnelling or/and 4. band to band mechanisms. The main mechanism for interface and bulk transport depends on the material crystallographic structure, doping, temperature, and band alignment.

7.3.1 Bulk transport

In a classical wide-bands crystalline semiconductor, excited carriers move independently —no interaction between them— in the crystal bands as an electron/hole sea, feeling an effective potential. They follow band theory equations of delocalized conduction —drift and diffusion— with occasional scattering effects —rare defects like ionized impurities, lattice vibration— and their effective mass mainly depends on crystal structure. The two classical temperature dependencies of mobility in case of lattice scattering or ionized charge impurities scattering predominance follow $\mu \propto T^{-3/2}$ and $\mu \propto T^{3/2}$ respectively, with μ the mobility and T the temperature.

In amorphous semiconductors, the concentration of defects is large and defect states cannot be considered anymore only as isolated defects with discrete energy levels, but as whole defect bands instead. In those bands, states near the defect states average energy are likely

to be numerous so that atoms orbitals can overlap one another resulting in an extended wave function through the whole solid. In that case, conduction will be delocalized and is called "extended states conduction", similar to crystalline conduction but with many scattering effects —the transport is considered as diffusive only— and carriers have a higher effective mass (lower mobility, activation energy of around half the gap) compared to the crystalline case [Roberts 1980]. States further away from the average energy states, near the band edges, are less numerous and can be considered isolated (Anderson localization). In that case, carriers are trapped in localized states and have to cross an energy barrier to move to surrounding states via thermionic emission, tunnelling or a combination of both. The latter is the most probable to occur (in case of a purely thermionic mechanism, the temperature to reach would be high enough so that the extended state conduction dominates the transport) and is called TAT, known as "hopping" [Cox 1992, Roberts 1980]. This is an important component of transport in amorphous materials. It is characterized by a mobility following the Mott law of variable range hopping [Roberts 1980, Baranovski 2006] for three dimension solids:

$$\mu \propto exp(-(T_0/T)^{1/4}) \tag{7.1}$$

with T_0 a temperature constant characteristic of the system. In case of two-dimension materials, like thin films, the relation becomes:

$$\mu \propto exp(-(T_0/T)^{1/3}) \tag{7.2}$$

TAT predominates at a lower temperature than the extended states conduction, and depends on the extent of localization (degree of disorder relative to the band width). In the limit of a large disorder, all states in the band would be localized while for a small one, the states would be localized only near the band edges. Boundary between localized to delocalized states conduction is sharp and is called the "mobility edge" [Cox 1992].

Conduction in narrow bands and/or polar semiconductor compounds, like some transition-metal oxides, can be of another kind. Because of narrow bands, carriers have a higher effective mass compared with the simple crystal case, making them too slow to cross several lattices during one phonon vibration period. In that case, the charge carrier is not spread over many lattices, and its movement, presence or absence does influence the ions of the surrounding lattice, contrary to band theory case. The carrier causes deformation and/or polarization of the surrounding lattice which acts back on it, resulting in an electron-phonon coupling (quasiparticle) called "polaron" with a higher effective mass than the single carrier [Mott 1974, Roberts 1980]. This phenomenon is important to consider in semiconducting oxides due to strong polar bonding between the metal cations and oxygen [Cox 1992]. Polarization effects can further reduce the width of the bands, and here, we use the term "bare" carriers to evoke properties of the narrow band compounds without the influence of polarization. In case of a coupling energy smaller compared with the band width of the bare carrier (conduction(valence) band for electrons(holes)), the carrier-phonon coupling is averaged over a few

lattices, making the transport delocalized but still affected by polarization. Such quasiparticle is called a “large polaron”, with higher effective mass compared with the bare carrier, and so lower mobilities. When the coupling energy is large compared with the bare carrier band width (generally the case for bands smaller than 3 eV), the carrier is self-trapped —-a trap created by the lattice polarization— in the lattice, and forms a quasiparticle called “small polaron” [Cox 1992]. The traps are localized energy states, through which small polarons can jump via hopping from one to another. Small polaron hopping conduction is characterized by [Roberts 1980]:

$$\mu \propto \frac{1}{T^{\beta}} exp(-E/k_B T) \tag{7.3}$$

with $1 < \beta < 5/2$ due to different regimes of polaron hopping, k_B the Boltzmann constant and E the activation energy for the hopping (generally complicated term). Large and small polaron conduction are two transport mechanism in competition, and it is sometimes hard to distinguish them, like in reduced metal oxides which shows ambivalent behaviors — carrier with high effective masses— indicating strong interaction with lattice (small polaron), but a mobility higher than that expected in that case, more characteristic of large polaron [Goodenough 1971]. At sufficiently high temperatures, the electron-phonon coupling dominates, with small polaron mobility expected to increase with temperature while large polarons one expected to decrease [Cox 1992]. At low enough temperatures, a delocalized band transport called "narrow band conduction" may be privileged [Roberts 1980]. Additionally, presence of defects states originating from crystal imperfections (e.g. amorphous compounds, atom vacancies, impurities, etc.) and small polaron formation are synergistic effects, strongly influencing each other and making small polaron formation possible in compounds with bands even wider than 3 eV [Cox 1992].
Finally, excitons originating from electron-hole coupling (neutral quasiparticle) by Coulomb force, can also be formed when the thermal energy $k_B T$ is less than the exciton binding energy so that the lattice vibration does not impede their formation (generally very low temperatures) [Cox 1992]. Contrary to other kind of transports, such quasiparticles convey energy without conveying charge. Equivalently to polarons, large (Wannier-Mott exciton, delocalized transport) and small (Frenkel exciton, localized transport) exciton can exist, depending on the solid relative permittivity (dielectric constant) and bands width. An intermediate of these two cases is also possible, and is known as “charge transfer exciton”. They have been observed in organic crystals [Lanzani 2012] and in some TMOs like cuprates [Baumeister 1961, Ellis 2008] or TiO_2 [Cox 1992, Baldini 2017]. Yet, this is not a general rule in TMOs, in which they can only exist at very low temperatures because they are strongly disturbed by lattice vibration, and hole-electron coupling is generally lost due to strong interaction of carriers with the lattice [Cox 1992].

The thermally evaporated nm-thin MoO_{3-x} we use as a hole selective contact in this thesis is amorphous and defective. Transport mechanisms related to amorphous structures such as

extended state conduction or TAT through localized states are likely to occur. TAT through the defective states —due to the sub-stoichiometry nature of MoO_{3-x}— can also exist and is possibly the main mechanism responsible for carrier transport in the bulk of the material according to literature. Due to the significant electro-negativity difference between Mo and O, the chemical bond in MoO_{3-x} is likely to be polar. Large polarons or small polarons could then additionally exist and change the nature of transport. So far, no fundamental study have been conducted to verify the nature of dominant transport —delocalized or TAT through disordered, defect or polaron states— in such thin film MoO_{3-x} applied to PV, neither the existence of polarons. Such evaluation are yet highly challenging for thin films stacked with other materials.

7.3.2 Transport at an interface

At an interface between two different materials, carriers generally have to cross an energy barrier. The contact can be ohmic when the *J-V* characteristic of the contact is linear (typically if the resistance to cross the contact is negligible compared with total series resistance of the device, meaning the energy barrier to overcome is low enough so that the voltage drop is negligible), or non ohmic. The two main mechanisms for a carrier to cross an energy barrier are thermionic emission and direct tunnelling, generally both occurring and competing [Sze 1995] (see Fig. 7.1.b)).
In the former case (called TE), carriers are thermally activated so that they can surpass the barrier. The critical parameter for that way of conduction is the barrier height —the barrier shape has no strong influence— defined by the difference between the Fermi level of the carriers at the interface and the maximum energy of the barrier. Thermionic emission can happen when there is negligible drift-diffusion transport in the barrier layer and width of the barrier is thinner than the mean free path of the crossing carriers. For thermionic-emission-dominant transport, the current of carriers follows the law:

$$J = A^* T^2 \exp \frac{-\phi_b}{k_B T} \tag{7.4}$$

with ϕ_b the barrier height and A^* the effective Richardson constant depending on carriers effective mass [Sze 1995].
In case of tunnelling transport ("direct tunnelling" or “field emission”, called DT and FE respectively), the quantum tunnelling probability critically depends on the barrier width at the carrier energy, and carriers’ effective mass, and barrier height in a lower extent. The tunnelling current has a more complex expression compared with thermionic emission, involving the tunnelling probability, Fermi-Dirac distributions and densities of states of each contacting regions. Exact tunnelling current calculation requires analytic computation. Tunnelling is favorized by high carrier concentrations and low temperatures [Sze 1995]. For contacts involving barrier layers around 2 nm, predominance of one or the other mechanisms depends on temperature and carrier concentration. For thermionic emission predominant transport with no or little tunnelling (typically carriers concentration below 10×10^{17} cm^{-3} to 10×10^{18} cm^{-3}

at room temperature), J_0 follows a diode-like equation and remains constant with carrier concentration, and the ideality factor n is around unity. For increasing carrier concentration and/or lower temperatures, tunnelling starts to influence the carrier transport. In that case, J_0 and n increases with carrier concentration and transport is led by both thermal and tunnelling mechanisms (thermionic-field emission, called TFE). Tunnelling predominates the transport at very high carrier concentrations (at 300K, typically for concentrations around 10×10^{19} cm^{-3} to 10×10^{20} cm^{-3} and above, like degenerated semiconductors) [Sze 1995].
In the case of above-2-nm-thick defective layers —or defective interfaces— and in particular for heterojunctions like a-Si:H/c-Si, TAT via sub-gap states in the bulk of the layer or near the interface can also occur and eventually be the main mechanism for carriers to cross the junction under certain bias, temperature or carrier concentration [Riben 1966, Matsuura 1984, Rubinelli 1989, Mimura 1992, van Cleef 1996, Taguchi 2008, Mikolášek 2014, Procel 2020]. Several forms of TAT transport can exist in the junction, like TAT through dangling bonds, tail states or in the band spike [van Cleef 1996, Procel 2020]. As briefly mentioned in Chapter 5, an interesting path to investigate the delocalized or localized nature of transport at the interface could be made by probing the contact resistance ρ_c dependence on TCO carrier concentration, as Procel *et al.* evidenced that when TAT dominates the transport, ρ_c is more sensitive to the TCO carrier concentration [Procel 2020]. At a recombination junction – holes extraction to the external metallic electrodes, see Fig. 7.1.b) mechanisms number 3' and 4 – , holes can recombine with electrons through band to band recombination mechanism when the band alignment is favorable (e.g. conduction band of the n-type material is close to valence band of hole layer), or via hopping of electrons and holes through defects states in the gap [Procel 2020].

Yet, it is generally hard to characterize transport in a stack of materials by using fundamental properties such as mobility, and properties of isolated layers can significantly differ from the stacked ones. In the case of solar cell contacts transport study, methods are generally based on the device *J-V* characteristics.

7.4 Low temperature-dependent measurements of silicon heterojunction solar cells

7.4.1 State of the art of low temperature solar cells *J-V* curves measurements

A common approach to probe recombination, selectivity and transport resides in the analysis of V_{OC} and *FF* evolution with temperature, extracted from temperature-dependent *J-V* curves generally over 0 °C to 80 °C, described by temperature coefficient (TC) [King 1997, Green 2003]. According to semiconductors theory, V_{OC} is supposed to decrease linearly by increasing temperature, following the iV dependency on intrinsic carrier concentration [Arora 1982, Taguchi 2008], $n_i^2 \propto exp\frac{E_g}{k_B T}$, with E_g the band gap energy (see Chapter 2 for more information about the equations), and eventually silicon band gap narrowing with temperature

[Bludau 1974, Ponce-Alcántara 2014], and selectivity. The *FF* is a more complex term, involving several parameters such as selectivity, passivation, series and contact resistance, or/and injection, but it can approximately be stated that its temperature dependency is dictated by the one of V_{OC} and R_s [Green 2003]. For standard SHJ, a similar trend with temperature is observed for V_{OC} and *FF*. The existence of many transport mechanisms (see previous section about transport) can provoke the deviation of the cell parameters from the theoretical aforementioned behavior, which occurs at a different temperature depending on the contact quality. Researchers generally studied the dark *J*-*V* characteristics with temperature to identify them [Matsuura 1984, Mimura 1992, van Cleef 1996, Taguchi 2008, Mikolášek 2014], which is yet not fully representative of the solar cell state under illumination. To a lesser extent, illuminated measurement at low temperatures were also performed, and slope changes in the V_{OC} and *FF* dependencies were observed, with three regimes each [Taguchi 2008, Sachenko 2016, Mikolášek 2017, Cattin 2019]. In a first region, by decreasing temperature from 80 °C, they both present a linear increase in accordance with the classical semiconductor theory. In a second region, V_{OC} displays a slope change (saturation or reduced slope), and eventually a decrease in a third region. The *FF* undergoes a decrease from the second region followed by a steeper linear decrease in the third region, with generally higher temperatures regime transitions than the V_{OC} ones (see Fig. 7.3). Only few studies are available concerning the interpretation of such behavior, but the V_{OC} and *FF* deviations are thought to originate from different mechanisms. The V_{OC} deviation, in region 2 and 3, would be ascribed to the influence of the ITO/a-Si:H Shottcky barrier combined with depletion of the doped a-Si:H layer, provoking selectivity reduction [Mikolášek 2017]. In region 2, two mechanisms would be competing: with cooling, the V_{OC} starts to decrease due to lower selectivity (doped layer depletion), while it is still increasing following the n_i^2 decrease (expected variation from the theory). The slope in this region would also be closely linked to defect state density at the a-Si:H/c-Si interface, with a higher slope for higher defect concentration [Mikolášek 2017]. At low enough temperature, in region 3, V_{OC} eventually starts to decrease, a phenomenon which has not been explained yet. The *FF* deviation would stem from an increase of the global series resistance, mostly due to contact resistance (crossing of the band offsets, band spikes, Schottky barriers, TAT through defect states near the interface) which involves mechanisms generally favoured with higher temperature, in addition to be impacted by V_{OC} variations. Taguchi *et al.* also underlined the importance of (*i*)a-Si:H layer thickness in the *FF* slope change intensity [Taguchi 2008]. Cattin *et al.* experimentally confirmed the (*p*)a-Si:H doping and thickness influence on V_{OC} and *FF* in the ITO/(*p*)a-Si:H/(*n*)c-Si hole contact [Cattin 2019]. Hence, this low temperature characterization method could help understanding transport mechanisms at stake and estimating selectivity strength of different contacts in SHJ solar cells.

To our knowledge, low temperature measurements using metal-oxide based SHJ have never been reported and could bring additional understanding to this kind of analysis. Concerning MoO_{3-x}, charged carriers (electrons) concentration is known to originate from oxygen vacancies forming shallow donor levels (see Chapter 3). As for standard SHJ with doped a-Si:H-based

contacts, dopants should freeze upon cooling and MoO_{3-x} layer should be depleted below a given temperature. However, work function should remain high compared with the (*n*)c-Si or TCO one and even be increased with the depletion, meaning that band bending should be kept (or exacerbated) and selectivity maintained (see Fig. 7.2.a) and b)). Still, the work function mismatch between ITO and MoO_{3-x} should increase and may hinder the electron transport. In other words, band alignment should stay favourable to hole extraction even at very low temperatures in the MoO_{3-x}-based case contrary to the (*p*)a-Si:H-based one, even though electrons may be blocked at the TCO/MoO_{3-x} interface. Concerning the transport however, both structures are similar. First, hole transport at the (*i*)a-Si:H/c-Si interface should be of same kind for the two devices, with a TAT through defect states or extended state conduction. Second, transport at the MoO_{3-x}/(*i*)a-Si:H interface should be similar to the ITO/(*p*)a-Si:H (band to band with the right band alignment or TAT recombination, impact of layer thickness due to lower free carrier concentration at low temperature) as sketched in Fig. 7.2.a), with two main differences. First, in (*p*)a-Si:H-based samples, carriers which are conveyed through the (*p*)a-Si:H layer are holes while they are electrons in the MoO_{3-x} layer. Second, the material properties at stake are also significantly different, including for instance TAT through oxygen vacancies or polarons for MoO_{3-x} while it may occur via tail states and dangling bonds in (*p*)a-Si:H.
In conclusion, selectivity should be maintained or improved via enhanced upward band bending upon cooling the device involving MoO_{3-x}, but transport should be similar in both structures. Based on literature interpretation, we should obtain quite different V_{OC} evolution with temperature, while following our transport analysis, the *FF* trends should be similar. Yet, these assumptions are simplistic and conceals several phenomena like the band gap narrowing under cooling (shrinkage from conduction or valence band). Additionally, we have no idea about the strength of work function variation with cooling, which might be different for each materials.

7.4.2 Experimental results for MoO_{3-x}-based hole contacts and discussion

Comparison between (*p*)a-Si:H and MoO_{3-x}-based solar cells behavior with temperature

We measured several MoO_{3-x}-based devices at temperatures down to −160 °C. Fig. 7.3 presents the V_{OC} and *FF* variation with temperature, from 80 °C to −160 °C at 1 sun, of our standard (*p*)a-Si:H -based ((*i*)a-Si:H 6 nm, (*p*)a-Si:H 12 nm) and one of our best MoO_{3-x}-based ((*i*)a-Si:H 6 nm, MoO_{3-x} 4 nm, with an efficiency of 23.5%) hole contact device. The solar cells were prepared as presented in Chapter 2 with no annealing prior to MoO_{3-x} layer deposition for the MoO_{3-x}-based one. For temperatures above 25 °C, both contacts behave linearly as expected by the semiconductor theory. They also show similar TC even though MoO_{3-x}-based contact has a slightly better *FF* one, a result already observed in literature [Sacchetto 2017, Le 2021].
At lower temperatures, MoO_{3-x}-based devices exhibit the same V_{OC} and *FF* comportment than the standard SHJ, with a saturation/slope change followed by a decrease for the V_{OC}, and a

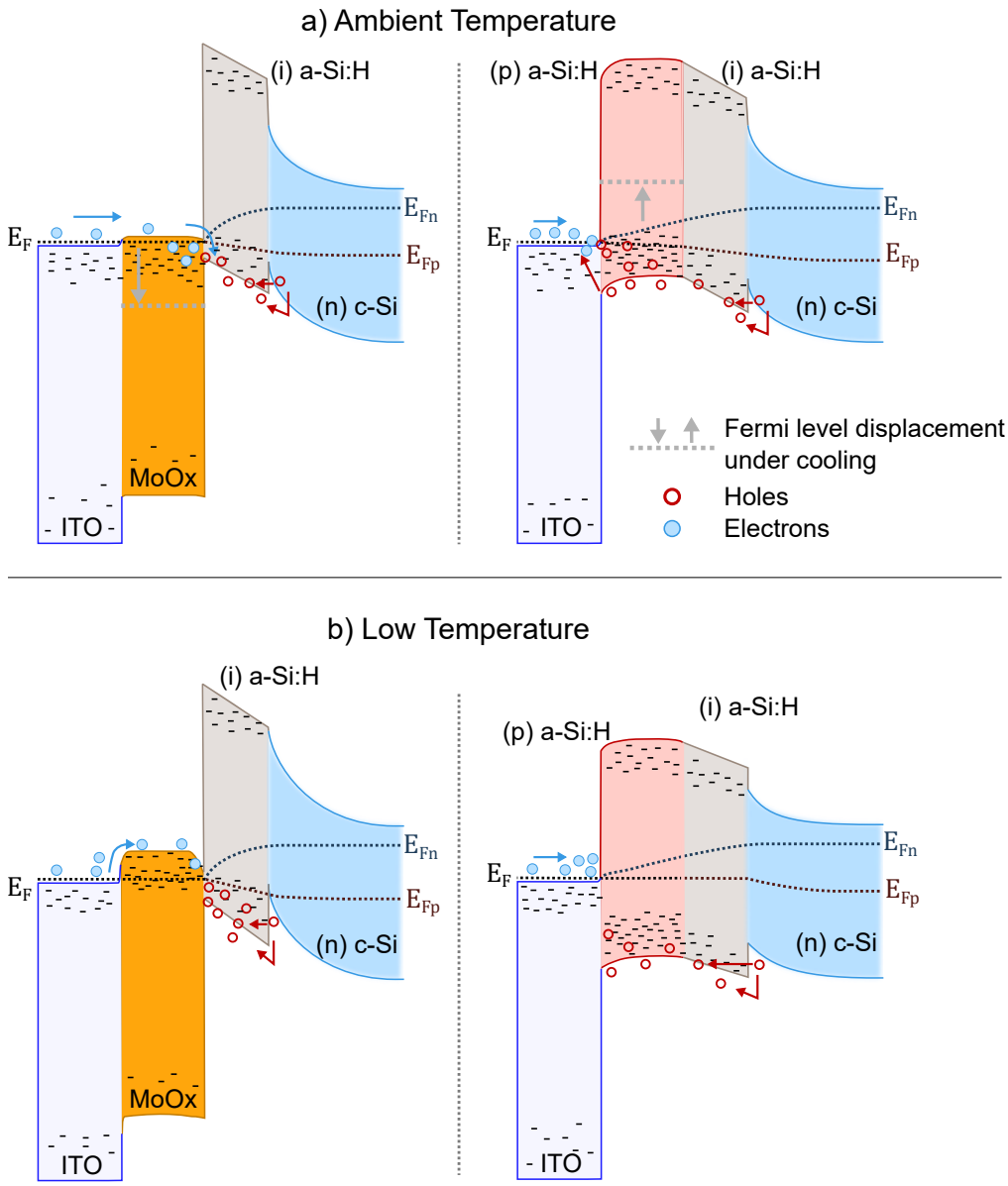

Figure 7.2: Band diagram scheme of MoO_{3-x}-based and (*p*)a-Si:H-based SHJ solar cells hole contact under operation at ambient temperature (a) and low temperature (b). Electrons and holes transport in both case is also reported. The Fermi level shift from the standard ambient temperature case to low temperature is exaggeratedly represented with the grey arrows and dashed line.

two-step decrease for *FF*.

The V_{OC} deviation of the (*p*)a-Si:H-based device from linearity starts around −30 °C (beginning of the "saturation" region) and ends at −130 °C. The fact that MoO_{3-x}-based cells follow the same V_{OC} trend is not expected based on the prior interpretations from literature concerning a-Si:H selective contacts and our hypothesis on MoO_{3-x}-based contact behaviour at low temperature (enhanced upward band-bending). This observation questions the role of the

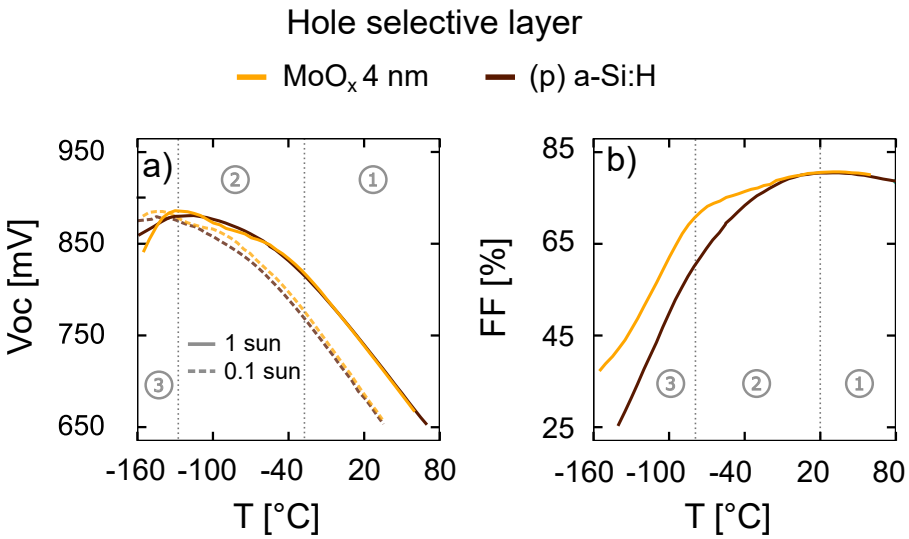

Figure 7.3: V_{OC} and *FF* variation with temperature (extracted from 1 sun temperature dependent *J*-*V* characteristics for a standard SHJ a-Si:H-based and a MoO_{3-x}-based SHJ. Numbers 1, 2 and 3 on both figures indicate the three different regimes of the solar device behavior.

aforementioned dopants depletion in the V_{OC} decline, since this depletion is not supposed to alter MoO_{3-x} selectivity. In the same region, the MoO_{3-x}-based cell additionally exhibits somewhat a S-shaped response, which is not explained. The following V_{OC} decrease seems to be stronger for MoO_{3-x}-based solar cell than for the (*p*)a-Si:H-based one. For lower illumination measurement (0.1 sun in Fig. 7.3.a)), the V_{OC} deviation is shifted to lower temperatures for both devices (as well as the S-shape present on the MoO_{3-x}-based cell response). In region 3, low illuminated V_{OC}s reach the same values for both MoO_{3-x} and (*p*)a-Si:H-based samples, and are higher compared to the 1 sun ones, as already reported in [Cattin 2019]. The latter observation would stem from high injection regime reached at 1 sun in the (*p*)a-Si:H layer, flattening the band bending [Bivour 2014], while it is not the case of 0.1 sun. Again, such an hypothesis should not be applicable to the MoO_{3-x}-based contact, which yet exhibit the same —or even stronger— behavior.

Similarly to V_{OC}, *FF* deviation showed in Fig. 7.3.b) follows the simulated and experimentally observed deviation of previously reported studies, with a linear increase by decreasing temperature from 80 °C to around 20 °C for both samples, followed by the two-step decrease at lower temperatures (region 2 and 3 [Taguchi 2008, Sachenko 2016, Mikolášek 2017, Cattin 2019]. For MoO_{3-x}-based cells, the *FF* decrease in the two regions is less pronounced than for the (*p*)a-Si:H-based samples, and which is higher in all the different regions. This difference originates from a better V_{mpp} below 20 °C for MoO_{3-x} cells compared with (*p*)a-Si:H ones, due to a less strong S-shape present in the *J*-*V* curves (see Fig. 7.7c.) and .d) and Fig. 7.4 for a schematic illustration). Such results could highlight the previously mentioned beneficial band alignment obtained for MoO_{3-x}-based hole contact (inducing stronger band bending

in (*i*)a-Si:H so less sub-gap oxygen vacancy defects to cross for carriers in MoO_{3-x}, see Fig. 7.2) or that TAT through oxygen vacancies is more efficient at low temperature than the one occuring in (*p*)a-Si:H. Contrary to the *FF* of the (*p*)a-Si:H-based cells, which follows a linear decrease in region 3, MoO_{3-x}-based device *FF* seems to recover near the lowest temperatures, with a slope change in this area, eventually indicating the beginning of a 4th region. This difference stems from a higher V_{mpp} to V_{OC} ratio: from around −130 °C, V_{OC} drops (see Fig. 7.3) while V_{mpp} is still decreasing linearly for both samples. This effect should actually appear for the (*p*)a-Si:H sample too, but it is erased by a severe J_{mpp} drop (from −100 °C while the J_{mpp} decrease is maintained much higher for the MoO_{3-x}-based one, as shown in Fig. 7.7.b). This J_{mpp} drop comes from the stronger S-shape influence (see Fig. 7.7.c) and d)) compared with MoO_{3-x}-based sample, that could also indicate a change in transport mechanism.

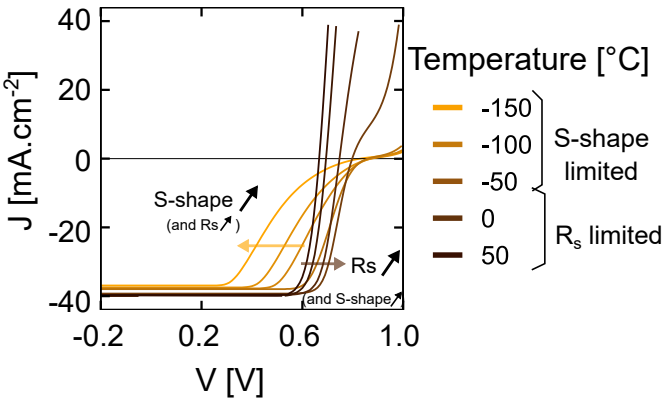

Figure 7.4: Illustration of the evolution of R_s and the S-shape with decreasing temperature. Both an increase of R_s and strengthening of the S-shape degrade the *FF*. A *J*-*V*(T) evolution at all temperatures can be found in appendices, Fig. E.1

Influence of MoO_{3-x} and (*i*)a-Si:H layer thickness on the solar cells low temperature behavior

Fig. 7.5 displays the V_{OC} and *FF* as function of temperature, from solar cells integrating different MoO_{3-x} and a-Si:H layers thickness, as prepared in Chapter 4. As a first examination, MoO_{3-x} layer thickness impacts the V_{OC} slope decrease in the lowest temperature region (region 3), with a steeper slope for thicker MoO_{3-x} observed for every (*i*)a-Si:H layer thickness. Conversely, (*i*)a-Si:H layer thickness seems to influence *FF* evolution mostly, which is coherent with Taguchi *et al.* observation [Taguchi 2008]. MoO_{3-x} thickness appears to influence other mechanisms when it is used with the thinnest (*i*)a-Si:H layer (6 nm). The sample with the 4-nm-thick MoO_{3-x} layer (and thinnest (*i*)a-Si:H) has a V_{OC} deviation starting at higher temperature but preserves a higher slope, compared with its 6-nm-thick MoO_{3-x} counterpart (Fig. 7.5). According to discussion of section 7.4, it would indicate a more defective a-Si:H/c-Si interface [Mikolášek 2017] for the device with 4 nm of MoO_{3-x}. Yet, this singular behavior should not be taken as a generality and measurements should be repeated for further investigation. Thinning down MoO_{3-x} layer from 6 to 4 nm —still for the samples with the thinnest (*i*)a-Si:H

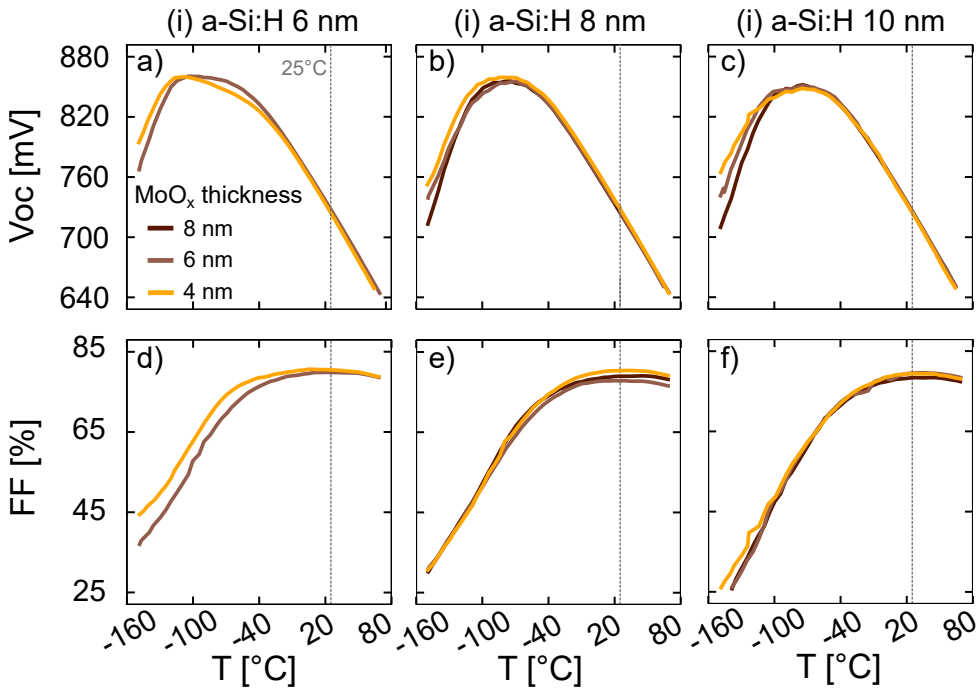

Figure 7.5: V_{OC} and *FF* behavior with temperature, for three different MoO_{3-x} and (*i*)a-Si:H thickenesses. The evolution can be divided in 3 main regions as detailed in Fig. 7.3.

layer— seems to shift the *FF* maximum to lower temperature, due to higher V_{mpp} for thin MoO_{3-x} (not shown here). On the contrary, the *FF* slope decrease in the third region is kept the same for the two different MoO_{3-x} thickness, indicating that the bulk transport in the MoO_{3-x} layer is not the limiting mechanism at these temperatures. The *FF* slope change at the lowest temperatures as mentioned for MoO_{3-x}-based cells in the previous section, is also present here for both samples. These results are not observed for the two thickest (*i*)a-Si:H layers, for which V_{OC} deviation from linearity begins at lower temperatures than the thinnest (*i*)a-Si:H-based cells, but V_{OC} decrease starts at higher ones, resulting in a shrunk region 2. MoO_{3-x} layer thickness has almost no influence on *FF* variation of regions 2 and 3. Comparing the present results with the ones of previous section, the absence of the *FF* slope change at the lowest temperatures —as well as the J_{mpp} drop— seems to be linked to a-Si:H layers in general —doped as well as undoped— or the total contact layer thickness (selective layer + (*i*)a-Si:H layer) eventually. Similar conclusions were actually found in [Cattin 2019]. These results highlight that transport via band tail or dangling bond states that exist in in a-Si:H layers, could be the limiting mechanism in this temperature range and for a-Si:H layers above 6 nm.

Pre-annealing effects on V_{OC} and *FF* variation with temperature

We finally investigated the influence of the temperature of the pre-annealing step (an annealing step prior to MoO_{3-x} deposition which is supposed to reduce hydrogen content in the (*i*)a-Si:H

layer, see Chapter 6 for more information), from 0 °C to 275 °C, on the behavior of 4-nm-thick $MoO_{3-x}$and 6-nm-thick (*i*)a-Si:H-based solar cells at low temperatures.
In Fig. 7.6.a), the V_{OC} deviation starts at the same temperature for the three different samples, while the V_{OC} decline (beginning of the third region) happens at higher temperatures for samples receiving a warmer annealing but decreases with the same slope, in the lowest temperatures range (region 3) for all the samples. The latter result about V_{OC} slope confirms that it mostly depends on MoO_{3-x} thickness, as observed in previous section in which samples from a different lot are used. It is interesting to note that the highest V_{OC} slope in region 2 —supposed to be higher for more defective (*i*)a-Si:H/c-Siinterfaces, see previous paragraphs— is held by the sample which was not pre-annealed although it should be the least defective one (higher hydrogen content and higher measured iV_{OC}). It means that either the pre-annealing does not affect the (*i*)a-Si:H/c-Si interface quality, and on the contrary, improves it —which is not coherent with the measured iV_{OC} after pre-annealing, MoO_{3-x} and front ITO deposition— , or the theory which connects defective interface with V_{OC}(T) slope in this region [Mikolášek 2017] is not the only one to consider to explain such behavior. It is worth noticing that the present not pre-annealed sample was the best among this series, with a 23.5% and near 82% certified record efficiency and *FF* respectively [Dréon 2020] while the two other samples had poorer performances, which strengthen the second hypothesis.
The *FF*(T) variation, presented in Fig. 7.6.b), appears to follow the same trend with the pre-annealing temperature than the V_{OC} one, with poorer *FF* values for warmer pre-annealings, in region 2 and 3. The samples without and with 245 °C pre-annealing yet keep the same decreasing slope in region 3. The softer slope decrease from −130 °C to −160 °C originates from a weaker V_{mpp} decrease compared with the V_{OC} one in this region, as observed in the two previous sections. The *FF*(T) variation of the sample with the highest pre-annealing temperature (275 °C) has globally slightly lower performances than the 245 °C-pre-annealed one, yet it becomes better below −100 °C. This is due to an earlier *FF* decrease softening originating from both better V_{mpp} and J_{mpp} compared to the 245 °C-pre-annealed sample. Reasons of this unexpected variation could be eventually linked to a change in the (*i*)a-Si:H crystallographic structure due to a strong H effusion out of the layer, following the 275 °C pre-annealing. Yet, this hypothesis requires more investigation to be validated.

Observation on J_{SC} and J_{mpp}

In first approximation, J_{SC} should decrease linearly under cooling following materials band-gap widening [Varshni 1967] as long as it equals the photo-generated current J_L. In Fig. 7.7.a) we plotted the J_{SC} dependence of the solar devices presented in Fig. 7.3. A linear decrease under cooling is indeed observed, yet, a peculiarity —not predicted by Varshni formula— appears abruptly from −10 °C and −40 °C for both the (*p*)a-Si:Hand MoO_{3-x}-based samples respectively, and vanishes around −100 °C. The corresponding *J*-*V* curves in Fig. 7.7.c) and d) evidence that at low temperatures, J_{SC} still equals J_L despite the presence on a S-shape, and measurements are not distorted by noise. In other words, this kink is not an "artefact" linked to the defition of J_{SC}, but to a physical phenomena affecting the photo-generated

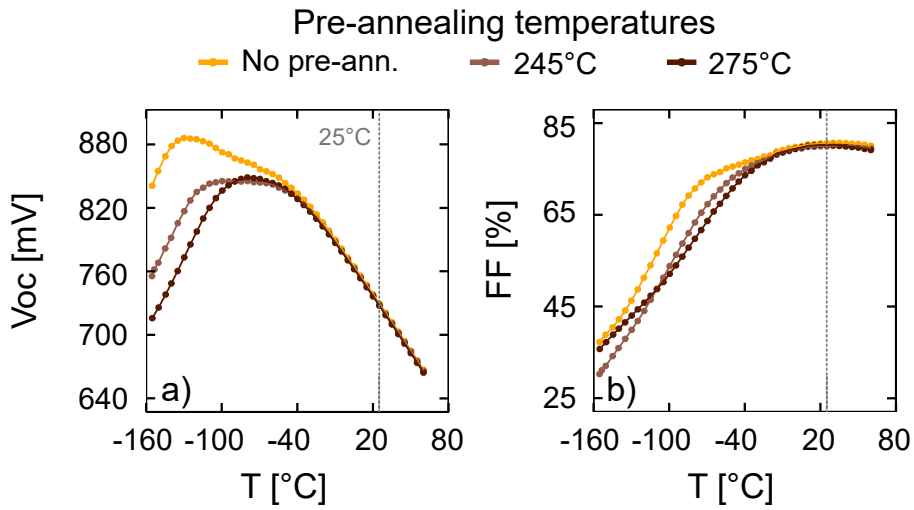

Figure 7.6: V_{OC} and *FF* behavior with temperature, for solar cells processed at three different pre-annealing temperatures.

current. To compare with another contact, we plotted the J_{SC} evolution of (*p*)μc-Si:H-based hole selective contact solar cell, as processed in [Antognini 2021]. The device presents a similar but stronger kink, starting and ending at the same temperatures than the (*p*)a-Si:H-based one. Since all three devices should have the same c-Si bulk properties (resistivity, purity, thickness, texturization), this effect is most likely related to interfaces. The same kind of deviation was observed in literature for light emitting diodes, with an S-shaped shift in the emission spectra over a certain (low) temperature range [Cho 1998, Li 2005]. The phenomenon was ascribed to specific recombination processes in band tail or localized states [Li 2005]. In our case, the kink could be also linked to a change in dominant recombination mechanism on this temperature scope, occurring at the interfaces or in the contacts. EQE measurement at these temperatures would help characterizing it. We performed more J_{SC}(T) measurements on diverse MoO_{3-x}-based samples, which showed behaviors similar to the present MoO_{3-x}-based and (*p*)μc-Si:H-based devices, with more or less strong deviations. The measures did not allow to establish a clear correlation with contact properties such as MoO_{3-x} and (*i*)a-Si:H layer thickness or pre-annealing temperature. More investigation on this effect could lead to a new method for defects/traps concentration determination in a contact stack, or even polarons or excitons trasnport characterization. A measurement artefact origin should not be excluded neither, even though the procedure was carefully controlled and no obvious issue was identified.

The aforementioned J_{mpp} evolution with temperature is represented in Fig. 7.3.b). Below −100 °C, J_{mpp} of the (*p*)a-Si:H-based device drops with decreasing temperature, while the one of the two other samples maintain the quasi same slope than above −100 °C. The *J*-*V* curves of Fig. 7.3.c), .d) and .e) highlight that a more sever S-shape for the (*p*)a-Si:H-based sample compared with the two others, and so strongly impacting J_{mpp}. This also suggests that even though MoO_{3-x}-based solar cells characteristics exhibit S-shapes at 25 °C, transport in those solar cells and on this low temperature range is more efficient than in the standard

(*p*)a-Si:H-based ones, probably because the transport mechanisms involved have different properties.

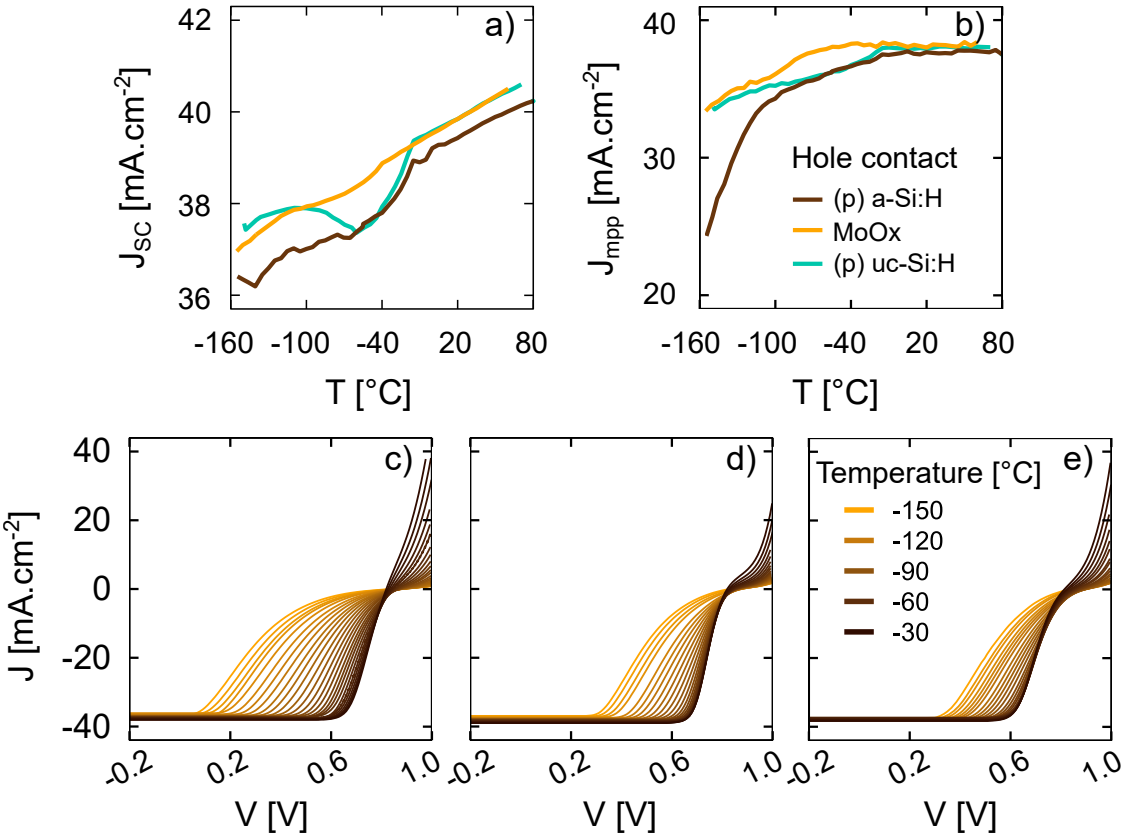

Figure 7.7: J_{SC} (a)) and J_{mpp} (b)) behavior with temperature of (*p*)a-Si:H-, MoO_{3-x}- and (*p*)μc-Si:H-based SHJ solar cells. *J-V*s over −150 °C to −30 °C of the c) (*p*)a-Si:H-, d) MoO_{3-x}-, e) (*p*)μc-Si:H-based samples are plotted.

7.5 S-shape characterization of MoO_{3-x}-based solar cells *J-V* curves

Even though low temperature measurement can provide valuable information, the measurement to get the data is time consuming and cannot be applied to all the solar cells processed. On the contrary, S-shape analysis only rely on the measurement of *J-V* characteristics at 25 °C which generally takes a couple of seconds to measure.

7.5.1 Origin of S-shapes

Solar cell *J-V* characteristics is well known to be exponential-like, following Shockley diode equation altered by series and shunt resistances R_s and R_{sh} (see the "one diode model", equation 2.5 in Chapter 2). It can be electrically modelled by the "one diode model" presented in Chapter 1. Yet, from p-n junctions and solar cells early stage development, some

devices manifest anomalous characteristics —namely, unusually high ideality factor— which cannot be physically acceptable. The high ideality factor was mostly attributed to the presence of recombination centers originating from impurities or defects in the bulk material, or/and tunnelling at levels inside the band-gap [Chynoweth 1957, Yajima 1958, Queisser 1962]. These studies initiated the development of multi-diodes models. Today, among anomalous characteristics under illumination, sigmoid-like singularities in the *J-V* curves, commonly called "S-shape" or "S-kink", is the most spread one in the photovoltaic field —organic PV and occasionally in inorganic PV— and have been discussed extensively. It was observed as early as 1976 and described as a parasitic rectifying contact between the substrate (Mo or C) and p-type InP film [Bachmann 1976, Saitoh 1977]. S-shapes are now commonly ascribed to undesired energy barriers at a contact —in contact-limited devices— arising from bands misalignment, that impede carrier extraction. Band misalignment can easily be induced by several factors, like work functions mismatch due to materials properties [Schulze 2006, Uhrich 2008, Kumar 2009, Tress 2011a, Wagner 2012], carrier accumulation at the interface [Gupta 2010, Wagenpfahl 2010, Wang 2011], widely reported dipole formation [Ishii 1997, Kumar 2009, Hwang 2009, Irfan 2010, Meyer 2012b, Guo 2014, Gerling 2015c, Gerling 2015a], reduced carrier mobility near the interface [Nelson 2004, Andersson 2011, Tress 2011b, Tress 2011a, Finck 2013, Sandberg 2014], disorder and defects near the interface or in the selective layers [Tress 2011b, Tress 2011a, Wagner 2012, Sandberg 2014], presence of an interfacial oxide layer [Gerling 2015c, Sacchetto 2017] or polaron states [Hwang 2009]. S-shapes curve can also be influenced by several parameters like high series resistance [Jin 2009] or morphology and thickness of the active layer [Kim 2009]. Several models have been developed to understand S-shapes physical meaning. Models are generally based on Poisson and continuity equations [Nelson 2004, Kumar 2009, Wagenpfahl 2010, Tress 2011a, Sandberg 2014, Chavali 2014] or equivalent electrical circuits. Among the latter, the S-shaped *J-V* curves are properly described by involving at least two diodes in the equivalent circuit. Fig. 7.8 schemes one example of such equivalent circuits. The first diode stands for free carriers recombination as in the classical "one diode model", and at least another diode is present in the "lumped-parameter circuit" to describe "linear" [Niemegeers 1997, Araujo de Castro 2010], or exponential-like [Mazhari 2006, García-Sánchez 2013, Roland 2016, Yu 2019, Yu 2020] S-shapes.

7.5.2 The model proposed by Roe *et al.*

Roe *et al.* introduced a new model, that resemble the Nelson *et al.* model [Nelson 2004], based on Poisson and continuity equations derivation to calculate carrier transfer rate on both sides of the device, contrary to the previously-mentioned models. Short introduction, explanatory scheme and $J(V)$ *J-V* equation can be found in Chapter 2 section 2.3.5. Roe *et al.* model actually also resembles Garcia-Sanchez *et al.* electrical model [García-Sánchez 2013] in which the "lumped-parameter" sub-circuit involves two opposing diodes in parallel. Roe *et al.* model predicts that all contact-limited solar cells *J-V* characteristics should exhibit a double S-shape, or two "steps". When both contacts are good, the two steps —electron step and hole step— are

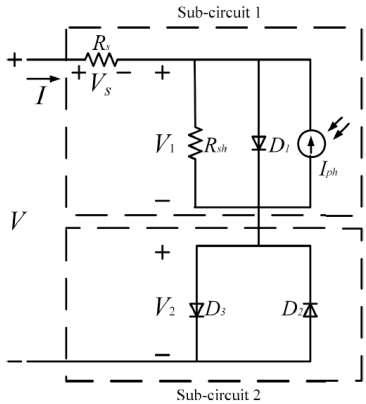

Figure 7.8: Solar cell equivalent electrical circuit involving three diodes modelling S-shapes in *J-V* characteristics, reproduced from [Yu 2020, García-Sánchez 2013]. Sub-circuit 1 represents the "one diode model" with resistive losses, and sub-circuit 2 the "lumped" parameter, responsible for the S-shape.

located far in the recombination region (high current densities) and are generally not visible in the common measurement region. However, when one(both) of the contact is(are) limiting enough, one(two) step(s) appear(s) in the active or near-recombination region. Fig. 7.9 shows a scheme of the two steps (also showed in Chapter 2 section 2.3.5), here the most limiting being the hole contact, obtained by a simulation of Roe *et al.* proposed *J-V* equation. Following the latter, the steps features provide precious information about the exchange current densities and so selectivity ability. The steps heights H, presented in Fig. 7.9, are given by:

$$H_p = J_L + j_{0p}^{e-} + J_{0p}^{h+} \qquad\qquad H_n = J_L + j_{0n}^{h+} + J_{0n}^{e-} \tag{7.5}$$

while voltage of the center of the steps V (inflexion point abscissa) can be written:

$$V_p = V_T\, ln\left(\frac{J_{0p}^{h+}}{j_{0p}^{e-}}\right) \qquad\qquad V_n = V_T\, ln\left(\frac{J_{0n}^{e-}}{j_{0n}^{h+}}\right) \tag{7.6}$$

with V_T the thermal voltage $k_B T/q$ (k_B the Boltzmann constant, T the temperature and q the elementary charge). Roe *et al.* define the "carrier selectivity" (not to confuse with "contact selectivity") as the ratio $S_p = \frac{J_{0p}^{h+}}{j_{0p}^{e-}}$ and $Sn = \frac{J_{0n}^{e-}}{j_{0n}^{h+}}$ for hole and electron selectivity respectively. It is worth noticing that this selectivity involves the currents of a same carrier kind at the two different contacts, whereas the contact selectivity involves the majority and minority current of both carriers at a same contact (J_{0p}^{h+}/j_{0n}^{h+} for the hole-selective contact and J_{0n}^{e-}/j_{0p}^{e-} for the electron-selective contact.

With these four equations, it is possible to rapidly determine the four exchange current densities —or at least the two of the most limiting contact when only one step is visible— by a simple reading of the *J-V* curve and can qualitatively replace fitting algorithms which can be time consuming. Assuming that J_L is much bigger than j_0, and that j_0 is negligible compared

with J_0 —reasonable for solar cells efficiency above 16% —, J_0 can be easily determined by the step height and then j_0 by the inflexion point abscissa.

7.5.3 Extension of the model

Roe *et al.* model turns out to be an efficient way of selectivity investigation for devices whose characteristics produce S-shape(s) in/near the active quadrant —that is, for not excellent contacts. Yet, the S-shape steps are not always as well distinguishable as the simulated example of Fig. 7.9, and their parameters (inflexion point and height) not clearly identified. This is the case of the present thesis, for which the S-shaped *J-V* curves of MoO_{3-x}-based devices generally exhibit only one step whose features are hardly perceptible (see Fig. 7.10.a) and .b)). We propose here to extend Roe *et al.* method by using the *J-V* derivative as a help to detect the steps heights and inflexion point abscissa of the indistinct S-shapes. The derivative maxima should indicate the *J-V* inflexion points (V_p and V_n) and decrease to 0 $mA\,cm^{-2}\,V^{-1}$ when reaching the "plateaus". In Fig. 7.9, we plotted the simulated *J-V* curve and its derivative to illustrate our statements.

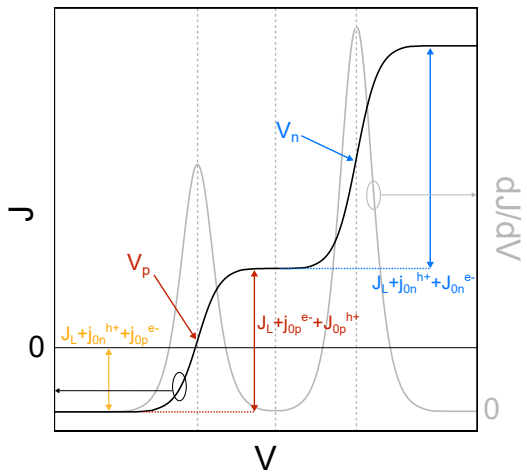

Figure 7.9: *J-V* characteristics simulated by the formula developed in Roe *et al.* [Roe 2019] and associated derivative curve.

7.5.4 Application to experimental data: preliminary results

We applied our "extended" Roe *et al.* method by calculating the derivative of MoO_{3-x}-based devices experimental *J-V* characteristics already presented in this thesis. Yet, at that stage, further analysis and calculation is necessary to fully and quantitatively exploit the methodology, and the study hereunder is restrained to graphical qualitative results.

Experimental introduction to the method: comparison between high and low performance devices

Fig. 7.10 introduces the typical plots and interpretations that will be presented in the section. In Fig. 7.10.a) and b), low performance (efficiency around 19%) and high performance (23.5%) MoO_{3-x}-based devices *J-V* and their derivative curves are plotted. As expected, one step only is present (one maximum in the derivative) which is ascribed to the hole contact limitation. The derivative maxima of the low performance device is located at V_p =685 mV, below V_{OC}, underlying that the S-shape affects the solar cell in the active quadrant. For the higher performance device, it is shifted to higher voltage (V_p =753 mV) by 68 mV, in the upper quadrant. A higher V_p indicates a higher hole selectivity (see previous paragraph). The derivative maximum (at V_p) of the low performance device is also smaller compared with the one of the high performance solar cell, also indicating a higher hole current at the hole-selective contact J_{0p}^{h+} for the latter compared to the former. In the *J-V* characteristics, the "plateau" following the step is absent, possibly hidden by too close V_p and V_n, the influence of bulk recombinations or series resistances. As a consequence, the derivative minimum never reaches 0 mA cm^{-2} V^{-1}. Even though close, it might not indicate the plateau position with high accuracy and for that reason, this feature will not be used in the next paragraphs to determine the step height. Assuming here that the abscissa of the minimum is accurate, a fast graphical estimation would approximately give J_{0p}^{h+} = 50 mA cm^{-2} and J_{0p}^{h+} = 120 mA cm^{-2} for the low and high performance solar cells respectively, which is in the order of magnitude of previously fitted J_{0p}^{h+}. In Fig. 7.10.c), the two derivatives are plotted together for clear comparison. In the following, similar comparative plots will be used for the derivatives analysis.

The next paragraphs take another look to previously exposed results, using the above extended method. It is worth noticing that this method generally requires a wider voltage scan and current range than the active quadrant to observe the first (and eventually the second for poor contacts performances) step of the S-shape since it is measured out of the standard measurements.

Effects of pre- and post- annealings

The pre- and post-annealings effects on MoO_{3-x}-based cells selectivity and passivation have been previously discussed in Chapter 6. All experimental details about sample preparation are provided in the same chapter. Fig. 7.11.a) compares the *J-V* derivatives of a MoO_{3-x}-based sample which was not pre-annealed and samples which received a pre-annealing at different temperatures (from 230 °C to 275 °C. The samples were all post-annealed at 130 °C, the standard curing temperature for the silver paste used in our MoO_{3-x}-based devices fabrication process. At that stage, there is no significant difference between V_ps of the different samples (6 mV difference), neither maxima heights, indicating similar hole selectivity and hole currents J_{0p}^{h+}. This result confirms the analysis of Chapter 6 in which the V_{OC} loss with increasing pre-annealing temperature was only ascribed to a passivation degradation due to H effusion from the (*i*)a-Si:H layer. Derivatives of the samples pre-annealed at 230 °C and 275 °C

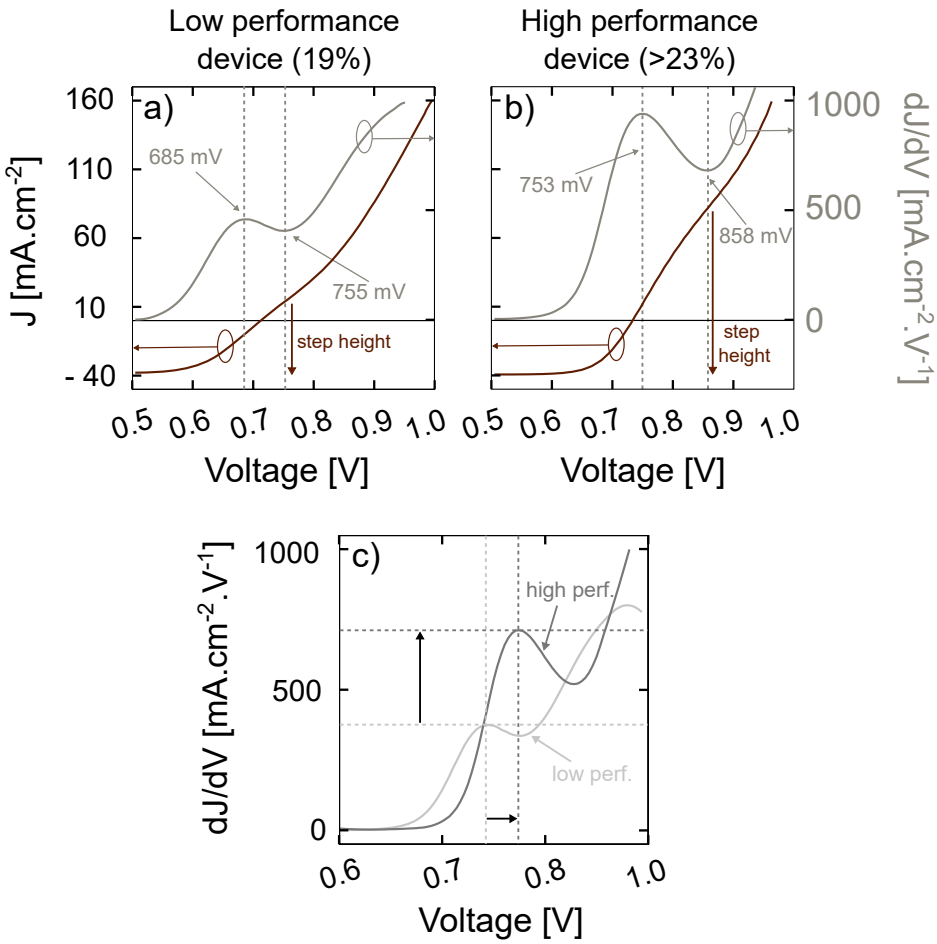

Figure 7.10: S-shaped *J-V* characteristics comparison of two MoO_{3-x}-based cells with different performances. The associated derivative are also represented to indicate the correlation between the relevant features. Fig. c) compares the two derivative together.

which underwent subsequent post-annealings are shown in Fig. 7.11.b) and c). Data for the samples which was not pre-annealed is unfortunately not available. Both samples exhibit a strong hole selectivity loss upon increasing post-annealing temperature (V_p decrease), with $V_{p_{130}} - V_{p_{190}} = \Delta V_{p_{190}} = 50\,\text{mV}$. Assuming that the V_p shift comes from the J_{0p}^{h+} reduction only (j_{0p}^{e-} stays constant), we estimated that J_{0p}^{h+} of the samples post-annealed at 190 °C are around 7.4 times lower than their 130 °C-post-annealed counterpart, for both samples. These results supports the previous stability analysis, yet more calculation is required to quantify the absolute J_{0p}^{h+} reduction from this data. According to stability study of Chapter 6, we expect a higher resilience —maintains its V_{OC} and *FF*— of the 275 °C-pre-annealed device towards post-annealing temperatures of 130 °C to 170 °C, compared with the 230 °C-pre-annealed one. We attributed the better results to a protected selectivity through H removal from the (*i*)a-Si:H layer. With the present data, the V_p shift calculation gives $\Delta V_{p_{170}}^{preann230} = 30\,\text{mV}$ $\Delta V_{p_{170}}^{preann275} = 33\,\text{mV}$ for the two samples. Both figures are very similar, indicating that the hole selectivity — that is the J_{0p}^{h+}/j_{0p}^{e-} ratio — undergoes the same degradation and is not protected upon

170 °C-post-annealing with a 275 °C pre-annealing treatment. The stronger selectivity loss for the 230 °C pre-annealed sample, observed through V_{OC} and *FF* degradation in Chapter 6, would thus come from a contact selectivity loss, defined by the ratio of currents at the same (hole) contact $J_{0p}^{h+} / j_{0n}^{h+}$. This result corroborates the conclusion drawn in Chapter 4, which states that MoO_{3-x} work function reduction —which strongly affects V_{OC} and *FF*— results in the increase of the parasitic electron current at the hole contact, in addition to the hole current decrease. In conclusion, V_{OC} and *FF* reduction detailed in Chapter 6 indeed comes from a selectivity loss (carrier selectivity, and contact selectivity at some point), but the stronger decrease at low-temperature post-annealing observed for the low-temperature-pre-annealed sample (compared to the 275 °C-pre-annealed one) mainly comes from a contact selectivity loss (j_{0n}^{h+} increase).

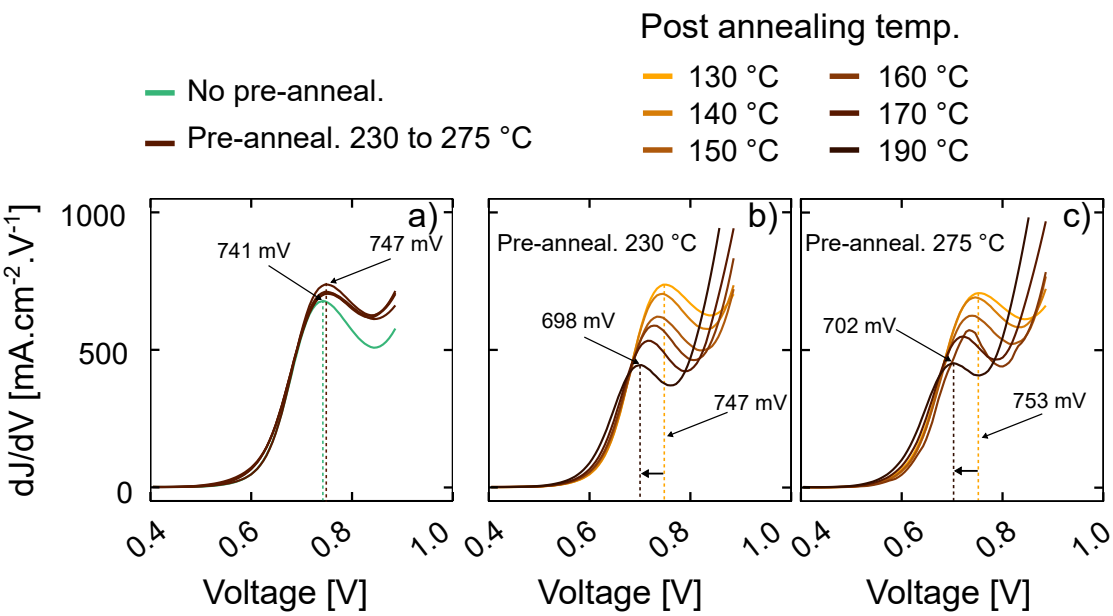

Figure 7.11: Experimental *J*-*V* derivatives of: a) pre-annealed and not pre-annealed MoO_{3-x}-based solar devices which received the standard post-process curing at 130 °C; same samples (b) pre-annealed at 230 °C and c) at 275 °C) receiving successive post-anealings, from 130 °C to 190 °C. Vertical dashed lines indicate V_p.

Effects of MoO_{3-x} and (*i*)a-Si:H thickness

Fig. 7.12 shows the *J*-*V* derivatives from MoO_{3-x}-based samples of Chapter 4 (and 5 for the 2-nm-thick-MoO_{3-x} sample), with a MoO_{3-x} (Fig. 7.12.a)) and (*i*)a-Si:H (Fig. 7.12.b)) layer thickness variation. The 4-nm-thick device exhibits the best properties. Because the S-shape step is almost invisible in the 2-nm-thick-MoO_{3-x} *J*-*V* curve, possibly due to a lower barrier for holes, its derivative maximum might not be well located and V_p = 700 mV underestimated. Still, V_p seems to be lower than the one of the 4-nm-thick sample as a possible consequence of ITO work function influence (see Chapter 5). By thickening the MoO_{3-x} layer from 4 to 9 nm, V_p decreases. Assuming that the parasitic hole current at the electron contact j_{0p}^{e-}

does not vary, the V_p difference of 22 mV suggests that the hole exchange current J_{0p}^{h+} of the 9-nm-thick-MoO_{3-x} device is 2.4 times lower than its 4-nm counterpart, making this device more than twice less hole selective. The decrease is unlikely linked to an increased intrinsic bulk resistance of the MoO_{3-x} layer which would reduce J_{0p}^{h+} —as well as j_{0n}^{h+}— and leaves j_{0p}^{e-} at the electron contact identical, since we showed in Chapter 4 that it has a negligible impact on total series resistance. However, MoO_{3-x} thickness can influence band alignment or interfaces morphology of the full hole contact stack and so alter hole selectivity. Interestingly, the (*i*)a-Si:H layer thickness variation of 4-nm-thick MoO_{3-x}-based samples reveals the same trend and similar figures. (*i*)a-Si:H layer thickness is not supposed to influence selectivity, and as for MoO_{3-x}, we previously showed that its bulk resistance should not affect the total series resistance on the range considered. It can however be sensitive to MoO_{3-x} work function, and a thin (*i*)a-Si:H layer is more likely to be fully depleted by the strong band bending induced by the selective material than a thick (*i*)a-Si:H layer. In the first case, MoO_{3-x} will generate a stronger upward band bending at the c-Si interface than in the second case. The hole extraction (J_{0p}^{h+}) would probably be enhanced with a thin (*i*)a-Si:H layer, which could explain the tendency observed in Fig. 7.12.b).

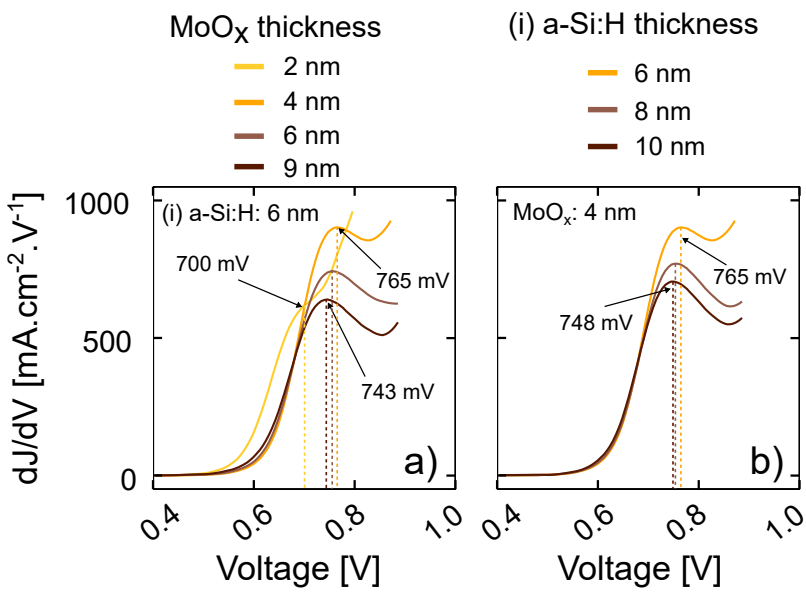

Figure 7.12: Experimental *J-V* derivatives of MoO_{3-x}-based solar cells with: a)variable MoO_{3-x} layer thickness, and b) variable (*i*)a-Si:H layer thickness.

Effect of forward bias, illumination and UV-induced degradation

Forward bias To enlarge the study, we analysed MoO_{3-x}-based solar cells which received a forward bias treatment (see Chapter 6) and the evolution of the S-shape with illumination. Fig. 7.13.a) compares the two derivative of the same 4-nm-thick MoO_{3-x}-based solar device, before and after the forward bias treatment. V_p shifts by 10 mV towards higher voltages and the maxima height lightly increase. Both effects suggest a moderate hole selectivity improvement.

This confirms that the substantial *FF* enhancement (more than 1 $\%_{\text{absolute}}$ observed after the forward bias treatment in Chapter 6 could be essentially ascribed to passivation recovery.

Illumination Besides, reducing illumination from 1 sun to 0.05 sun induces a V_p increase by 24 mV. Under illumination reduction, carrier concentrations in the device are reduced and tend to low injection regime, in which band bending induced by the contacts is stronger. Selectivity should thus be improved, be it contact or carrier selectivity. The present V_p shift proves that J_{0p}^{h+} decreases slower than j_{0p}^{e-}, so carrier (hole) selectivity is improved at the hole contact in low illuminated MoO_{3-x}-based devices.

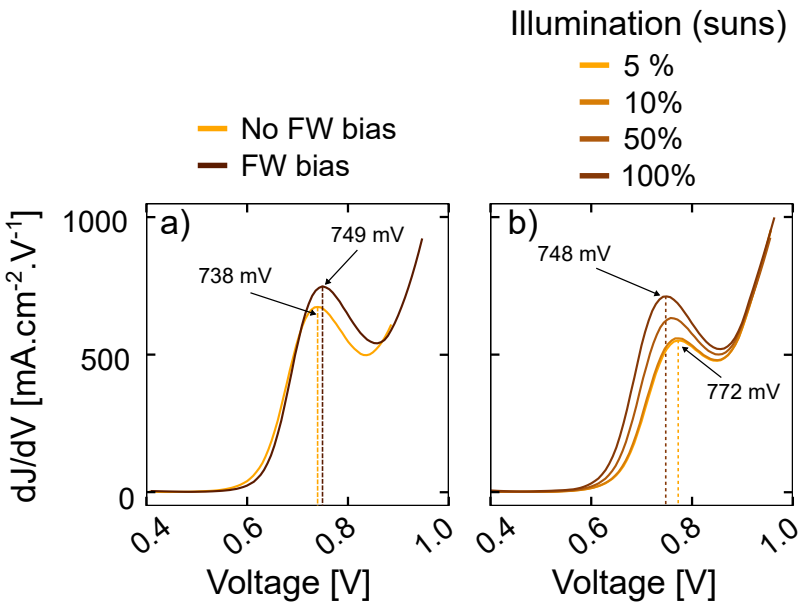

Figure 7.13: Experimental *J-V* derivatives of MoO_{3-x}-based solar cells: a) which received a forward bias treatment as described in Chapter 6; and b) under different illuminations.

UV-induced degradation In Chapter 6 section 6.6, we found that MoO_{3-x}-based SHJ encapsulation losses would be related to passivation issues, while UV treatment (from UV radiations and other causes linked to chamber parameters or polymer influence) to selectivity and passivation degradation. To confirm —or invalidate— our conclusions from the study, we plot here the *J-V* derivatives and apply our method. The plots in Fig. 7.14 explicitly highlight that the (carrier) selectivity is not impacted by the encapsulation process (from cutting to lamination, see Chapter 6) as the derivative maxima voltage V_p does not shift, for both the UV-transparent- and UV-absorbent-based modules. As soon as the samples are exposed to UV radiations, V_p decreases for all the samples. In the UV-transparent case, the performances are too affected and *J-V* S-shape disappear which makes the V_p shift quantification impossible and point out one of the method limitations. For the UV-absorbent sample, V_p reduces by around 37 mV after 1000 h of exposure. The present shift echoes the severe R_s increase that

occur independently from UV irradiation, as evidenced in the previous chapter, and that could be related to other mechanisms (UV-free light, temperature (set at 65 °C), humidity (20%)).

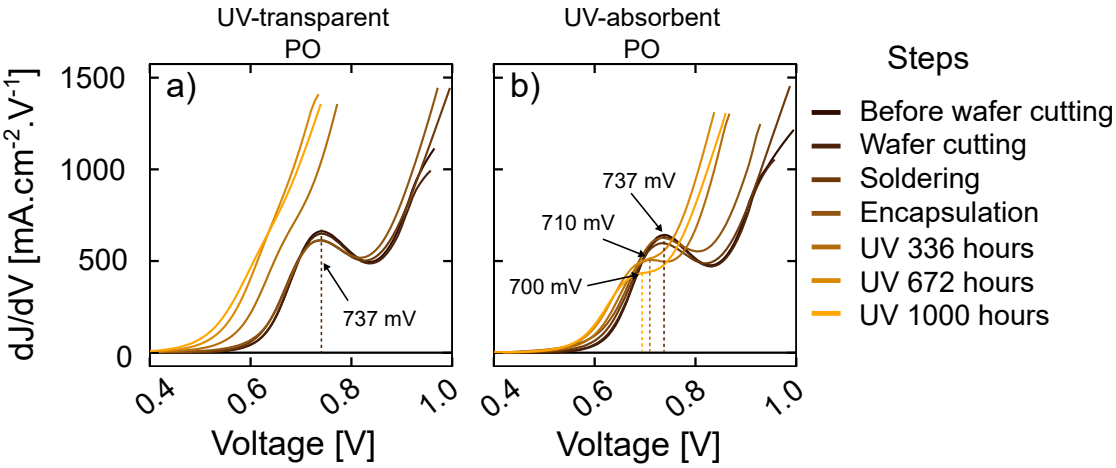

Figure 7.14: Experimental *J*-*V* derivatives of MoO_{3-x}-based solar cells through the encapsulation process steps and under 1000 h of UV-readiation exposure. Half of the mini-modules (presented in Chapter 6) are encapsulated with a UV-transparent polymer (UV-cut-off: 333 nm) while the other half has a UV-absorbent one (UV-cut-off: 383 nm).

7.6 Conclusion

This chapter has introduced exploratory concepts for contact-limited solar cells and exposed preliminary experimental results as a basis for future investigation. Both of the presented methods have the potential to provide information about transport mechanisms of solar cells in the operating condition range through measurements far from this regime.

For the first time, MoO_{3-x}-based SHJ were measured at temperatures from −160 °C to 70 °C. The V_{OC} and *FF* evolution showed similar behavior than the (*p*)a-Si:H-based SHJ, which is in accordance with the preliminary discussed band diagrams comparison at low temperature and the similarities of transport mechanisms in both structures. We reported an anomalous kink in J_{SC} behavior which is not explained by the classical band gap narrowing upon cooling and could be a consequence of specific recombination at/in the contact stack, yet measurement artefact should not be excluded. Performing EQE in the same range of temperature would help elucidate this. This new set of data brings complementary insight to the existing reports on low temperature *J*-*V* measurements and questions the current interpretations from literature. In addition to the influence of layers thickness and annealing processes reported here, an investigation of ITO doping influence, for instance using the same solar cells than that of Chapter 5, would bring helpful additional insights to further understand the physics. Varying the electron selective contact by replacing it with another not Si-based material (transition metal oxides or alkali metals for instance) would also be highly valuable.

We also proposed an alternative utilization of the the Roe *et al.* model to examine S-shaped *J*-*V* curves and extract information on the different internal currents. Preliminary results

were obtained on experimental data and showed that quantities like the inflexion point or step height abscissa, more easily extracted through the derivative calculation, are valuable to estimate selectivity strength. The method also proved that it is possible to decorrelate carrier selectivity from contact selectivity with the proper complementary measurements. The derivative analysis attested to be a useful and fast graphical help to observe selectivity evolution. For future improvements, a polynomial fitting or the second derivative calculation could also be used to accurately extract V_p or V_n through algorithms for instance. An automated extraction of the different parameters enlarges possibilities for new investigation, such as $V_{p,n}$ evolution with series resistance, V_{OC} and iV_{OC}, or event with temperature to combine with the low temperature study.
At the moment, no direct link could be drawn between the observations and fundamental bulk or interface transport involving traps, polarons or other exotic quasi-particles, and the complexity of materials stack interaction involved in heterojunctions suggests that more quantitative and thermodynamic modelizations are required for such purpose. Yet, the little data collected so far already brings many questions raising strong interest for more research on the topic.

8 Conclusions & Perspectives

8.1 Overview

This thesis aimed at analysing and boosting the performances of MoO_{3-x} as an alternative material to constitute the hole selective contact of SHJ solar cells, evaluate its potential in comparison to standard doped a-Si:H layers and further understand the heterocontact behavior. For this, MoO_{3-x} and (*i*)a-Si:H layer thicknesses were varied to assess transparency, passivation and selectivity full potential and estimate their limits. Power deposition and doping of the ITO top layer were modified to further estimate the passivation and selectivity strength of ultra-thin MoO_{3-x} layers (4 and 2 nm), and diverse stability tests were conducted for the first time on such structures. Studying the contact properties out of the standard ranges of current, voltage, illumination and temperature proved to enable a better understanding of the origin of contact-limited losses. This work allowed to improve the average efficiency of the MoO_{3-x}-based SHJ solar cell from 19% to > 23%.
Fig. 8.1 summarizes the performances evolution of MoO_{3-x}-based SHJ developed in this thesis, as a function of the MoO_{3-x} layer thickness.

The influence of combined MoO_{3-x} and (*i*)a-Si:H thickness variation was evaluated in the first chapter. We showed that increasing the (*i*)a-Si:H layer did not meaningfully improve the solar cell performances whereas thinning down the MoO_{3-x} layer to 4 nm significantly increased the hole contact transparency while holding excellent passivation and selectivity. Devices with 4-nm-thick MoO_{3-x} achieved an efficiency of 23.5% with *FF* near 82%, with no post-treatment enhancement. By replacing the (*p*)a-Si:H layer by 4 nm of MoO_{3-x}, the J_{SC} increased by 1.3 mA cm^{-2}. Under 4 nm of MoO_{3-x}, solar cell performances are readily affected by MoO_{3-x}-surrounding-materials properties, such as ITO work function, poor passivation and wafer quality like surface defects or damages. Under favorable circumstances, appreciable efficiencies could be obtained with 2 nm of MoO_{3-x} (22.5%). The implementation of a characterization method based on a model developed by Roe *et al.* allows the estimation of partial hole and electron currents at the contacts. We highlighted that the MoO_{3-x} work function reduction induces both a reduction in the ability of the contact to extract holes, and

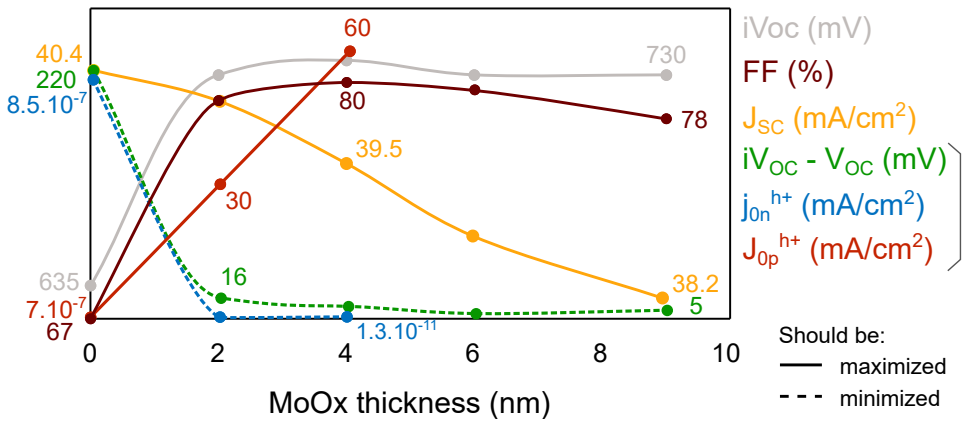

Figure 8.1: Summary of averaged MoO_{3-x}-based solar cell performances evolution with MoO_{3-x} layer thickness. iV_{OC} of the final devices measures the passivation quality, *FF* the transport performance, and J_{SC} the contact transparency. The three metrics $iV_{OC} - V_{OC}$, j_{0n}^{h+} the electron exchange current density at the hole contact (parasitic current) and J_{0p}^{h+} the hole exchange current density at the hole contact (majority current) measure the selectivity ability of the hole contact. $iV_{OC} - V_{OC}$ and j_{0n}^{h+} should be as small as possible while J_{0p}^{h+} as high as possible.

its ability to screen electrons.

We then turned to the influence of the capping ITO layer and observed that varying the ITO carrier concentration from 3×10^{19} cm^{-3} to 6×10^{20} cm^{-3} is responsible for a ~ 0.2 eV change in ITO work function in practice, for our devices. We also highlighted that 4 nm of MoO_{3-x} is sufficient to completely screen such ITO work function change, whereas with 2 nm, the device V_{OC} is influenced. Lowering the ITO sputtering deposition power did not enhanced the final device passivation (at least on the present power range and 6-nm-thick (*i*)a-Si:H layers), but produces a nearly amorphous material which, specifically for MoO_{3-x}-based contacts, enhanced the *FF* by more than 1 $\%_{absolute}$ compared with the baseline ITO. With these results, we finally could reproducibly improve the efficiency of 4-nm-thick MoO_{3-x}-based SHJ to 23%. PECVD-deposited SiO_x:H is not suited for MoO_{3-x}-based SHJ DARC treatment as it induces a strong *FF* loss. Preliminary results using evaporated 80-nm-thick MgF_2 showed J_{SC} increase with no *FF* loss.

Stability tests proved that MoO_{3-x}-based solar cells are highly stable over time when stored in ambient air and in the dark. Annealing of the wafer prior to MoO_{3-x} deposition, aiming at reducing the H content of the (*i*)a-Si:H layer to prevent its subsequent effusion in the MoO_{3-x} layer, slightly reduces the passivation provided by the (*i*)a-Si:H layer but turned out to be beneficial for MoO_{3-x}-based devices post treatment at temperatures from 130 °C to 170 °C. Subjecting MoO_{3-x}-based devices to current injection in forward bias was shown to be beneficial and significantly improved the *FF*. The *FF* evolution appears to be stronger for MoO_{3-x}-based cells than for a-Si:H-based ones. Application of the treatment during one week on 4-nm MoO_{3-x}-based solar cells boost the efficiency from 23.1% to 23.7%, which is the best reported MoO_{3-x}-based SHJ efficiency. The same treatment, combined with a 80-nm-thick

MgF_2 DARC on 2-nm-thick MoO_{3-x}-based devices bring the efficiency to an impressive value of 23.5%. UV-induced degradation was also performed on encapsulated devices, and proved to damage the cells selectivity, while a UV-free mechanism, happening during the degradation procedure, drastically increases R_s and does not seem to be linked with ITO sheet resistance increase.

Literature about main transport mechanism occurring in the heterocontacts studied in this thesis, is gathered in the last chapter. An application of the transport theories to the MoO_{3-x}-based contact and a comparison with the (*p*)a-Si:H-based one at low temperature is also proposed. *J-V* measurements of MoO_{3-x}-based devices over −160 °C to 70 °C, a scarcely used method for SHJ solar cell, showed similar trends with the (*p*)a-Si:H-based solar cells, confirming the expectations proposed for the MoO_{3-x}-based contact behavior at low temperature. Finally, we suggested an extension of the Roe *et al.* model to rapidly characterize selectivity losses and distinguish between carrier and contact selectivity when it was not possible in previous analysis.

8.2 Perspectives

To further improve the MoO_{3-x}-based device performance, processing the same 4-nm-based MoO_{3-x} contact but using Cu plating instead of Ag screen printing could substantially enhance the solar cell *FF*. A contact combining a ITO with a low carrier concentration (higher work function) and deposited at low power, and 2-nm-thick-MoO_{3-x} layer, followed by a forward bias treatment, could be developed. Combined with a MgF_2 DARC, this device should exhibit high currents and high *FF*.
MoO_{3-x} is mainly used as a front contact due to its high transparency. However, using it at the back side of the cell would also be interesting. For bifacial or IBC modules, its transparency could enhance the bifaciality factor or current gain of IBC for instance. Such devices have already been developed by Lin *et al.* and Wu *et al.* [Lin 2021, Wu 2018] but could be further improved. At the back side, MoO_{3-x} would be also protected from the UV degradation observed in the stability tests analysis. Adding a very thin Ni or $Ni_{1-x}O$ layer between the MoO_{3-x} and ITO could also help in reducing the parasitic electron current at the hole contact, since $Ni_{1-x}O$ is a p-type material with a high work function. Masmitjà *et al.* and Li *et al.* have actually already used this strategy for V_2O_{5-x}-based and MoO_{3-x}-based rear contacts respectively, which gave promising results [Masmitjà 2018, Li 2021].
The use of MoO_{3-x} in partial contacts could also be an interesting path to follow to overcome the limited surface passivation it provides, further increase transparency and reduce contact resistance. Such architectures were already used with TMOs and provided high efficiencies [Bullock 2019].

More research could be conducted on the comparison between MoO_{3-x}-based and (*p*)a-Si:H-based contacts. For instance, resistive effects should be investigated in more details. We demonstrated that the TCO crystallinity strongly influenced the contacts involving MoO_{3-x},

but preliminary results showed that it barely influenced the (*p*)a-Si:H-based contact. The study of contact R_s evolution with MoO_{3-x} thickness and ITO doping should be continued and compared to (*p*)a-Si:H-based contact as well. These considerations should be connected with the observation of Procel *et al.*, according to which ρ_c evolution with the activation energy (of a doped a-Si:H layer) and TCO carrier concentration depends on the transport kind (band to band or TAT).
In general, a more intense development of alternative test architectures, on glass samples or wafers, could also complementary help for the understanding of the contact.

From low-temperature *J-V* measurements and transport analysis in the heterocontacts, we learned that both MoO_{3-x}- and (*p*)a-Si:H-based contacts behave similarly. Yet, the V_{OC} and *FF* evolution with temperature exhibit different slopes between the two devices. More calculations and simulations could provide quantitative insights in the carrier population and dominant transport kind occurring in each contact. Testing these measurement with different ITO carrier concentrations would be a good start to identify the origin of the V_{OC} drop in the lowest temperature ranges. The latter suggestion could also be coupled with Procel *et al.* conclusions on ρ_c dependency with the transport type. Evolution of V_p and J_{0p}^{h+} with temperature for both structures would bring meaningful insight to follow selectivity variation.

At present, MoO_{3-x} is the most efficient alternative material used in SHJ selective contacts. According to the recent results, V_2O_{5-x} could reach similar efficiencies with ALD processes while $Ni_{1-x}O$ has the perfect electronic fit for hole selective contact and could be more explored in the future even though its integration seems complex in practice (see Chapter 3). Focusing on 2-nm- to 4-nm-thick-MoO_{3-x}-based hole selective contact appears to be the most concrete path to bring MoO_{3-x}-based SHJ to the industrial stage with an efficiency of 25%. To do so, samples should be fully processed in an inert atmosphere, the front TCO further optimized (transport in MoO_{3-x}-based contacts showed to be highly sensitive to the TCO crystallographic structure and work function) and double or triple anti-reflective coatings should be deposited. The O rate during MoO_{3-x} evaporation on larger area should be controlled, by using HWOSD for instance, as proposed by [Li 2020a]. The development of such transparent contacts would also be an asset for bifacial module deployment.

In the end, many TMO-based contacts for SHJ solar cells were developed over the last ten years, whose performances today compete with the conventional a-Si:H-based ones. However, the ideal material have still not been found, and the current alternative materials require the same amount of process steps as used to produce the standard SHJ to reach high efficiency (presence of the (*i*)a-Si:H passivation or additional layers, TCO). Additionally, evaporation, widely used to provide MoO_{3-x}-based devices best efficiencies, is not standard in the PV industry, and it will require more work to design tools with the proper productivity and cost of ownership. However, research on this topic is still flourishing, owing to TMOs special electronic properties, and most of the material library has not been tested as contacts in SHJ yet. Many other metal-compound-based contacts such as LiF_{1-x}/Al, MgF_{2-x}, MgO_{1-x}, ZnS, TiN, GaP, GaN, or CuI are developing and enlarge the possibility to find the ideal electron- or hole-selective contact. The

coming 10-year research will be essential to unveil these alternative materials' full potential.

Appendices

A Evaporated MoO_{3-x} thickness homogeneity

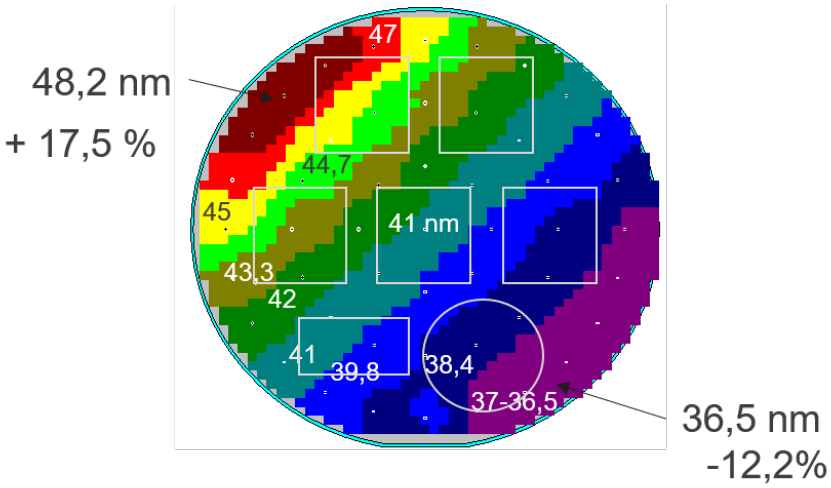

Figure A.1: Measurement of the thickness homogeneity of MoO_{3-x} deposition in the Leybold evaporator. The evaporation was made on a polished wafer and the thickness determined by ellipsometry mapping. The 2x2 cm^2 solar cell design used in this thesis is scaled on the wafer to estimate inhomogeneity on each solar cells. The targeted thickness was 40 nm. The deviation +17.5% and -12.5% are calculated compared with the 40 nm target.

B Temperature control during ITO and Ag sputtering in MRC II

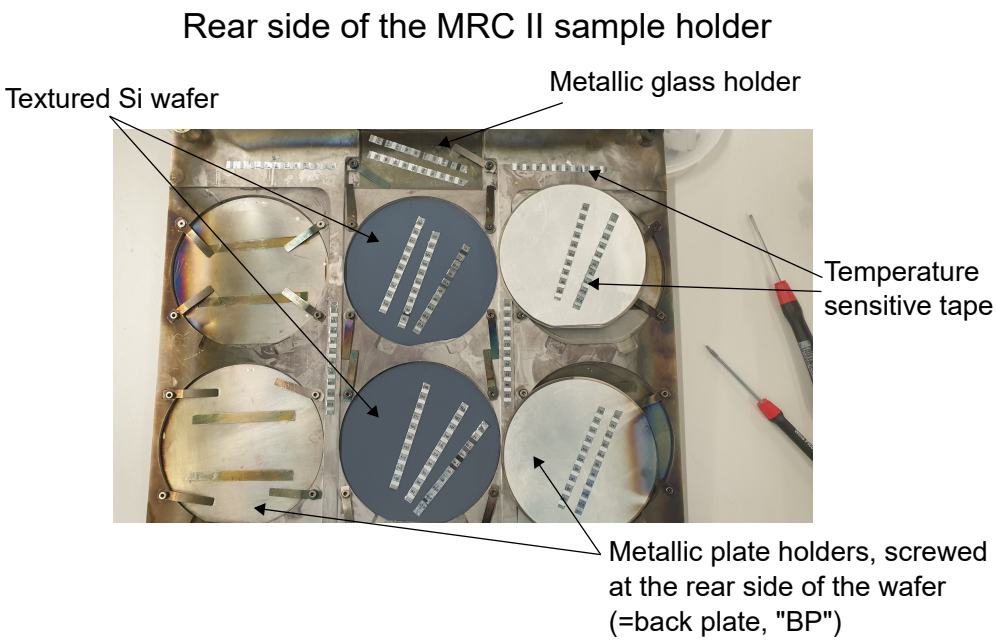

Figure B.1: Picture of the wafer holder (back side) used in the sputtering deposition tool (MRC II). Temperature-sensitive tape was deposited in strategic places to determine the holder and wafers temperature during the standard processes.

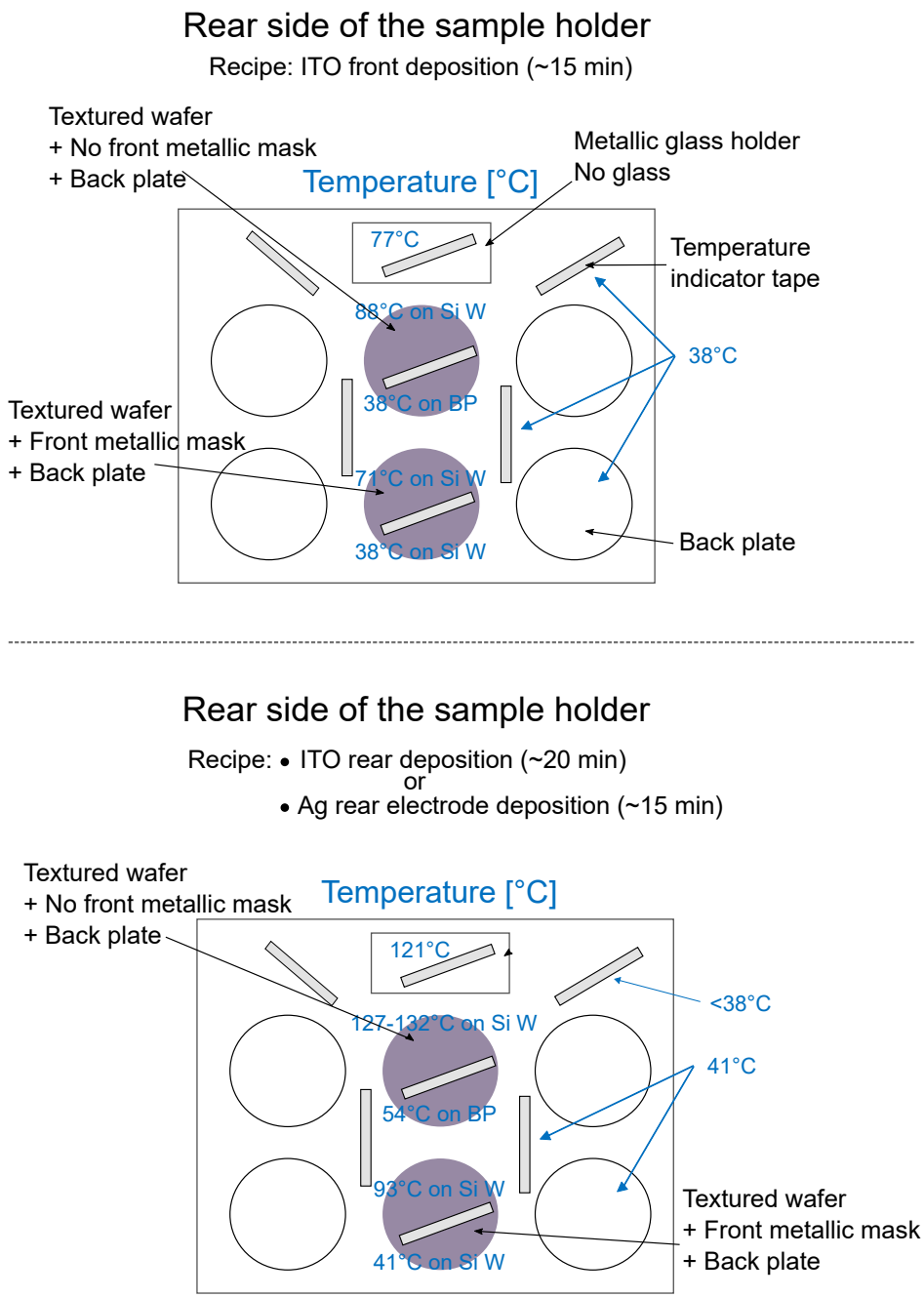

Figure B.2: Scheme of the wafer holder (back side) used in the sputtering deposition tool (MRC II). Temperature control during the ITO front depostion and during the ITO back side deposition.

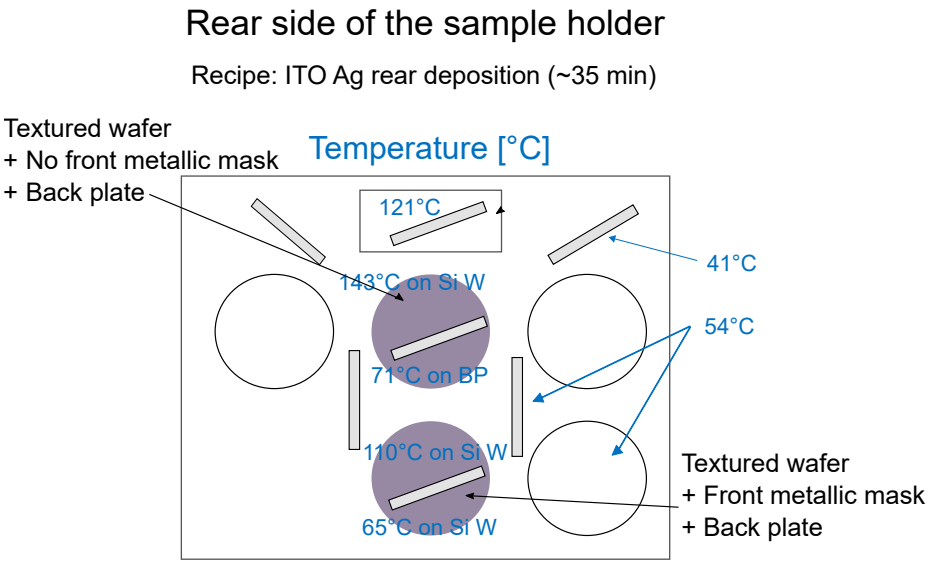

Figure B.3: Scheme of the wafer holder (back side) used in the sputtering deposition tool (MRC II). Temperature control during the ITO/Ag back side electrode depostion.

C Appendices for Chapter 5

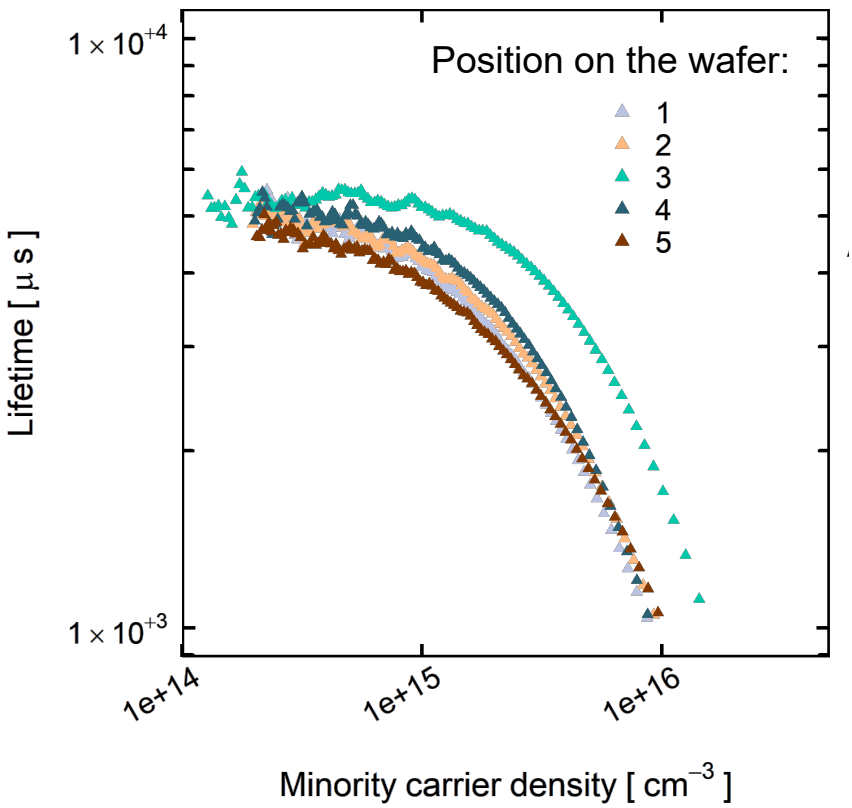

Figure C.1: Lifetime measurement of a same wafer after PECVD (deposition of the two (*i*)a-Si:H layers and the rear (*n*)a-Si:H layer), at 5 different locations.

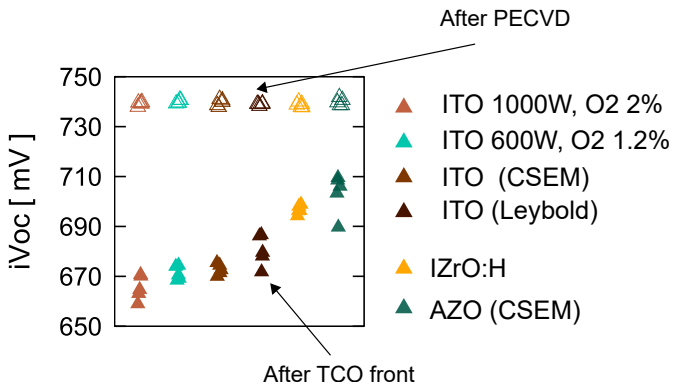

Figure C.2: iV_{OC} measurement after deposition of (*i*)a-Si:H front and (*i*)a-Si:H/(*n*)a-Si:H rear layers by PECVD, and TCO front sputtering deposition for MoO_{3-x}-based devices. IZrO:H and AZO show the highest iV_{OC}. As mentioned in Chapter 5, this MoO_{3-x}-based soalr cells series underperformed, probably due to climatic perturbation during the process (high humidity) and experiment should be repeated to confirm the conclusions.

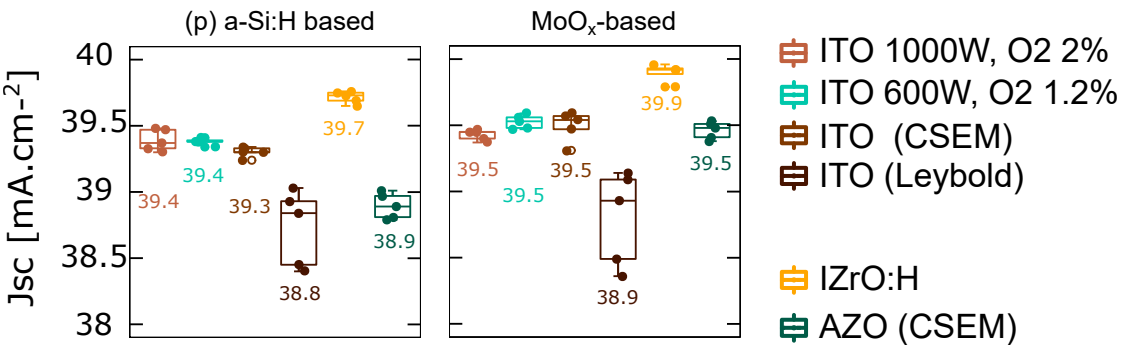

Figure C.3: J_{SC} of the (*p*)a-Si:H- and MoO_{3-x}-based solar cells, using different front TCOs. IZrO:H demonstrates the highest performances. As mentioned in Chapter 5, this MoO_{3-x}-based solar cells series underperformed, probably due to climatic perturbation during the process (high humidity) and experiment should be repeated to confirm the results.

D Appendices for Chapter 6

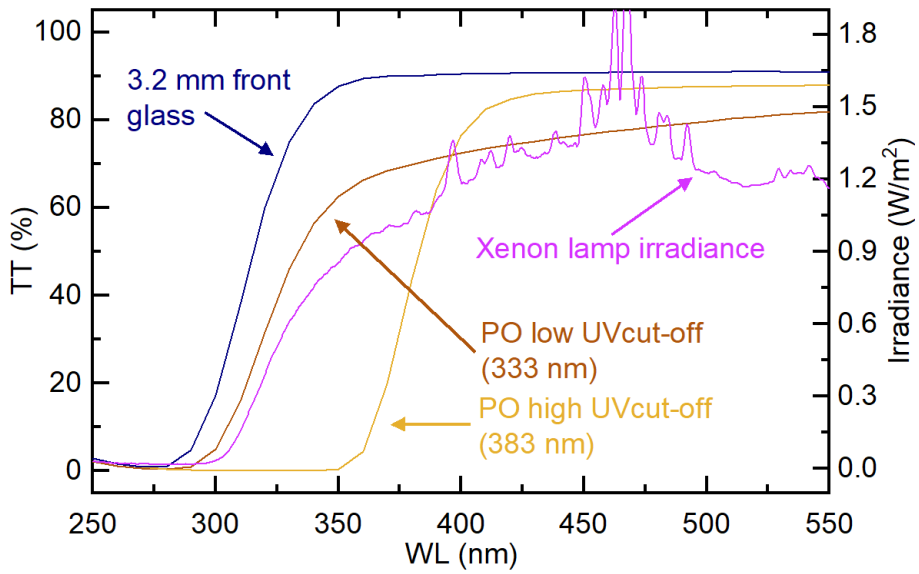

Figure D.1: Transmittance spectra of the glass sheet and the two encapsulant polymers used for UV-induced degradation. The Xenon lamp spectra is also showed.

E Appendices for Chapter 7

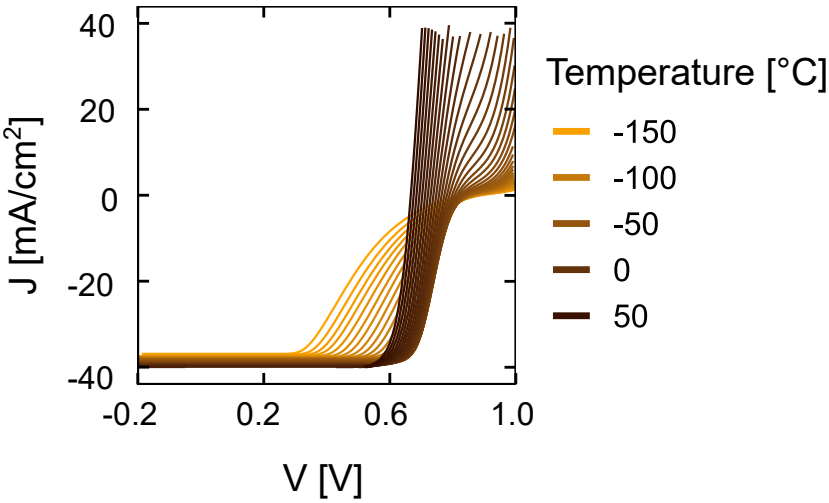

Figure E.1: J-V(T) showed at all the measured temperatures.

Bibliography

[Adachi 1988a] Chihaya Adachi, Shizuo Tokito, Tetsuo Tsutsui and Shogo Saito. *Electroluminescence in Organic Films with Three-Layer Structure.* Japanese Journal of Applied Physics, vol. 27, no. Part 2, No. 2, pages L269–L271, February 1988.

[Adachi 1988b] Chihaya Adachi, Shizuo Tokito, Tetsuo Tsutsui and Shogo Saito. *Organic Electroluminescent Device with a Three-Layer Structure.* Japanese Journal of Applied Physics, vol. 27, no. 4A, page L713, April 1988.

[Adachi 1990] Chihaya Adachi, Tetsuo Tsutsui and Shogo Saito. *Blue Light-emitting Organic Electroluminescent Devices.* Applied Physics Letters, vol. 56, no. 9, pages 799–801, February 1990.

[Adachi 1995] Chihaya Adachi, Kazukiyo Nagai and Nozomu Tamoto. *Molecular Design of Hole Transport Materials for Obtaining High Durability in Organic Electroluminescent Diodes.* Applied Physics Letters, vol. 66, no. 20, pages 2679–2681, May 1995.

[Adachi 2015] Daisuke Adachi, José Luis Hernández and Kenji Yamamoto. *Impact of Carrier Recombination on Fill Factor for Large Area Heterojunction Crystalline Silicon Solar Cell with 25.1% Efficiency.* Applied Physics Letters, vol. 107, no. 23, page 233506, December 2015.

[Adler 1970] David Adler and Julius Feinleib. *Electrical and Optical Properties of Narrow-Band Materials.* Physical Review B, vol. 2, no. 8, pages 3112–3134, October 1970.

[Ali 2018] Haider Ali, Supriya Koul, Geoffrey Gregory, James Bullock, Ali Javey, Akihiro Kushima and Kristopher O. Davis. *Thermal Stability of Hole-Selective Tungsten Oxide: In Situ Transmission Electron Microscopy Study.* Scientific Reports, vol. 8, no. 1, page 12651, 2018.

[Almora 2017] Osbel Almora, Luis G. Gerling, Cristóbal Voz, Ramón Alcubilla, Joaquim Puigdollers and Germà Garcia-Belmonte. *Superior Performance of V2O5 as Hole Selective Contact over Other Transition Metal Oxides in Silicon Heterojunction Solar Cells.* Solar Energy Materials and Solar Cells, vol. 168, pages 221–226, August 2017.

[Altermatt 1996] Pietro P. Altermatt, Gernot Heiser, Armin G. Aberle, Aihua Wang, Jianhua Zhao, Stephen J. Robinson, Stuart Bowden and Martin A. Green. *Spatially Resolved*

Analysis and Minimization of Resistive Losses in High-Efficiency Si Solar Cells. Progress in Photovoltaics: Research and Applications, vol. 4, no. 6, pages 399–414, 1996.

[Anderson 1974] J.S. Anderson and R.J.D Tilley. In Surface and Defect Properties of Solid, volume 3. London Chemical Society, London, m . w. roberts, j. m . thomas édition, 1974.

[Andersson 2011] L. Mattias Andersson, Christian Müller, Bekele H. Badada, Fengling Zhang, Uli Würfel and Olle Inganäs. *Mobility and Fill Factor Correlation in Geminate Recombination Limited Solar Cells.* Journal of Applied Physics, vol. 110, no. 2, page 024509, July 2011.

[Antognini 2021] Luca Antognini, Vincent Paratte, Jan Haschke, Jean Cattin, Julie Dréon, Mario Lehmann, Laurie-Lou Senaud, Quentin Jeangros, Christophe Ballif and Mathieu Boccard. *Influence of the Dopant Gas Precursor in P-Type Nanocrystalline Silicon Layers on the Performance of Front Junction Heterojunction Solar Cells.* IEEE Journal of Photovoltaics, vol. 11, no. 4, pages 944–956, July 2021.

[Araujo de Castro 2010] Fernando Araujo de Castro, Jakob Heier, Frank Nüesch and Roland Hany. *Origin of the Kink in Current-Density Versus Voltage Curves and Efficiency Enhancement of Polymer-C* $_{\backslash bf60}$ *Heterojunction Solar Cells.* IEEE Journal of Selected Topics in Quantum Electronics, vol. 16, no. 6, pages 1690–1699, November 2010.

[Arora 1982] N. D. Arora and J. R. Hauser. *Temperature Dependence of Silicon Solar Cell Characteristics.* Solar Energy Materials, vol. 6, no. 2, pages 151–158, January 1982.

[Bachmann 1976] K. J. Bachmann, E. Buehler, J. L. Shay and S. Wagner. *Polycrystalline Thin-film InP/CdS Solar Cell.* Applied Physics Letters, vol. 29, no. 2, pages 121–123, July 1976.

[Baldini 2017] E. Baldini, L. Chiodo, A. Dominguez, M. Palummo, S. Moser, M. Yazdi-Rizi, G. Auböck, B. P. P. Mallett, H. Berger, A. Magrez, C. Bernhard, M. Grioni, A. Rubio and M. Chergui. *Strongly Bound Excitons in Anatase TiO2 Single Crystals and Nanoparticles.* Nature Communications, vol. 8, no. 1, page 13, April 2017.

[Bao 2009] Qiaoliang Bao, Chang Ming Li, Lei Liao, Hongbin Yang, Wei Wang, Chang Ke, Qunliang Song, Haifeng Bao, Ting Yu, Kian Ping Loh and Jun Guo. *Electrical Transport and Photovoltaic Effects of Core–Shell CuO/C60nanowire Heterostructure.* Nanotechnology, vol. 20, no. 6, January 2009.

[Bao 2016] Jie Bao, Weiliang Wu, Zongtao Liu and Hui Shen. *Silicon Based Solar Cells Using a Multilayer Oxide as Emitter.* AIP Advances, vol. 6, no. 8, page 085304, August 2016.

[Baranovski 2006] Sergei Baranovski. Charge transport in disordered solids with applications in electronics, volume 17. John Wiley & Sons, 2006.

[Barraud 2013] L. Barraud, Z. C. Holman, N. Badel, P. Reiss, A. Descoeudres, C. Battaglia, S. De Wolf and C. Ballif. *Hydrogen-Doped Indium Oxide/Indium Tin Oxide Bilayers for High-Efficiency Silicon Heterojunction Solar Cells.* Solar Energy Materials and Solar Cells, vol. 115, pages 151–156, August 2013.

[Battaglia 2014a] Corsin Battaglia, Silvia Martín de Nicolás, Stefaan De Wolf, Xingtian Yin, Maxwell Zheng, Christophe Ballif and Ali Javey. *Silicon Heterojunction Solar Cell with Passivated Hole Selective MoOx Contact.* Applied Physics Letters, vol. 104, no. 11, page 113902, March 2014.

[Battaglia 2014b] Corsin Battaglia, Xingtian Yin, Maxwell Zheng, Ian D. Sharp, Teresa Chen, Stephen McDonnell, Angelica Azcatl, Carlo Carraro, Biwu Ma, Roya Maboudian, Robert. M. Wallace and Ali Javey. *Hole Selective MoOx Contact for Silicon Solar Cells.* Nano Letters, vol. 14, no. 2, pages 967–971, February 2014.

[Baumeister 1961] Philip W. Baumeister. *Optical Absorption of Cuprous Oxide.* Physical Review, vol. 121, no. 2, pages 359–362, January 1961.

[Bellingham 1991a] J. R. Bellingham, A. P. Mackenzie and W. A. Phillips. *Precise Measurements of Oxygen Content: Oxygen Vacancies in Transparent Conducting Indium Oxide Films.* Applied Physics Letters, vol. 58, no. 22, pages 2506–2508, June 1991.

[Bellingham 1991b] J. R. Bellingham, W. A. Phillips and C. J. Adkins. *Amorphous Indium Oxide.* Thin Solid Films, vol. 195, no. 1, pages 23–32, January 1991.

[Berry 2010] Joseph J. Berry, N. Edwin Widjonarko, Brian A. Bailey, Ajaya K. Sigdel, David S. Ginley and Dana C. Olson. *Surface Treatment of NiO Hole Transport Layers for Organic Solar Cells.* IEEE Journal of Selected Topics in Quantum Electronics, vol. 16, no. 6, pages 1649–1655, November 2010.

[Beyer 1989] W. Beyer, J. Herion and H. Wagner. *Fermi Energy Dependence of Surface Desorption and Diffusion of Hydrogen in A-Si:H.* Journal of Non-Crystalline Solids, vol. 114, no. PART 1, pages 217–219, 1989.

[Bivour 2012] Martin Bivour, Christian Reichel, Martin Hermle and Stefan W. Glunz. *Improving the A-Si:H(p) Rear Emitter Contact of n-Type Silicon Solar Cells.* Solar Energy Materials and Solar Cells, vol. 106, pages 11–16, 2012.

[Bivour 2013] Martin Bivour, Sebastian Schröer and Martin Hermle. *Numerical Analysis of Electrical TCO / a-Si:H(p) Contact Properties for Silicon Heterojunction Solar Cells.* Energy Procedia, vol. 38, pages 658–669, January 2013.

[Bivour 2014] M. Bivour, M. Reusch, S. Schröer, F. Feldmann, J. Temmler, H. Steinkemper and M. Hermle. *Doped Layer Optimization for Silicon Heterojunctions by Injection-Level-Dependent Open-Circuit Voltage Measurements.* IEEE Journal of Photovoltaics, vol. 4, no. 2, pages 566–574, March 2014.

[Bivour 2015] Martin Bivour, Jan Temmler, Heiko Steinkemper and Martin Hermle. *Molybdenum and Tungsten Oxide: High Work Function Wide Band Gap Contact Materials for Hole Selective Contacts of Silicon Solar Cells.* Solar Energy Materials and Solar Cells, vol. 142, pages 34–41, November 2015.

[Bivour 2016] Martin Bivour, Jan Temmler, Florian Zähringer, Stefan Glunz and Martin Hermle. *High Work Function Metal Oxides for the Hole Contact of Silicon Solar Cells.* In 2016 IEEE 43rd Photovoltaic Specialists Conference (PVSC), pages 0215–0220, June 2016.

[Bivour 2017] Martin Bivour, Florian Zähringer, Paul Ndione and Martin Hermle. *Sputter-Deposited WOx and MoOx for Hole Selective Contacts.* Energy Procedia, vol. 124, pages 400–405, September 2017.

[Bludau 1974] W. Bludau, A. Onton and W. Heinke. *Temperature Dependence of the Band Gap of Silicon.* Journal of Applied Physics, vol. 45, no. 4, pages 1846–1848, April 1974.

[Boccard 2012] Mathieu Boccard, Corsin Battaglia, Franz-Josef Haug, Matthieu Despeisse and Christophe Ballif. *Light Trapping in Solar Cells: Analytical Modeling.* Applied Physics Letters, vol. 101, no. 15, page 151105, 2012.

[Boccard 2015] Mathieu Boccard, Laura Ding, Priyaranga Koswatta, Mariana Bertoni and Zachary Holman. *Evaluation of Metal Oxides Prepared by Reactive Sputtering as Carrier-Selective Contacts for Crystalline Silicon Solar Cells.* In 2015 IEEE 42nd Photovoltaic Specialist Conference (PVSC), pages 1–3, June 2015.

[Boccard 2021] Mathieu Boccard, Luca Antognini, Vincent Paratte, Jan Haschke, Minh Truong, Jean Cattin, Julie Dreon, Wenjie Lin, Lou Laurie Senaud, Bertrand Paviet-Salomon, Sylvain Nicolay, Matthieu Despeisse and Christophe Ballif. *Hole-Selective Front Contact Stack Enabling 24.1%-Efficient Silicon Heterojunction Solar Cells.* IEEE Journal of Photovoltaics, vol. 11, no. 1, pages 9–15, 2021.

[Bowden 2001] S. Bowden and Ajeet Rohatgi. *Rapid and Accurate Determination of Series Resistance and Fill Factor Losses in Industrial Silicon Solar Cells.* October 2001.

[BP 2020] BP. *Energy Mix.* Rapport technique, Our World in Data, based on the BP Statistical Review of World Energy, https://ourworldindata.org/energy-mix ; https://www.bp.com/en/global/corporate/energy-economics/statistical-review-of-world-energy.html, 2020.

[Brendel 2016] Rolf Brendel and Robby Peibst. *Contact Selectivity and Efficiency in Crystalline Silicon Photovoltaics.* IEEE Journal of Photovoltaics, vol. 6, no. 6, pages 1413–1420, November 2016.

[Bullock 2014] James Bullock, Andres Cuevas, Thomas Allen and Corsin Battaglia. *Molybdenum Oxide MoOx: A Versatile Hole Contact for Silicon Solar Cells.* Applied Physics Letters, vol. 105, no. 23, page 232109, December 2014.

[Bullock 2015] James Bullock, Christian Samundsett, Andrés Cuevas, Di Yan, Yimao Wan and Thomas Allen. *Proof-of-Concept p-Type Silicon Solar Cells With Molybdenum Oxide Local Rear Contacts.* IEEE Journal of Photovoltaics, vol. 5, no. 6, pages 1591–1594, November 2015.

[Bullock 2016] James Bullock, Mark Hettick, Jonas Geissbühler, Alison J. Ong, Thomas Allen, Carolin M. Sutter-Fella, Teresa Chen, Hiroki Ota, Ethan W. Schaler, Stefaan De Wolf, Christophe Ballif, Andrés Cuevas and Ali Javey. *Efficient Silicon Solar Cells with Dopant-Free Asymmetric Heterocontacts.* Nature Energy, vol. 1, no. 3, page 15031, March 2016.

[Bullock 2018] James Bullock, Yimao Wan, Zhaoran Xu, Stephanie Essig, Mark Hettick, Hanchen Wang, Wenbo Ji, Mathieu Boccard, Andres Cuevas, Christophe Ballif, others and Ali Javey. *Stable Dopant-Free Asymmetric Heterocontact Silicon Solar Cells with Efficiencies above 20%.* ACS Energy Letters, vol. 3, no. 3, pages 508–513, March 2018.

[Bullock 2019] James Bullock, Yimao Wan, Mark Hettick, Xu Zhaoran, Sieu Pheng Phang, Di Yan, Hanchen Wang, Wenbo Ji, Chris Samundsett, Ziv Hameiri, Daniel Macdonald, Andres Cuevas and Ali Javey. *Dopant-Free Partial Rear Contacts Enabling 23% Silicon Solar Cells.* Advanced Energy Materials, vol. 9, no. 9, page 1803367, March 2019.

[Burrows 1994] P. E. Burrows, L. S. Sapochak, D. M. McCarty, S. R. Forrest and M. E. Thompson. *Metal Ion Dependent Luminescence Effects in Metal Tris-quinolate Organic Heterojunction Light Emitting Devices.* Applied Physics Letters, vol. 64, no. 20, pages 2718–2720, May 1994.

[Burstein 1954] Elias Burstein. *Anomalous Optical Absorption Limit in InSb.* Physical Review, vol. 93, no. 3, pages 632–633, February 1954.

[Calnan 2010] S. Calnan and A. N. Tiwari. *High Mobility Transparent Conducting Oxides for Thin Film Solar Cells.* Thin Solid Films, vol. 518, no. 7, pages 1839–1849, January 2010.

[Cattin 2019] Jean Cattin. *Characterisation of Silicon Heterojunction Solar Cells Beyond Standard Test Conditions.* PhD thesis, 2019.

[Cattin 2020] Jean Cattin, Mathieu Boccard and Christophe Ballif. *Characterization of Silicon Heterojunction Solar Cells beyond Standard Test Conditions.* PhD thesis, 2020.

[Cattin 2021] Jean Cattin, Laurie-Lou Senaud, Jan Haschke, Bertrand Paviet-Salomon, Matthieu Despeisse, Christophe Ballif and Mathieu Boccard. *Influence of Light Soaking on Silicon Heterojunction Solar Cells With Various Architectures.* IEEE Journal of Photovoltaics, vol. 11, no. 3, pages 575–583, May 2021.

[Centurioni 2003] Emanuele Centurioni and Daniele Iencinella. *Role of Front Contact Work Function on Amorphous Silicon/Crystalline Silicon Heterojunction Solar Cell Performance.* IEEE Electron Device Letters, vol. 24, no. 3, pages 177–179, 2003.

[Chan 2002] I-Min Chan, Tsung-Yi Hsu and Franklin C. Hong. *Enhanced Hole Injections in Organic Light-Emitting Devices by Depositing Nickel Oxide on Indium Tin Oxide Anode.* Applied Physics Letters, vol. 81, no. 10, pages 1899–1901, September 2002.

[Chan 2004] I-Min Chan and Franklin C. Hong. *Improved Performance of the Single-Layer and Double-Layer Organic Light Emitting Diodes by Nickel Oxide Coated Indium Tin Oxide Anode.* Thin Solid Films, vol. 450, no. 2, pages 304–311, March 2004.

[Chang 2005] Chan-Ching Chang, Jenn-Fang Chen, Shiao-Wen Hwang and Chin H. Chen. *Highly Efficient White Organic Electroluminescent Devices Based on Tandem Architecture.* Applied Physics Letters, vol. 87, no. 25, page 253501, December 2005.

[Chavali 2014] Raghu Vamsi Krishna Chavali, John Robert Wilcox, Biswajit Ray, Jeffery Lynn Gray and Muhammad Ashraful Alam. *Correlated Nonideal Effects of Dark and Light I–V Characteristics in a-Si/c-Si Heterojunction Solar Cells.* IEEE Journal of Photovoltaics, vol. 4, no. 3, pages 763–771, May 2014.

[Chen 2013] Lung-Chien Chen. *Review of Preparation and Optoelectronic Characteristics of Cu2O-based Solar Cells with Nanostructure.* Materials Science in Semiconductor Processing, vol. 16, no. 5, pages 1172–1185, October 2013.

[Chen 2015] Wei Chen, Yongzhen Wu, Jian Liu, Chuanjiang Qin, Xudong Yang, Ashraful Islam, Yi-Bing Cheng and Liyuan Han. *Hybrid Interfacial Layer Leads to Solid Performance Improvement of Inverted Perovskite Solar Cells.* Energy & Environmental Science, vol. 8, no. 2, pages 629–640, February 2015.

[Chiang 2018] Chien-Hung Chiang, Cheng-Chiang Chen, Mohammad Khaja Nazeeruddin and Chun-Guey Wu. *A Newly Developed Lithium Cobalt Oxide Super Hydrophilic Film for Large Area, Thermally Stable and Highly Efficient Inverted Perovskite Solar Cells.* Journal of Materials Chemistry A, vol. 6, no. 28, pages 13751–13760, 2018.

[Cho 1998] Yong-Hoon Cho, G. H. Gainer, A. J. Fischer, J. J. Song, S. Keller, U. K. Mishra and S. P. DenBaars. *"S-shaped" Temperature-Dependent Emission Shift and Carrier Dynamics in InGaN/GaN Multiple Quantum Wells.* Applied Physics Letters, vol. 73, no. 10, pages 1370–1372, September 1998.

[Cho 2019] Jinyoun Cho, Neerja Nawal, Afshin Hadipour, Maria Recaman Payo, Arvid van der Heide, Hariharsudan Sivaramakrishnan Radhakrishnan, Maarten Debucquoy, Ivan Gordon, Jozef Szlufcik and Jef Poortmans. *Interface Analysis and Intrinsic Thermal Stability of MoOx Based Hole-Selective Contacts for Silicon Heterojunction Solar Cells.* Solar Energy Materials and Solar Cells, vol. 201, page 110074, October 2019.

[Chua 1971] L. Chua. *Memristor-The Missing Circuit Element.* IEEE Transactions on Circuit Theory, vol. 18, no. 5, pages 507–519, September 1971.

[Chynoweth 1957] A. G. Chynoweth and K. G. McKay. *Internal Field Emission in Silicon p - n Junctions.* Physical Review, vol. 106, no. 3, pages 418–426, May 1957.

[Cox 1992] P. A. Cox. Transition Metal Oxides: An Introduction to their Electronic Structure and Properties. Oxford University Press, 1992.

[Cruz 2004] L. R Cruz, C Legnani, I. G Matoso, C. L Ferreira and H. R Moutinho. *Influence of Pressure and Annealing on the Microstructural and Electro-Optical Properties of RF Magnetron Sputtered ITO Thin Films.* Materials Research Bulletin, vol. 39, no. 7, pages 993–1003, June 2004.

[Cruz 2019] Alexandros Cruz, Er-Chien Wang, Anna B. Morales-Vilches, Daniel Meza, Sebastian Neubert, Bernd Szyszka, Rutger Schlatmann and Bernd Stannowski. *Effect of Front TCO on the Performance of Rear-Junction Silicon Heterojunction Solar Cells: Insights from Simulations and Experiments.* Solar Energy Materials and Solar Cells, vol. 195, pages 339–345, June 2019.

[Cuevas 2015] Andres Cuevas, Thomas Allen, James Bullock, Yimao Wan, Di Yan and Xinyu Zhang. *Skin Care for Healthy Silicon Solar Cells.* In 2015 IEEE 42nd Photovoltaic Specialist Conference (PVSC), pages 1–6, June 2015.

[Cuevas 2018] Andres Cuevas, Yimao Wan, Di Yan, Christian Samundsett, Thomas Allen, Xinyu Zhang, Jie Cui and James Bullock. *Carrier Population Control and Surface Passivation in Solar Cells.* Solar Energy Materials and Solar Cells, vol. 184, pages 38–47, September 2018.

[Cui 2017] Jie Cui, Yimao Wan, Yanfeng Cui, Yifeng Chen, Pierre Verlinden and Andres Cuevas. *Highly Effective Electronic Passivation of Silicon Surfaces by Atomic Layer Deposited Hafnium Oxide.* Applied Physics Letters, vol. 110, no. 2, page 021602, January 2017.

[De Wolf 2009] Stefaan De Wolf and Michio Kondo. *Nature of Doped A-Si:H/c-Si Interface Recombination.* Journal of Applied Physics, vol. 105, no. 10, 2009.

[De Wolf 2011] Stefaan De Wolf, Bénédicte Demaurex, Antoine Descoeudres and Christophe Ballif. *Very Fast Light-Induced Degradation of a-Si:H/c-Si(100) Interfaces.* Physical Review B, vol. 83, no. 23, page 233301, June 2011.

[Deneuville 1979] A. Deneuville and M. H. Brodsky. *Influence of Preparation Conditions on Forward-Bias Currents of Amorphous Silicon Schottky Diodes.* Journal of Applied Physics, vol. 50, no. 3, pages 1414–1421, 1979.

[Descoeudres 2011] A. Descoeudres, L. Barraud, Stefaan De Wolf, B. Strahm, D. Lachenal, C. Guérin, Z. C. Holman, F. Zicarelli, B. Demaurex, J. Seif, J. Holovsky and C. Ballif. *Improved Amorphous/Crystalline Silicon Interface Passivation by Hydrogen Plasma Treatment.* Applied Physics Letters, vol. 99, no. 12, page 123506, September 2011.

[DeWolf 2012] Stefaan DeWolf, Antoine Descoeudres, Zachary C. Holman and Christophe Ballif. *High-Efficiency Silicon Heterojunction Solar Cells: A Review.* Green, vol. 2, no. 1, pages 7–24, 2012.

[Dréon 2020] Julie Dréon, Quentin Jeangros, Jean Cattin, Jan Haschke, Luca Antognini, Christophe Ballif and Mathieu Boccard. *23.5%-Efficient Silicon Heterojunction Silicon Solar Cell Using Molybdenum Oxide as Hole-Selective Contact.* Nano Energy, vol. 70, page 104495, April 2020.

[Dréon 2021] Julie Dréon, Jean Cattin, Gabriel Christmann, Davi Fébba, Vincent Paratte, Luca Antognini, Wenjie Lin, Sylvain Nicolay, Christophe Ballif and Mathieu Boccard. *Performance Limitations and Analysis of Silicon Heterojunction Solar Cells Using Ultra-Thin MoOx Hole-Selective Contacts.* IEEE Journal of Photovoltaics, vol. 11, no. 5, pages 1158–1166, September 2021.

[Drude 1900] P. Drude. *Zur Elektronentheorie Der Metalle.* Annalen der Physik, vol. 306, no. 3, pages 566–613, 1900.

[Du 2021a] Guanlin Du, Yanhui Bai, Jin Huang, Juan Zhang, Jilei Wang, Yinyue Lin, Linfeng Lu, Liyou Yang, Shaojuan Bao, Zhongxi Huang, Xiaoyuan Chen, Min Yin and Dongdong Li. *Surface Passivation of ITO on Heterojunction Solar Cells with Enhanced Cell Performance and Module Reliability.* ECS Journal of Solid State Science and Technology, vol. 10, no. 3, page 035008, March 2021.

[Du 2021b] Guanlin Du, Le Li, Xinbo Yang, Xi Zhou, Zhenhuang Su, Peihong Cheng, Yinyue Lin, Linfeng Lu, Jilei Wang, Liyou Yang, Xingyu Gao, Xiaoyuan Chen and Dongdong Li. *Improved V2OX Passivating Contact for P-Type Crystalline Silicon Solar Cells by Oxygen Vacancy Modulation with a SiOX Tunnel Layer.* Advanced Materials Interfaces, vol. n/a, no. n/a, page 2100989, 2021.

[Eades 1984a] Wendell D. Eades and Richard M. Swanson. *Determination of the Capture Cross Section and Degeneracy Factor of Si-SiO2 Interface States.* Applied Physics Letters, vol. 44, no. 10, pages 988–990, May 1984.

[Eades 1984b] Wendell D. Eades and Richard M. Swanson. *Improvements in the Determination of Interface State Density Using Deep Level Transient Spectroscopy.* Journal of Applied Physics, vol. 56, no. 6, pages 1744–1751, September 1984.

[El Mhamdi 2014] El Mahdi El Mhamdi, Jakub Holovsky, Bénédicte Demaurex, Christophe Ballif and Stefaan De Wolf. *Is Light-Induced Degradation of a-Si:H/c-Si Interfaces Reversible?* Applied Physics Letters, vol. 104, no. 25, page 252108, June 2014.

[Elfadill 2015] Nezar G. Elfadill, M. R. Hashim and K. A. Th. Thabit. *The Role of Using Seed-Layer Assisted Electrodeposition Method on the Growth and the Photovoltaic Properties of p-Cu2O/n-Si Heterojunctions.* Journal of Materials Science: Materials in Electronics, vol. 26, no. 2, pages 985–991, 2015.

[Ellis 2008] D. S. Ellis, J. P. Hill, S. Wakimoto, R. J. Birgeneau, D. Casa, T. Gog and Young-June Kim. *Charge-Transfer Exciton in La 2 CuO 4 Probed with Resonant Inelastic x-Ray Scattering.* Physical Review B, vol. 77, no. 6, page 060501, February 2008.

[Essig 2018] Stephanie Essig, Julie Dréon, Esteban Rucavado, Mathias Mews, Takashi Koida, Mathieu Boccard, Jérémie Werner, Jonas Geissbühler, Philipp Löper, Monica Morales-Masis, Lars Korte, Stefaan De Wolf and Christophe Ballif. *Toward Annealing-Stable Molybdenum-Oxide-Based Hole-Selective Contacts For Silicon Photovoltaics.* Solar RRL, vol. 2, no. 4, page 1700227, 2018.

[Faes 2018] Antonin Faes, Agata Lachowicz, Armand Bettinelli, Pierre-Jean Ribeyron, Jean-François Lerat, Delfina Munoz, Jonas Geissbühler, Heng-Yu Li, Christophe Ballif and Matthieu Despeisse. *Metallization and Interconnection for High-Efficiency Bifacial Silicon Heterojunction Solar Cells and Modules.* page 13, 2018.

[Faughnan 1975] B.W. Faughnan, R.S. Crandall and P.M. Heyman. *Electrochromism in WO3 Amorphous Films.* vol. RCA Rev. 36, pages 177–197, 1975.

[Fay 2003] Sylvie Fay. *L'OXYDE DE ZINC PAR DÉPOT CHIMIQUE EN PHASE VAPEUR COMME CONTACT ÉLECTRIQUE TRANSPARENT ET DIFFUSEUR DE LUMIÈRE POUR LES CELLULES SOLAIRES.* TH2899, EPFL, 2003.

[Finck 2013] B. Y. Finck and B. J. Schwartz. *Understanding the Origin of the S-curve in Conjugated Polymer/Fullerene Photovoltaics from Drift-Diffusion Simulations.* Applied Physics Letters, vol. 103, no. 5, page 053306, July 2013.

[Fioretti 2019] Angela N Fioretti, Mathieu Boccard, Raphael Monnard and Christophe Ballif. *Low-Temperature $ p $-Type Microcrystalline Silicon as Carrier Selective Contact for Silicon Heterojunction Solar Cells.* IEEE Journal of Photovoltaics, 2019.

[Fisher 1946] R. A. Fisher. *Statistical Methods for Research Workers.* Statistical methods for research workers., no. 10th. ed., 1946.

[Fujiwara 2007] Hiroyuki Fujiwara and Michio Kondo. *Effects of a-Si:H Layer Thicknesses on the Performance of a-Si:H/c-Si Heterojunction Solar Cells.* Journal of Applied Physics, vol. 101, no. 5, page 054516, March 2007.

[Gao 2012] Fei Gao, Xiao-Jing Liu, Jun-Shan Zhang, Mei-Zhou Song and Ning Li. *Photovoltaic Properties of the P-CuO/n-Si Heterojunction Prepared through Reactive Magnetron Sputtering.* Journal of Applied Physics, vol. 111, no. 8, page 084507, April 2012.

[Gao 2018] Ming Gao, Dongyun Chen, Baichao Han, Wenlei Song, Miao Zhou, Xiaomin Song, Fei Xu, Lei Zhao, Yonghua Li and Zhongquan Ma. *Bifunctional Hybrid A-SiOx(Mo) Layer for Hole-Selective and Interface Passivation of Highly Efficient MoOx/a-SiOx(Mo)/n-Si Heterojunction Photovoltaic Device.* ACS Applied Materials & Interfaces, vol. 10, no. 32, pages 27454–27464, August 2018.

[Gao 2020] Yang Gao, Qiming Sun, Jason M. Yu, Mario Motta, James McClain, Alec F. White, Austin J. Minnich and Garnet Kin-Lic Chan. *Electronic Structure of Bulk Manganese Oxide and Nickel Oxide from Coupled Cluster Theory.* Physical Review B, vol. 101, no. 16, page 165138, April 2020.

[García-Hernansanz 2018] R. García-Hernansanz, E. García-Hemme, D. Montero, J. Olea, A. del Prado, I. Mártil, C. Voz, L.G. Gerling, J. Puigdollers and R. Alcubilla. *Transport Mechanisms in Silicon Heterojunction Solar Cells with Molybdenum Oxide as a Hole Transport Layer.* Solar Energy Materials and Solar Cells, vol. 185, pages 61–65, 2018.

[García-Sánchez 2013] Francisco J. García-Sánchez, Denise Lugo-Muñoz, Juan Muci and Adelmo Ortiz-Conde. *Lumped Parameter Modeling of Organic Solar Cells' S-Shaped I–V Characteristics.* IEEE Journal of Photovoltaics, vol. 3, no. 1, pages 330–335, January 2013.

[Garcia 2012] Andres Garcia, Gregory C. Welch, Erin L. Ratcliff, David S. Ginley, Guillermo C. Bazan and Dana C. Olson. *Improvement of Interfacial Contacts for New Small-Molecule Bulk-Heterojunction Organic Photovoltaics.* Advanced Materials, vol. 24, no. 39, pages 5368–5373, 2012.

[GCP 2021] GCP. *CO2 Emissions by Fuel.* Rapport technique, Our World in Data, based on The Global Carbon Project. Supplemental data of Global Carbon Project, https://doi.org/10.18160/gcp-2021, 2021.

[Geissbühler 2015] Jonas Geissbühler, Jérémie Werner, Silvia Martin de Nicolas, Loris Barraud, Aïcha Hessler-Wyser, Matthieu Despeisse, Sylvain Nicolay, Andrea Tomasi, Bjoern Niesen, Stefaan De Wolf and Christophe Ballif. *22.5% Efficient Silicon Heterojunction Solar Cell with Molybdenum Oxide Hole Collector.* Applied Physics Letters, vol. 107, no. 8, page 081601, August 2015.

[Gerling 2015a] Luis G. Gerling, Somnath Mahato, Anna Morales-Vilches, Gerard Masmitja, Pablo Ortega, Cristobal Voz, Ramon Alcubilla and Joaquim Puigdollers. *Transition Metal Oxides as Hole-Selective Contacts in Silicon Heterojunctions Solar Cells.* Solar Energy Materials and Solar Cells, vol. 145, pages 109–115, 2015.

[Gerling 2015b] Luis G. Gerling, Somnath Mahato, Cristobal Voz, Ramon Alcubilla and Joaquim Puigdollers. *Characterization of Transition Metal Oxide/Silicon Heterojunctions for Solar Cell Applications.* Applied Sciences, vol. 5, no. 4, pages 695–705, December 2015.

[Gerling 2015c] Luis G. Gerling, Cristobal Voz, Ramón Alcubilla and Joaquim Puigdollers. *Origin of Passivation in Hole-Selective Transition Metal Oxides for Crystalline Silicon Heterojunction Solar Cells.* Journal of Materials Research, vol. 32, no. 2, pages 260–268, 2015.

[Gerling 2016] Luis G. Gerling, Gerard Masmitja, Cristobal Voz, Pablo Ortega, Joaquim Puigdollers and Ramón Alcubilla. *Back Junction N-Type Silicon Heterojunction Solar Cells with V2O5 Hole-selective Contact.* Energy Procedia, vol. 92, pages 633–637, August 2016.

[Gibson 2009] Elizabeth A. Gibson, Amanda L. Smeigh, Loïc Le Pleux, Jérôme Fortage, Gerrit Boschloo, Errol Blart, Yann Pellegrin, Fabrice Odobel, Anders Hagfeldt and Leif Hammarström. *A P-Type NiO-Based Dye-Sensitized Solar Cell with an Open-Circuit Voltage*

of 0.35 V. Angewandte Chemie International Edition, vol. 48, no. 24, pages 4402–4405, 2009.

[Glatthaar 2010] M. Glatthaar, J. Haunschild, R. Zeidler, M. Demant, J. Greulich, B. Michl, W. Warta, S. Rein and R. Preu. *Evaluating Luminescence Based Voltage Images of Silicon Solar Cells.* Journal of Applied Physics, vol. 108, no. 1, pages 1–5, 2010.

[Glunz 2007] S W Glunz, J Nekarda, H Mäckel and A Cuevas. *ANALYZING BACK CONTACTS OF SILICON SOLAR CELLS BY SUNS-VOC-MEASUREMENTS AT HIGH ILLUMINATION DENSITIES.* no. September, 2007.

[Goodenough 1971] John B. Goodenough. *Metallic Oxides.* Progress in Solid State Chemistry, vol. 5, pages 145–399, January 1971.

[Goodman 2008] Steven Goodman. *A Dirty Dozen: Twelve P-Value Misconceptions.* Seminars in Hematology, vol. 45, no. 3, pages 135–140, July 2008.

[Granqvist 1995] C. G. Granqvist. Handbook of Inorganic Electrochromic Materials. Elsevier, March 1995.

[Green 1982] M. A. Green. Solar cells: Operating principles, technology, and system applications. January 1982.

[Green 2003] Martin A. Green. *General Temperature Dependence of Solar Cell Performance and Implications for Device Modelling.* Progress in Photovoltaics: Research and Applications, vol. 11, no. 5, pages 333–340, 2003.

[Greenwood 1997] N. N. Greenwood and A. Earnshaw. Chemistry of the elements, volume Chapter 24. Butterworth-Heinemann, Oxford ; Boston, 2nd ed édition, 1997.

[Greiner 2012a] Mark T. Greiner, Lily Chai, Michael G. Helander, Wing-Man Tang and Zheng-Hong Lu. *Transition Metal Oxide Work Functions: The Influence of Cation Oxidation State and Oxygen Vacancies.* Advanced Functional Materials, vol. 22, no. 21, pages 4557–4568, 2012.

[Greiner 2012b] Mark T. Greiner, Michael G. Helander, Wing-Man Tang, Zhi-Bin Wang, Jacky Qiu and Zheng-Hong Lu. *Universal Energy-Level Alignment of Molecules on Metal Oxides.* Nature Materials, vol. 11, no. 1, pages 76–81, 2012.

[Greiner 2013a] Mark T. Greiner, Lily Chai, Michael G. Helander, Wing-Man Tang and Zheng-Hong Lu. *Metal/Metal-Oxide Interfaces: How Metal Contacts Affect the Work Function and Band Structure of MoO_3.* Advanced Functional Materials, vol. 23, no. 2, pages 215–226, January 2013.

[Greiner 2013b] Mark T. Greiner and Zheng-Hong Lu. *Thin-Film Metal Oxides in Organic Semiconductor Devices: Their Electronic Structures, Work Functions and Interfaces.* NPG Asia Materials, vol. 5, no. 7, pages e55–e55, 2013.

[Grilli 2016] Maria Luisa Grilli, Sakir Aydogan and Mehmet Yilmaz. *A Study on Non-Stoichiometric p-NiOx/n-Si Heterojunction Diode Fabricated by RF Sputtering: Determination of Diode Parameters.* Superlattices and Microstructures, vol. 100, pages 924–933, December 2016.

[Gudovskikh 2017] Alexander S. Gudovskikh, Alexander V. Uvarov, Ivan A. Morozov, Artem I. Baranov, Dmitry A. Kudryashov, Ekaterina V. Nikitina and Jean-Paul Kleider. *N-GaP/p-Si Heterojunction Solar Cells Fabricated by PE-ALD.* physica status solidi c, vol. 14, no. 10, page 1700150, 2017.

[Guo 2014] Yuzheng Guo and John Robertson. *Origin of the High Work Function and High Conductivity of MoO_3.* Applied Physics Letters, vol. 105, no. 22, page 222110, December 2014.

[Gupta 2010] Dhritiman Gupta, Sabyasachi Mukhopadhyay and K. S. Narayan. *Fill Factor in Organic Solar Cells.* Solar Energy Materials and Solar Cells, vol. 94, no. 8, pages 1309–1313, August 2010.

[Han 2008] H. Han, N. D. Theodore and T. L. Alford. *Improved Conductivity and Mechanism of Carrier Transport in Zinc Oxide with Embedded Silver Layer.* Journal of Applied Physics, vol. 103, no. 1, page 013708, January 2008.

[Haschke 2019a] Jan Haschke, Raphael Lemerle, Brahim Aissa, Amir A. Abdallah, Maulid M. Kivambe, Mathieu Boccard and Christophe Ballif. *Annealing of Silicon Heterojunction Solar Cells: Interplay of Solar Cell and Indium Tin Oxide Properties.* IEEE Journal of Photovoltaics, vol. 9, no. 5, pages 1202–1207, September 2019.

[Haschke 2019b] Jan Haschke, Raphaël Lemerle, Brahim Aïssa, Amir A. Abdallah, Maulid M. Kivambe, Mathieu Boccard and Christophe Ballif. *Annealing of Silicon Heterojunction Solar Cells: Interplay of Solar Cell and Indium Tin Oxide Properties.* IEEE Journal of Photovoltaics, vol. 9, no. 5, pages 1202–1207, September 2019.

[Haschke 2019c] Jan Haschke, Christoph Messmer, Jean Cattin, Martin Bivour, Mathieu Boccard and Christophe Ballif. *Injection-Dependent Lateral Resistance in Front-Junction Solar Cells with Nc-Si : H and a-Si : H Hole Selective Contact.* In PVSC-46 Chicago, 2019.

[Haug 2021] F. J. Haug and C. Ballif. *A Recalculation of the Efficiency Limit in Crystalline Si/Si Tandem Solar Cells.* Solar Energy Materials and Solar Cells, vol. 224, page 111008, June 2021.

[He 2003] Tao He and Jiannian Yao. *Photochromism of Molybdenum Oxide.* Journal of Photochemistry and Photobiology C: Photochemistry Reviews, vol. 4, no. 2, pages 125–143, October 2003.

[Helfrich 1965] W. Helfrich and W. G. Schneider. *Recombination Radiation in Anthracene Crystals.* Physical Review Letters, vol. 14, no. 7, pages 229–231, February 1965.

[Henrich 1996] Victor E. Henrich and P. A. Cox. The Surface Science of Metal Oxides. Cambridge University Press, 1996.

[Herasimenka 2016] Stanislau Y Herasimenka, William J Dauksher, Mathieu Boccard and Stuart Bowden. *ITO/SiOx:H Stacks for Silicon Heterojunction Solar Cells.* Solar Energy Materials and Solar Cells, vol. 158, pages 98–101, December 2016.

[Hirashima 1986] Hiroshi Hirashima, Michihisa Ide and Tetsuro Yoshida. *Memory Switching of V2O5/TeO2 Glasses.* Journal of Non-Crystalline Solids, vol. 86, no. 3, pages 327–335, October 1986.

[Holman 2012] Zachary C. Holman, Antoine Descoeudres, Loris Barraud, Fernando Zicarelli Fernandez, Johannes P. Seif, Stefaan De Wolf and Christophe Ballif. *Current Losses at the Front of Silicon Heterounction Solar Cells.* IEEE Journal of Photovoltaics, vol. 2, no. No. 1, 2012.

[Hong 2011] Kihyon Hong, Kisoo Kim, Sungjun Kim, Illhwan Lee, Hyunsu Cho, Seunghyup Yoo, Ho Won Choi, Nam-Yang Lee, Yoon-Heung Tak and Jong-Lam Lee. *Optical Properties of WO3/Ag/WO3 Multilayer As Transparent Cathode in Top-Emitting Organic Light Emitting Diodes.* The Journal of Physical Chemistry C, vol. 115, no. 8, pages 3453–3459, March 2011.

[Hotovy 1999] I Hotovy, J Huran, L Spiess, S Hascik and V Rehacek. *Preparation of Nickel Oxide Thin Films for Gas Sensors Applications.* Sensors and Actuators B: Chemical, vol. 57, no. 1, pages 147–152, September 1999.

[Hüfner 1994] S. Hüfner. *Electronic Structure of NiO and Related 3d-Transition-Metal Compounds.* Advances in Physics, vol. 43, no. 2, pages 183–356, April 1994.

[Hwang 2009] Jaehyung Hwang, Alan Wan and Antoine Kahn. *Energetics of Metal–Organic Interfaces: New Experiments and Assessment of the Field.* Materials Science and Engineering: R: Reports, vol. 64, no. 1, pages 1–31, March 2009.

[Ibarra-Michel 2022] Jesus Ibarra-Michel, Julie Dreon, Mathieu Boccard, James Bullock and Bart Macco. *Carrier-Selective Contacts Using Metal Compounds for Crystalline Silicon Solar Cells.* Accepted, 2022.

[IEA 2019] IEA. *World Energy Outlook.* Rapport technique, International Energy Agency, https://www.iea.org/reports/world-energy-outlook2019/electricity, 2019.

[Il Park 2011] Sang Il Park, Seung Jae Baik, Jong-San Im, Liang Fang, Jin-Wan Jeon and Koeng Su Lim. *Towards a High Efficiency Amorphous Silicon Solar Cell Using Molybdenum Oxide as a Window Layer Instead of Conventional P-Type Amorphous Silicon Carbide.* Applied Physics Letters, vol. 99, no. 6, page 063504, 2011.

[Imran 2016] Hassan Imran, Tarek M. Abdolkader and Nauman Z. Butt. *Carrier-Selective NiO/Si and TiO2/Si Contacts for Silicon Heterojunction Solar Cells.* IEEE Transactions on Electron Devices, vol. 63, no. 9, pages 3584–3590, September 2016.

[Ingle 2001] N. J. C. Ingle, R. H. Hammond and M. R. Beasley. *Growth of the Cr Oxides via Activated Oxygen Reactive Molecular Beam Epitaxy: Comparison of the Mo and W Oxides.* Journal of Applied Physics, vol. 89, no. 8, pages 4631–4635, April 2001.

[IPCC 2018] IPCC. *IPCC Special Report on the Impacts of Global Warming of 1.5 °C - Summary for Policy Makers.* Rapport technique, Intergovernmental Panel for Climate Change (IPCC), October 2018.

[IPCC 2021] IPCC. *Climate Change 2021: The Physical Science Basis.* Rapport technique, Intergovernmental Panel for Climate Change (IPCC), https://www.ipcc.ch/2021/08/09/ar6-wg1-20210809-pr/, August 2021.

[Irfan 2010] Irfan, Huanjun Ding, Yongli Gao, Do Young Kim, Jegadesan Subbiah and Franky So. *Energy Level Evolution of Molybdenum Trioxide Interlayer between Indium Tin Oxide and Organic Semiconductor.* Applied Physics Letters, vol. 96, no. 7, page 073304, February 2010.

[Irfan 2012] Irfan Irfan, Alexander James Turinske, Zhenan Bao and Yongli Gao. *Work Function Recovery of Air Exposed Molybdenum Oxide Thin Films.* Applied Physics Letters, vol. 101, no. 9, page 093305, 2012.

[Irwin 2008] Michael D. Irwin, D. Bruce Buchholz, Alexander W. Hains, Robert P. H. Chang and Tobin J. Marks. *P-Type Semiconducting Nickel Oxide as an Efficiency-Enhancing Anode Interfacial Layer in Polymer Bulk-Heterojunction Solar Cells.* Proceedings of the National Academy of Sciences, vol. 105, no. 8, pages 2783–2787, February 2008.

[Irwin 2011] Michael D. Irwin, Jonathan D. Servaites, D. Bruce Buchholz, Benjamin J. Leever, Jun Liu, Jonathan D. Emery, Ming Zhang, Jung-Hwan Song, Michael F. Durstock, Arthur J. Freeman, Michael J. Bedzyk, Mark C. Hersam, Robert P. H. Chang, Mark A. Ratner and Tobin J. Marks. *Structural and Electrical Functionality of NiO Interfacial Films in Bulk Heterojunction Organic Solar Cells.* Chemistry of Materials, vol. 23, no. 8, pages 2218–2226, April 2011.

[Ishii 1997] H. Ishii and K. Seki. *Energy Level Alignment at Organic/Metal Interfaces Studied by UV Photoemission: Breakdown of Traditional Assumption of a Common Vacuum Level at the Interface.* IEEE Transactions on Electron Devices, vol. 44, no. 8, pages 1295–1301, August 1997.

[Islam 2014] Raisul Islam and Krishna C. Saraswat. *Metal/Insulator/Semiconductor Carrier Selective Contacts for Photovoltaic Cells.* In 2014 IEEE 40th Photovoltaic Specialist Conference (PVSC), pages 0285–0289, June 2014.

[Islam 2017] Raisul Islam, Gang Chen, Pranav Ramesh, Junkyo Suh, Nobi Fuchigami, Donovan Lee, Karl A. Littau, Kurt Weiner, Reuben T. Collins and Krishna C. Saraswat. *Investigation of the Changes in Electronic Properties of Nickel Oxide (NiOx) Due to UV/Ozone Treatment.* ACS Applied Materials & Interfaces, vol. 9, no. 20, pages 17201–17207, May 2017.

[ITRPV 2020] ITRPV. *International Technology Roadmap for Photovoltaic. Results 2019 Including Maturity Report 2020.* Rapport technique, ITRPV, 2020.

[ITRPV 2021] ITRPV. *International Technology Roadmap for Photovoltaic. Results 2020.* Rapport technique, ITRPV, 2021.

[Janssen 2007] A. G. F. Janssen, T. Riedl, S. Hamwi, H.-H. Johannes and W. Kowalsky. *Highly Efficient Organic Tandem Solar Cells Using an Improved Connecting Architecture.* Applied Physics Letters, vol. 91, no. 7, page 073519, August 2007.

[Jeng 2014] Jun-Yuan Jeng, Kuo-Cheng Chen, Tsung-Yu Chiang, Pei-Ying Lin, Tzung-Da Tsai, Yun-Chorng Chang, Tzung-Fang Guo, Peter Chen, Ten-Chin Wen and Yao-Jane Hsu. *Nickel Oxide Electrode Interlayer in CH3NH3PbI3 Perovskite/PCBM Planar-Heterojunction Hybrid Solar Cells.* Advanced Materials, vol. 26, no. 24, pages 4107–4113, 2014.

[Jeong 2010] Jin-A Jeong, Yong-Seok Park and Han-Ki Kim. *Comparison of Electrical, Optical, Structural, and Interface Properties of IZO-Ag-IZO and IZO-Au-IZO Multilayer Electrodes for Organic Photovoltaics.* Journal of Applied Physics, vol. 107, no. 2, page 023111, January 2010.

[Ji 2020] Wenbo Ji, Thomas Allen, Xinbo Yang, Guosong Zeng, De Stefaan Wolf and Ali Javey. *Polymeric Electron-Selective Contact for Efficiency Exceeding 19%.* 2020.

[Jin 2009] Hui Jin, Markus Tuomikoski, Jussi Hiltunen, Pälvi Kopola, Arto Maaninen and Flavio Pino. *Polymer-Electrode Interfacial Effect on Photovoltaic Performances in Poly(3-Hexylthiophene):Phenyl-C61-butyric Acid Methyl Ester Based Solar Cells.* The Journal of Physical Chemistry C, vol. 113, no. 38, pages 16807–16810, September 2009.

[Kaltenbrunner 2015] Martin Kaltenbrunner, Getachew Adam, Eric Daniel Głowacki, Michael Drack, Reinhard Schwödiauer, Lucia Leonat, Dogukan Hazar Apaydin, Heiko Groiss, Markus Clark Scharber, Matthew Schuette White, Niyazi Serdar Sariciftci and Siegfried Bauer. *Flexible High Power-per-Weight Perovskite Solar Cells with Chromium Oxide–Metal Contacts for Improved Stability in Air.* Nature Materials, vol. 14, no. 10, pages 1032–1039, October 2015.

[Kamino 2019] Brett A. Kamino, Bertrand Paviet-Salomon, Soo-Jin Moon, Nicolas Badel, Jacques Levrat, Gabriel Christmann, Arnaud Walter, Antonin Faes, Laura Ding, Juan J. Diaz Leon, Adriana Paracchino, Matthieu Despeisse, Christophe Ballif and Sylvain Nicolay. *Low-Temperature Screen-Printed Metallization for the Scale-Up of Two-Terminal Perovskite–Silicon Tandems.* ACS Applied Energy Materials, page acsaem.9b00502, May 2019.

[Kanno 2006] H. Kanno, R. J. Holmes, Y. Sun, S. Kena-Cohen and S. R. Forrest. *White Stacked Electrophosphorescent Organic Light-Emitting Devices Employing MoO3 as a Charge-Generation Layer.* Advanced Materials, vol. 18, no. 3, pages 339–342, 2006.

[Kern 1990] Werner Kern. *The Evolution of Silicon Wafer Cleaning Technology.* Journal of The Electrochemical Society, vol. 137, no. 6, pages 1887–1892, June 1990.

[Kidowaki 2012] H. Kidowaki, T. Oku and T. Akiyama. *Fabrication and Characterization of CuO/ZnO Solar Cells.* Journal of Physics: Conference Series, vol. 352, page 012022, March 2012.

[Kim 2000] J. S. Kim, B. Lägel, E. Moons, N. Johansson, I. D. Baikie, W. R. Salaneck, R. H. Friend and F. Cacialli. *Kelvin Probe and Ultraviolet Photoemission Measurements of Indium Tin Oxide Work Function: A Comparison.* Synthetic Metals, vol. 111, pages 311–314, 2000.

[Kim 2005] Soo Young Kim, Jeong Min Baik, Hak Ki Yu, Kwang Young Kim, Yoon-Heung Tak and Jong-Lam Lee. *Rhodium-Oxide-Coated Indium Tin Oxide for Enhancement of Hole Injection in Organic Light Emitting Diodes.* Applied Physics Letters, vol. 87, no. 7, page 072105, August 2005.

[Kim 2009] Myung-Su Kim, Bong-Gi Kim and Jinsang Kim. *Effective Variables To Control the Fill Factor of Organic Photovoltaic Cells.* ACS Applied Materials & Interfaces, vol. 1, no. 6, pages 1264–1269, June 2009.

[Kim 2010] Won-Sik Kim, Hong-Chan Kim and Seong-Hyeon Hong. *Gas Sensing Properties of MoO3 Nanoparticles Synthesized by Solvothermal Method.* Journal of Nanoparticle Research, vol. 12, no. 5, pages 1889–1896, June 2010.

[Kim 2011] Joo Hyung Kim, You Jong Lee, Yoon Sung Jang, Jin Nyoung Jang, Doo Hyun Kim, Byung Chul Song, Dong Hyeok Lee, Soon Nam Kwon and MunPyo Hong. *The Effect of Ar Plasma Bombardment upon Physical Property of Tungsten Oxide Thin Film in Inverted Top-Emitting Organic Light-Emitting Diodes.* Organic Electronics, vol. 12, no. 2, pages 285–290, February 2011.

[Kim 2012] Dae-Ho Kim, Tae-Min Kim, Won-Ik Jeong and Jang-Joo Kim. *Rhenium Oxide as an Efficient* p *-Dopant to Overcome S-shaped Current Density-Voltage Curves in Organic Photovoltaics with a Deep Highest Occupied Molecular Orbital Level Donor Layer.* Applied Physics Letters, vol. 101, no. 15, page 153303, October 2012.

[Kim 2015] Jun Ho Kim, Han-Kyeol Lee, Jin-Young Na, Sun-Kyung Kim, Young-Zo Yoo and Tae-Yeon Seong. *Dependence of Optical and Electrical Properties on Ag Thickness in TiO2/Ag/TiO2 Multilayer Films for Photovoltaic Devices.* Ceramics International, vol. 41, no. 6, pages 8059–8063, July 2015.

[Kim 2020] Sung-Hae Kim, Jin-Young Jung, Ralf B. Wehrspohn and Jung-Ho Lee. *All-Room-Temperature Processed 17.25%-Crystalline Silicon Solar Cell.* ACS Applied Energy Materials, vol. 3, no. 4, pages 3180–3185, April 2020.

[King 1997] D.L. King, J.A. Kratochvil and W.E. Boyson. *Temperature Coefficients for PV Modules and Arrays: Measurement Methods, Difficulties, and Results.* In Conference Record

of the Twenty Sixth IEEE Photovoltaic Specialists Conference - 1997, pages 1183–1186, September 1997.

[Kirchartz 2013] Thomas Kirchartz, Florent Deledalle, Pabitra Shakya Tuladhar, James R. Durrant and Jenny Nelson. *On the Differences between Dark and Light Ideality Factor in Polymer:Fullerene Solar Cells.* Journal of Physical Chemistry Letters, vol. 4, no. 14, pages 2371–2376, 2013.

[Kleider 2008] J. P. Kleider, A. S. Gudovskikh and P. Roca I Cabarrocas. *Determination of the Conduction Band Offset between Hydrogenated Amorphous Silicon and Crystalline Silicon from Surface Inversion Layer Conductance Measurements.* Applied Physics Letters, vol. 92, no. 16, 2008.

[Kobayashi 2016a] Eiji Kobayashi, Stefaan De Wolf, Jacques Levrat, Gabriel Christmann, Antoine Descoeudres, Sylvain Nicolay, Matthieu Despeisse, Yoshimi Watabe and Christophe Ballif. *Light-Induced Performance Increase of Silicon Heterojunction Solar Cells.* Applied Physics Letters, vol. 109, no. 15, page 153503, October 2016.

[Kobayashi 2016b] Eiji Kobayashi, Yoshimi Watabe, Tetsuya Yamamoto and Yoichi Yamada. *Cerium Oxide and Hydrogen Co-Doped Indium Oxide Films for High-Efficiency Silicon Heterojunction Solar Cells.* Solar Energy Materials and Solar Cells, vol. 149, pages 75–80, May 2016.

[Kobayashi 2017] Eiji Kobayashi, Stefaan De Wolf, Jacques Levrat, Antoine Descoeudres, Matthieu Despeisse, Franz-Josef Haug and Christophe Ballif. *Increasing the Efficiency of Silicon Heterojunction Solar Cells and Modules by Light Soaking.* Solar Energy Materials and Solar Cells, vol. 173, pages 43–49, December 2017.

[Kohler 2020] Malte Kohler, Friedhelm Finger, Uwe Rau, Kaining Ding, Manuel Pomaska, Alexandr Zamchiy, Andreas Lambertz, Weiyuan Duan, Florian Lentz, Shenghao Li, Vladimir Smirnov and Thomas Kirchartz. *Optimization of Transparent Passivating Contact for Crystalline Silicon Solar Cells.* IEEE Journal of Photovoltaics, vol. 10, no. 1, pages 46–53, 2020.

[Kröger 2009] M. Kröger, S. Hamwi, J. Meyer, T. Riedl, W. Kowalsky and A. Kahn. *Role of the Deep-Lying Electronic States of MoO3 in the Enhancement of Hole-Injection in Organic Thin Films.* Applied Physics Letters, vol. 95, no. 12, page 123301, September 2009.

[Kumar 2009] Ankit Kumar, Srinivas Sista and Yang Yang. *Dipole Induced Anomalous S-shape I-V Curves in Polymer Solar Cells.* Journal of Applied Physics, vol. 105, no. 9, page 094512, May 2009.

[Lajaunie 2015] L. Lajaunie, F. Boucher, R. Dessapt and P. Moreau. *Quantitative Use of Electron Energy-Loss Spectroscopy Mo-M2,3 Edges for the Study of Molybdenum Oxides.* Ultramicroscopy, vol. 149, pages 1–8, 2015.

[Lanzani 2012] Guglielmo Lanzani. The Photophysics behind Photovoltaics and Photonics. John Wiley & Sons, 2012.

[Le Comber 1970] P. G. Le Comber and W. E. Spear. *Electronic Transport in Amorphous Silicon Films*. Physical Review Letters, vol. 25, no. 8, pages 509–511, 1970.

[Le 2016] Ngoc Minh Le and Byung-Teak Lee. *ZnMgBeO/Ag/ZnMgBeO Transparent Multilayer Films with UV Energy Bandgap and Very Low Resistance*. Ceramics International, vol. 42, no. 4, pages 5258–5262, 2016.

[Le 2021] Anh Huy Tuan Le, Julie Dréon, Jesús Ibarra Michel, Mathieu Boccard, James Bullock, Nino Borojevic and Ziv Hameiri. *Temperature-Dependent Performance of Silicon Heterojunction Solar Cells with Transition-Metal-Oxide-Based Selective Contacts*. Progress in Photovoltaics: Research and Applications, vol. n/a, no. n/a, 2021.

[Lee 2016] Youngseok Lee, Cheolmin Park, Jinjoo Park, Donghyun Oh, Youn-Jung Lee and Junsin Yi. *Bias-Induced Instability in an Intrinsic Hydrogenated Amorphous Silicon Layer for Thin-Film Solar Cells*. Materials Research Bulletin, vol. 82, pages 122–125, October 2016.

[Leem 2007] Dong-Seok Leem, Hyung-Dol Park, Jae-Wook Kang, Jae-Hyun Lee, Ji Whan Kim and Jang-Joo Kim. *Low Driving Voltage and High Stability Organic Light-Emitting Diodes with Rhenium Oxide-Doped Hole Transporting Layer*. Applied Physics Letters, vol. 91, no. 1, page 011113, July 2007.

[Li 2005] Q Li, S J Xu, M H Xie and S Y Tong. *Origin of the 'S-shaped' Temperature Dependence of Luminescent Peaks from Semiconductors*. Journal of Physics: Condensed Matter, vol. 17, no. 30, pages 4853–4858, August 2005.

[Li 2006] Weiyang Li, Fangyi Cheng, Zhanliang Tao and Jun Chen. *Vapor-Transportation Preparation and Reversible Lithium Intercalation/Deintercalation of α-MoO3 Microrods*. The Journal of Physical Chemistry B, vol. 110, no. 1, pages 119–124, 2006.

[Li 2019] Ru-song Li, Fei Li, Jin-tao Wang, Du-qiang Xin, Ji-jun Luo and Peng Lin. *Effect of Correlation on Electronic Properties of NiO: A Study from Dynamical Mean Field Theory*. Chinese Journal of Physics, vol. 60, pages 228–238, August 2019.

[Li 2020a] Fengchao Li, Yurong Zhou, Ying Yang, Gangqiang Dong, Yuqin Zhou, Fengzhen Liu and Donghong Yu. *Silicon Heterojunction Solar Cells with MoOx Hole-Selective Layer by Hot Wire Oxidation–Sublimation Deposition*. Solar RRL, vol. 4, no. 3, page 1900514, 2020.

[Li 2020b] Jingye Li, Tianyu Pan, Jilei Wang, Shuangying Cao, Yinyue Lin, Bram Hoex, Zhongquan Ma, Linfeng Lu, Liyou Yang, Baoquan Sun and Dongdong Li. *Bilayer MoOX/CrOX Passivating Contact Targeting Highly Stable Silicon Heterojunction Solar Cells*. ACS Applied Materials & Interfaces, vol. 12, no. 32, pages 36778–36786, August 2020.

[Li 2021] Le Li, Guanlin Du, Yinyue Lin, Xi Zhou, Zeyu Gu, Linfeng Lu, Wenzhu Liu, Jin Huang, Jilei Wang, Liyou Yang, Shan-Ting Zhang and Dongdong Li. *NiOx/MoOx Bilayer as an Efficient Hole-Selective Contact in Crystalline Silicon Solar Cells.* Cell Reports Physical Science, vol. 2, no. 12, page 100684, December 2021.

[Lin 2012] F. Lin, B. Hoex, Y. H. Koh, J. Lin and A. G. Aberle. *Low-Temperature Surface Passivation of Moderately Doped Crystalline Silicon by Atomic-Layer-Deposited Hafnium Oxide Films.* ECS Journal of Solid State Science and Technology, vol. 2, no. 1, page N11, November 2012.

[Lin 2018a] Wenjie Lin, Weiliang Wu, Jie Bao, Zongtao Liu, Kaifu Qiu, Lun Cai, Zhirong Yao, Youjun Deng, Zongcun Liang and Hui Shen. *Novel Hole Selective CrOx Contact for Dopant-Free Back Contact Silicon Solar Cells.* Materials Research Bulletin, vol. 103, pages 77–82, July 2018.

[Lin 2018b] Wenjie Lin, Weiliang Wu, Zongtao Liu, Kaifu Qiu, Lun Cai, Zhirong Yao, Bin Ai, Zongcun Liang and Hui Shen. *Chromium Trioxide Hole-Selective Heterocontacts for Silicon Solar Cells.* ACS Applied Materials & Interfaces, vol. 10, no. 16, pages 13645–13651, April 2018.

[Lin 2021] Wenjie Lin, Julie Dréon, Sihua Zhong, Vincent Paratte, Luca Antognini, Jean Cattin, Zongtao Liu, Zongcun Liang, Pingqi Gao, Hui Shen, Christophe Ballif and Mathieu Boccard. *Dopant-Free Bifacial Silicon Solar Cells.* Solar RRL, vol. 5, no. 5, page 2000771, 2021.

[Liu 2020] Wenzhu Liu, Liping Zhang, Xinbo Yang, Jianhua Shi, Lingling Yan, Lujia Xu, Zhuopeng Wu, Renfang Chen, Jun Peng, Jingxuan Kang, Kai Wang, Fanying Meng, Stefaan De Wolf and Zhengxin Liu. *Damp-Heat-Stable, High-Efficiency, Industrial-Size Silicon Heterojunction Solar Cells.* Joule, vol. 4, no. 4, pages 913–927, April 2020.

[Longi 2021] Longi. *LONGi Breaks World Record for HJT Solar Cell Efficiency Twice in One Week (https://en.longi-solar.com/home/events/press_detail/id/364.html).* Longi Solar Press, October 2021.

[LUT 2020] LUT and SPE. *100% Renewable Europe, How To Make Europe's Energy System Climate-Neutral Before 2050.* Rapport technique, LUT University and Solar Power Europe, https://www.solarpowereurope.org/100-renewable-europe/, April 2020.

[Macco 2015] B. Macco, M. F. J. Vos, N. F. W. Thissen, A. A. Bol and W. M. M. Kessels. *Low-Temperature Atomic Layer Deposition of MoOx for Silicon Heterojunction Solar Cells.* physica status solidi (RRL) – Rapid Research Letters, vol. 9, no. 7, pages 393–396, 2015.

[Macdonald 1999a] D. Macdonald and A. Cuevas. *Trapping of Minority Carriers in Multicrystalline Silicon.* Applied Physics Letters, vol. 74, no. 12, pages 1710–1712, March 1999.

[Macdonald 1999b] Daniel Macdonald, Mark Kerr and Andrés Cuevas. *Boron-Related Minority-Carrier Trapping Centers in* p *-Type Silicon.* Applied Physics Letters, vol. 75, no. 11, pages 1571–1573, September 1999.

[Macdonald 2000] Daniel Macdonald and Andres Cuevas. *Reduced Fill Factors in Multicrystalline Silicon Solar Cells Due to Injection-Level Dependent Bulk Recombination Lifetimes.* Progress in Photovoltaics: Research and Applications, vol. 8, no. 4, pages 363–375, 2000.

[Mahtani 2013] Pratish Mahtani, Renaud Varache, Bastien Jovet, Christophe Longeaud, Jean-Paul Kleider and Nazir P. Kherani. *Light Induced Changes in the Amorphous—Crystalline Silicon Heterointerface.* Journal of Applied Physics, vol. 114, no. 12, page 124503, September 2013.

[Manders 2013] Jesse R. Manders, Sai-Wing Tsang, Michael J. Hartel, Tzung-Han Lai, Song Chen, Chad M. Amb, John R. Reynolds and Franky So. *Solution-Processed Nickel Oxide Hole Transport Layers in High Efficiency Polymer Photovoltaic Cells.* Advanced Functional Materials, vol. 23, no. 23, pages 2993–3001, 2013.

[Martin de Nicolás 2011] S. Martin de Nicolás, D. Muñoz, A.S. Ozanne, N. Nguyen and P.J. Ribeyron. *Optimisation of Doped Amorphous Silicon Layers Applied to Heterojunction Solar Cells.* Energy Procedia, vol. 8, pages 226–231, January 2011.

[Masmitjà 2017] Gerard Masmitjà, Luís G. Gerling, Pablo Ortega, Joaquim Puigdollers, Isidro Martín, Cristóbal Voz and Ramón Alcubilla. *V2Ox-based Hole-Selective Contacts for c-Si Interdigitated Back-Contacted Solar Cells.* Journal of Materials Chemistry A, vol. 5, no. 19, pages 9182–9189, 2017.

[Masmitjà 2018] G. Masmitjà, P. Ortega, J. Puigdollers, L. G. Gerling, I. Martín, C. Voz and R. Alcubilla. *Interdigitated Back-Contacted Crystalline Silicon Solar Cells with Low-Temperature Dopant-Free Selective Contacts.* Journal of Materials Chemistry A, vol. 6, no. 9, pages 3977–3985, 2018.

[Masudy-Panah 2014] Saeid Masudy-Panah, Goutam Kumar Dalapati, K. Radhakrishnan, Avishek Kumar and Hui Ru Tan. *Reduction of Cu-rich Interfacial Layer and Improvement of Bulk CuO Property through Two-Step Sputtering for p-CuO/n-Si Heterojunction Solar Cell.* Journal of Applied Physics, vol. 116, no. 7, page 074501, August 2014.

[Masuko 2014] Keiichiro Masuko, Masato Shigematsu, Taiki Hashiguchi, Daisuke Fujishima, Motohide Kai, Naoki Yoshimura, Tsutomu Yamaguchi, Yoshinari Ichihashi, Takahiro Mishima, Naoteru Matsubara, Tsutomu Yamanishi, Tsuyoshi Takahama, Mikio Taguchi, Eiji Maruyama and Shingo Okamoto. *Achievement of More Than 25% Conversion Efficiency With Crystalline Silicon Heterojunction Solar Cell.* IEEE Journal of Photovoltaics, vol. 4, no. 6, pages 1433–1435, November 2014.

[Matsui 2017] Takuya Matsui, Martin Bivour, Paul Ndione, Paul Hettich and Martin Hermle. *Investigation of Atomic-Layer-Deposited TiOx as Selective Electron and Hole Contacts to Crystalline Silicon.* Energy Procedia, vol. 124, pages 628–634, September 2017.

[Matsui 2020] Takuya Matsui, Martin Bivour, Martin Hermle and Hitoshi Sai. *Atomic-Layer-Deposited TiOx Nanolayers Function as Efficient Hole-Selective Passivating Contacts in Silicon Solar Cells.* ACS Applied Materials & Interfaces, vol. 12, no. 44, pages 49777–49785, November 2020.

[Matsuura 1984] Hideharu Matsuura, Tetsuhiro Okuno, Hideyo Okushi and Kazunobu Tanaka. *Electrical Properties of N-amorphous/P-crystalline Silicon Heterojunctions.* Journal of Applied Physics, vol. 55, no. 4, pages 1012–1019, February 1984.

[Mazhari 2006] B. Mazhari. *An Improved Solar Cell Circuit Model for Organic Solar Cells.* Solar Energy Materials and Solar Cells, vol. 90, no. 7, pages 1021–1033, May 2006.

[Mazzarella 2015] L. Mazzarella, S. Kirner, B. Stannowski, L. Korte, B. Rech and R. Schlatmann. *P-Type Microcrystalline Silicon Oxide Emitter for Silicon Heterojunction Solar Cells Allowing Current Densities above 40 mA/Cm2.* Applied Physics Letters, vol. 106, no. 2, pages 0–5, 2015.

[Mazzarella 2018] Mazzarella, Ana Belen Morales-vilches, Max Hendrichs, Simon Kirner, Lars Korte, Rutger Schlatmann and Bernd Stannowski. *Nanocrystalline N-Type Silicon Oxide Front Contacts for Silicon Heterojunction Solar Cells : Photocurrent Enhancement on Planar and Textured Substrates.* vol. 8, no. 1, pages 70–78, 2018.

[Mazzarella 2020] L. Mazzarella, A. Alcañiz-Moya, E. Kawa, P.A. Procel Moya, Y. Zhao, C. Han, G. Yang, M. Zeman and O. Isabella. *Interface Treatment to Improve the (I)a-Si:H/MoOx Stack for Passivating Contact Solar Cells.* Presentation at EUPVSEC conference, 2020.

[Mazzarella 2021] Luana Mazzarella, Alba Alcañiz, Paul Procel, Eliora Kawa, Yifeng Zhao, Urša Tiringer, Can Han, Guangtao Yang, Peyman Taheri, Miro Zeman and Olindo Isabella. *Strategy to Mitigate the Dipole Interfacial States in (i)a-Si:H/MoOx Passivating Contacts Solar Cells.* Progress in Photovoltaics: Research and Applications, vol. 29, no. 3, pages 391–400, 2021.

[McIntosh 2000] Keith R. McIntosh, Pietro P Altermatt and Gernot Heiser. *Depletion-Region Recombination in Silicon Solar Cells: When Does mDR = 2?* 16th European Photovoltaic Solar Energy Conference, no. May, pages 250–253, 2000.

[McIntosh 2021] K. McIntosh and S. Baker-Finch. *OPAL 2: Rapid Optical Simulation of Silicon Solar Cells", 2012. [Online].*, 2021.

[McNaught 1997] Alan D. McNaught, Andrew Wilkinson and International Union of Pure and Applied Chemistry, editeurs. Compendium of chemical terminology: IUPAC recommendations. Blackwell Science, Oxford [England] ; Malden, MA, USA, 2nd ed édition, 1997.

[Menchini 2016] Francesca Menchini, Maria Luisa Grilli, Theodoros Dikonimos, Alberto Mittiga, Luca Serenelli, Enrico Salza, Rosa Chierchia and Mario Tucci. *Application of NiOx Thin Films as P-Type Emitter Layer in Heterojunction Solar Cells.* physica status solidi c, vol. 13, no. 10-12, pages 1006–1010, 2016.

[Messmer 2018] Christoph Messmer, Martin Bivour, Jonas Schön, Stefan W Glunz and Martin Hermle. *Numerical Simulation of Silicon Heterojunction Solar Cells Featuring Metal Oxides as Carrier-Selective Contacts.* Ieee Journal of Photovoltaics, vol. 1, no. 2, pages 1–9, March 2018.

[Mews 2016] Mathias Mews, Lars Korte and Bernd Rech. *Oxygen Vacancies in Tungsten Oxide and Their Influence on Tungsten Oxide/Silicon Heterojunction Solar Cells.* Solar Energy Materials and Solar Cells, vol. 158, pages 77–83, December 2016.

[Mews 2017] Mathias Mews, Antoine Lemaire and Lars Korte. *Sputtered Tungsten Oxide as Hole Contact for Silicon Heterojunction Solar Cells.* IEEE Journal of Photovoltaics, vol. 7, no. 5, pages 1209–1215, September 2017.

[Meyer 2007] J. Meyer, S. Hamwi, T. Bülow, H.-H. Johannes, T. Riedl and W. Kowalsky. *Highly Efficient Simplified Organic Light Emitting Diodes.* Applied Physics Letters, vol. 91, no. 11, page 113506, September 2007.

[Meyer 2010] J. Meyer, A. Shu, M. Kröger and A. Kahn. *Effect of Contamination on the Electronic Structure and Hole-Injection Properties of MoO3/Organic Semiconductor Interfaces.* Applied Physics Letters, vol. 96, no. 13, page 133308, March 2010.

[Meyer 2011a] J. Meyer, K. Zilberberg, T. Riedl and A. Kahn. *Electronic Structure of Vanadium Pentoxide: An Efficient Hole Injector for Organic Electronic Materials.* Journal of Applied Physics, vol. 110, no. 3, page 033710, August 2011.

[Meyer 2011b] Jens Meyer and Antoine L. Kahn. *Electronic Structure of Molybdenum-Oxide Films and Associated Charge Injection Mechanisms in Organic Devices.* Journal of Photonics for Energy, vol. 1, no. 1, page 011109, January 2011.

[Meyer 2012a] B. K. Meyer, A. Polity, D. Reppin, M. Becker, P. Hering, P. J. Klar, Th. Sander, C. Reindl, J. Benz, M. Eickhoff, C. Heiliger, M. Heinemann, J. Bläsing, A. Krost, S. Shokovets, C. Müller and C. Ronning. *Binary Copper Oxide Semiconductors: From Materials towards Devices.* physica status solidi (b), vol. 249, no. 8, pages 1487–1509, 2012.

[Meyer 2012b] Jens Meyer, Sami Hamwi, Michael Kröger, Wolfgang Kowalsky, Thomas Riedl and Antoine Kahn. *Transition Metal Oxides for Organic Electronics: Energetics, Device Physics and Applications.* Advanced Materials, vol. 24, no. 40, pages 5408–5427, 2012.

[Mikolášek 2014] Miroslav Mikolášek, Michal Nemec, Marian Vojs, Ján Jakabovič, Vlastimil Řeháček, Dong Zhang, Miro Zeman and Ladislav Harmatha. *Electrical Transport*

Mechanisms in Amorphous/Crystalline Silicon Heterojunction: Impact of Passivation Layer Thickness. Thin Solid Films, vol. 558, pages 315–319, May 2014.

[Mikolášek 2017] Miroslav Mikolášek, Juraj Racko and Ladislav Harmatha. *Analysis of Low Temperature Output Parameters for Investigation of Silicon Heterojunction Solar Cells.* Applied Surface Science, vol. 395, pages 166–171, February 2017.

[Mimura 1992] Hidenori Mimura and Yoshinori Hatanaka. *Carrier Transport Mechanisms of P-type Amorphous–N-type Crystalline Silicon Heterojunctions.* Journal of Applied Physics, vol. 71, no. 5, pages 2315–2320, March 1992.

[Misho 1988] R. H. Misho, W. A. Murad, G. H. Fatahalah, I. M. Abdul Aziz and H. M. Al-Doori. *Preparation and Optical Properties of Thin Nickel Oxide Solid Films.* physica status solidi (a), vol. 109, no. 2, pages K101–K104, 1988.

[Mora-Seró 2005] Iván Mora-Seró and Juan Bisquert. *Effect of Reduced Selectivity of Contacts on the Current-Potential Characteristics and Conversion Performance of Solar Cells.* Solar Energy Materials and Solar Cells, vol. 85, no. 1, pages 51–62, January 2005.

[Morikawa 1999] Hiroshi Morikawa and Miya Fujita. *Crystallization and Decrease in Resistivity on Heat Treatment of Amorphous Indium Tin Oxide Thin Films Prepared by d.c. Magnetron Sputtering.* Thin Solid Films, vol. 339, no. 1, pages 309–313, February 1999.

[Morikawa 2000] Hiroshi Morikawa and Miya Fujita. *Crystallization and Electrical Property Change on the Annealing of Amorphous Indium-Oxide and Indium-Tin-Oxide Thin Films.* Thin Solid Films, vol. 359, no. 1, pages 61–67, January 2000.

[Moss 1954] T. S. Moss. *The Interpretation of the Properties of Indium Antimonide.* Proceedings of the Physical Society. Section B, vol. 67, no. 10, pages 775–782, October 1954.

[Mott 1974] N. F. Mott. *Metal-Insulator Transitions*, 1974.

[Mrazkova 2018] Zuzana Mrazkova, Igor Paul Sobkowicz, Martin Foldyna, Kamil Postava, Ileana Florea, Jaromír Pištora and Pere Roca i Cabarrocas. *Optical Properties and Performance of Pyramidal Texture Silicon Heterojunction Solar Cells: Key Role of Vertex Angles.* Progress in Photovoltaics: Research and Applications, vol. 26, no. 6, pages 369–376, 2018.

[Nattestad 2010] A. Nattestad, A. J. Mozer, M. K. R. Fischer, Y.-B. Cheng, A. Mishra, P. Bäuerle and U. Bach. *Highly Efficient Photocathodes for Dye-Sensitized Tandem Solar Cells.* Nature Materials, vol. 9, no. 1, pages 31–35, 2010.

[Nayak 2019] Mrutyunjay Nayak, Sourav Mandal, Ashutosh Pandey, Sapna Mudgal, Sonpal Singh and Vamsi K. Komarala. *Nickel Oxide Hole-Selective Heterocontact for Silicon Solar Cells: Role of SiOx Interlayer on Device Performance.* Solar RRL, vol. 3, no. 11, page 1900261, 2019.

[Ndione 2013] Paul F. Ndione, Andres Garcia, N. Edwin Widjonarko, Ajaya K. Sigdel, K. Xerxes Steirer, Dana C. Olson, Philip A. Parilla, David S. Ginley, Neal R. Armstong, Robin E. Richards, Erin L. Ratcliff and Joseph J. Berry. *Highly-Tunable Nickel Cobalt Oxide as a Low-Temperature P-Type Contact in Organic Photovoltaic Devices.* Advanced Energy Materials, vol. 3, no. 4, pages 524–531, 2013.

[Nelson 2004] Jenny Nelson, James Kirkpatrick and P. Ravirajan. *Factors Limiting the Efficiency of Molecular Photovoltaic Devices.* Physical Review B, vol. 69, no. 3, page 035337, January 2004.

[Newell 2020] R. G. Newell, D. Raimi, S. Villanueva and B. Prest. *Global Energy Outlook 2020: Energy Transition or Energy Addition?* Resource for the Future, 2020.

[Niemegeers 1997] Alex Niemegeers and Marc Burgelman. *Effects of the Au/CdTe Back Contact on IV and CV Characteristics of Au/CdTe/CdS/TCO Solar Cells.* Journal of Applied Physics, vol. 81, no. 6, pages 2881–2886, March 1997.

[Odobel 2013] Fabrice Odobel and Yann Pellegrin. *Recent Advances in the Sensitization of Wide-Band-Gap Nanostructured p-Type Semiconductors. Photovoltaic and Photocatalytic Applications.* The Journal of Physical Chemistry Letters, vol. 4, no. 15, pages 2551–2564, August 2013.

[Ohmori 1993] Yutaka Ohmori, Akihiko Fujii, Masao Uchida, Chikayoshi Morishima and Katsumi Yoshino. *Observation of Spectral Narrowing and Emission Energy Shift in Organic Electroluminescent Diode Utilizing 8-hydroxyquinoline Aluminum/Aromatic Diamine Multilayer Structure.* Applied Physics Letters, vol. 63, no. 14, pages 1871–1873, October 1993.

[Olibet 2007] Sara Olibet, Evelyne Vallat-Sauvain, Christophe Ballif and Luc Fesquet. *Recombination through Amphoteric States at the Amorphous/Crystalline Silicon Interface: Modelling and Experiment.* page 13, 2007.

[Oukassi 2009] S. Oukassi, R. Salot and J. P. Pereira-Ramos. *Elaboration and Characterization of Crystalline RF-deposited V2O5 Positive Electrode for Thin Film Batteries.* Applied Surface Science, vol. 256, no. 1, pages 149–155, October 2009.

[Paduthol 2018] Appu Paduthol, Mattias K. Juhl, Gizem Nogay, Philipp Löper, Andrea Ingenito and Thorsten Trupke. *Impact of Different Capping Layers on Carrier Injection Efficiency between Amorphous and Crystalline Silicon Measured Using Photoluminescence.* Solar Energy Materials and Solar Cells, vol. 187, no. March, pages 55–60, 2018.

[Parashar 2019] Piyush K. Parashar and Vamsi K. Komarala. *Sputter Deposited Sub-Stochiometric MoOx Thin Film as Hole-Selective Contact Layer for Silicon Based Heterojunction Devices.* Thin Solid Films, vol. 682, pages 76–81, July 2019.

[Park 2015] Jong Hoon Park, Jangwon Seo, Sangman Park, Seong Sik Shin, Young Chan Kim, Nam Joong Jeon, Hee-Won Shin, Tae Kyu Ahn, Jun Hong Noh, Sung Cheol Yoon,

Cheol Seong Hwang and Sang Il Seok. *Efficient CH3NH3PbI3 Perovskite Solar Cells Employing Nanostructured P-Type NiO Electrode Formed by a Pulsed Laser Deposition.* Advanced Materials, vol. 27, no. 27, pages 4013–4019, 2015.

[Pashmakov 1993] B. Pashmakov, B. Claflin and H. Fritzsche. *Photoreduction and Oxidation of Amorphous Indium Oxide.* Solid State Communications, vol. 86, no. 10, pages 619–622, June 1993.

[Patil 2002] P. S Patil and L. D Kadam. *Preparation and Characterization of Spray Pyrolyzed Nickel Oxide (NiO) Thin Films.* Applied Surface Science, vol. 199, no. 1, pages 211–221, October 2002.

[Pern 1991] F.J. Pern, A.W. Czanderna, K.A. Emery and R.G. Dhere. *Weathering Degradation of EVA Encapsulant and the Effect of Its Yellowing on Solar Cell Efficiency.* In The Conference Record of the Twenty-Second IEEE Photovoltaic Specialists Conference - 1991, pages 557–561, Las Vegas, NV, USA, 1991. IEEE.

[Peters 2019] Ian Marius Peters, Carlos David Rodriguez Gallegos, Sarah Elizabeth Sofia and Tonio Buonassisi. *The Value of Efficiency in Photovoltaics.* Joule, vol. 3, no. 11, pages 2732–2747, November 2019.

[Plagwitz 2008] Heiko Plagwitz, Barbara Terheiden and Rolf Brendel. *Staebler–Wronski-like Formation of Defects at the Amorphous-Silicon–Crystalline Silicon Interface during Illumination.* Journal of Applied Physics, vol. 103, no. 9, page 094506, May 2008.

[Ponce-Alcántara 2014] Salvador Ponce-Alcántara, James Patrick Connolly, Guillermo Sánchez, José Manuel Míguez, Volker Hoffmann and Ramón Ordás. *A Statistical Analysis of the Temperature Coefficients of Industrial Silicon Solar Cells.* Energy Procedia, vol. 55, pages 578–588, January 2014.

[Powar 2013] Satvasheel Powar, Torben Daeneke, Michelle T. Ma, Dongchuan Fu, Noel W. Duffy, Günther Götz, Martin Weidelener, Amaresh Mishra, Peter Bäuerle, Leone Spiccia and Udo Bach. *Highly Efficient P-Type Dye-Sensitized Solar Cells Based on Tris(1,2-Diaminoethane)Cobalt(II)/(III) Electrolytes.* Angewandte Chemie International Edition, vol. 52, no. 2, pages 602–605, 2013.

[Powell 1970] R. J. Powell and W. E. Spicer. *Optical Properties of NiO and CoO.* Physical Review B, vol. 2, no. 6, pages 2182–2193, September 1970.

[Pramanik 1990] P. Pramanik and S. Bhattacharya. *A Chemical Method for the Deposition of Nickel Oxide Thin Films.* Journal of The Electrochemical Society, vol. 137, no. 12, page 3869, December 1990.

[Procel 2020] Paul Procel, Haiyuan Xu, Aurora Saez, Carlos Ruiz-Tobon, Luana Mazzarella, Yifeng Zhao, Can Han, Guangtao Yang, Miro Zeman and Olindo Isabella. *The Role of*

Heterointerfaces and Subgap Energy States on Transport Mechanisms in Silicon Heterojunction Solar Cells. Progress in Photovoltaics: Research and Applications, vol. 28, no. 9, pages 935–945, 2020.

[Pysch 2007] D. Pysch, A. Mette and S. W. Glunz. *A Review and Comparison of Different Methods to Determine the Series Resistance of Solar Cells.* Solar Energy Materials and Solar Cells, vol. 91, no. 18, pages 1698–1706, November 2007.

[Qin 2011a] Pingli Qin, Guojia Fang, Nanhai Sun, Xi Fan, Qiao Zheng, Fei Chen, Jiawei Wan and Xingzhong Zhao. *Composition-Dependent Phase Separation Effects of Organic Solar Cells Using P3HT:PCBM as Active Layer and Chromium Oxide as Hole Transporting Layer.* Applied Surface Science, vol. 257, no. 9, pages 3952–3958, February 2011.

[Qin 2011b] Pingli Qin, Guojia Fang, Nanhai Sun, Xi Fan, Qiao Zheng, Fei Chen, Jiawei Wan and Xingzhong Zhao. *Organic Solar Cells with P-Type Amorphous Chromium Oxide Thin Film as Hole-Transporting Layer.* Thin Solid Films, vol. 519, no. 13, pages 4334–4341, April 2011.

[Qin 2016] Ping-Li Qin, Hong-Wei Lei, Xiao-Lu Zheng, Qin Liu, Hong Tao, Guang Yang, Wei-Jun Ke, Liang-Bin Xiong, Ming-Chao Qin, Xing-Zhong Zhao and Guo-Jia Fang. *Copper-Doped Chromium Oxide Hole-Transporting Layer for Perovskite Solar Cells: Interface Engineering and Performance Improvement.* Advanced Materials Interfaces, vol. 3, no. 14, page 1500799, 2016.

[Qin 2018] Pingli Qin, Qin He, Guang Yang, Xueli Yu, Lun Xiong and Guojia Fang. *Metal Ions Diffusion at Heterojunction Chromium Oxide/CH3NH3PbI3 Interface on the Stability of Perovskite Solar Cells.* Surfaces and Interfaces, vol. 10, pages 93–99, March 2018.

[Queisser 1962] H. J. Queisser. *Forward Characteristics and Efficiencies of Silicon Solar Cells.* Solid-State Electronics, vol. 5, no. 1, pages 1–10, January 1962.

[Rao 1978] C. N.R. Rao and K. J. Rao. Phase Transitions in Solids. McGraw-Hili, New York, 1978.

[Rao 1989] C N R Rao. *Transition Metal Oxides.* vol. 40, pages 291–326, 1989.

[Rao 1997] C. N. R. Rao and J. Gopalakrishnan. *New Directions in Solid State Chemistry.* New Directions in Solid State Chemistry, February 1997.

[Ratcliff 2013] Erin L. Ratcliff, Andres Garcia, Sergio A. Paniagua, Sarah R. Cowan, Anthony J. Giordano, David S. Ginley, Seth R. Marder, Joseph J. Berry and Dana C. Olson. *Investigating the Influence of Interfacial Contact Properties on Open Circuit Voltages in Organic Photovoltaic Performance: Work Function Versus Selectivity.* Advanced Energy Materials, vol. 3, no. 5, pages 647–656, 2013.

[Ravindra 2017] Pramod Ravindra, Rudra Mukherjee and Sushobhan Avasthi. *Hole-Selective Electron-Blocking Copper Oxide Contact for Silicon Solar Cells.* IEEE Journal of Photovoltaics, vol. 7, no. 5, pages 1278–1283, September 2017.

[Ray 2021] Douglas Ray. *Lazard's Levelized Cost of Energy Analysis—Version 15.0.* page 21, 2021.

[Razzaq 2022] Arsalan Razzaq, Thomas G. Allen, Wenzhu Liu, Zhengxin Liu and Stefaan De Wolf. *Silicon Heterojunction Solar Cells: Techno-Economic Assessment and Opportunities.* Joule, Accepted, 2022.

[Riben 1966] A. R. Riben and D. L. Feucht. *nGe-pGaAs Heterojunctions.* Solid-State Electronics, vol. 9, no. 11, pages 1055–1065, November 1966.

[Richter 2013] Armin Richter, Martin Hermle and Stefan W. Glunz. *Reassessment of the Limiting Efficiency for Crystalline Silicon Solar Cells.* IEEE Journal of Photovoltaics, vol. 3, no. 4, pages 1184–1191, October 2013.

[Ritzau 2014] Kurt Ulrich Ritzau, Martin Bivour, Sebastian Schröer, Heiko Steinkemper, Patrick Reinecke, Florian Wagner and Martin Hermle. *TCO Work Function Related Transport Losses at the A-Si:H/TCO-contact in SHJ Solar Cells.* Solar Energy Materials and Solar Cells, vol. 131, pages 9–13, 2014.

[Ritzau 2016] Kurt-Ulrich Ritzau, Torge Behrendt, Daniele Palaferri, Martin Bivour and Martin Hermle. *Hydrogen Doping of Indium Tin Oxide Due to Thermal Treatment of Hetero-Junction Solar Cells.* Thin Solid Films, vol. 599, pages 161–165, January 2016.

[Roberts 1980] G.G. Roberts, N. Apsley and R.W. Munn. *Temperature Dependent Electronic Conduction in Semiconductors.* Physics Reports, vol. 60, no. 2, pages 59–150, 1980.

[Roe 2019] Ellis T. Roe, Kira E. Egelhofer and Mark C. Lonergan. *Exchange Current Density Model for the Contact-Determined Current-Voltage Behavior of Solar Cells.* Journal of Applied Physics, vol. 125, no. 22, page 225302, June 2019.

[Roland 2016] Paul J. Roland, Khagendra P. Bhandari and Randy J. Ellingson. *Electronic Circuit Model for Evaluating S-kink Distorted Current-Voltage Curves.* In 2016 IEEE 43rd Photovoltaic Specialists Conference (PVSC), pages 3091–3094, June 2016.

[Ros Costals 2021] Eloi Ros Costals, Gerard Masmitjà, Estefania Rosa Almache, Benjamin andres Pusay, Kunal Tiwari, Edgardo Saucedo, Byung Chul Kim, C. Justin Raj, Isidro Martín, Joaquim Puigdollers, Cristóbal Voz and Pablo Ortega. *Atomic Layer Deposition of Vanadium Oxide Films for Crystalline Silicon Solar Cells.* Materials Advances, page 10.1039.D1MA00812A, 2021.

[Roth 1981] A. P. Roth, J. B. Webb and D. F. Williams. *Absorption Edge Shift in ZnO Thin Films at High Carrier Densities.* Solid State Communications, vol. 39, no. 12, pages 1269–1271, September 1981.

[Roth 1982] Alain P. Roth, James B. Webb and Digby F. Williams. *Band-Gap Narrowing in Heavily Defect-Doped ZnO.* Physical Review B, vol. 25, no. 12, pages 7836–7839, June 1982.

[Ru 2020] Xiaoning Ru, Minghao Qu, Jianqiang Wang, Tianyu Ruan, Miao Yang, Fuguo Peng, Wei Long, Kun Zheng, Hui Yan and Xixiang Xu. *25.11% Efficiency Silicon Heterojunction Solar Cell with Low Deposition Rate Intrinsic Amorphous Silicon Buffer Layers.* Solar Energy Materials and Solar Cells, vol. 215, page 110643, September 2020.

[Rubinelli 1989] F. Rubinelli, S. Albornoz and R. Buitrago. *Amorphous-Crystalline Silicon Heterojunction: Theoretical Evaluation of the Current Terms.* Solid-State Electronics, vol. 32, no. 10, pages 813–825, October 1989.

[Rucavado 2019] Esteban Rucavado. *Defect Passivation in Zinc Tin Oxide: Improving the Transparency-Conductivity Trade-off and Comparing with Indium-Based Materials.* PhD thesis, 2019.

[Sacchetto 2017] Davide Sacchetto, Quentin Jeangros, Gabriel Christmann, Loris Barraud, Antoine Descoeudres, Jonas Geissbuhler, Matthieu Despeisse, Aicha Hessler-Wyser, Sylvain Nicolay and Christophe Ballif. *ITO/MoOx/a-Si:H(i) Hole-Selective Contacts for Silicon Heterojunction Solar Cells: Degradation Mechanisms and Cell Integration.* IEEE Journal of Photovoltaics, vol. 7, no. 6, pages 1584–1590, November 2017.

[Sachenko 2016] A. V. Sachenko, Yu. V. Kryuchenko, V. P. Kostylyov, R. M. Korkishko, I. O. Sokolovskyi, A. S. Abramov, S. N. Abolmasov, D. A. Andronikov, A. V. Bobyl', I. E. Panaiotti, E. I. Terukov, A. S. Titov and M. Z. Shvarts. *The Temperature Dependence of the Characteristics of Crystalline-Silicon-Based Heterojunction Solar Cells.* Technical Physics Letters, vol. 42, no. 3, pages 313–316, March 2016.

[Sai 2018] Hitoshi Sai, Hiroshi Umishio, Takuya Matsui, Shota Nunomura, Tomoyuki Kawatsu, Hidetaka Takato and Koji Matsubara. *Impact of Silicon Wafer Thickness on Photovoltaic Performance of Crystalline Silicon Heterojunction Solar Cells.* Japanese Journal of Applied Physics, vol. 57, no. 8S3, page 08RB10, August 2018.

[Saitoh 1977] Tadashi Saitoh, Sunao Matsubara and Shigekazu Minagawa. *Polycrystalline Indium Phosphide Solar Cells Fabricated on Molybdenum Substrates.* Japanese Journal of Applied Physics, vol. 16, no. 5, pages 807–812, May 1977.

[Sandberg 2014] Oskar J. Sandberg, Mathias Nyman and Ronald Österbacka. *Effect of Contacts in Organic Bulk Heterojunction Solar Cells.* Physical Review Applied, vol. 1, no. 2, page 024003, March 2014.

[Sato 1993] H. Sato, T. Minami, S. Takata and T. Yamada. *Transparent Conducting P-Type NiO Thin Films Prepared by Magnetron Sputtering.* Thin Solid Films, vol. 236, no. 1, pages 27–31, 1993.

[Schmidt 2007] M. Schmidt, L. Korte, A. Laades, R. Stangl, Ch Schubert, H. Angermann, E. Conrad and v. K. Maydell. *Physical Aspects of A-Si:H/c-Si Hetero-Junction Solar Cells.* Thin Solid Films, vol. 515, no. 19 SPEC. ISS., pages 7475–7480, 2007.

[Schroder 1984] D.K. Schroder and D.L. Meier. *Contact Resistance: Its Measurement and Relative Importance to Power Loss in a Solar Cell.* IEEE Transactions on Electron Devices, vol. 31, no. 5, pages 647–653, May 1984.

[Schulz 2016] Philip Schulz, Jan O. Tiepelt, Jeffrey A. Christians, Igal Levine, Eran Edri, Erin M. Sanehira, Gary Hodes, David Cahen and Antoine Kahn. *High-Work-Function Molybdenum Oxide Hole Extraction Contacts in Hybrid Organic–Inorganic Perovskite Solar Cells.* ACS Applied Materials & Interfaces, vol. 8, no. 46, pages 31491–31499, November 2016.

[Schulze 2006] K. Schulze, C. Uhrich, R. Schüppel, K. Leo, M. Pfeiffer, E. Brier, E. Reinold and P. Bäuerle. *Efficient Vacuum-Deposited Organic Solar Cells Based on a New Low-Bandgap Oligothiophene and Fullerene C60.* Advanced Materials, vol. 18, no. 21, pages 2872–2875, 2006.

[Scirè 2020] Daniele Scirè, Paul Procel, Antonino Gulino, Olindo Isabella, Miro Zeman and Isodiana Crupi. *Sub-Gap Defect Density Characterization of Molybdenum Oxide: An Annealing Study for Solar Cell Applications.* Nano Research, vol. 13, no. 12, pages 3416–3424, December 2020.

[Shah 2010] A Shah and W Beyer. *BASIC PROPERTIES OF HYDROGENATED AMORPHOUS SILICON ({a-Si:H}).* In A Shah and A Shah, editeurs, Thin-Film Silicon Solar Cells, pages 17–96. 2010.

[Shalan 2016] Ahmed Esmail Shalan, Tomoya Oshikiri, Sudhakar Narra, Mahmoud M. Elshanawany, Kosei Ueno, Hui-Ping Wu, Keisuke Nakamura, Xu Shi, Eric Wei-Guang Diau and Hiroaki Misawa. *Cobalt Oxide (CoOx) as an Efficient Hole-Extracting Layer for High-Performance Inverted Planar Perovskite Solar Cells.* ACS Applied Materials & Interfaces, vol. 8, no. 49, pages 33592–33600, December 2016.

[Shao 2010] Shuyan Shao, Fengmin Liu, Zhiyuan Xie and Lixiang Wang. *High-Efficiency Hybrid Polymer Solar Cells with Inorganic P- and N-Type Semiconductor Nanocrystals to Collect Photogenerated Charges.* The Journal of Physical Chemistry C, vol. 114, no. 19, pages 9161–9166, May 2010.

[Shen 2011] Liang Shen, Yang Xu, Fanxu Meng, Fumin Li, Shengping Ruan and Weiyou Chen. *Semitransparent Polymer Solar Cells Using V2O5/Ag/V2O5 as Transparent Anodes.* Organic Electronics, vol. 12, no. 7, pages 1223–1226, July 2011.

[Shen 2013] Chao Shen, Henner Kampwerth, Martin Green, Thorsten Trupke, Jürgen Carstensen and Andreas Schütt. *Spatially Resolved Photoluminescence Imaging of Essential Silicon Solar Cell Parameters and Comparison with CELLO Measurements.* Solar Energy Materials and Solar Cells, vol. 109, pages 77–81, 2013.

[Sheng 2014] Jiang Sheng, Ke Fan, Dan Wang, Can Han, Junfeng Fang, Pingqi Gao and Jichun Ye. *Improvement of the SiO x Passivation Layer for High-Efficiency Si/PEDOT:PSS Heterojunction Solar Cells.* ACS Applied Materials & Interfaces, vol. 6, no. 18, pages 16027–16034, September 2014.

[Shin 2017] Hyeondeok Shin, Ye Luo, Panchapakesan Ganesh, Janakiraman Balachandran, Jaron T. Krogel, Paul R. C. Kent, Anouar Benali and Olle Heinonen. *Electronic Properties of Doped and Defective NiO: A Quantum Monte Carlo Study.* Physical Review Materials, vol. 1, no. 7, page 073603, December 2017.

[Shirota 1994] Yasuhiko Shirota, Yoshiyuki Kuwabara, Hiroshi Inada, Takeo Wakimoto, Hitoshi Nakada, Yoshinobu Yonemoto, Shin Kawami and Kunio Imai. *Multilayered Organic Electroluminescent Device Using a Novel Starburst Molecule, 4,4',4'-tris(3-methylphenylphenylamino)Triphenylamine, as a Hole Transport Material.* Applied Physics Letters, vol. 65, no. 7, pages 807–809, August 1994.

[Shockley 1952] W. Shockley and W. T. Read. *Statistics of the Recombinations of Holes and Electrons.* Physical Review, vol. 87, no. 5, pages 835–842, September 1952.

[Shockley 1960] William Shockley and Hans J Queisser. *Detailed Balance Limit of Efficiency of P-n Junction Solar Cells.* page 11, 1960.

[Si 2018] Fengjuan Si, Fuling Tang and Hongtao Xue. *Electronic Properties of NiO (1 1 0)/CH3NH3PbI3 (1 0 0) Interface from the First-Principles Calculations.* Chemical Physics Letters, vol. 707, pages 133–139, September 2018.

[Sinha 2021] Archana Sinha, Katherine Hurst, Sona Ulicna, Laura T. Schelhas, David C. Miller and Peter Hacke. *Assessing UV-Induced Degradation in Bifacial Modules of Different Cell Technologies.* In 2021 IEEE 48th Photovoltaic Specialists Conference (PVSC), pages 0767–0770, Fort Lauderdale, FL, USA, June 2021. IEEE.

[Sinton 1996a] R.A. Sinton, A. Cuevas and M. Stuckings. *Quasi-Steady-State Photoconductance, a New Method for Solar Cell Material and Device Characterization.* In Conference Record of the Twenty Fifth IEEE Photovoltaic Specialists Conference - 1996, pages 457–460, 1996.

[Sinton 1996b] Ronald A. Sinton and Andres Cuevas. *Contactless Determination of Current-Voltage Characteristics and Minority-Carrier Lifetimes in Semiconductors from Quasi-Steady-State Photoconductance Data.* Applied Physics Letters, vol. 69, no. 17, pages 2510–2512, 1996.

[Sinton 2000] RA Sinton and Andrés Cuevas. *A Quasi-Steady-State Open-Circuit Voltage Method for Solar Cell Characterization.* 16th European Photovoltaic Solar . . . , no. May, pages 1–4, 2000.

[Soleimanpour 2013] Amir M. Soleimanpour, Ahalapitiya H. Jayatissa and Gamini Sumanasekera. *Surface and Gas Sensing Properties of Nanocrystalline Nickel Oxide Thin Films.* Applied Surface Science, vol. 276, pages 291–297, July 2013.

[Song 2012] Chunyan Song, Hong Chen, Yi Fan, Jinsong Luo, Xiaoyang Guo and Xingyuan Liu. *High-Work-Function Transparent Conductive Oxides with Multilayer Films.* Applied Physics Express, vol. 5, no. 4, page 041102, March 2012.

[Stabler 1977] D. L. Stabler and C. R. Wronski. *Reversible Conductive Charges in This Charge-produced Amorphous Silicon.* Applied Physics Letters, vol. 31, page 292, 1977.

[Strukov 2008] Dmitri B. Strukov, Gregory S. Snider, Duncan R. Stewart and R. Stanley Williams. *The Missing Memristor Found.* Nature, vol. 453, no. 7191, pages 80–83, May 2008.

[Sugiyama 2000] Kiyoshi Sugiyama, Hisao Ishii, Yukio Ouchi and Kazuhiko Seki. *Dependence of Indium-Tin-Oxide Work Function on Surface Cleaning Method as Studied by Ultraviolet and x-Ray Photoemission Spectroscopies.* Journal of Applied Physics, vol. 87, no. 1, pages 295–298, 2000.

[Swanson 1960] L. D. Swanson. *Private Communication with M.* Wolf and H. Rauschenbach (see [3]), 1960.

[Sze 1995] S. M. Sze and K Ng Kwok. Physics of Semiconductor Devices, volume 10 of *America.* 1995.

[Taguchi 2000] Mikio Taguchi, Kunihiro Kawamoto, Sadaji Tsuge, Toshiaki Baba, Hitoshi Sakata, Masashi Morizane, Kenji Uchihashi, Noboru Nakamura, Seiichi Kiyama and Osamu Oota. *HITTM Cells?High-Efficiency Crystalline Si Cells with Novel Structure.* Progress in Photovoltaics: Research and Applications, vol. 8, no. 5, pages 503–513, September 2000.

[Taguchi 2008] Mikio Taguchi, Eiji Maruyama and Makoto Tanaka. *Temperature Dependence of Amorphous/Crystalline Silicon Heterojunction Solar Cells.* Japanese Journal of Applied Physics, vol. 47, no. 2R, page 814, February 2008.

[Talledo 1995] A. Talledo and C. G. Granqvist. *Electrochromic Vanadium–Pentoxide–Based Films: Structural, Electrochemical, and Optical Properties.* Journal of Applied Physics, vol. 77, no. 9, pages 4655–4666, May 1995.

[Tan 2013] Zhan'ao Tan, Liangjie Li, Fuzhi Wang, Qi Xu, Shusheng Li, Gang Sun, Xiaohe Tu, Xuliang Hou, Jianhui Hou and Yongfang Li. *Solution-Processed Rhenium Oxide: A Versatile Anode Buffer Layer for High Performance Polymer Solar Cells with Enhanced Light Harvest.* Advanced Energy Materials, vol. 4, no. 1, page 1300884, 2013.

[Tanaka 1992] Makoto Tanaka, Mikio Taguchi, Takao Matsuyama, Toru Sawada, Shinya Tsuda, Shoichi Nakano, Hiroshi Hanafusa and Yukinori Kuwano. *Development of New A-Si/c-Si Heterojunction Solar Cells: ACJ-HIT (Artificially Constructed Junction-Heterojunction with Intrinsic Thin-Layer).* Japanese Journal of Applied Physics, vol. 31, no. Part 1, No. 11, pages 3518–3522, November 1992.

[Tang 1987] C. W. Tang and S. A. VanSlyke. *Organic Electroluminescent Diodes.* Applied Physics Letters, vol. 51, no. 12, pages 913–915, September 1987.

[Tilley 1980] R.J.D Tilley. In Chemical Physics of Solids and Surfaces, volume 8. London Chemical Society, London, m . w. roberts, j. m . thomas édition, 1980.

[Tokito 1996] Shizuo Tokito, Koji Noda and Yasunori Taga. *Metal Oxides as a Hole-Injecting Layer for an Organic Electroluminescent Device.* Journal of Physics D: Applied Physics, vol. 29, page 2750, 1996.

[Tour 2008] James M. Tour and Tao He. *The Fourth Element.* Nature, vol. 453, no. 7191, pages 42–43, May 2008.

[Tran 2020] Tuan Anh Tran, Thanh Thuy Trinh, Truong Doan Viet, Le Van Ngoc, Huy Binh Do, Ngo Thi Thanh Giang, Sangho Kim, Duy Phong Pham, Junsin Yi and Vinh-Ai Dao. *Effects of Oxidation State on Photovoltaic Properties of Reactively Magnetron Sputtered Hole-Selective WO x Contacts in Silicon Heterojunction Solar Cells.* Semiconductor Science and Technology, vol. 35, no. 4, page 045020, March 2020.

[Tress 2011a] Wolfgang Tress, Karl Leo and Moritz Riede. *Influence of Hole-Transport Layers and Donor Materials on Open-Circuit Voltage and Shape of I–V Curves of Organic Solar Cells.* Advanced Functional Materials, vol. 21, no. 11, pages 2140–2149, 2011.

[Tress 2011b] Wolfgang Tress, Annette Petrich, Markus Hummert, Moritz Hein, Karl Leo and Moritz Riede. *Imbalanced Mobilities Causing S-shaped IV Curves in Planar Heterojunction Organic Solar Cells.* Applied Physics Letters, vol. 98, no. 6, page 063301, February 2011.

[Tress 2012] Wolfgang Tress, Karl Leo and Moritz Riede. *Optimum Mobility, Contact Properties, and Open-Circuit Voltage of Organic Solar Cells: A Drift-Diffusion Simulation Study.* Physical Review B, vol. 85, no. 15, page 155201, April 2012.

[Tsumura 1997] T Tsumura and M Inagaki. *Lithium Insertion/Extraction Reaction on Crystalline MoO3.* Solid State Ionics, vol. 104, no. 3, pages 183–189, December 1997.

[Tsur 1999] Y. Tsur and I. Riess. *Self-Compensation in Semiconductors.* Physical Review B - Condensed Matter and Materials Physics, vol. 60, no. 11, pages 8138–8146, 1999.

[Uhrich 2008] Christian Uhrich, David Wynands, Selina Olthof, Moritz K. Riede, Karl Leo, Stefan Sonntag, Bert Maennig and Martin Pfeiffer. *Origin of Open Circuit Voltage in Planar and Bulk Heterojunction Organic Thin-Film Photovoltaics Depending on Doped Transport Layers.* Journal of Applied Physics, vol. 104, no. 4, page 043107, August 2008.

[Um 2016] Han-Don Um, Namwoo Kim, Kangmin Lee, Inchan Hwang, Ji Hoon Seo and Kwanyong Seo. *Dopant-Free All-Back-Contact Si Nanohole Solar Cells Using MoOx and LiF Films.* Nano Letters, vol. 16, no. 2, pages 981–987, February 2016.

[van Cleef 1996] M. W. M. van Cleef, M. W. H. Philippens, F. A. Rubinelli, M. Kolter and R. E. I. Schropp. *Electrical Transport Mechanisms in P+a-SiC:H/n c-Si Heterojunctions: Dark J-V-T Characteristics.* MRS Online Proceedings Library, vol. 420, no. 1, pages 239–244, December 1996.

[Van sark 2012] Wilfried G.J.H.M Van sark, Francesco Roca and Lars Korte. Physics and technology of amorphous-crystalline heteronstrutures sillicon solar cells. 2012.

[Varkey 1993] A. J. Varkey and A. F. Fort. *Solution Growth Technique for Deposition of Nickel Oxide Thin Films*. Thin Solid Films, vol. 235, no. 1, pages 47–50, November 1993.

[Varshni 1967] Y. P. Varshni. *Temperature Dependence of the Energy Gap in Semiconductors*. Physica, vol. 34, no. 1, pages 149–154, January 1967.

[Victoria 2021] Marta Victoria, Nancy Haegel, Ian Marius Peters, Ron Sinton, Arnulf Jäger-Waldau, Carlos del Cañizo, Christian Breyer, Matthew Stocks, Andrew Blakers, Izumi Kaizuka, Keiichi Komoto and Arno Smets. *Solar Photovoltaics Is Ready to Power a Sustainable Future*. Joule, vol. 5, no. 5, pages 1041–1056, May 2021.

[Vos 2016] Martijn F. J. Vos, Bart Macco, Nick F. W. Thissen, Ageeth A. Bol and W. M. M. (Erwin) Kessels. *Atomic Layer Deposition of Molybdenum Oxide from (NtBu)2(NMe2)2Mo and O2 Plasma*. Journal of Vacuum Science & Technology A, vol. 34, no. 1, page 01A103, January 2016.

[Wagenpfahl 2010] A. Wagenpfahl, D. Rauh, M. Binder, C. Deibel and V. Dyakonov. *S-Shaped Current-Voltage Characteristics of Organic Solar Devices*. Physical Review B, vol. 82, no. 11, page 115306, September 2010.

[Wagner 2012] Julia Wagner, Mark Gruber, Andreas Wilke, Yuya Tanaka, Katharina Topczak, Andreas Steindamm, Ulrich Hörmann, Andreas Opitz, Yasuo Nakayama, Hisao Ishii, Jens Pflaum, Norbert Koch and Wolfgang Brütting. *Identification of Different Origins for S-Shaped Current Voltage Characteristics in Planar Heterojunction Organic Solar Cells*. Journal of Applied Physics, vol. 111, no. 5, page 054509, March 2012.

[Wang 2010] Mingdong Wang, Qin Tang, Jin An, Fangyan Xie, Jian Chen, Shizhao Zheng, King Young Wong, Qian Miao and Jianbin Xu. *Performance and Stability Improvement of P3HT:PCBM-Based Solar Cells by Thermally Evaporated Chromium Oxide (CrOx) Interfacial Layer*. ACS Applied Materials & Interfaces, vol. 2, no. 10, pages 2699–2702, October 2010.

[Wang 2011] J. C. Wang, X. C. Ren, S. Q. Shi, C. W. Leung and Paddy K. L. Chan. *Charge Accumulation Induced S-shape J–V Curves in Bilayer Heterojunction Organic Solar Cells*. Organic Electronics, vol. 12, no. 6, pages 880–885, June 2011.

[Wang 2014] Kuo-Chin Wang, Jun-Yuan Jeng, Po-Shen Shen, Yu-Cheng Chang, Eric Wei-Guang Diau, Cheng-Hung Tsai, Tzu-Yang Chao, Hsu-Cheng Hsu, Pei-Ying Lin, Peter Chen, Tzung-Fang Guo and Ten-Chin Wen. *P-Type Mesoscopic Nickel Oxide/Organometallic Perovskite Heterojunction Solar Cells*. Scientific Reports, vol. 4, no. 1, page 4756, April 2014.

[Watahiki 2015] Tatsuro Watahiki, Takeo Furuhata, Tsutomu Matsuura, Tomohiro Shinagawa, Yusuke Shirayanagi, Takayuki Morioka, Tetsuro Hayashida, Yohei Yuda, Shintaro Kano,

Yuichi Sakai, Hidetada Tokioka, Yoshihiko Kusakabe and Hiroyuki Fuchigami. *Rear-Emitter Si Heterojunction Solar Cells with over 23% Efficiency.* 2015.

[Wei 2014] Jie Wei, Yan Lei, Huimin Jia, Jiamei Cheng, Hongwei Hou and Zhi Zheng. *Controlled in Situ Fabrication of Ag 2 O/AgO Thin Films by a Dry Chemical Route at Room Temperature for Hybrid Solar Cells.* Dalton Transactions, vol. 43, no. 29, pages 11333–11338, 2014.

[Werner 2015] J. Werner, G. Dubuis, A. Walter, P. Löper, S.-J. Moon, S. Nicolay, M. Morales-Masis, S. De Wolf, B. Niesen and C. Ballif. *Sputtered Rear Electrode with Broadband Transparency for Perovskite Solar Cells.* Solar Energy Materials and Solar Cells, vol. 141, 2015.

[Werner 2016] Jérémie Werner, Jonas Geissbühler, Ali Dabirian, Sylvain Nicolay, Monica Morales-Masis, Stefaan De Wolf, Bjoern Niesen and Christophe Ballif. *Parasitic Absorption Reduction in Metal Oxide-Based Transparent Electrodes: Application in Perovskite Solar Cells.* ACS Applied Materials & Interfaces, vol. 8, no. 27, pages 17260–17267, July 2016.

[Wilson 2020] Gregory M Wilson, Mowafak Al-Jassim, Wyatt K Metzger, Stefan W Glunz, Pierre Verlinden, Gang Xiong, Lorelle M Mansfield, Billy J Stanbery, Kai Zhu, Yanfa Yan, Joseph J Berry, Aaron J Ptak, Frank Dimroth, Brendan M Kayes, Adele C Tamboli, Robby Peibst, Kylie Catchpole, Matthew O Reese, Christopher S Klinga, Paul Denholm, Mahesh Morjaria, Michael G Deceglie, Janine M Freeman, Mark A Mikofski, Dirk C Jordan, Govindasamy TamizhMani and Dana B Sulas-Kern. *The 2020 Photovoltaic Technologies Roadmap.* Journal of Physics D: Applied Physics, vol. 53, no. 49, page 493001, December 2020.

[Witteck 2017a] Robert Witteck, Henning Schulte-Huxel, Boris Veith-Wolf, Malte Ruben Vogt, Fabian Kiefer, Marc Kontges, Robby Peibst and Rolf Brendel. *Reducing UV Induced Degradation Losses of Solar Modules with C-Si Solar Cells Featuring Dielectric Passivation Layers.* In 2017 IEEE 44th Photovoltaic Specialist Conference (PVSC), pages 1366–1370, June 2017.

[Witteck 2017b] Robert Witteck, Boris Veith-Wolf, Henning Schulte-Huxel, Arnaud Morlier, Malte R. Vogt, Marc Köntges and Rolf Brendel. *UV-induced Degradation of PERC Solar Modules with UV-transparent Encapsulation Materials.* Progress in Photovoltaics: Research and Applications, vol. 25, no. 6, pages 409–416, 2017.

[Wolf 1963] Martin Wolf and Hans Rauschenbach. *Series Resistance Effects on Solar Cell Measurements.* Advanced Energy Conversion, vol. 3, no. 2, pages 455–479, April 1963.

[Woods-Robinson 2020] Rachel Woods-Robinson, Angela N. Fioretti, Jan Haschke, Mathieu Boccard, Kristin A. Persson and Christophe Ballif. *Linking Simulation and Synthesis of Nickel Oxide Hole-Selective Contacts for Silicon Heterojunction Solar Cells.* In 2020 47th IEEE Photovoltaic Specialists Conference (PVSC), pages 0569–0573, June 2020.

[Woods-Robinson 2021] Rachel Woods-Robinson, Angela N. Fioretti, Jan Haschke, Mathieu Boccard, Kristin A. Persson and Christophe Ballif. *Evaluating Materials Design Parameters of Hole-Selective Contacts for Silicon Heterojunction Solar Cells.* IEEE Journal of Photovoltaics, vol. 11, no. 2, pages 247–258, March 2021.

[Wu 2004] Qi-Hui Wu, A Thissen, W Jaegermann and Meilin Liu. *Photoelectron Spectroscopy Study of Oxygen Vacancy on Vanadium Oxides Surface.* Applied Surface Science, vol. 236, no. 1, pages 473–478, September 2004.

[Wu 2016] Weiliang Wu, Jie Bao, Xuguang Jia, Zongtao Liu, Lun Cai, Binhui Liu, Jingwei Song and Hui Shen. *Dopant-Free Back Contact Silicon Heterojunction Solar Cells Employing Transition Metal Oxide Emitters.* physica status solidi (RRL) – Rapid Research Letters, vol. 10, no. 9, pages 662–667, 2016.

[Wu 2017a] Weiliang Wu, Jie Bao, Zongtao Liu, Wenjie Lin, Xiao Yu, Lun Cai, Binhui Liu, Jingwei Song and Hui Shen. *Multilayer MoOx/Ag/MoOx Emitters in Dopant-Free Silicon Solar Cells.* Materials Letters, vol. 189, pages 86–88, February 2017.

[Wu 2017b] Weiliang Wu, Wenjie Lin, Jie Bao, Zongtao Liu, Binhui Liu, Kaifu Qiu, Yifeng Chen and Hui Shen. *Dopant-Free Multilayer Back Contact Silicon Solar Cells Employing V2Ox/Metal/V2Ox as an Emitter.* RSC Advances, vol. 7, no. 38, pages 23851–23858, April 2017.

[Wu 2018] Weiliang Wu, Wenjie Lin, Sihua Zhong, Bertrand Paviet-Salomon, Matthieu Despeisse, Zongcun Liang, Mathieu Boccard, Hui Shen and Christophe Ballif. *22% Efficient Dopant-Free Interdigitated Back Contact Silicon Solar Cells.* AIP Conference Proceedings, vol. 1999, no. 1, page 040025, August 2018.

[Wu 2020] Weiliang Wu, Wenjie Lin, Sihua Zhong, Bertrand Paviet-Salomon, Matthieu Despeisse, Quentin Jeangros, Zongcun Liang, Mathieu Boccard, Hui Shen and Christophe Ballif. *Dopant-Free Back-Contacted Silicon Solar Cells with an Efficiency of 22.1%.* physica status solidi (RRL) – Rapid Research Letters, vol. 14, no. 4, page 1900688, 2020.

[Wurfel 2015] Uli Wurfel, Andres Cuevas and Peter Wurfel. *Charge Carrier Separation in Solar Cells.* IEEE Journal of Photovoltaics, vol. 5, no. 1, pages 461–469, January 2015.

[Würfel 2016] Peter Würfel and Uli Würfel. Physics of Solar Cells: From Basic Principles to Advanced Concepts. John Wiley & Sons, September 2016.

[Xu 2021] Zhiyuan Xu, Shanglong Peng, Hao Lin, Shuhao Tian, Zilei Wang, Jian He, Lun Cai, Juan Hou and Pingqi Gao. *Solution-Processed Copper-Doped Chromium Oxide with Tunable Oxygen Vacancy for Crystalline Silicon Solar Cells Hole-Selective Contacts.* Solar RRL, vol. 5, no. 5, page 2100064, 2021.

[Xue 2017] Muyu Xue, Raisul Islam, Andrew C. Meng, Zheng Lyu, Ching-Ying Lu, Christian Tae, Michael R. Braun, Kai Zang, Paul C. McIntyre, Theodore I. Kamins, Krishna C. Saraswat

and James S. Harris. *Contact Selectivity Engineering in a 2 Mm Thick Ultrathin C-Si Solar Cell Using Transition-Metal Oxides Achieving an Efficiency of 10.8%.* ACS Applied Materials & Interfaces, vol. 9, no. 48, pages 41863–41870, December 2017.

[Yajima 1958] Tatsuo Yajima and Leo Esaki. *Excess Noise in Narrow Germanium P-n Junctions.* Journal of the Physical Society of Japan, vol. 13, no. 11, pages 1281–1287, November 1958.

[Yang 2006] Y. Yang, X.W. Sun, B.J. Chen, C.X. Xu, T.P. Chen, C.Q. Sun, B.K. Tay and Z. Sun. *Refractive Indices of Textured Indium Tin Oxide and Zinc Oxide Thin Films.* Thin Solid Films, vol. 510, no. 1-2, pages 95–101, July 2006.

[Yang 2008a] J. Joshua Yang, Matthew D. Pickett, Xuema Li, Douglas A. A. Ohlberg, Duncan R. Stewart and R. Stanley Williams. *Memristive Switching Mechanism for Metal/Oxide/Metal Nanodevices.* Nature Nanotechnology, vol. 3, no. 7, pages 429–433, July 2008.

[Yang 2008b] Woo-Young Yang, Wan-Gee Kim and Shi-Woo Rhee. *Radio Frequency Sputter Deposition of Single Phase Cuprous Oxide Using Cu2O as a Target Material and Its Resistive Switching Properties.* Thin Solid Films, vol. 517, no. 2, pages 967–971, November 2008.

[Yang 2016] Xinbo Yang, Qunyu Bi, Haider Ali, Kristopher Davis, V. Winston Schoenfeld and Klaus Weber. *High-Performance TiO2-Based Electron-Selective Contacts for Crystalline Silicon Solar Cells.* Advanced Materials, pages 5891–5897, 2016.

[Yang 2017] Zhenhai Yang, Pingqi Gao, Jian He, Wenchao Chen, Wen-yan Yin, Yuheng Zeng, Wei Guo, Jichun Ye and Yi Cui. *Tuning of the Contact Properties for High- E Ffi Ciency Si/PEDOT:PSS Heterojunction Solar Cells.* 2017.

[Yang 2018] Xueliang Yang, Wei Liu, Jingwei Chen and Yun Sun. *On the Annealing-Induced Enhancement of the Interface Properties of NiO:Cu/Wet-SiOx/n-Si Tunnelling Junction Solar Cells.* Applied Physics Letters, vol. 112, no. 17, page 173904, April 2018.

[Yang 2020] Xinbo Yang, Hang Xu, Wenzhu Liu, Qunyu Bi, Lujia Xu, Jingxuan Kang, Mohamed N. Hedhili, Baoquan Sun, Xiaohong Zhang and Stefaan De Wolf. *Atomic Layer Deposition of Vanadium Oxide as Hole-Selective Contact for Crystalline Silicon Solar Cells.* Advanced Electronic Materials, vol. 6, no. 8, page 2000467, 2020.

[Yoshikawa 2017] Kunta Yoshikawa, Hayato Kawasaki, Wataru Yoshida, Toru Irie, Katsunori Konishi, Kunihiro Nakano, Toshihiko Uto, Daisuke Adachi, Masanori Kanematsu, Hisashi Uzu and Kenji Yamamoto. *Silicon Heterojunction Solar Cell with Interdigitated Back Contacts for a Photoconversion Efficiency over 26%.* Nature Energy, vol. 2, no. 5, page 17032, March 2017.

[You 2007] Han You, Yanfeng Dai, Zhiqiang Zhang and Dongge Ma. *Improved Performances of Organic Light-Emitting Diodes with Metal Oxide as Anode Buffer.* Journal of Applied Physics, vol. 101, no. 2, page 026105, January 2007.

[Yu 2018] Zhengshan J. Yu, Joe V. Carpenter and Zachary C. Holman. *Techno-Economic Viability of Silicon-Based Tandem Photovoltaic Modules in the United States.* Nature Energy, vol. 3, no. 9, pages 747–753, September 2018.

[Yu 2019] Fei Yu, Gongyi Huang, Wei Lin and Chuanzhong Xu. *Lumped-Parameter Equivalent Circuit Model for S-Shaped Current–Voltage Characteristics of Organic Solar Cells.* IEEE Transactions on Electron Devices, vol. 66, no. 1, pages 670–677, January 2019.

[Yu 2020] Fei Yu, Ying Liang, Xiaofang Sun, Gongyi Huang and Chuanzhong Xu. *Modelling Solar Cells' S-shaped I-V Characteristics with an Analytical Solution to Lumped-Parameter Equivalent Circuit Model.* Solar Energy, vol. 202, pages 498–506, May 2020.

[Zhang 2013] D. Zhang, I. A. Digdaya, R. Santbergen, R. A. C. M. M. van Swaaij, P. Bronsveld, M. Zeman, J. A. M. van Roosmalen and A. W. Weeber. *Design and Fabrication of a SiOx/ITO Double-Layer Anti-Reflective Coating for Heterojunction Silicon Solar Cells.* Solar Energy Materials and Solar Cells, vol. 117, pages 132–138, October 2013.

[Zhang 2016a] Hong Zhang, Jiaqi Cheng, Francis Lin, Hexiang He, Jian Mao, Kam Sing Wong, Alex K.-Y. Jen and Wallace C. H. Choy. *Pinhole-Free and Surface-Nanostructured NiOx Film by Room-Temperature Solution Process for High-Performance Flexible Perovskite Solar Cells with Good Stability and Reproducibility.* ACS Nano, vol. 10, no. 1, pages 1503–1511, January 2016.

[Zhang 2016b] Xinyu Zhang, Yimao Wan, James Bullock, Thomas Allen and Andres Cuevas. *Low Resistance Ohmic Contact to P-Type Crystalline Silicon via Nitrogen-Doped Copper Oxide Films.* Applied Physics Letters, vol. 109, no. 5, page 052102, August 2016.

[Zhang 2018] Tian Zhang, Chang-Yeh Lee, Yimao Wan, Sean Lim and Bram Hoex. *Investigation of the Thermal Stability of MoOx as Hole-Selective Contacts for Si Solar Cells.* Journal of Applied Physics, vol. 124, no. 7, page 073106, August 2018.

[Zhao 2008] L. Zhao, C. L. Zhou, H. L. Li, H. W. Diao and W. J. Wang. *Role of the Work Function of Transparent Conductive Oxide on the Performance of Amorphous/Crystalline Silicon Heterojunction Solar Cells Studied by Computer Simulation.* Physica Status Solidi (A) Applications and Materials Science, vol. 205, no. 5, pages 1215–1221, 2008.

[Zhong 2020] Sihua Zhong, Julie Dreon, Quentin Jeangros, Erkan Aydin, Stefaan De Wolf, Fan Fu, Mathieu Boccard and Christophe Ballif. *Mitigating Plasmonic Absorption Losses at Rear Electrodes in High-Efficiency Silicon Solar Cells Using Dopant-Free Contact Stacks.* Advanced Functional Materials, vol. 30, no. 5, page 1907840, 2020.

[Zhu 2014] Zonglong Zhu, Yang Bai, Teng Zhang, Zhike Liu, Xia Long, Zhanhua Wei, Zilong Wang, Lixia Zhang, Jiannong Wang, Feng Yan and Shihe Yang. *High-Performance Hole-Extraction Layer of Sol–Gel-Processed NiO Nanocrystals for Inverted Planar Perovskite Solar Cells.* Angewandte Chemie International Edition, vol. 53, no. 46, pages 12571–12575, 2014.

[Ziegler 2015] Johannes Ziegler, Mathias Mews, Kai Kaufmann, Thomas Schneider, Alexander N. Sprafke, Lars Korte and Ralf B. Wehrspohn. *Plasma-Enhanced Atomic-Layer-Deposited MoOxemitters for Silicon Heterojunction Solar Cells.* Applied Physics A, vol. 120, no. 3, pages 811–816, September 2015.

[Zielke 2015] Dimitri Zielke, Claudia Niehaves, Wilfried Lövenich, Andreas Elschner, Matthias Hörteis and Jan Schmidt. *Organic-Silicon Solar Cells Exceeding 20% Efficiency.* Energy Procedia, vol. 77, pages 331–339, 2015.

[Zilberberg 2011] Kirill Zilberberg, Sara Trost, Hans Schmidt and Thomas Riedl. *Solution Processed Vanadium Pentoxide as Charge Extraction Layer for Organic Solar Cells.* Advanced Energy Materials, vol. 1, no. 3, pages 377–381, 2011.

[Zuo 2015] Chuantian Zuo and Liming Ding. *Solution-Processed Cu2O and CuO as Hole Transport Materials for Efficient Perovskite Solar Cells.* Small, vol. 11, no. 41, pages 5528–5532, 2015.

Publication list

Publications as first author

1. J. Dréon, Q. Jeangros, J. Cattin, J. Haschke, L. Antognini, C.Ballif and M. Boccard, *"23.5%-efficient silicon heterojunction solar cell using molybdenum oxide as hole-selective contact"*, Nano Energy (2020)

2. J. Dréon, J. Cattin, G. Chrsitmann, D. Fébba, V. Paratte, L. Antognini, W. Lin, S. Nicolay, C.Ballif and M. Boccard, *"Performance Limitations and Analysis of Silicon Heterojunction Solar Cells Using Ultra-Thin MoOx Hole-Selective Contacts"*, IEEE Journal of Photovoltaics (2021)

Publications as first co-author

3. J. Dréon*, J. Ibarra-Michel*, M. Boccard, J. Bullock and B. Macco, *"Carrier-selective contacts using metal compounds for crystalline silicon solar cells"*, Progress in Photovoltaics, Accepted (2022) (*: contributed equally as first co-authors)

Publications as second author

1. S. Essig, J. Dréon, J. Werner, P. Löper, S. De Wolf, M. Boccard and C. Ballif *"MoOx and WOx based hole-selective contacts for wafer-based Si solar cells"*, IEEE 44th Photovoltaic Specialist Conference (PVSC) (2017)

2. S. Essig, J. Dréon, E. Rucavado, M. Mews, T. Koida, M. Boccard, J. Werner, J. Geissbühler, P. Löper, M. Morales-Masi, L. Korte, S. De Wolf, and C. Ballif *"Toward Annealing-Stable Molybdenum-Oxide-Based Hole-Selective Contacts For Silicon Photovoltaics"*, Solar RRL (2018)

3. S. Zhong, J. Dréon, Q. Jeangros, E. Aydin, A. De Wolf, F. Fu, M. Boccard and C. Ballif, *"Mitigating Plasmonic Absorption Losses at Rear Electrodes in High-Efficiency Silicon Solar Cells Using Dopant-Free Contact Stacks"* Advanced Functional Materials (2019)

4. W. Lin, J. Dréon, S. Zhong, V. Paratte, L. Antognini, J. Cattin, Z. Liu, Z. Liang, P. Gao,

H. Shen, C. Ballif and M. Boccard, *"Dopant-Free Bifacial Silicon Solar Cells"* Solar RRL (2021)

5. A.H.T. Le, J. Dréon, J. Ibarra-Michel, M. Boccard, J. Bullock, N. Borojevic, Z. Hameiri, *"Temperature-dependent performance of silicon heterojunction solar cells with transition-metal-oxide-based selective contacts"*, Progress in Photovoltaics: Research and Applications (2021)

Publications as co-author

1. M. Boccard, L. Antognini, J. Cattin, J. Dréon, O. Dupré, A. Fioretti, J. Haschke, R. Monnard, M. Morales-Masis, V. Paratte, E. Rucavado, L.-L. Senaud, S. Zhong, B. Paviet-Salomon, M. Despeisse, C. Ballif, *"Paths for maximal light incoupling and excellent electrical performances in silicon heterojunction solar cells"*, 2019 IEEE 46th Photovoltaic Specialists Conference (PVSC) (2019)

2. M. Boccard, L. Antognini, V. Paratte, J. Haschke, M. Truong, J. Cattin, J. Dréon, W. Lin, L.-L. Senaud, B. Paviet-Salomon, S. Nicolay, M. Despeisse, C. Ballif, *"Hole-selective front contact stack enabling 24.1%-efficient silicon heterojunction solar cells"*, IEEE Journal of Photovoltaics (2020)

3. W. Lin, M. Boccard, S. Zhong, V. Paratte, Q. Jeangros, L. Antognini, J. Dreon, J. Cattin, J. Thomet, Z. Liu, Z. Chen, Z. Liang, P. Gao, H. Shen, C. Ballif, *"Degradation Mechanism and Stability Improvement of Dopant-Free ZnO/LiFx/Al Electron Nanocontacts in Silicon Heterojunction Solar Cells"*, ACS Applied Nano Materials (2020)

4. D. Fébba, V. Paratte, L. Antognini, J. Dréon, J. Hurni, J. Thomet, R. Rubinger, E. Bortoni, C. Ballif, M. Boccard, *"Effects of Work Function and Electron Affinity on the Performance of Carrier-Selective Contacts in Silicon Solar Cells Using $ZnSn_xGe_{1-x}N$ as a Case Study"*, IEEE Journal of Photovoltaics (2021)

5. L. Antognini, V. Paratte, J. Haschke, J. Cattin, J. Dréon, M. Lehmann, L.-L. Senaud, Q. Jeangros, C. Ballif, M. Boccard, *"Influence of the Dopant Gas Precursor in P-Type Nanocrystalline Silicon Layers on the Performance of Front Junction Heterojunction Solar Cells"*, IEEE Journal of Photovoltaics (2021)

6. D. Fébba, V. Paratte, L. Antognini, J. Dréon, J. Hurni, J. Thomet, C. Ballif, M. Boccard, *"$ZnSn_xGe_{1-x}N_2$ as electron-selective contact for silicon heterojunction solar cells"*, 2021 IEEE 48th Photovoltaic Specialists Conference (PVSC) (2021)

Conference presentations

1. J. Dréon, C. Ballif, M. Boccard, *"Influence of MoOx and (i)a-Si:H layer thicknesses on the properties and stability of c-Si heterojunction solar cells"*, **Oral** presentation, presented

at the EMRS Spring 2019, Nice, France (2019)

2. J. Dréon, M. Boccard, L. Antognini, J. Cattin, O. Dupré, A.N. Fioretti, J. Haschke, V. Paratte, S. Zhong and C. Ballif, *"Design and Characterization of High Efficiency Silicon Heterojunction Solar Cells"*, **Oral** presentation, presented at the 36th European Photovoltaic Solar Energy Conference, Marseille, France (2019)

3. J. Dréon, L. Wenjie, V. Paratte, J. Cattin, G. Christmann, L. Antognini, C. Ballif and M. Boccard, *"Final study of MoOx Thickness Variation Influence on Partial Dopant-Free Silicon Heterojunction Solar Cells "*, **Plenary oral** presentation, presented at the 37th European Photovoltaic Solar Energy Conference, Online (2021)